

Engineering Contractile 2D and 3D Human Skeletal and Cardiac Muscle Microtissues

Submitted in partial fulfillment of the requirements for

the degree of

Doctor of Philosophy

in

Biomedical engineering

Rebecca Marie Duffy

B.S., Biomedical Engineering, Virginia Commonwealth University

Carnegie Mellon University
Pittsburgh, PA

August, 2016

Dedication

In memory of Sue, Phil, and Bill.

You are always in my heart

Thank you to my parents, Jerry and Lisa, for always encouraging me to do my best. I wouldn't be the person I am today without all of the valuable lessons you've taught me - following through on things you start, understanding how to juggle priorities, the importance of family, how to stay true to yourself, and how to stand up for yourself. You've always told me you'd be proud of me as long as I did my best...and it looks like you've served me pretty well with that attitude. I'm so grateful for all of the sacrifices the two of you have made (that I'm probably unaware of) to make my life better and give me all of the best opportunities you could over the years.

Thank you to my grandparents, Shelby and Jimmy - you two are such an important part of my life, and I want to thank you for busting your butts to raise two amazing kids and for reminding me to have perspective on how lucky I have been to be blessed with the opportunities life has given me.

My grandparents Big Ed, Margaret, and BK. You all were also testaments to working hard to achieve your goals and provide for your families, and I just hope I continue to make you proud.

To Kevin, thank you for keeping me balanced through this whole experience. The distance hasn't made things easy the last 3 years, but it's been so worth it. Thank you for believing in me even when I don't believe in myself, for bringing me back to reality when I start to take myself too seriously, and for always being able to make me laugh when I need it most. Here's to starting our next adventure (together)!

To Lacy - my sister from another mister. You've been my partner in crime for almost 20 years now! I have always been able to lean on you through good times and bad, and I'm so excited that we've been able to encourage each other to follow our dreams (and actually see it happen in real time), from running around like hooligans on the playground, to the hilariously nerdy phases of middle and high school, to the current chapter where you're totally killing it as an editor, and I'm going to try and be the crazy mad scientist.

To Kristy - I can't believe how lucky I was to start of my Pittsburgh adventure with you as my roommate. So many things have changed since I moved in with you 5 years ago, and I'm excited to see where the next 5 years take us. Thank you for everything you brilliant, glittering, witty, incandescent lioness!

To Savannah, Zak, and Gabe. I love you guys like my own siblings and can't imagine getting to this step without all of your love and support. I decided to head off on this journey right after we all went through one of the most devastating losses I've ever experienced. But you all helped keep me strong and have always encouraged my nerd-ness (even if you show it by relentless teasing). Just don't let me turn into Dr. Steve....

And to all of my extended Duffy, Loehr, Durham and Aycock families. I've been so blessed to have such large families on all sides of my family. You all make life way more fun, and I've been able to count on all of you throughout the years.

Acknowledgements

The biggest of thank yous to all of the friends, mentors, collaborators, and funding sources that made all of this possible.

To Professor Feinberg, thank you for taking me under your wing in a new lab and always encouraging me to do more than I thought I could. It's been a rollercoaster at times, but I've learned more than I even thought possible when I first started. You've enabled me to continue to work on projects that I still get very excited about (even if it's not as obvious to others that I am, in fact, very excited), and your encouragement helped me land a job that I didn't even think I'd be able to get. I'm excited to see where the next few years lead.

My committee members - Professors Phil Campbell, Chris Bettinger, and Fabrisia Ambrosio. Thank you for your words of encouragement, insightful discussions, and input through the years.

Thank you also to all of the faculty and staff that have made my experience here at CMU a really enjoyable one! Thank you to Dr. Wang, I remember our initial conversations when I was visiting before I chose grad school, and your commitment to having happy and healthy students was a significant part of why I chose to come here. To all of the staff (Kristin, Vanessa, Kristyn, Ryan, Keri, Julie and Crystal and Maryia) who have made my years as a grad student fun and have helped deal with all of the fun administrative stuff.

For specific contributions to this dissertation:

Yiyi Yu from Ge Yang's lab in Biomedical Engineering at CMU assisted with initial SDS-PAGE gels for analysis of laminin weight in Chapter 4.

Logan Plath from Mark Bier's lab in Chemistry at CMU for performed the MALDI-TOF mass spectroscopy analysis of laminin in Chapter4.

Breanna Duffy from Lauren Black's lab at Tufts performed LCMS analysis of laminin compositions in Chapter 4.

Tong Lu from Carmel Majidi's lab in Mechanical Engineering at CMU - thank you for providing countless laser cut inserts for the 3D cardiac muscle tissues in Chapter 6.

Wei Chen and Recep Onler from the Burak Ozdoganlar lab in Mechanical Engineering for 3D prints of molds used in Chapter 6 and for use of the profilometer to obtain insert thicknesses.

Mathilde Vermeer and Dr. Peter Van Der Meer for getting our human embryonic stem cell culture off the ground.

Seth Thompson from Professor Huard's lab at University of Pittsburgh for providing the first vial of human SkMDC cells and insights into the fickle nature of human derived cells.

To all of my lab mates, thanks for making the adventure interesting. John Szymanski for being the brave one as the first grad student in our lab (and for training me in the nanofab facility for the SU-8 stamps used in Chapter 5). Quentin Jallerat and Ivan Batalov, thank you for all of your stem cell culture expertise and the countless laughs and pain that went along with differentiating cardiomyocytes. Thank you to TJ Hinton for initial 3D printed molds, designing the physical temperature controlled stage used for 2D and 3D experiments, and laser cutter training. Thank you to Yan Sun, visiting scholar from Beijing University, for training me and

passing the torch on the initial muscular thin film project. Thanks to Alkiviadis Tsamis for generating bending models of inserts and lookup tables for bending inserts for Chapter 6.

Rachelle Palchesko Simko, I can't thank you enough for all of the mentoring, sound boarding, lunches, and generally keeping me sane and encouraging me to keep going. You've been an amazing role model and I'm going to feel like I'm missing my right hand when I move to my new job without you around.

Molly Bank, I'm so happy that grad school brought us together. We've had countless adventures through the years, and I'm so excited to see what your career evolves into. I can't thank you enough for always being there – you let me be a temporary live in roommate during my proposal exam when my leases didn't overlap, you let me vent to you on an almost daily basis while you were wrapping up your own PhD and made it look easy, and you've always been a shoulder to lean on, an inspiration, and one of the most generous people I've had the honor of knowing.

Stephanie Wong, Elaine Soohoo, Stephanie Chang, Natasha Loghmanpour - you ladies have also been such an important part of this whole experience, general commiserating, bouncing ideas around, developing cat lady habits, and making a lot of wonderful memories inside and outside of the PTC and Scott Hall.

All of my undergrads I've had the pleasure of working with: Briana Larkin, Lucas Friedman, Sabrina Liu, Stacy Chang, Eileen Ge, and Ally Vendetti. I wish you the best in your future endeavors!

Also, to Jaci who is undertaking the behemoth that is the 3D cardiac MIFIs, I'm so happy to be leaving this in capable hands! I look forward to us working together, even if it's from afar, to wrap up some of my initial work. Best of luck during your grad career.

Finally, I was fortunate to receive the John and Clair Bertucci Fellowship as part of my funding during my studies here. My work (and stipend...and tuition) has also been made possible by Professor Feinberg's funding sources from the NIH and HFSP. I also want to thank the Biomedical Engineering Department as a whole for accepting me in the program and providing so many wonderful resources throughout the completion of my degree.

Abstract

Skeletal and cardiac muscles are crucial biological actuators with limited capacity to repair themselves after significant trauma or disease states. Engineering these complex tissues using human derived cells has potential applications to serve as more physiologically relevant and economical test beds for regenerative medicine therapies compared to animal models and costly human trials. However, before we can engineer these tissues, we must first gain a better understanding of how the structure and composition of the extracellular matrix (ECM) influences differentiation and maturation into contractile muscle *in vitro*. To do this, we used traditional microcontact printing techniques to determine how ECM composition and line geometry influenced differentiating human skeletal muscle in 2D, and we incorporated these differentiating human myotubes into a muscular thin film (MTF) assay previously developed to measure 2D cardiomyocyte (CM) contractility. We also engineered contractile 3D cardiac microtissues with integrated force indicators (MIFIs) by seeding embryonic stem cell derived CMs and cardiac fibroblasts in biologically derived ECM hydrogels. From the 2D work, we found that human skeletal muscle derived cells had significantly higher myotube formation on laminin (LAM) lines, and C2C12 mouse myoblasts required more specific LAM line geometries than differentiating human skeletal muscle myoblasts to form uniaxially aligned myotubes. Additionally, we found that LAM with trace amounts of perlecan significantly increased human myotube formation compared to more purified LAM solutions. We also determined that 2D human skeletal muscle was limited to 1 week of differentiation before differentiating myoblasts delaminated from patterned polydimethylsiloxane. For the 3D engineered muscle constructs, we found that cardiac MIFIs could be maintained in culture for at least 2 weeks, exerted twitch forces $\sim 1 - 7 \mu\text{N}$ and responded as expected to excitatory pharmacological stimuli. We

developed the 3D MIFI assay using CMs with the intention of applying this platform to patient specific CMs from induced pluripotent stem cells as well as to differentiating skeletal muscle.

The findings we have made by engineering contractile 2D human skeletal muscle and 3D human cardiac microtissues have future applications as patient specific regenerative therapy models, test beds for pharmaceutical therapies, building blocks for engineering functional muscle replacements, and as soft robotics actuators.

Table of Contents

| | |
|--|-------------|
| List of Figures and Illustrations | xiii |
| List of Tables | xv |
| List of Acronyms | xvi |
| Chapter 1 Introduction to Engineering Contractile Skeletal and Cardiac Muscle | |
| 1.1 Introduction..... | 1 |
| 1.2 Dissertation Organization | 4 |
| 1.2.1 Chapter 2: Background on Engineered Skeletal and Cardiac Muscle | 4 |
| 1.2.2 Chapter 3: Understanding the Role of ECM Protein Composition and Geometric Micropatterning for Engineering Human Skeletal Muscle | 5 |
| 1.2.3 Chapter 4: Trace Amounts of Perlecan in Isolated Laminin Influences 2D Human Myotube Formation..... | 5 |
| 1.2.4 Chapter 5: Engineering Skeletal Muscular Thin Films: Troubleshooting and Future Directions..... | 6 |
| 1.2.5 Chapter 6: Engineering Cardiac Microtissues with Integrated Force Indicators for Force and Beat Frequency Analysis..... | 7 |
| Chapter 2 Background on Engineered Skeletal and Cardiac Muscle | |
| 2.1 Formation, Structure, and Function of Skeletal Muscle | 8 |
| 2.1.1. Myogenesis in Embryonic Development and Muscle Repair..... | 8 |
| 2.1.2. Hierarchical Organization and Control of the Contractile Apparatus | 9 |
| 2.2 Engineering the Microenvironment to Guide Skeletal Muscle Formation | 11 |
| 2.2.1. The Role of Substrate Stiffness and the Mechanical Environment | 11 |
| 2.2.2. Extracellular Matrix and the Spatial Organization of Biochemical Cues | 14 |
| 2.2.3. Physical and Topographical Cues that Guide Muscle Alignment | 16 |
| 2.2.4. Bioreactors for Mechanical and Electrical Conditioning..... | 18 |
| 2.3 Contractile Engineered Skeletal Muscle | 21 |
| 2.3.1. 2D Cantilever-Based Skeletal Muscle Actuators..... | 21 |
| 2.3.2. Tissue Engineered Skeletal Muscle Using ECM Protein Scaffolds | 23 |
| 2.3.3 Self-Organizing Myooids..... | 26 |
| 2.3.4 Scaffold-free Constructs | 26 |

| | |
|---|----|
| 2.4. Muscle-powered Soft Robotic Devices | 27 |
| 2.4.1. Basic Muscle-Powered Devices..... | 28 |
| 2.4.2. Muscle-Powered Soft Robots that Walk and Swim..... | 30 |
| 2.5 References for Chapters 1 and 2 | 33 |

Chapter 3 Understanding the Role of ECM Protein Composition and Geometric Patterning for Engineering Human Skeletal Muscle

| | |
|---|----|
| 3.1 Introduction..... | 37 |
| 3.2 Materials and Methods..... | 40 |
| 3.2.1 Substrate Fabrication | 40 |
| 3.2.2 Cell Culture | 41 |
| 3.2.3 Immunofluorescence Staining and Imaging | 42 |
| 3.2.4 Image Analysis..... | 42 |
| 3.2.5 Statistical Analysis..... | 43 |
| 3.3 Results..... | 43 |
| 3.3.1 C2C12 differentiation into myotubes is dependent on ECM composition and patterning | 43 |
| 3.3.2 LAM line width and spacing dictates C2C12 myotube differentiation and alignment..... | 47 |
| 3.3.3 Human SkMDCs differentiation into myotubes is dependent on ECM composition..... | 50 |
| 3.3.4 LAM line width and spacing has limited effect on human SkMDC myotube differentiation and alignment..... | 52 |
| 3.3.5 Micropattern geometries that maximize formation of aligned muscle is species specific..... | 54 |
| 3.4 Discussion | 56 |
| 3.5 Conclusions..... | 61 |
| 3.6 Acknowledgements..... | 61 |
| 3.7 References | 62 |

Chapter 4 Trace Amounts of Perlecan in Isolated Laminin Influences 2D Human Myotube Formation

| | |
|--|----|
| 4.1 Introduction..... | 65 |
| 4.2 Materials and Methods..... | 67 |
| 4.2.1 Microcontact Printing | 67 |
| 4.2.2 Cell culture: C2C12 | 68 |
| 4.2.3 Cell Culture: Human SkMDC..... | 68 |
| 4.2.4 Immunofluorescence Staining and Imaging | 69 |
| 4.2.5 Image Analysis..... | 69 |
| 4.2.6 Deglycosylation of LAMs and Polyacrylamide Gel Electrophoresis | 69 |
| 4.2.7 Mass spectroscopy | 71 |
| 4.2.8 Statistical Analysis..... | 71 |
| 4.3 Results..... | 72 |
| 4.3.1 C2C12 and Human SkMDC Myotube Formation on LAM Lines is Brand Dependent | 72 |
| 4.3.2 Molecular Weight and Glycan Comparison of Laminins | 74 |
| 4.3.3 Mass Spectroscopy Analysis of Laminins | 77 |
| 4.4 Discussion and Conclusions | 80 |
| 4.5 References..... | 83 |

Chapter 5 Engineering Skeletal Muscular Thin Films: Troubleshooting and Future Directions

| | |
|---|----|
| 5.1 Introduction..... | 84 |
| 5.2 Materials and Methods..... | 86 |
| 5.2.1 Stamp Fabrication – SPR 220.3 | 86 |
| 5.2.2 Stamp Fabrication – SU-8 2015..... | 87 |
| 5.2.3 Thin Film Fabrication and Thickness Measurement | 87 |
| 5.2.4 Microcontact Printing on Thin Films..... | 88 |
| 5.2.5 Cell Culture - C2C12 | 89 |
| 5.2.6 Cell Culture - Human SkMDCs..... | 90 |
| 5.2.7 MTF Stimulation..... | 90 |

| | |
|---|-----|
| 5.2.8 Patterning Fibronectin Lines with Genipin Crosslinker | 91 |
| 5.2.9 Fixing, Immunostaining, and Imaging | 91 |
| 5.2.10 Image Analysis..... | 92 |
| 5.2.11 Statistical Analysis..... | 92 |
| 5.3 Results..... | 93 |
| 5.3.1 Engineering Skeletal MTFs with LAM Lines | 93 |
| 5.3.2 Standardizing Length of Released MTF | 94 |
| 5.3.3 Equalizing ECM Transfer on Modified TFs | 98 |
| 5.3.4 Genipin Crosslinking of Fibronectin to PDMS to Maintain 2D Myotube Culture..... | 99 |
| 5.4 Discussion | 102 |
| 5.5. Conclusions..... | 105 |
| 5.6 References..... | 106 |

Chapter 6 Engineering Cardiac Microtissues with Integrated Force Indicators for Force and Beat Frequency Analysis

| | |
|---|-----|
| 6.1 Introduction..... | 108 |
| 6.2 Materials and Methods..... | 112 |
| 6.2.1 Design and preparation of PDMS wells and inserts | 112 |
| 6.2.2 Elastic modulus verification of PDMS inserts..... | 113 |
| 6.2.3 Cell Culture - HUES9-CMs | 113 |
| 6.2.4 Cell Culture - Human Cardiac Fibroblasts..... | 115 |
| 6.2.5 Cell Culture - C2C12s..... | 115 |
| 6.2.6 Casting Microtissues with Integrated Force Indicators | 116 |
| 6.2.7 Image Analysis of Tissue Compaction Tracking | 117 |
| 6.2.8 Contractility Assay..... | 117 |
| 6.2.9 Pharmacology assay..... | 118 |
| 6.2.10 Fixing and Immunofluorescence Staining | 118 |
| 6.2.11 Force measurements from bending inserts | 119 |
| 6.2.12 Statistical Analysis..... | 120 |
| 6.3 Results..... | 121 |
| 6.3.1 Design of 3D Platform for Microtissues with Integrated Force Indicators | 121 |

| | |
|--|------------|
| 6.3.2 Fibroblast Co-culture with HUES9-CM MIFIs | 125 |
| 6.3.3. Immunofluorescence Staining of Microtissues with Integrated Force Indicators..... | 127 |
| 6.3.4 Microtissues with Integrated Force Indicators Exert Measurable Force and Respond to Drugs in Contractility Assay..... | 130 |
| 6.4 Discussion and Conclusions | 141 |
| 6.5 References | 148 |
| Chapter 7 Summary and Future Directions | 149 |
| 7.1 Summary | 149 |
| 7.2 Future Directions | 152 |
| Appendix A LCMS Spectral Counts..... | 155 |
| Appendix B MIFI Length to Force Lookup Tables | 163 |
| Appendix C MATLAB Code - MIFI Length Measurement..... | 168 |
| Appendix D MATLAB Code - MIFI Force from Lookup Tables..... | 170 |
| Appendix E Presentations, Publications, and Posters..... | 171 |

List of Figures and Illustrations

| | |
|---|----|
| Figure 2.1 Schematics of the myogenesis process and hierarchical contractile apparatus of skeletal muscle tissue | 9 |
| Figure 2.2 Myoblast fusion into myotubes is sensitive to the mechanical properties of the underlying substrate | 13 |
| Figure 2.3 Micropatterned ECM proteins guide myoblast differentiation and alignment | 16 |
| Figure 2.4. Myotube alignment can be controlled using engineered substrate microtopography | 18 |
| Figure 2.5 Examples of different bioreactor designs and microfabricated electrodes for the electrical stimulation of engineered skeletal muscle constructs | 21 |
| Figure 2.6 . Engineered skeletal muscle tissue in the format of 2D cantilever-based actuators where the myotubes are integrated along the length of the beam | 22 |
| Figure 2.7 Examples of different types of 3D engineered skeletal muscle tissue | 25 |
| Figure 2.8 Examples of basic muscle-powered actuators and devices | 29 |
| Figure 2.9 Examples of muscle-powered soft robots that can walk and swim | 32 |
| | |
| Figure 3.1 Phase contrast images of C2C12 cells differentiated on FN, LAM, Col IV, and Col I | 44 |
| Figure 3.2 C2C12 myoblasts delaminate rapidly on Col I and Col IV | 45 |
| Figure 3.3 C2C12 myoblasts form longer, more nucleated myotubes on LAM lines | 46 |
| Figure 3.4 Myotubes formed on isotropic coatings of LAM | 47 |
| Figure 3.5 Representative images of C2C12 cells differentiated on 16 different line patterns of LAM | 48 |
| Figure 3.6 Quantification of C2C12 myotube alignment, area, length, and MFI on 16 LAM line geometries | 50 |
| Figure 3.7 C2C12 myotube area normalized for area LAM lines | 51 |
| Figure 3.8 Human SkMDCs form longer, more nucleated myotubes on LAM | 52 |
| Figure 3.9 Representative images of human myotube formation after 6 days of differentiation on 9 line patterns of LAM | 53 |

| | |
|---|-----|
| Figure 3.10 Quantification of human SkMDC myotube alignment, area, length, and MFI on 9 LAM line geometries | 54 |
| Figure 3.11 Human SkMDC myotube area normalized for area LAM | 55 |
| Figure 3.12 Scatterplots of myotube orientation v. percent area myotubes..... | 56 |
| Figure 3.13 Phase images of human SkMDCs on μ CP 100x20 lines of LAM..... | 57 |
| | |
| Figure 4.1 C2C12 myoblasts differentiated on BD and Invitrogen brand LAM | 72 |
| Figure 4.2 Human SkMDCs differentiated on different LAM brands..... | 74 |
| Figure 4.3 Quantification of myotube formation on different brands of LAM | 75 |
| Figure 4.4 SDS-PAGE of various LAM brands | 76 |
| Figure 4.5 MALDI-TOF Mass Spectroscopy Analysis of Different LAM Brands | 78 |
| Figure 4.6 Liquid Chromatography Mass Spectroscopy Analysis of LAMs..... | 80 |
| | |
| Figure 5.1 Fabrication of MTFs..... | 93 |
| Figure 5.2 Examples of best-case scenario C2C12 MTFs | 94 |
| Figure 5.3 Modification of MTF fabrication to standardize MTF release length..... | 95 |
| Figure 5.4 Differentiating C2C12 myotubes delaminate from LAM lines on PDMS in region with PIPAAm underneath PDMS | 97 |
| Figure 5.5 Myotube formation on PDMS and thin films with isotropically coated FN or LAM..... | 98 |
| Figure 5.6 Quantification of Myotube Area on FN and LAM PDMS Substrates | 99 |
| Figure 5.7 MTF assay is not robust enough for further development..... | 100 |
| Figure 5.8 Myotube differentiation time is limited by myotube delamination after myotubes reach a certain size | 101 |
| Figure 5.9 Analysis of Percent Area of Human Myotubes Differentiated for 3 to 6 Days | 101 |
| Figure 5.10 Genipin crosslinked FN lines on PDMS to prevent myotube peeling..... | 102 |
| | |
| Figure 6.1 Design Concept for Microtissue with Integrated Force Indicator | 111 |
| Figure 6.2 Iterative Plastic Mold and PDMS Insert Design Process | 122 |
| Figure 6.3 Finalized Mold and Insert Design. | 124 |

| | |
|--|-----|
| Figure 6.4 Cardiac Fibroblast Coculture is Necessary to Compact 3D Cardiac Microtissues | 125 |
| Figure 6.5 Representative Immunofluorescence Staining of Cardiac Microtissues with 10% Fibroblasts | 127 |
| Figure 6.6 Representative Immunofluorescence Staining of Cardiac Microtissues with 20% Fibroblasts | 128 |
| Figure 6.7 3D Collagen I Structure and Cell Organization..... | 129 |
| Figure 6.8 Finite Element Modeling of PDMS Insert Bending | 130 |
| Figure 6.9 Measuring Force Generation and Drug Response of Cardiac MIFIs | 133 |
| Figure 6.10 Force Plots of Day 14, 10% Fibroblast Constructs | 136 |
| Figure 6.11 Cardiac Microtissues Twitch Force and Beat Frequency Response to Stimulatory Drugs | 138 |
| Figure 6.12 Approximate Microtissue Cross-sectional Area Per Sample | 140 |
| Figure 6.13 Twitch Force Normalized for Approximate Microtissue and CM Area | 141 |

List of Tables

| | |
|---|----|
| Table 4.1 Manufacturer Information on Supplied Laminins..... | 71 |
|---|----|

List of Acronyms

| | |
|--|--------------|
| Beckton Dickinson..... | BD |
| Cardiomyocyte..... | CM |
| Collagen type I..... | Col I |
| Collagen type IV..... | Col IV |
| Extracellular Matrix..... | ECM |
| Embryonic stem cell..... | ESC |
| Fibroblast..... | FB |
| Fibronectin..... | FN |
| Invitrogen..... | Inv |
| Induced pluripotent stem cell..... | iPSC |
| Laminin..... | LAM |
| Microcontact printing/printed..... | μ CP |
| Myosin heavy chain..... | MHC |
| Microtissue with integrated force indicator..... | MIFI |
| Muscular thin film..... | MTF |
| Microtissue..... | μ tissue |
| Molecular weight..... | MW |
| Polydimethylsiloxane..... | PDMS |
| Poly(n-isopropylacrylamide)..... | PIPAAm |
| Skeletal muscle derived cell..... | SkMDC |

Chapter 1

Introduction to Engineering Contractile Skeletal and Cardiac Muscle

1.1 Introduction

Engineered *in vitro* contractile skeletal and cardiac muscle have potential applications as model organoids for more economical pharmaceutical testing compared to *in vivo* animal trials, as well as tools for understanding the relationship between extracellular matrix (ECM) and tissue morphogenesis and future building blocks for engineered organ replacements or as soft robotics actuators. Skeletal muscle serves as the primary actuator system in animals and can perform tasks over a wide range of length and time scales, spatial configurations and force regimes. Additionally, cardiac muscle serves as the a critical actuator in the body as it maintains blood flow for efficient nutrient and oxygen delivery and waste exchange throughout the organism. At the molecular scale, the protein machinery that makes up the contractile apparatus is constantly being replaced while the muscle is functioning, enabling contraction for decades through billions of cycles. At the tissue scale, skeletal muscle *in vivo* can repair small injuries, preventing loss of muscle mass¹. However, both muscle systems have limitations for regenerating significant injuries or defects. Specifically, skeletal muscle is unable to regenerate significant defects caused by severe trauma or surgery, and muscular dystrophies also inhibit the innate ability of skeletal muscle to maintain and repair normal function. Cardiac muscle, in contrast, has virtually no regenerative capability to repair damaged muscle after cardiac infarctions². For these reasons, the

ability to engineer functional skeletal and cardiac muscle from its most basic building blocks, differentiating cells and ECM, will garner insights into how to harness and augment the body's innate ability to repair smaller defects. Additionally, engineered *in vitro* models of normal and disease state skeletal and cardiac muscle will enable development of more economical platforms for development and testing of pharmaceuticals that may affect genetic diseases such as muscular dystrophies. Finally, functional engineered skeletal muscle has further future applications as self-repairing soft robotics actuators.

Engineering skeletal muscle requires the ability to guide muscle pre-cursor cells to differentiate into skeletal muscle cells (myotubes) and then to organize these cells into a functional tissue. For skeletal muscle, this muscle formation process (termed myogenesis) is well documented *in vivo*^{1, 3, 4}, but has proven difficult to replicate *in vitro*, a challenge that faces the field of tissue engineering and regenerative medicine. Current research is focused on understanding the physical, mechanical and chemical cues necessary to guide myogenesis and how to recapitulate them. Initial results demonstrate that the ECM is a key component to the myogenesis process and can serve as an instructive template for engineering skeletal and cardiac muscle. Major factors include (i) substrate stiffness and the mechanical environment, (ii) the spatial organization of biochemical cues, (iii) physical and topographical cues, and (iv) electrical and mechanical conditioning. Researchers have integrated these engineered muscle tissues into various devices from simple grippers to semi-autonomous walking and swimming soft robots. These proof-of-concept examples highlight the unique capabilities of engineered muscle and the fact that current technology can begin leveraging muscle as *in vitro* models to understand basic muscle development and drug-response as well as actuator systems in engineered devices. Additionally, engineered skeletal and cardiac muscle have often been developed in parallel with

each other because of the similarities that exist between functional tissues of either type. More specifically, both muscle types should visibly contract upon electrical stimulation, but skeletal muscle myoblasts have to undergo myogenesis (a minimum 1 - 4 week process) after placement within the 2D or 3D construct, while cardiomyocytes (CMs) can be harvested from animal models and seeded directly within 2D or 3D platforms and should begin to beat visibly within a few days. For this reason, engineered muscle platforms have often been prototyped and developed with CMs before integrating differentiating skeletal muscle within a similar context⁵⁻⁸.

For this dissertation, we wanted to engineer contractile muscle systems in 2D and 3D platforms as there are inherent benefits and limitations to both. Specifically, 2D platforms that utilize microcontact printing (μ CP) allow us to dictate the specific ECM cues we expose differentiating cells to, in terms of protein composition and geometry⁹. For this reason, we wanted to apply the techniques previously used to μ CP fibronectin (FN) alignment cues on thin polydimethylsiloxane (PDMS) films to integrate contractile, aligned CM constructs to engineer aligned, contractile skeletal muscle^{5, 10}. In this way, we planned to investigate how specific ECM proteins found in the basement membrane of skeletal muscle influenced myotube formation, in terms of myotube formation and contractility. This 2D platform also allowed methodical investigation how patterned line geometry influenced the alignment of differentiating myotubes. However, 2D engineered muscle platforms are often limited by the amount of time engineered muscle constructs are able to be maintained to form robust, functionally mature tissue systems.

3D muscle microtissues have been engineered by mixing myoblasts or CMs with biologically derived hydrogels and casting the cell+gel mixture in a mold that will dictate final tissue shape upon polymerization of the hydrogel¹¹⁻¹⁵. Confining these cells within 3D matrix enables longer term culture compared to 2D assays and allows contractile cells to continually

exercise against the surrounding ECM hydrogel environment and become more contractile and mature, similar to *in vivo* muscle tissue morphogenesis. For this reason, we also wanted to engineer a 3D platform that allowed longer-term culture of both engineered cardiac and skeletal muscle cells. This 3D platform provides less control over the specific microgeometry and protein alignment cues to which differentiating myoblasts or differentiated CMs are exposed. However, 3D platforms do allow longer periods of culture time to engineer more mature contractile muscle tissues by restricting cells to a 3D hydrogel microenvironment.

1.2 Dissertation Organization

This dissertation is organized into several chapters to demonstrate the various methods we have used to engineer functional skeletal or cardiac muscle in 2D and 3D assays. Specifically, chapters 3 – 5 focus on better understanding how to control the skeletal muscle myogenesis process in 2D using patterned ECM cues to form aligned, contractile myotubes from mouse and human myoblasts. Chapter 6 focuses on engineering a 3D contractile muscle, both with skeletal muscle or cardiomyocytes, with applications as an *in vitro* test bed for general pharmaceutical screening, development of patient specific regenerative therapeutics, and as soft robotics actuators.

1.2.1 Chapter 2: Background on Engineered Skeletal and Cardiac Muscle

Extensive background on current methods of engineering 2D and 3D skeletal or cardiac muscle tissues is presented in this chapter. We will discuss the ECM characteristics, such as stiffness, ECM composition, and microgeometry, that have been demonstrated to be important to directing skeletal muscle formation *in vitro*. Additionally, we will examine the contractile 2D skeletal muscle platforms in existence. Further, we discuss the current 3D platforms of

engineered cardiac and skeletal muscle that have been engineered as *in vitro* models of tissue function or for applications as soft robotics actuators.

1.2.2 Chapter 3: Understanding the Role of ECM Protein Composition and Geometric Micropatterning for Engineering Human Skeletal Muscle

In this chapter, we examine how specific matrix composition and line patterning (in terms of width and spacing) influence the formation and alignment of C2C12 and human primary skeletal muscle myotubes. We use traditional μ CP techniques to pattern 4 different components of the ECM in 16 different line geometries. Specifically, we hypothesized that components found in the basement membrane of skeletal muscle (collagen type IV or laminin(LAM)) would significantly increase 2D myotube formation compared to FN or collagen type I. Additionally, we hypothesized that line spacing and width of patterned ECM lines would affect myotube alignment with patterns and myotube differentiation, as measured by nuclei per myotube, percent area of myotube coverage, and myotube lengths. We found that both C2C12 and human myoblasts had significantly higher myotube formation on LAM lines, but we also demonstrated that there are species specific differences that should be taken into consideration, especially since many tissue engineering techniques are often developed with cell lines or primary cells from other species, leading to difficulties in translating those methods directly to human primary cells.

1.2.3 Chapter 4: Trace Amounts of Perlecan in Isolated Laminin Influences 2D Human Myotube Formation

We observed that myotube formation by both C2C12 and human skeletal muscle derived cells was severely impaired when we changed the manufacturer of isolated LAM 111. While side-by-side comparison of the manufacturer descriptions of the differently source LAMs appeared to list identical proteins, we observed severe myoblast peeling from Beckton Dickinson

sourced LAM compared to Invitrogen, which we demonstrated in the previous chapter fostered significantly higher myotube formation than other ECM proteins. We hypothesized that the purification process used by manufacturers to isolate LAM from the Engelbreth-Holm-Swarm mouse sarcoma resulted in removal of a protein or post-translational protein-modifications that were critical to *in vitro* myotube formation in 2D. To test this, we compared C2C12 and human myotube formation on varying LAM samples from the two manufacturers, and we ran extensive mass spectroscopy analysis of the LAMs to determine the differences between LAMs. We ultimately found that the Invitrogen LAM that fostered significantly higher myotube formation contained trace amounts of perlecan, a crucial protein in the basement membrane of skeletal muscle and other tissues.

1.2.4 Chapter 5: Engineering Skeletal Muscular Thin Films: Troubleshooting and Future Directions

The motivation behind Chapters 3 and 4 was to determine the ECM composition and geometry that would maximize human myotube formation and alignment in 2D to engineer contractile muscular thin films (MTFs) from human primary myoblasts. In this chapter, we modified the previously established methods used to engineer skeletal MTFs from C2C12 myotubes to engineer contractile human myotube MTFs. We cover the challenges associated with differentiating contractile mouse and human skeletal muscle consistently in this 2D assay. Specifically, we determined that small changes in the fabrication of thin film substrates can impact the ability of differentiating myoblasts to form myotubes. Ultimately, despite initial demonstrations that contractile MTFs could be engineered with C2C12 myoblasts, we determine that this assay is not ideal for skeletal muscle due to severely limited differentiation time (~ 1 week) compared to the longer culture time allowed by 3D assays (1 - 4 weeks). Skeletal muscle

myoblasts typically need longer than 1 week to differentiate into contractile myotubes capable of exerting 10s of kPa of twitch stress on the PDMS film, but we found that even when we cross-linked FN to the PDMS surface, myotubes were only maintained in 2D on patterned PDMS substrates for ~ 1 week. We discuss other potential solutions to maintaining myotubes in 2D for longer periods of time to engineer contractile 2D skeletal muscle constructs.

1.2.5 Chapter 6: Engineering Cardiac Microtissues with Integrated Force Indicators for Force and Beat Frequency Analysis

Due to the limitations of the 2D MTF assay for engineering functional skeletal muscle, we designed a 3D muscle microtissue system that integrated a thin, PDMS, U-shaped insert with both ends of uniaxially aligned cardiac or skeletal muscle construct. We discuss the iterative design process used to engineer muscle microtissues with integrated force indicators (MIFIs). Specifically, both ends of the U-shaped inserts act as anchoring points to which differentiating microtissues attach, and the insert serves as a force indicator, because the change in bending induced by contracting muscle can be measured and calculated to muscle twitch force using finite elemental modeling. We cast C2C12 or HUES9-CMs mixed in collagen type I + Matrigel™ around these inserts to integrate the microtissues with inserts. As previously mentioned, already differentiated and beating cardiomyocytes have been shown to serve as an appropriate prototype cell to establish methods that translate to engineering contractile skeletal muscle. We showed that we can engineer cardiac and skeletal muscle MIFIs that are capable of visibly bending inserts to measure muscle force generation, and we also showed that these microtissues respond to excitatory pharmaceutical stimuli as expected.

Chapter 2

Background on Engineered Skeletal and Cardiac Muscle

2.1 Formation, Structure, and Function of Skeletal Muscle

2.1.1. *Myogenesis in Embryonic Development and Muscle Repair*

Engineering skeletal muscle *in vitro* requires an understanding of the cues that guide myogenesis *in vivo*. As skeletal muscle forms during embryogenesis, muscle stem cells differentiate into myoblasts that align and then undergo membrane fusion to form multinucleated myotubes that will mature into myofibers¹⁶ (Figure 2.1A). Primary myotubes form autonomously when Myf5 and MyoD are expressed in proliferating muscle precursor cells¹⁷. Secondary myotubes then form using primary myotubes and neurons as a guide¹⁸. In other words, secondary myotubes use primary myotubes as a scaffold to guide their alignment and differentiation during embryonic myogenesis¹⁹. As the organism grows the myotubes become larger (hypertrophy) and new myotubes are added (hyperplasia) to increase muscle volume. In this way, the myogenesis process yields muscle tissue composed of parallel bundles of myofibers. Thus, except for the earliest stages of embryonic development, myogenesis requires an existing tissue structure to build upon. A similar process occurs during post-natal muscle repair after injury. Satellite cells (muscle precursor cells) are activated after muscle injury. Activation of satellite cells leads to their proliferation, differentiation, and fusion, at the site of injury, using the basal lamina as a guide¹ (Figure 2.1B). In fact, one of the reasons that large muscle deficits do not regenerate is

because the basal lamina has been destroyed and there is no ECM structure to direct growth. Therefore, to engineer functional skeletal muscle constructs, it is necessary to develop methods that recapitulate myogenesis *in vitro* and use some type of scaffold to direct myoblast alignment, fusion, and differentiation into dense, aligned myotubes.

2.1.2. Hierarchical Organization and Control of the Contractile Apparatus

The unique performance characteristics of skeletal muscle are based on the hierarchical organization of the contractile apparatus and the integrated control system that enables force

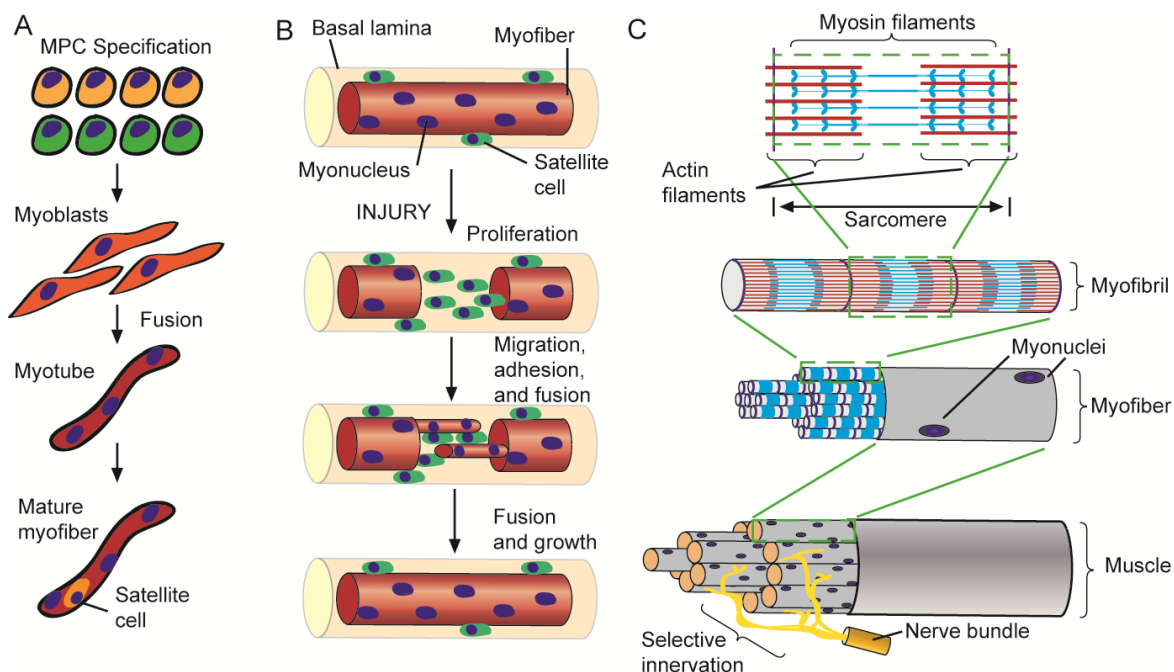


Figure 2.2. Schematics of the myogenesis process and hierarchical contractile apparatus of skeletal muscle tissue. (A) In embryonic myogenesis, muscle precursor cells (MPCs) differentiate into myoblasts that proliferate and then align and fuse to form primary and then secondary myotubes. Maturation yields larger myotubes with peripherally located nuclei and a resident satellite cell population (a stem cell capable of self-renewal and differentiation into myoblasts) (B) After injury, skeletal muscle repair begins when satellite cells migrate into the wound site, proliferate, differentiate, and fuse following the basal lamina to repair the defect. (C) The basic contractile apparatus of skeletal muscle is the sarcomere, which runs from Z-disk to Z-disk. Overlapping actin and myosin heavy chain filaments in each sarcomere form dense, uniaxially aligned arrays of molecular motors that enable skeletal muscle contraction. Sarcomeres are organized into specialized cytoskeletal filaments termed myofibrils that, in turn, are densely packed within myotubes to form uniaxially aligned bundles. Multinucleated myotubes are organized within the muscle tissue and are innervated with motor neurons forming neuromuscular junctions. In between the myotubes are blood vessels, nerve fibers and an ECM network that, in part, holds the muscle tissue together. (A) Adapted from Koch U et al. Stem cells living with a notch. *Development*. 2013, 140:689-704. (B) Adapted from Abmayr et al. Myoblast fusion: lessons from flies and mice. *Development*. 2012, 139: 641-656.

modulation. The basic contractile unit of skeletal muscle, the sarcomere, is composed of parallel actin and myosin heavy chain filaments (Figure 2.1C)²⁰. Myosin is a molecular motor complex that uses the energy stored in adenosine triphosphate (ATP) to walk along actin filaments. Briefly, muscle contraction occurs when the muscle cell is depolarized by acetylcholine release from its respective motor neuron. This activates voltage gated Ca^{2+} channels in the sarcoplasmic reticulum, flooding the cytoplasm of the myotube with Ca^{2+} . At rest, the troponin-tropomyosin complex blocks the myosin binding site on actin, but Ca^{2+} binds the troponin complex, allowing the myosin heads to access the actin and begin the cross-bridge cycle (i.e., walking along the actin filament) that results in muscle contraction. Each myosin motor generates picoNewton scale forces, but the muscle is composed of millions of repeating units of these sarcomeres, allowing the molecular scale cross-bridge movement to translate into macroscale muscle contractions. To maximize force, all the sarcomeres need to be pointing in the same direction, and thus skeletal muscle has a predominantly uniaxial alignment of myotubes to achieve this. Controlling the assembly of sarcomeres into organized myofibrils and myotubes is one of the basic objectives necessary to achieve functional skeletal muscle constructs.

Skeletal muscle is densely packed with myotubes, but each myotube is electrophysiologically independent and innervated by a single motor neuron. Each motor neuron can innervate multiple myotubes, which constitutes a single motor unit within the larger muscle tissue²¹. Motor units can be selectively activated, allowing tunable force generation dependent upon the number of motor neurons that are initiating muscle contraction. In addition to this spatial recruitment, muscle force generation can be tuned temporally by controlling the frequency of depolarization of the myotubes. The frequency range is quite broad, and can scale from essentially 0 to 100 Hz. Skeletal muscle has a positive force-frequency relationship,

meaning that the faster it is stimulated the more force is generated²². At high contraction rates skeletal muscle will enter tetanus, where it stays in a fully contracted state and generates maximum force. In contrast, cardiac and smooth muscle are connected by gap junctions, forming a syncytium that results in synchronous contractions that cannot be controlled by selective activation of the desired portion of tissue. Further, cardiac muscle must continually contract at ~1 Hz while smooth muscle contracts very slowly, making these tissues less desirable for soft robotics applications²¹. Thus, differentiated cardiomyocytes can serve as a template cell type for developing these 2D and 3D contractile tissues, but the spatial and temporal control of muscle contraction that is unique to native skeletal muscle should enable comparable tunability of engineered skeletal muscle for soft robotic actuators.

2.2 Engineering the Microenvironment to Guide Skeletal Muscle Formation

2.2.1. The Role of Substrate Stiffness and the Mechanical Environment

Skeletal muscle is a soft tissue composed of myotubes, blood vessels, nerves and an interconnected network of ECM. The elastic modulus of muscle tissue depends on the specific type, but is reported to be in the range of 10-40 kPa²³. This is important, because tissue compliance is required in order for the muscle to shorten up to 40% during contraction²⁴. For muscle cells to be able to deform an engineered muscle tissue the elastic modulus of the scaffold must be a primary consideration, and in fact, studies have shown that stiffness dramatically influences cell behavior^{25,26}. For example, myoblasts cultured directly on glass ($E \sim 70$ GPa) fuse into myotubes, however, they do not form sarcomeres even though they are positive for myosin heavy chain (Figure 2.2A-B)²⁵. In contrast, when a second layer of myotubes is grown on top of this first layer, the second layer is able to form striated myotubes with well-organized sarcomeres. This implies that having a softer substrate with stiffness comparable to muscle tissue yields myotubes with more developed and organized sarcomeres. To rule out the possible

role of cell-cell signaling in this effect, myotubes were cultured on polyacrylamide gel substrates with elastic moduli similar to muscle tissue (1 to 23 kPa) and on glass controls²⁶. Well-organized sarcomeres were observed in myotubes on substrates closest to the elastic modulus of skeletal muscle cells (8 and 11 kPa), but not the softer or harder surfaces (Figure 2.1C). While the force generated by these myotubes was not measured, more highly-organized sarcomeres typically indicate more mature myotubes capable of higher force production than those with little to no sarcomere organization. Similar results have been found with stem cells, where specification of mesenchymal stem cells towards a myogenic lineage was enhanced on substrates with an elastic modulus of ~ 10 kPa²⁷. Thus, when engineering skeletal muscle, the literature would suggest that optimal scaffold stiffness on the order of ~ 10 kPa is necessary to maximize differentiation into functional muscle. However, other data suggests that a wider range of scaffold mechanical properties may benefit additional aspects of myotube maturation. For example, myotubes cultured on polydimethylsiloxane (PDMS) substrates with elastic moduli ranging from 5 kPa (Figure 2.2D) to 2.7 MPa (Figure 2.2E) were found to be longer on the stiffer formulations (Figure 2.2F), indicating more myoblasts were fused into each myotube²⁸. Longer myotubes *in vitro* are often larger in cross-sectional area with more sarcomeres, suggesting they will generate greater force. Thus, while the ideal mechanical properties to engineer skeletal muscle are still under research, what the data does demonstrate is that myotube fusion index, length and sarcomere organization can be controlled by modulating the mechanical properties of the scaffold.

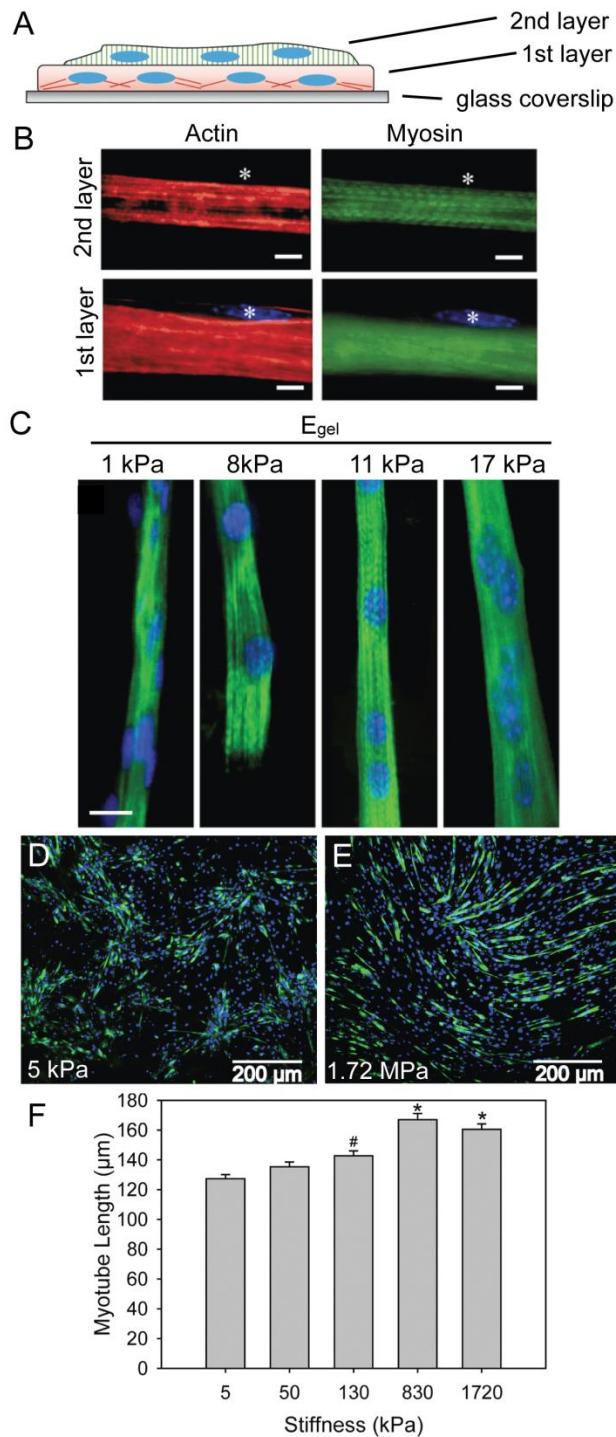


Figure 2.2. Myoblast fusion into myotubes is sensitive to the mechanical properties of the underlying substrate. (A) A schematic showing a side view of a 1st layer of myotubes on a glass substrate with actin filaments and a 2nd layer of striated myotubes with well-formed sarcomeres, growing on the 1st layer. (B) Immunofluorescent images of the 1st and 2nd layer myotubes where actin and myosin only show striations in the 2nd layer of myotubes. The nucleus (asterisk) is only visible in the 1st layer myotube, confirming that there are two, distinct layers of myotubes. (C) Myotubes differentiated for 4 weeks on polyacrylamide hydrogels with varying elastic moduli of 1, 8, 11 and 17 kPa only form striations and sarcomeres on substrates with intermediate elastic moduli of 8 and 11 kPa, comparable to muscle tissue. (D and E) C2C12 myoblasts differentiated into myotubes on PDMS with elastic moduli of 5 kPa and 2.72 MPa showed different responses, with myotubes on the soft PDMS preferring to clump together versus forming parallel myotubes (green = myosin heavy chain, blue = nuclei). (F) Myotubes grown on stiffer PDMS substrates (130 kPa, 830 kPa, and 2.72 MPa) were significantly longer than myotubes grown on softer 5 and 50 kPa substrates (* indicates $p < .0001$, # indicates $p < .001$). (A-B) Adapted from Ref 25. (C) Adapted from Ref 26. (D-F) Adapted from Ref 28. Scale bars are (A and B) 10 μm ; (C) 20 μm ; (D and E) 200 μm .

2.2.2. Extracellular Matrix and the Spatial Organization of Biochemical Cues

The composition and structure of the ECM *in vivo* are key regulators of cell behavior, and are equally important factors when engineering skeletal muscle constructs *in vitro*. Recreating the complex 3D architecture of the ECM within muscle tissue is beyond current technology, but scaffolds composed of the ECM proteins collagen type I (COLI), collagen type IV (COL4) and laminin (LAM) can still be engineered to control myogenesis. For example, Matrigel™ (primarily LAM and COL4) mixed with varying amounts of COLI and fibrin were cast as isotropic gels and used to engineer 3D skeletal muscle from C2C12 myoblasts or primary rat skeletal myoblasts (rSKMs)⁸. In these cases the embedded cells remodel the ECM hydrogels over time and compact it into a cell-dense tissue construct. The C2C12 myoblasts compacted high fibrin content hydrogels more than those with high collagen content, indicating the rate of remodeling is ECM dependent. Further, neonatal rSKMs grown in ECM hydrogels comprised of varying ratios of Matrigel™, fibrinogen, and/or COL1, showed that the hydrogel composition can have a larger effect on contractility and peak stress generation than other factors such as electrical stimulation, co-culture with other cell types, or added growth factors¹³. These examples demonstrate that the interaction of cells with the extracellular environment plays a key role in skeletal muscle cell differentiation and that ECM protein composition is an important component.

The spatial organization (i.e. patterning) of ECM proteins can be used to control skeletal muscle formation and direct myotube organization. Most patterning techniques are optimized for 2D, where photolithography-based approaches can be used to define micro- and nanoscale features on the surface. For example, geometrically patterning ECM proteins by microcontact printing (μ CP) has been used to guide cell attachment and probe the influence of spatial

organization of chemical cues on cell behavior (see here for a general review of μ CP⁹). The μ CP of FN and/or LAM has been used to engineer all main muscle types including smooth^{29,30}, cardiac^{31,32}, and skeletal^{33,34}. For skeletal muscle, one of the main uses of μ CP is the engineering of uniaxially aligned myotubes using patterned ECM lines to better mimic myotube organization *in vivo*. Researchers have shown that increasing the width of LAM lines from 100 to 300 to 500 μ m (Figure 2.3A-B) decreased C2C12 proliferation but increased differentiation into myotubes (Figure 2.3C-D)³³. Parallel FN lines an order-of-magnitude narrower (10, 20, and 50 μ m wide) are also effective at aligning C2C12 myoblasts and controlling orientation upon differentiation into myotubes³⁴. Further, both line spacing and line width are important factors. For example, on uniform FN surfaces myotubes are isotropic (Figure 2.3E), but when patterned on 50 μ m wide, 10 μ m spaced (50x10) lines the myotubes become aligned, but at approximately a 30° angle to the underlying pattern⁶ (Figure 2.3F). Increasing the line spacing to 20 μ m keeps the myotubes on the 50 μ m wide FN lines and creates uniaxially aligned muscle tissue, but the overall myotube density on the surface is decreased (Figure 2.3G). Increasing the line width to 200 μ m increases the myotube density on the surface, but the myotubes align at an approximately 10° angle to the underlying pattern (Figure 2.3H). What this demonstrates is that μ CP of ECM proteins is a useful tool to control and probe myoblast proliferation, differentiation, and alignment at the cellular level. Future investigations need to examine differences in myoblast or myotube behavior among varying ECM proteins in addition to the influence of geometric cues. By doing this, we will have a better understanding of how to control the microenvironment when engineering functional skeletal muscle.

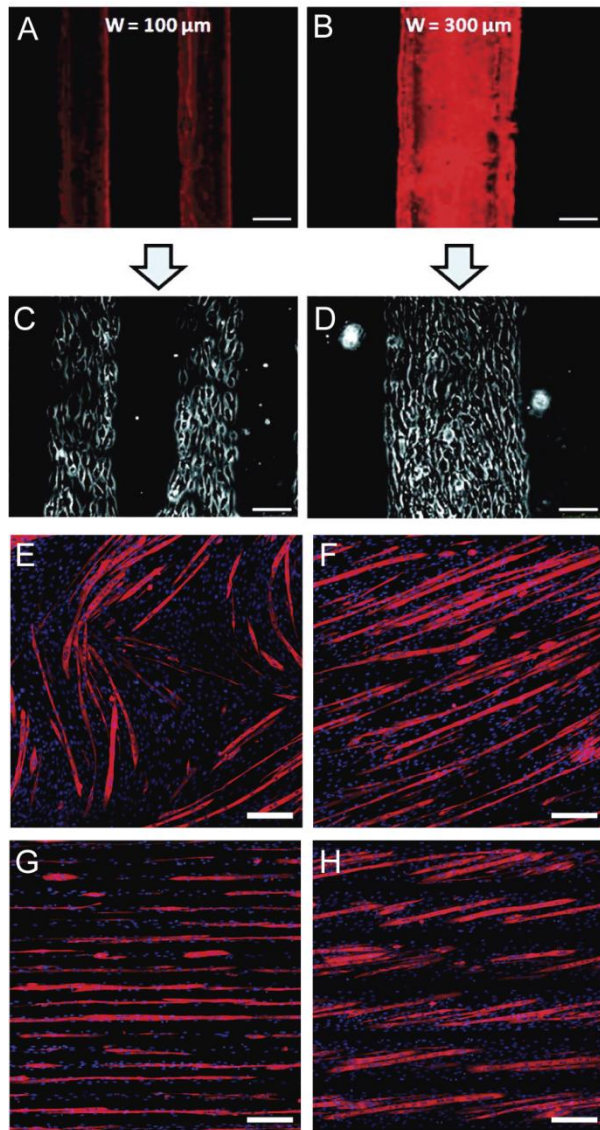


Figure 2.3. Micropatterned ECM proteins guide myoblast differentiation and alignment. Examples of μ CP lines of LAM immunofluorescently labelled with widths of (A) 100 μ m and (B) 300 μ m. Phase contrast images of myoblasts seeded onto (C) the 100 μ m and (D) the 300 μ m wide lines, demonstrating cell confinement to the pattern. (E) C2C12 myoblasts seeded onto a PDMS surface with a uniform FN coating differentiate into myotubes with isotropic (random) alignment. (F) The μ CP of FN lines 50 μ m wide and 10 μ m spaced (50x10) induces myotube alignment, but not in the direction of the underlying pattern because the myotubes can bridge the spacing (pattern runs left-to-right). (G) Increasing the line spacing to 20 μ m (50x20) keeps myotubes on the FN lines and forms a myotubes with uniaxial alignment but fewer overall myotubes. (H) Increasing the FN line width to 200 μ m increase the number of myotubes, but decrease alignment. (A-D) Adapted with permission from Ref 33. Copyright 2012 American Chemical Society. (E-H) Adapted from Ref 6, Copyright 2013, with permission from Elsevier. Scale bars are (A to D) 100 μ m and (E to H) 200 μ m.

2.2.3. Physical and Topographical Cues that Guide Muscle Alignment

Physical and topographical features within the cell microenvironment are able to guide myoblasts and direct their fusion into aligned myotubes. Termed contact guidance, this process has been studied in many cell types with similar results³⁵. Grooves (i.e., channels) and fibers on the nanometer to micrometer scale are able to direct uniaxial alignment of skeletal muscle and are similar to the diameter of many of the protein filaments within the native muscle ECM, suggesting that cells are intrinsically sensitive to physical features in this size range. Typical

microtopographies include parallel microgrooves (Figure 2.4), posts, and holes in substrates composed of polymers such as PDMS, polystyrene, gelatin methacrylate (gelMA), and poly(L-lactic acid) (PLA)³⁶⁻⁴⁰. Groove depth, width and spacing (Figure 2.4A) can range from hundreds of nanometers³⁹ to tens of micrometers⁴⁰. In general, myotubes organize in parallel to the groove direction (Figure 2.4B), which is enhanced with increasing groove depth to width ratio and is less sensitive to the groove width itself^{37, 39}. Parallel grooves are also more effective at aligning myotubes than square posts³⁸, presumably due to the increased contact area between the myotube and the topographical feature. Compared to flat controls (Figure 2.4C), microtopographies are effective at guiding myotube alignment (Figure 2.4D), with comparable results to micropatterned ECM protein lines³⁶. Nanometer and micrometer scale fibers, when organized into aligned scaffolds, are also effective at guiding myotube formation and alignment. Electrospinning is the most common technique to create fibers at this scale, which uses an electric field applied between an extrusion needle and a collector to draw out the polymer fibers. Electrospinning techniques have been optimized to give control over fiber alignment and diameter. For example, uniaxially aligned polypropylene fibers coated with LAM were used to form aligned sheets of C2C12 myoblasts⁴¹, with a fiber spacing of 55 μm or less found to be optimal to form continuous myoblast sheets. Fibers at the nanometer scale are also effective at guiding muscle alignment. For example, electrospun polycaprolactone and polyaniline nanofibers have been used to direct the differentiation of C2C12 myoblasts into uniaxially aligned myotubes⁴². Other fiber spinning techniques such as spinneret-based tunable engineered parameter (STEP) polystyrene nanofibers 668 ± 63 nm in diameter were used similarly to direct the differentiation of C2C12 myoblasts into uniaxially aligned myotubes⁴³. In total, these examples demonstrate that nanometer and micrometer scale topographic features can be used to direct the uniaxial alignment of myotubes.

However, more research is necessary to determine whether there is a specific size or morphology that is optimal. For tissue engineering and soft robotics applications, a key limitation is that these techniques are primarily 2D, limiting the thickness of the engineered muscle tissue to $< 100 \mu\text{m}$.

2.2.4. Bioreactors for Mechanical and Electrical Conditioning

Once muscle tissue forms it needs to actively contract and work against a load in order to continue to mature. While most researchers have focused on the problem of initial myogenesis, electrical stimulation and mechanical loading are important for further muscle development. Bioreactors designed as advanced *in vitro* culture systems provide this capability and have been used to engineer improved skeletal muscle constructs. Field stimulation is used to excite skeletal muscle constructs *in vitro* without requiring innervation⁴⁴ and is effective for conditioning and testing force generation capabilities. Typically, electrodes (platinum or carbon) are placed on either side of the muscle tissue construct during culture

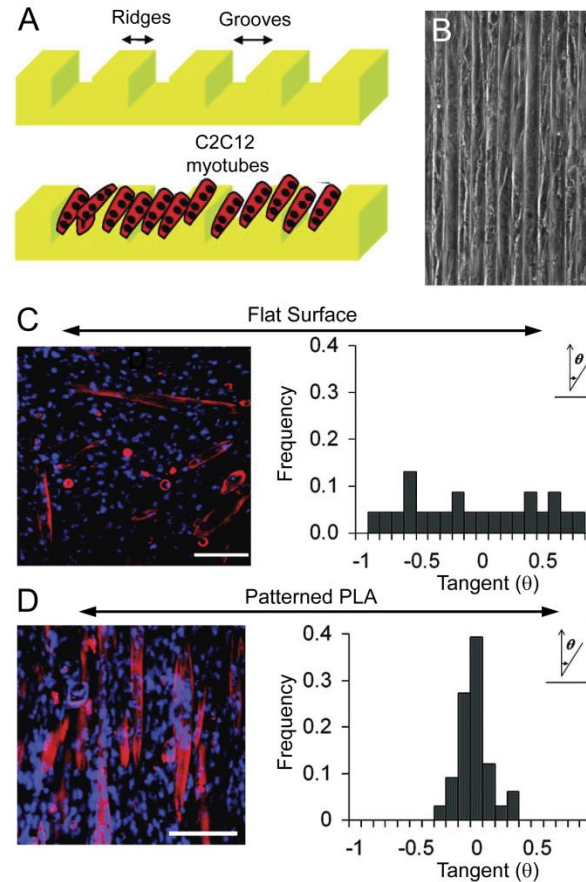


Figure 2.4. Myotube alignment can be controlled using engineered substrate microtopography. (A) Schematic of micro-grooves (i.e., channels) in a surface with controlled groove width, depth and spacing that can induce the alignment of myotubes differentiated on the surface. (B) DIC image of myotubes grown on a surface with parallel micro-grooves. (C) Myotubes differentiated for 10 days on a flat surface and stained for Troponin I (red) and DAPI (blue) are isotropic with no orientation preference. (D) In contrast, myotubes grown on the PLA membrane patterned with rectangular holes induced uniaxial myotube alignment. (A) Adapted from Ref 40. (B) Adapted from Ref 38, Copyright 2009, with permission from Elsevier. (C-D) Adapted from Ref 36. Scale bars are (B) $20 \mu\text{m}$ and (C and D) $50 \mu\text{m}$.

(Figure 2.5A) and a square wave in the range of 0 to 100 V in amplitude, 10 to 20 ms in duration and from 0 to 100 Hz is applied. In almost all cases, the addition of electrical stimulation cause the myotubes to contract and induce a mechanical stress and increases differentiation, alignment and force generation. For example, electrical pulse stimulation (EPS) of C2C12 myotubes at 1 Hz increased sarcomere assembly within as little as 2 hours⁴⁵. Similarly, EPS of C2C12 myotubes on deformable collagen strips resulted in significantly higher force generation compared to no EPS controls⁴⁶. In addition to more organized sarcomeres, electrically stimulating C2C12 myotubes resulted in increased glucose uptake²⁸. Researchers have also tried replicating the electrical stimulation patterns experienced by muscle cells during development in order to produce more mature myotubes (Figure 2.5A)⁴⁷. The peak stress generated by these constructs was 60 – 120 Pa, considerably less than the >100 kPa of native skeletal muscle⁴⁸. However, these constructs did show significantly higher force generation and increased excitability compared to constructs that were not stimulated or conditioned with a suboptimal stimulation pattern⁴⁸. Muscle constructs engineered using C2C12s were exposed to EPS of 0 (control), 0.5, 1, or 2 Hz during culture to determine if EPS rate affected myotube formation, and 1 Hz was determined to significantly increase muscle protein and muscle construct force⁴⁹. A limitation of field stimulation is that continuously exciting cell cultures with electrodes (platinum or carbon) can cause electrolysis of the media, leading to heating, changes in pH and electrode corrosion. Contactless electrodes are one potential solution, and recent work has demonstrated excitation of C2C12 myoblasts was possible without causing electrolysis of the media or other adverse effects (Figure 2.5B)⁵⁰. Electrodes have also been miniaturized to stimulate small, micropatterned lines of myotubes in order to selectively actuate a subset of cells, similar to

innervated motor units (Figure 2.5C)⁵¹. With this type of approach it is possible to control stimulation of individual myotube strands separated by as few as 200 μm (Figure 2.5D).

Mechanical stress can also be created by stretching skeletal muscle constructs using an externally applied load, and has also resulted in increased force generation⁵². For example, cyclical, mechanical strain of human bioartificial muscles consisting of collagen I, Matrigel™, and human primary skeletal muscle cells resulted in a significant increase in the myofiber diameter and relative cross-sectional area compared to controls⁵³. Additionally, human primary myoblasts seeded on acellular matrix and mechanically conditioned by applying 10% stretch at hourly intervals had more highly organized myofibers than statically cultured controls, and after implantation and removal from an *in vivo* mouse model, responded to electrical field stimulation (EFS) after 2 weeks of implantation, in contrast to the statically cultured controls, which did not respond to EFS⁵⁴. Rat primary myoblasts have also been seeded on decellularized bladder matrix, mechanically strained following the same protocol, and implanted in a rat volumetric muscle defect with results demonstrating that pre-conditioned constructs resulted in improved *in vivo* function and up to 2.3x more functional recovery than non-conditioned constructs⁵⁵⁻⁵⁷. Similar studies have investigated the electrical and mechanical stimulation of engineered cardiac muscle constructs and shown significant improvement to maturation of the sarcomere structure and increased force generation⁵⁸. Thus, for engineering functional muscle constructs, control of electrical stimulation is important both in terms of the maturation during culture and even after implantation as well as for the modulation of contraction force and temporal actuation.

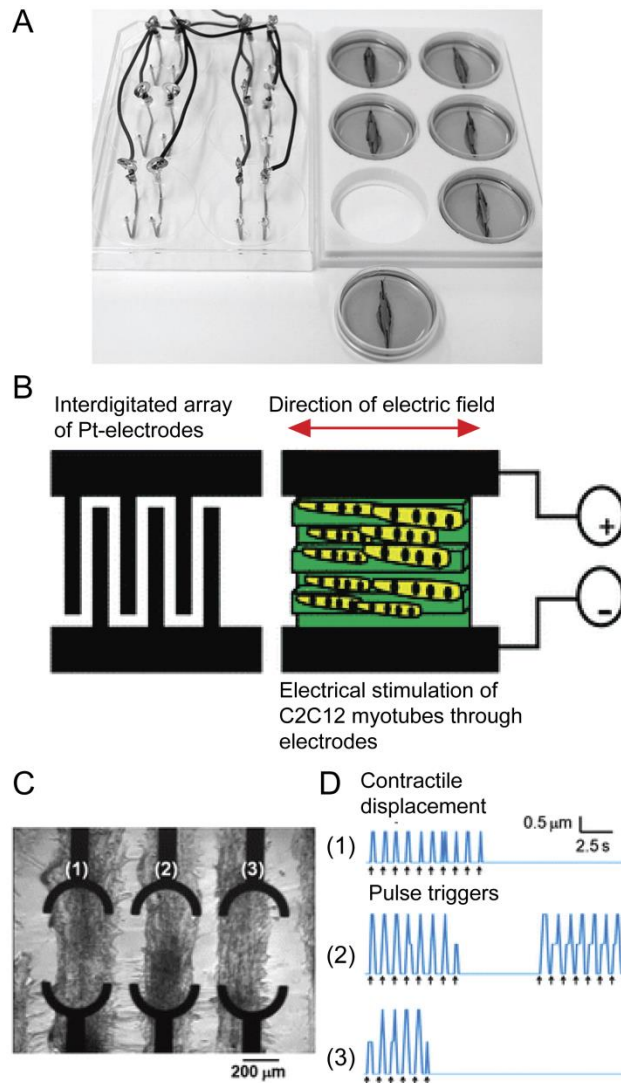


Figure 2.5. Examples of different bioreactor designs and microfabricated electrodes for the electrical stimulation of engineered skeletal muscle constructs. (A) A bioreactor based on a modified 6-well plate with platinum wire electrodes integrated into the lid capable of stimulating cultures of 3D engineered skeletal muscle tissue. (B) A schematic of contactless electrodes showing a top view of the design (black), which are positioned underneath a glass coverslip to isolate them from the cells and media. Myoblasts (yellow) cultured on top of microtopographically patterned gelMA (green) uniaxially align during culture. (C) Micropatterned lines of C2C12 myotubes can be selectively stimulated using microfabricated platinum electrode arrays. (D) Plots of displacement of the myotubes strands in (C) demonstrating the ability to independently stimulate the closely spaced muscle tissues (amplitude, 2 V; frequency, 1 Hz; duration, 10 ms). (A) Adapted from Ref 47. (B) Adapted from Ahadian S et al. *Lab Chip*. 2012, 12:3491:3503, doi: 10.1039/C2LC40479F, with permission of The Royal Society of Chemistry. (C-D) Adapted from Ref 52 with permission of The Royal Society of Chemistry.

2.3 Contractile Engineered Skeletal Muscle

2.3.1. 2D Cantilever-Based Skeletal Muscle Actuators

Skeletal muscle is a scalable actuator system that can potentially be used for a wide range of applications. Where relatively low force is required, 2D cantilever based actuators are a good choice because the muscle can be integrated as a thin layer ($<100\ \mu\text{m}$) directly onto the cantilever surface to control deflection. At the sub-millimeter scale, myotubes have been integrated with silicon cantilevers to create biological micro-electro-mechanical systems (bioMEMS) where the myotubes can be used as an actuator or the MEMs component can be

used to readout muscle force generation. For example, microfabricated silicon cantilevers have been coated with primary rat neonatal myoblasts or C2C12 myoblasts, differentiated into myotubes, and the contractile force recorded using an optical lever detection system comparable to that used in atomic force microscopy (Figure 2.6A-B)⁵⁹⁻⁶¹. The inherent shape of the silicon cantilever directs the myotubes to align along its length and the silicon is thin enough such that the myotube can deflect it during contraction. When stimulated to contract using field stimulation, these myotubes generated twitch stresses from 0.5 to 5 kPa and displayed potential as an *in vitro* platform to track muscle physiology for applications such as toxin detection⁶². For larger actuators at the millimeter scale and above, the silicon becomes too stiff and softer materials such as hydrogels or elastomers are required. For example, muscular thin films (MTFs) integrate a layer of anisotropic muscle tissue with a thin PDMS cantilever, and were originally developed using cardiac and vascular smooth muscle^{10,31}. Recently we have demonstrated that MTFs can also be engineered using C2C12 myoblasts to form skeletal muscle actuators capable of generating twitch stresses in the range of 1-2 kPa (Figure 2.6C-D)⁶.

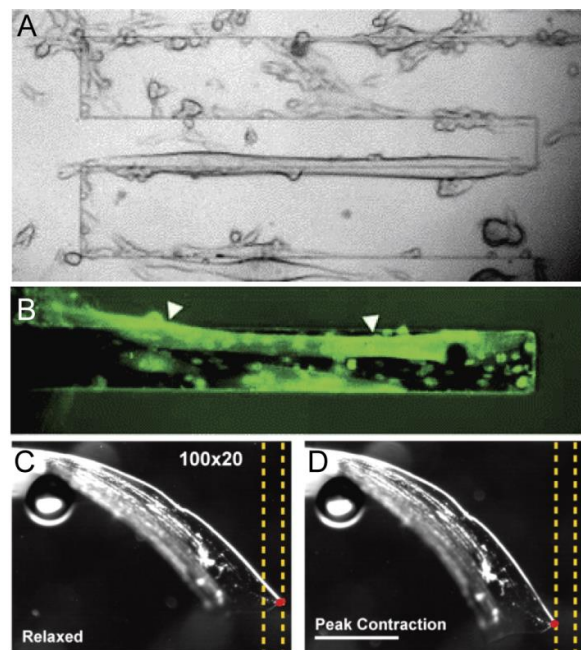


Figure 2.6. Engineered skeletal muscle tissue in the format of 2D cantilever-based actuators where the myotubes are integrated along the length of the beam. (A) An embryonic rat myotube differentiated on a DETA-modified silicon cantilever (phase-contrast image). (B) A C2C12 myotube on a vitronectin-modified silicon cantilever (α -actinin = green). Muscular thin films (MTFs) consisting of C2C12 myotubes of PDMS cantilevers showing a side view in (C) a relaxed state and (D) at peak contraction generating a twitch stress of ~ 2 kPa. The yellow lines indicate the position of the tip of the MTF between the relaxed and full contracted states (scale bars are 1 mm). (A) Adapted from Ref 59, Copyright 2006, with permission from Elsevier. (B) Adapted from Ref 60 with permission of The Royal Society of Chemistry. (C-D) Adapted from Ref 6, Copyright 2013, with permission from Elsevier.

While scalable up to the millimeter length scale, this is likely the upper limit for 2D cantilever-based systems since the total force generation is limited by the tissue thickness, which is typically in the range of 10-20 μm . Beyond this, a 3D skeletal muscle tissue is required to increase cross-sectional area and thus the volume of muscle that can contract.

2.3.2. Tissue Engineered Skeletal Muscle Using ECM Protein Scaffolds

3D skeletal muscle tissue is required to build larger scale soft robotic devices and, in the context of tissue engineering, has been explored using a range of cell types and scaffold technologies. By far the most widely used approach has been ECM hydrogel scaffolds that utilize the cell-driven compaction of the hydrogel to form relatively dense skeletal muscle tissue. For example, one of the first engineered skeletal muscle constructs was created by culturing primary avian skeletal muscle cells in a COLI gel cast within a stainless steel ring or mesh⁶³. This bioartificial muscle (BAM) set a precedent for the 3D engineering of skeletal muscle constructs *in vitro* and has since been optimized for C2C12 myoblasts to engineer BAMs with more mature sarcomeres⁶⁴. Demonstrating the scalability of this approach, engineered miniature BAMs (mBAMs) using specialized culture dishes to create linear muscle constructs (Figure 2.7A-B) form aligned myotubes (Figure 2.7C) and are capable of generating $\sim 30 - 50 \mu\text{N}$ of force (Figure 2.7D)⁶⁵. This scaled-down mBAM assay has proven capable of reading out changes in contractile function in response to pharmacological agents and has been used as a drug screening assay⁶⁶. More advanced techniques have also been used to augment muscle function, such as inhibition of miR133 (micro RNA 133) to promote maturation of skeletal muscle constructs⁶⁷. Similarly, genetically modified muscle cells have been used to secrete recombinant human growth hormone⁶⁸ or other bioactive compounds to improve the formation or function of the muscle construct. These approaches demonstrate that it is possible to engineer

functional 3D skeletal muscle in a linear muscle bundle with anchor points on both ends and a roughly circular cross-section, similar to that found *in vivo*. There are however limitations to the diameter of these constructs to <1 mm due to the lack of a vascular system and the limited diffusion length of oxygen. Larger-scale 3D skeletal muscle constructs have been engineered by forming anisotropic sheets using specially designed molds with rectangular posts (Figure 2.7E). For example, C2C12 and rat primary myoblasts have both been used to create porous, 3D networks of skeletal muscle within ECM gels composed of varying ratios of COLI or fibrinogen in Matrigel™ (Figure 2.7F))⁷. The rectangular posts' size and shape influences myotube orientation and force generation as well as providing conduits for enhanced nutrient transport within the constructs (Figure 2.7G)⁸. If engineered properly, myotubes within these constructs have a high degree of uniaxial alignment (Figure 2.7H) and can generate twitch stresses on par with native muscle. Myogenic cells from Sprague-Dawley rats were pre-seeded to isolate the 'adherent fraction' of cells prior to seeding in fibrin-based 3D gels that were dynamically cultured by gently rocking constructs during differentiation, and compared to controls that were not pre-cultured after isolation and were cultured statically, the dynamically cultured constructs with adherent cells were found to have significantly larger muscle area, ~9x force generation and a satellite cell pool during early culture⁶⁹. Using these methods, when constructs were implanted in a mouse dorsal window model, the native vasculature began to perfuse and organize throughout the engineered construct, and a pool of satellite cells was maintained. These examples demonstrate a growing ability to engineer functional skeletal muscle constructs that would have the ability to self-repair in both therapeutic and soft robotics applications. Recently, some of the first 3D engineered human skeletal muscle was demonstrated to both functionally contract and to respond as expected to pharmacological stimuli⁷⁰. Specifically, both electrical

stimulation and acetylcholine, the physiological stimulator of skeletal muscle, were able to induce visible muscle contractions, and statins, chloroquine, and clenbuterol all had the expected clinical effects on the muscle constructs, demonstrating the potential for this type of platform to

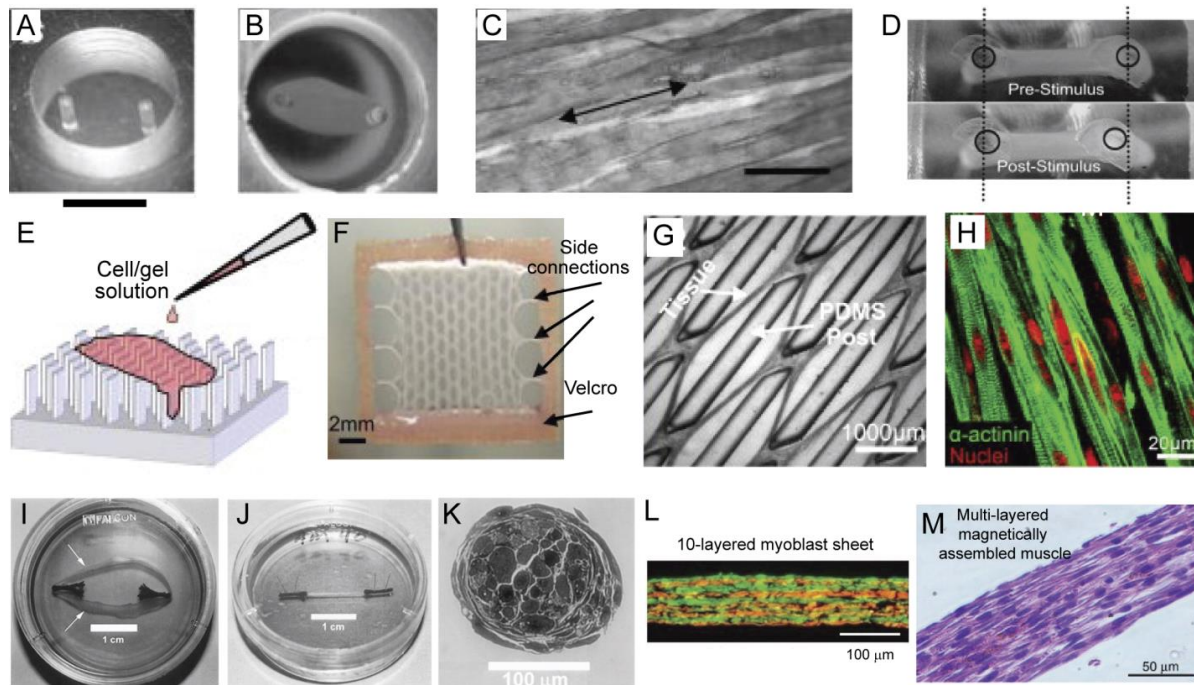


Figure 2.7. Examples of different types of 3D engineered skeletal muscle tissue. (A) Miniature bioartificial muscle (mBAM) is formed by casting an ECM hydrogel with embedded muscle cells into a specially designed, 7 mm diameter culture well with two, 700 μm diameter PDMS posts. (B) After 4 to 5 days of differentiation primary mouse myoblasts have begun to compact the gel around the posts. (C) mBAMs differentiated for 7 to 8 days were stained for sarcomeric tropomyosin (dark grey) showing aligned myotubes. (D) Contractile force generation was calculated from the bending of the PDMS posts during stimulation. (E) Sheets of engineered skeletal muscle consisting of a porous gel network were formed by casting ECM hydrogels with embedded muscle cells around a PDMS mold with rectangular posts. (F) The engineered muscle tissue network is attached to a Velcro frame and can be removed from the PDMS mold. (G) A top-down view of the skeletal muscle tissue showing the rectangular posts that guide anisotropic organization of the ECM as it is compacted by the cells. (H) Immunofluorescent staining of the sarcomeric α -actinin (green) and nuclei (red) of rSKMs differentiated into myotubes, demonstrating the uniaxial alignment and formation of sarcomeres. (I) Engineered skeletal muscle termed Myooids are formed by the self-organization of muscle cells from a monolayer on the bottom of a Petri dish around two ECM-coated anchoring structures (arrows indicate where the cell layer is rolling up). (J) The myooid construct once it has full organized into a linear muscle tissue in between the two sutures. (K) A Cross-section of a myooid showing myotubes in the center with a flattened layer of fibroblasts on the periphery (stained with toluidine blue). (L) A 10-layer engineered muscle tissue created by stacking myoblasts sheets released from temperature-responsive PIPAAm culture dishes. These are termed scaffold-free because the cells make their own ECM and the alternating layers were labelled with red or green CellTracker for verification. (M) C2C12 myoblasts labelled with magnetite cationic liposomes were seeded around a silicone ring with a magnet placed underneath the culture dish to produce a scaffold-free, multi-layered muscle construct. (A-D) Adapted from Ref 65 with permission from Wiley, Copyright 2008. (E-H) Adapted from Ref 8, Copyright 2009, with permission from Elsevier. (I-K) Adapted from Ref 66. (L) Adapted by permission from Macmillan Publishers Ltd: NATURE PROTOCOLS, Ref 77, Copyright 2012. (M) Adapted from Ref 78, Copyright 2009, with permission from Elsevier. Scale bars are (A) and (B) 4 mm, and otherwise as labelled.

be used as a pre-clinical *in vitro* test bed⁷⁰. However, constructs are still limited in thickness to <1 mm due to a lack of a vascular system prior to implantation in a host.

2.3.3 Self-Organizing Myooids

Self-organizing myooids are another example of a tissue engineered skeletal muscle construct that can be used to form functional muscle bundles. In this approach skeletal myoblasts and fibroblasts are seeded on a culture dish to form a sheet that over a period of time peels off the dish (Figure 2.7I) but remains anchored to two sutures placed in the dish and forms a compacted muscle bundle⁷¹. The end result is the formation of linear muscle construct termed a myooid that has sutures on either end and that can facilitate its integration with other devices (Figure 2.7J) and has dense myotubes in the interior with a layer of fibroblasts on the outside (Figure 2.7K). Myooids have been engineered from C2C12 and primary rat myoblasts^{72, 73} and optimized using a fibrin gel release surface has produced constructs capable of generating 36 kPa of tetanic stress⁷⁴, on par with native skeletal muscle. More advanced myooids have added additional tissue types, integrating self-organized tendon to connect the muscle portion of the myooid to steel anchor points⁷⁵. These constructs were capable of generating twitch stresses of 2 to 8 kPa and demonstrate a biomimetic approach for integrating soft, engineered muscle tissue with stiff materials. The limitations of the myooid construct are comparable to those of the ECM gel based scaffolds, limited in diameter to <1 mm due to a lack of a vascular system. Also, due to the self-organizing around anchor points, the myooids have been engineered mainly as linear constructs as opposed to sheets, porous networks, or other geometries.

2.3.4 Scaffold-free Constructs

Skeletal muscle constructs engineered using scaffold-free techniques are formed by having muscle cells synthesize and assemble their own ECM. The cell sheet method uses Petri

dishes coated with poly(N-isopropylacrylamide) (PIPAAm) to culture cells until they form a monolayer, allow them to synthesize an interconnected ECM and then release them as an intact tissue layer⁷⁶. PIPAAm is a thermally-sensitive polymer that is hydrophobic and cell adhesive at 37 °C but becomes hydrophilic and releases cells when the temperature is decreased below 32°C and the PIPAAm passes through its lower critical solution temperature. To form skeletal muscle sheets, myoblasts are cultured, differentiated into myotubes and then released by lowering the temperature to ambient. Once released these muscle sheets can be layered on top of one another to make constructs several cell sheets thick or constructs with alternating cell types, such as myoblasts and endothelial cells (Figure 2.7L)⁷⁷. Skeletal muscle constructs with up to 10 layers have been engineered; enabling a relatively thick, muscle dense tissue to be formed. While skeletal muscle sheets with uniaxial myotube alignment have not yet been demonstrated, anisotropic sheets of vascular smooth muscle suggest it should be possible²⁹. Other scaffold-free approaches also produce dense muscle tissues. For example, magnetic nanoparticles incorporated within C2C12 myoblasts by endocytosis can be used in combination with an applied magnetic field to hold the cells together in a specific geometric configuration (Fig. 7M)⁷⁸. These multi-layered, magnetically assembled constructs can be engineered as muscle rings that generate twitch forces from 10 to 17 μN ⁷⁹. For soft robotics, these scaffold-free techniques produce very dense muscle tissue that should have high force-to-weight ratios. However, thicknesses are limited to ~200 μm due to the diffusion limit of oxygen and lack of a vasculature.

2.4. Muscle-powered Soft Robotic Devices

Muscle-powered soft robotic devices have undergone significant development over the past decade and encompass basic devices and more complex soft robots that can walk and swim.

Though much work is still needed, these examples clearly demonstrate the potential of the technology and the ability to engineer muscle that is strong enough to support basic functionality. To date, many of the advanced soft robots have been engineered using neonatal rat cardiomyocytes^{31, 80, 81} rather than skeletal myoblasts or myotubes. This is because neonatal rat cardiomyocytes are easily harvested, already differentiated into a striated, beating muscle cells, respond predictably to microenvironmental cues, and can be seeded at high density. Together these properties make cardiomyocytes easier to work with than skeletal muscle, which must first be seeded as myoblasts that subsequently differentiate and fuse into myotubes. For this reason, many of the current examples of soft robotics devices are powered by cardiomyocytes; however, recent success in engineering MTFs with C2C12⁶ cells suggests that most of these examples can be replicated with skeletal muscle.

2.4.1. Basic Muscle-Powered Devices

A number of proof-of-concept soft robotic devices with basic functionality have been created using engineered muscle tissue. In general, these devices are fabricated from hydrogels or elastomers that provide a basic structure and then use the integrated muscle tissue to contract and cause deformation of part of the system. For example, at the micrometer-scale, an actuator was engineered by differentiating a single myotube on a sacrificial layer of PIPAAm between cantilevers, and generated forces from 0.2 to 1 μN ⁸². Myotubes have also been formed on dog hairs⁸³ or within rod-shaped collagen gels⁸⁴ to create micro-tweezers. At the millimeter-scale, grippers have been engineered from a PDMS frame with an integrated skeletal muscle construct that, when field stimulated, caused the gripper to close (Figure 2.8A)⁸⁵. Grippers have also been engineered from cardiac MTFs and demonstrated the ability to be kept in a closed state by stimulating the muscle tissue at a sufficient rate to induce tetanus³¹. For application in

microfluidics, a muscle-powered pump was formed by engineering a layer of cardiac muscle on the outside of a deformable chamber (Figure 2.8B and 2.8C), mimicking the basic pumping function of the heart, but at a much smaller scale⁸⁶. More advanced actuators have also been developed by using optogenetics to enable light to stimulate muscle contraction instead of an electric field. In the case of muscle tissue, introduction of channelrhodopsin-2, a light-sensitive cation channel, can depolarize the cell and trigger Ca^{2+} influx into the cytosol to initiate contraction. Genetically modified C2C12 myoblasts were grown in a COLI gel between PDMS pillars to produce contractile skeletal muscle constructs capable of selective stimulation with a specific wavelength of light⁸⁷. Depending on the size and location of the light, either the whole construct (Figure 2.8D) or a specific sub-region (Figure 2.8E) could be triggered to contract. The ability to trigger muscle contraction similar to innervation but without the need for an electrode interface opens up new opportunities to selectively control and modulate contraction for soft robotics devices. In total, these examples highlight the ability to integrate

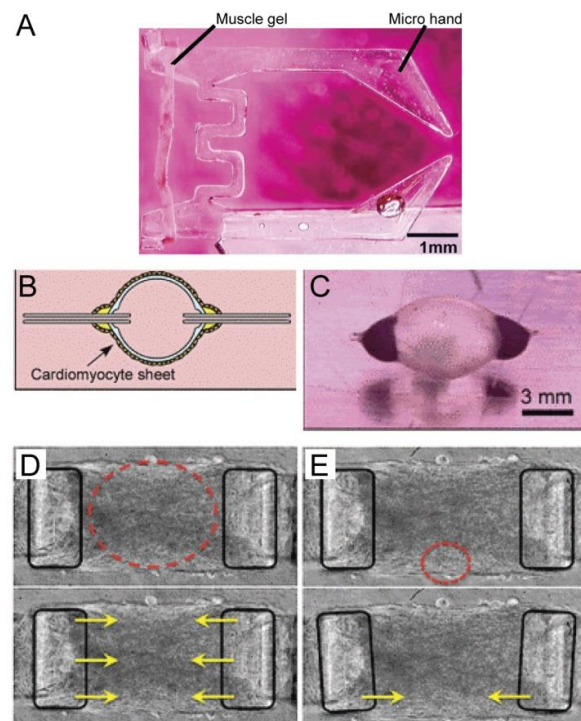


Figure 8. Examples of basic muscle-powered actuators and devices. (A) A skeletal muscle gel attached to a PDMS gripper (i.e., micro hand) that opens when the skeletal muscle is stimulated to contract. (B) Schematic of a muscle-powered microfluidic pump where a sheet of cardiomyocytes are cultured on the outside of a thin, hollow chamber. (C) The actual device where spontaneous or stimulated contraction of the cardiomyocytes causes the chamber to decrease in volume and pump fluid. (D) Optogenetically engineered skeletal muscle micro-tissue suspended between two PDMS posts is stimulated with blue light (red circle) by depolarizing the cells and results in contraction of the entire construct (yellow arrows). (E) Selective stimulation of a small region of the construct (red circle) results in contraction of just that region of the construct (yellow arrows), demonstrating light-based local control of activation. (A) Adapted from Ref 85. (B-C) Adapted from Ref 86 with permission of The Royal Society of Chemistry. (D) Adapted from Ref 87 with permission of The Royal Society of Chemistry.

engineered striated muscle in a range of devices across multiple length scales.

2.4.2. Muscle-Powered Soft Robots that Walk and Swim

The potential of engineered muscle to power soft robots is demonstrated by recent proof-of-concept examples that can walk and swim. A variety of soft robots have been engineered that can walk along the bottom of a Petri dish under spontaneous or field stimulated contractions. Microfabricated walkers have been created from Au and silicon and used cardiac muscle to power the devices motion (Figure 2.9A)⁸¹. Even though these were made from hard materials, it demonstrates the ability engineer a soft robot at the microscale. At a larger scale of a few millimeters, PDMS-based walkers have been engineered from microfabricated cantilevers⁸⁸ and hand-cut, MTFs formed into a 3D device³¹ (Figure 2.9B). In order to more rapidly engineer different devices designs, recent work has used photo-crosslinkable polyethylene glycol and stereolithography to 3D print soft robots termed biobots that can walk^{89, 90}. All of these examples used cardiac muscle tissue and demonstrated that slip-stick motion can enable the device to walk in a specific direction. There are also examples of swimming soft robots that are able to move through media or physiologic solutions when field stimulated to contract. At the simplest level, cardiac MTFs have been engineered with aligned muscle cells running from the base to tip of an isosceles triangle on the millimeter scale³¹. Due to this shape, the point of the triangle bends more and creates a tail that flaps when the muscle contracts and provides directed swimming motion. By controlling the field stimulation frequency, the cardiac MTF motion can be optimized to maximize swimming velocity. More advanced swimming soft robots have been engineered by mimicking the body plan (shape and muscle architecture) of the jellyfish to create a construct termed a medusoid⁸⁰. By testing a variety of body shapes and muscle designs (Figure 2.9C-D), it was shown that properly engineering both is required to have a medusoid that can swim (Figure 2.9E). This also shows that soft robots can effectively mimic the function of real

organisms, even though the materials and control schemes may be different. Larger muscle-powered soft robots have been engineered at the centimeter-scale, but the greater power needed to drive these devices has prevented the use of engineered muscle tissue. Instead, swimming robots with rigid bodies and flexible rubber tails have been engineered by explanting the semitendinosus muscle from frogs and attaching them to the robot to drive tail flapping⁹¹ (Figure 2.9F). This demonstrates that with a large enough muscle tissue, relatively-large robots can be actuated. In total, these proof-of-concept examples from the past decade highlight the advances that have been made in motile soft robots. However, challenges remain before these technologies can be scaled-up, and to date engineered muscle tissue cannot match the size or performance of explanted muscle tissue. We look to build on this body of work, in terms of using specific ECM cues to direct the alignment and differentiation of contractile, 2D human skeletal muscle myotubes as well as to engineer contractile 3D muscle constructs based on techniques that have been previously demonstrated to form contractile *in vitro* muscle constructs.

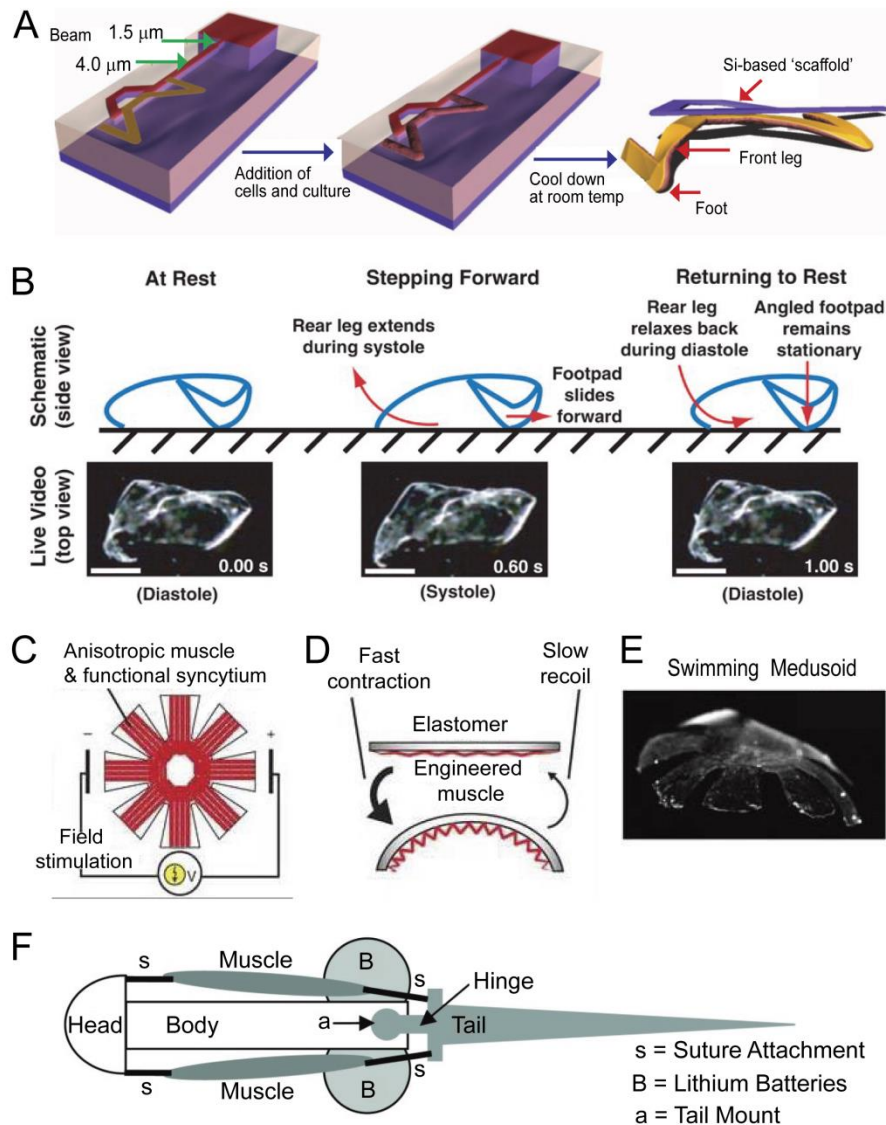


Figure 2.9. Examples of muscle-powered soft robots that can walk and swim. (A) Schematic of a microfabricated walker driven by cardiac muscle. Cardiomyocytes are seeded on the Au film (yellow) and form an integrated, microscale muscle tissue that is subsequently released by dissolving the PIPAAm. This produces a free-standing microdevice capable of walking when muscle cells are field stimulated to contract. (B) A schematic and corresponding microscopic images of an MTF with integrated cardiomyocytes formed into a construct termed a 'myopod'. When field stimulated to contract the myopod is capable of walking (scale bars are 1 mm). (C) Top down and (D) side view schematics of an MTF with integrated cardiomyocytes in the form of a tissue engineered jellyfish termed a 'medusoid.' The medusoid has a micropatterned muscle structure and body plan based on the actual jellyfish and when field stimulated to contract is capable of swimming. (E) A microscopic image of the medusoid floating in the Tyrode's solution in which it swims. (F) A top-down schematic of a swimming robot that mimics a fish and is powered by explanted frog muscles that are sutured onto the device. Integrated batteries supply the electric charge to alternately stimulate the muscles on either side of the robot to contract, thus actuating the tail in a side-to-side motion and enabling it to swim. (A) Adapted by permission from Macmillan Publishers Ltd: NATURE MATERIALS, Ref 82, Copyright 2005. (B) Adapted from Ref 32. Reprinted with permission from AAAS. (C-E) Adapted by permission from Macmillan Publishers Ltd: NATURE BIOTECHNOLOGY, Ref 80, Copyright 2012. (F) Adapted from Ref 92.

2.5 References for Chapters 1 and 2

1. Charge, S.B. & Rudnicki, M.A. Cellular and molecular regulation of muscle regeneration. *Physiol Rev* **84**, 209-38 (2004).
2. Bergmann, O. et al. Evidence for cardiomyocyte renewal in humans. *Science* **324**, 98-102 (2009).
3. Rudnicki, M.A. et al. MyoD or Myf-5 Is Required for the Formation of Skeletal-Muscle. *Cell* **75**, 1351-1359 (1993).
4. Sanger, J.W., Wang, J.S., Fan, Y.L., White, J. & Sanger, J.M. Assembly and Dynamics of Myofibrils. *Journal of Biomedicine and Biotechnology* (2010).
5. Feinberg, A.W. et al. Muscular thin films for building actuators and powering devices. *Science* **317**, 1366-70 (2007).
6. Sun, Y., Duffy, R., Lee, A. & Feinberg, A.W. Optimizing the structure and contractility of engineered skeletal muscle thin films. *Acta Biomaterialia* **9**, 7885-7894 (2013).
7. Bian, W., Liao, B., Badie, N. & Bursac, N. Mesoscopic hydrogel molding to control the 3D geometry of bioartificial muscle tissues. *Nat Protoc* **4**, 1522-34 (2009).
8. Bian, W. & Bursac, N. Engineered skeletal muscle tissue networks with controllable architecture. *Biomaterials* **30**, 1401-12 (2009).
9. Chen, C.S., Mrksich, M., Huang, S., Whitesides, G.M. & Ingber, D.E. Micropatterned surfaces for control of cell shape, position, and function. *Biotechnology Progress* **14**, 356-363 (1998).
10. Alford, P.W., Feinberg, A.W., Sheehy, S.P. & Parker, K.K. Biohybrid thin films for measuring contractility in engineered cardiovascular muscle. *Biomaterials* **31**, 3613-21 (2011).
11. Madden, L., Juhas, M., Kraus, W.E., Truskey, G.A. & Bursac, N. Bioengineered human myobundles mimic clinical responses of skeletal muscle to drugs. *Elife* **4**, e04885 (2015).
12. Zhang, D.H. et al. Tissue-engineered cardiac patch for advanced functional maturation of human ESC-derived cardiomyocytes. *Biomaterials* **34**, 5813-5820 (2013).
13. Hinds, S., Bian, W., Dennis, R.G. & Bursac, N. The role of extracellular matrix composition in structure and function of bioengineered skeletal muscle. *Biomaterials* **32**, 3575-83 (2011).
14. Vandemburgh, H.H., Karlisch, P. & Farr, L. Maintenance of Highly Contractile Tissue-Cultured Avian Skeletal Myotubes in Collagen Gel. *In Vitro Cellular & Developmental Biology* **23**, A24-A24 (1987).
15. Eschenhagen, T. et al. Three-dimensional reconstitution of embryonic cardiomyocytes in a collagen matrix: a new heart muscle model system. *FASEB J* **11**, 683-94 (1997).
16. Yaffe, D. & Feldman, M. The Formation of Hybrid Multinucleated Muscle Fibers from Myoblasts of Different Genetic Origin. *Dev Biol* **11**, 300-17 (1965).
17. Buckingham, M. et al. The formation of skeletal muscle: from somite to limb. *Journal of Anatomy* **202**, 59-68 (2003).
18. Ross, J.J., Duxson, M.J. & Harris, A.J. Formation of primary and secondary myotubes in rat lumbrical muscles. *Development* **100**, 383-94 (1987).
19. Ontell, M. & Kozeka, K. The Organogenesis of Murine Striated-Muscle - a Cytoarchitectural Study. *American Journal of Anatomy* **171**, 133-148 (1984).
20. Bers, D.M. Cardiac excitation-contraction coupling. *Nature* **415**, 198-205 (2002).
21. Stanfield, C. Principles of Human Physiology (Pearson Education Inc., San Francisco, 2011).
22. MacIntosh, B.R. & Willis, J.C. Force-frequency relationship and potentiation in mammalian skeletal muscle. *Journal of Applied Physiology* **88**, 2088-2096 (2000).
23. Collinworth, A.M., Zhang, S., Kraus, W.E. & Truskey, G.A. Apparent elastic modulus and hysteresis of skeletal muscle cells throughout differentiation. *American Journal of Physiology-Cell Physiology* **283**, C1219-C1227 (2002).
24. Madden, J.D.W. et al. Artificial muscle technology: Physical principles and naval prospects. *Ieee Journal Of Oceanic Engineering* **29**, 706-728 (2004).
25. Griffin, M.A., Sen, S., Sweeney, H.L. & Discher, D.E. Adhesion-contractile balance in myocyte differentiation. *Journal of Cell Science* **117**, 5855-5863 (2004).
26. Engler, A.J. et al. Myotubes differentiate optimally on substrates with tissue-like stiffness: pathological implications for soft or stiff microenvironments. *J Cell Biol* **166**, 877-87 (2004).
27. Engler, A.J., Sen, S., Sweeney, H.L. & Discher, D.E. Matrix elasticity directs stem cell lineage specification. *Cell* **126**, 677-689 (2006).
28. Palchesko, R.N., Zhang, L., Sun, Y. & Feinberg, A.W. Development of Polydimethylsiloxane Substrates with Tunable Elastic Modulus to Study Cell Mechanobiology in Muscle and Nerve. *PLoS One* **7** (2012).

29. Williams, C. et al. Aligned Cell Sheets Grown on Thermo-Responsive Substrates with Microcontact Printed Protein Patterns. *Advanced Materials* **21**, 2161-+ (2009).
30. Grosberg, A. et al. Muscle on a chip: In vitro contractility assays for smooth and striated muscle. *Journal of Pharmacological and Toxicological Methods* **65**, 126-135 (2012).
31. Feinberg, A.W. et al. Muscular thin films for building actuators and powering devices. *Science* **317**, 1366-1370 (2007).
32. Grosberg, A., Alford, P.W., McCain, M.L. & Parker, K.K. Ensembles of engineered cardiac tissues for physiological and pharmacological study: Heart on a chip. *Lab on a Chip* **11**, 4165-4173 (2011).
33. Zatti, S. et al. Micropatterning Topology on Soft Substrates Affects Myoblast Proliferation and Differentiation. *Langmuir* **28**, 2718-2726 (2012).
34. Altomare, L., Riehle, M., Gadegaard, N., Tanzi, M.C. & Fare, S. Microcontact printing of fibronectin on a biodegradable polymeric surface for skeletal muscle cell orientation. *Int J Artif Organs* **33**, 535-43 (2010).
35. Curtis, A. & Wilkinson, C. Review: Topographical Control of Cells. *Biomaterials* **18**, 1573-1583 (1997).
36. Flaibani, M. et al. Muscle Differentiation and Myotubes Alignment Is Influenced by Micropatterned Surfaces and Exogenous Electrical Stimulation. *Tissue Engineering Part A* **15**, 2447-2457 (2009).
37. Zhao, Y., Zeng, H.S., Nam, J. & Agarwal, S. Fabrication of Skeletal Muscle Constructs by Topographic Activation of Cell Alignment. *Biotechnology and Bioengineering* **102**, 624-631 (2009).
38. Gingras, J. et al. Controlling the Orientation and Synaptic Differentiation of Myotubes with Micropatterned Substrates. *Biophysical Journal* **97**, 2771-2779 (2009).
39. Wang, P.Y., Yu, H.T. & Tsai, W.B. Modulation of Alignment and Differentiation of Skeletal Myoblasts by Submicron Ridges/Grooves Surface Structure. *Biotechnology and Bioengineering* **106**, 285-294 (2010).
40. Hosseini, V. et al. Engineered contractile skeletal muscle tissue on a microgrooved methacrylated gelatin substrate. *Tissue Eng Part A* **18**, 2453-65 (2012).
41. Neumann, T., Hauschka, S.D. & Sanders, J.E. Tissue engineering of skeletal muscle using polymer fiber arrays. *Tissue Engineering* **9**, 995-1003 (2003).
42. Ku, S.H., Lee, S.H. & Park, C.B. Synergic effects of nanofiber alignment and electroactivity on myoblast differentiation. *Biomaterials* **33**, 6098-104 (2012).
43. Ker, E.D. et al. Bioprinting of growth factors onto aligned sub-micron fibrous scaffolds for simultaneous control of cell differentiation and alignment. *Biomaterials* **32**, 8097-107 (2011).
44. Yamasaki, K. et al. Control of myotube contraction using electrical pulse stimulation for bio-actuator. *Journal of Artificial Organs* **12**, 131-137 (2009).
45. Fujita, H., Nedachi, T. & Kanzaki, M. Accelerated de novo sarcomere assembly by electric pulse stimulation in C2C12 myotubes. *Experimental Cell Research* **313**, 1853-1865 (2007).
46. Fujita, H., Shimizu, K. & Nagamori, E. Novel Method for Measuring Active Tension Generation by C2C12 Myotube Using UV-Crosslinked Collagen Film. *Biotechnology and Bioengineering* **106**, 482-489 (2010).
47. Donnelly, K. et al. A novel bioreactor for stimulating skeletal muscle in vitro. *Tissue Eng Part C Methods* **16**, 711-8 (2010).
48. Edman, K.A.P. Contractile properties of mouse single muscle fibers, a comparison with amphibian muscle fibers. *Journal of Experimental Biology* **208**, 1905-1913 (2005).
49. Ito, A. et al. Induction of functional tissue-engineered skeletal muscle constructs by defined electrical stimulation. *Scientific Reports* **4** (2014).
50. Ahadian, S. et al. A contactless electrical stimulator: application to fabricate functional skeletal muscle tissue. *Biomed Microdevices* **15**, 109-15 (2013).
51. Nagamine, K. et al. Spatiotemporally controlled contraction of micropatterned skeletal muscle cells on a hydrogel sheet. *Lab on a Chip* **11**, 513-517 (2011).
52. Edman, K.A., Elzinga, G. & Noble, M.I. Enhancement of mechanical performance by stretch during tetanic contractions of vertebrate skeletal muscle fibres. *J Physiol* **281**, 139-55 (1978).
53. Powell, C.A., Smiley, B.L., Mills, J. & Vandenburgh, H.H. Mechanical stimulation improves tissue-engineered human skeletal muscle. *Am J Physiol Cell Physiol* **283**, C1557-65 (2002).
54. Moon, D.G., Christ, G., Stitzel, J.D., Atala, A. & Yoo, J.J. Cyclic mechanical preconditioning improves engineered muscle contraction. *Tissue Engineering Part A* **14**, 473-482 (2008).
55. Machingal, M.A. et al. A tissue-engineered muscle repair construct for functional restoration of an irrecoverable muscle injury in a murine model. *Tissue Eng Part A* **17**, 2291-303 (2011).
56. Corona, B.T. et al. Further Development of a Tissue Engineered Muscle Repair Construct In Vitro for Enhanced Functional Recovery Following Implantation In Vivo in a Murine Model of Volumetric Muscle Loss Injury. *Tissue Engineering Part A* **18**, 1213-1228 (2012).

57. Corona, B.T., Ward, C.L., Baker, H.B., Walters, T.J. & Christ, G.J. Implantation of In Vitro Tissue Engineered Muscle Repair Constructs and Bladder Acellular Matrices Partially Restore In Vivo Skeletal Muscle Function in a Rat Model of Volumetric Muscle Loss Injury. *Tissue Engineering Part A* **20**, 705-715 (2014).
58. Cannizzaro, C. et al. in *Tissue Engineering* (eds. Hauser, H. & Fussenegger, M.) 291-307 (Humana Press, 2007).
59. Das, M. et al. A defined system to allow skeletal muscle differentiation and subsequent integration with silicon microstructures. *Biomaterials* **27**, 4374-80 (2006).
60. Wilson, K., Molnar, P. & Hickman, J. Integration of functional myotubes with a Bio-MEMS device for non-invasive interrogation. *Lab on a Chip* **7**, 920-922 (2007).
61. Das, M., Wilson, K., Molnar, P. & Hickman, J.J. Differentiation of skeletal muscle and integration of myotubes with silicon microstructures using serum-free medium and a synthetic silane substrate. *Nat Protoc* **2**, 1795-801 (2007).
62. Wilson, K., Das, M., Wahl, K.J., Colton, R.J. & Hickman, J. Measurement of Contractile Stress Generated by Cultured Rat Muscle on Silicon Cantilevers for Toxin Detection and Muscle Performance Enhancement. *PLoS One* **5** (2010).
63. Vandenberg, H.H., Karlisch, P. & Farr, L. Maintenance of Highly Contractile Tissue-Cultured Avian Skeletal Myotubes in Collagen Gel. *In Vitro Cellular & Developmental Biology* **24**, 166-174 (1988).
64. Rhim, C. et al. Morphology and ultrastructure of differentiating three-dimensional mammalian skeletal muscle in a collagen gel. *Muscle Nerve* **36**, 71-80 (2007).
65. Vandenberg, H. et al. Drug-screening platform based on the contractility of tissue-engineered muscle. *Muscle & Nerve* **37**, 438-447 (2008).
66. Vandenberg, H. et al. Automated drug screening with contractile muscle tissue engineered from dystrophic myoblasts. *Neuromuscular Disorders* **19**, 614-614 (2009).
67. Rhim, C., Cheng, C.S., Kraus, W.E. & Truskey, G.A. Effect of microRNA modulation on bioartificial muscle function. *Tissue Eng Part A* **16**, 3589-97 (2010).
68. Vandenberg, H. et al. Tissue-engineered skeletal muscle organoids for reversible gene therapy. *Human Gene Therapy* **7**, 2195-2200 (1996).
69. Juhas, M. & Bursac, N. Roles of adherent myogenic cells and dynamic culture in engineered muscle function and maintenance of satellite cells. *Biomaterials* **35**, 9438-46 (2014).
70. Madden, L., Juhas, M., Kraus, W.E., Truskey, G.A. & Bursac, N. Bioengineered Human Myobundles Mimic Clinical Responses of Skeletal Muscle to Drugs. *Elife* **4** (2015).
71. Dennis, R.G. & Kosnik, P.E., 2nd. Excitability and isometric contractile properties of mammalian skeletal muscle constructs engineered in vitro. *In Vitro Cell Dev Biol Anim* **36**, 327-35 (2000).
72. Dennis, R.G., Kosnik, P.E., 2nd, Gilbert, M.E. & Faulkner, J.A. Excitability and contractility of skeletal muscle engineered from primary cultures and cell lines. *Am J Physiol Cell Physiol* **280**, C288-95 (2001).
73. Dennis, R.G. & Dow, D.E. Excitability of skeletal muscle during development, denervation, and tissue culture. *Tissue Eng* **13**, 2395-404 (2007).
74. Huang, Y.C., Dennis, R.G., Larkin, L. & Baar, K. Rapid formation of functional muscle in vitro using fibrin gels. *Journal of Applied Physiology* **98**, 706-713 (2005).
75. Larkin, L.M., Calve, S., Kostrominova, T.Y. & Arruda, E.M. Structure and functional evaluation of tendon-skeletal muscle constructs engineered in vitro. *Tissue Engineering* **12**, 3149-3158 (2006).
76. Akiyama, Y., Kikuchi, A., Yamato, M. & Okano, T. Ultrathin poly(N-isopropylacrylamide) grafted layer on polystyrene surfaces for cell adhesion/detachment control. *Langmuir* **20**, 5506-5511 (2004).
77. Haraguchi, Y. et al. Fabrication of functional three-dimensional tissues by stacking cell sheets in vitro. *Nature Protocols* **7**, 850-858 (2012).
78. Yamamoto, Y. et al. Preparation of artificial skeletal muscle tissues by a magnetic force-based tissue engineering technique. *Journal of Bioscience and Bioengineering* **108**, 538-543 (2009).
79. Yamamoto, Y. et al. Functional Evaluation of Artificial Skeletal Muscle Tissue Constructs Fabricated by a Magnetic Force-Based Tissue Engineering Technique. *Tissue Engineering Part A* **17**, 107-114 (2011).
80. Nawroth, J.C. et al. A tissue-engineered jellyfish with biomimetic propulsion. *Nature Biotechnology* **30**, 792-797 (2012).
81. Xi, J.Z., Schmidt, J.J. & Montemagno, C.D. Self-assembled microdevices driven by muscle. *Nature Materials* **4**, 180-U67 (2005).
82. Shimizu, K. et al. Assembly of skeletal muscle cells on a Si-MEMS device and their generative force measurement. *Biomedical Microdevices* **12**, 247-252 (2010).

83. Hoshino, T. & Morishima, K. Muscle-powered cantilever for microtweezers with an artificial micro skeleton and rat primary myotubes. *Journal of Biomechanical Science and Engineering* **5**, 245-251 (2010).
84. Akiyama, Y. et al. Rod-shaped tissue engineered skeletal muscle with artificial anchors to utilize as a bio-actuator. *Journal of Biomechanical Science and Engineering* **5**, 236-244 (2010).
85. Kabumoto, K., Hoshino, T. & Morishima, K. in International Conference on Biomedical Robotics and Biomechatronics 419-424 (The University of Tokyo, Tokyo, Japan, 2010).
86. Tanaka, Y. et al. A micro-spherical heart pump powered by cultured cardiomyocytes. *Lab on a Chip* **7**, 207-212 (2007).
87. Sakar, M.S. et al. Formation and optogenetic control of engineered 3D skeletal muscle bioactuators. *Lab Chip* **12**, 4976-85 (2012).
88. Kim, J. et al. Establishment of a fabrication method for a long-term actuated hybrid cell robot. *Lab on a Chip* **7**, 1504-1508 (2007).
89. Chan, V. et al. Development of Miniaturized Walking Biological Machines. *Scientific Reports* **2** (2012).
90. Cvetkovic, C. et al. Three-dimensionally printed biological machines powered by skeletal muscle. *Proceedings of the National Academy of Sciences of the United States of America* **111**, 10125-10130 (2014).
91. Herr, H. & Dennis, R.G. A swimming robot actuated by living muscle tissue. *J Neuroeng Rehabil* **1**, 6 (2004).

Chapter 3

Understanding the Role of ECM Protein Composition and Geometric Micropatterning for Engineering Human Skeletal Muscle

3.1 Introduction

Skeletal muscle is composed of billions of molecular motors that are organized into a contractile, multiscale system that provides force generation for a diverse array of living organisms¹. During the process of myogenesis, myoblasts align with one another, fuse membranes to form myotubes, and then begin to assemble the internal cell machinery into organized sarcomeres of myosin heavy chain (MHC) and actin, the portions of skeletal muscle that serve as actuators at the sub-cellular level^{2,3}. Skeletal muscle has unique capabilities including the ability to repair minor injuries and adapt to workloads by increasing volumetric muscle mass. However, in humans this ability to maintain or restore normal structure and function becomes impaired during disease and injury. Understanding how these repair and regeneration mechanisms work is therefore critical to developing new regenerative therapies for skeletal muscle diseases as well as for applications in *in vitro* pharmaceutical testing and as actuators for soft robotics and bioprosthetics⁴. Here we were specifically interested in understanding the role the extracellular matrix (ECM) plays in driving functional skeletal muscle formation since the ECM provides specific architectural and biochemical cues that guide tissue formation *in vivo*. Researchers have demonstrated that the cell-ECM interface can be leveraged

to engineer skeletal muscle in 2D and 3D *in vitro* systems^{5, 6}, and ECM from decellularized tissues has been used to promote regeneration of skeletal muscle defects in human patients⁷.

Engineering skeletal muscle tissue *in vitro* requires an understanding of the microenvironmental cues that drive myogenesis, including ECM composition and architecture, as well as species specific differences as we transition to human systems. A number of *in vitro* studies have shown that myotube formation and contractility depends on specific microenvironmental cues including stiffness⁸⁻¹⁰, patterning of ECM proteins¹¹⁻¹³, and ECM composition⁵. However, a quantitative understanding of how specific ECM proteins and their spatial patterning controls skeletal muscle differentiation and alignment is still needed. Skeletal muscle has been engineered from a variety of species *in vitro*, but it has proved much more difficult to differentiate and maintain human skeletal muscle^{14, 15}. The immortalized C2C12 mouse myoblast cell line is widely studied, and has been used by many researchers to engineer 2D myotube constructs¹⁶⁻¹⁹. There are also many examples of 3D engineered skeletal muscle constructs derived from primary rat muscle and fibroblast co-cultures²⁰, primary chick muscle²¹, primary mouse myoblasts²², and C2C12 myoblasts^{23, 24}. However, there are far fewer examples of engineered human skeletal muscle constructs *in vitro*. Vandeburgh and co-workers established a protocol to engineer contractile human bioartificial muscles that increased in maturity with mechanical stimulation²⁵. Recently, Bursac and co-workers developed a method to engineer functional human skeletal muscle constructs that integrated into *in vivo* mouse models and responded to pharmaceutical stimulation^{26, 27}. However, despite the advances of these 3D engineered human skeletal muscle constructs, they are formed by casting cell within isotropic hydrogels and rely on self-organization to compact into final form. For this reason, 2D platforms

are still attractive as tools to better understand the interplay between the ECM and myogenesis in engineered muscle constructs.

The aim of this study was to understand how the composition and microscale geometric patterning of ECM proteins on a surface controls the differentiation of myoblasts into aligned myotubes. Further, we wanted to determine whether the response was species specific and differed between standard murine C2C12s and more clinically relevant human cell lines. Previously, we differentiated C2C12s on micropatterned lines of fibronectin (FN) and quantified how line geometry influenced myotube formation¹². Specifically, these results led us to investigate how different ECM proteins affected myotube formation and alignment from C2C12 and human primary myoblasts. First, we wanted to determine if ECM proteins found in skeletal muscle would increase myotube differentiation, in terms of density (surface coverage) and length. To test this, we compared myotube differentiation on FN, collagen type IV (Col IV), laminin 111 (LAM), and collagen type I (Col I), all major components of skeletal muscle ECM²⁸⁻³¹. Second, we wanted to determine the critical line width and spacing to uniaxially align myotubes while simultaneously maximizing myotube density and uniaxial alignment. To test this, we differentiated myoblasts on microcontact printed (μ CP) ECM protein lines with 10, 15, 20, or 30 μ m spacings and 20, 50, 100, or 200 μ m widths, as well as on isotropically coated controls. Finally, we wanted to determine whether cell source affected myoblast response to ECM guidance cues. To test this, we differentiated C2C12 mouse myoblasts and human skeletal muscle derived cells (SkMDCs) on these ECM line patterns.

3.2 Materials and Methods

3.2.1 Substrate Fabrication

The ECM protein micropatterned substrates were fabricated based on previously published techniques^{12, 32}. Briefly, Sylgard 184 polydimethylsiloxane (PDMS; Dow Corning Corp.) base and curing agent were mixed at a 10:1 mass ratio, respectively. PDMS was spincoated onto 25 mm diameter glass coverslips at 4,000 rpm to create an approximately 15 μm thick PDMS layer. PDMS coated coverslips were cured at 65°C for at least 4 hours before use. PDMS stamps for μCP were fabricated as previously described with the exception that MF-26A (Dow Electronic Materials) was used as the developer for the SPR 220.3 positive photoresist (MicroChem Corp.)¹². PDMS stamps with 10, 15, 20, and 30 μm line spacings and 20, 50, 100, and 200 μm line widths were created for a total of 16 micropattern conditions. Patterns are referred to as width x spacing (e.g. a pattern with 50 μm lines and 10 μm spacings is 50x10).

All ECM proteins used for μCP were diluted with distilled water to final concentrations of 50 $\mu\text{g/mL}$ for human FN (Sigma-Aldrich), 200 $\mu\text{g/mL}$ for mouse LAM (Life Technologies), 200 $\mu\text{g/mL}$ for mouse Col IV (Life Technologies), and 500 $\mu\text{g/mL}$ for rat tail Col I (Corning). The procedure for μCP was followed as previously described¹². Briefly, PDMS stamps were sonicated feature side up for 30 minutes in 50% ethanol solution. Stamps were dried with a nitrogen air gun, the feature side was coated with protein solution and incubated for 1 hour at room temperature. Stamps were rinsed twice in distilled water and dried with the nitrogen gun. PDMS coated coverslips were UV ozone treated for 15 minutes and stamps were inverted and placed in conformal contact with the coverslip for 5 minutes to transfer the ECM protein lines. Stamps were then removed, and the patterned coverslips were incubated with 1% w/v Pluronic

F-127 solution for 5 minutes followed by three rinses of phosphate buffered saline (PBS). For isotropically coated coverslips, UV-ozone treated PDMS coverslips were inverted onto 200 μ L of protein solution for 15 minutes, followed by 3 rinses of PBS. Samples were used immediately or stored in PBS at 4°C for up to 2 weeks.

3.2.2 Cell Culture

Reagents were obtained from Life Technologies unless indicated otherwise. The murine C2C12 cell line (CRL-1722, ATCC) was cultured and differentiated as recommended by the supplier at 37°C and 10% CO₂. Cells were cultured and expanded in growth media (GM) (high glucose DMEM (Corning) supplemented with 10% fetal bovine serum, 1% penicillin-streptomycin, and 1% L-glutamine (200 mM)) and split at 1:10 ratios at 80% confluence. Cells were used at <12 passages from the supplier and were seeded at a density of 30,000 cells/cm² on micropatterned substrates. C2C12s proliferated in GM on substrates for 24 - 48 hours in order to reach 100% confluence on micropatterned lines. GM was then exchanged for differentiation media (DM) (high glucose DMEM (Corning) supplemented with 2% horse serum, 1% penicillin-streptomycin, and 1% L-glutamine (200 mM)), and exchanged daily for 6 days. After differentiation, samples were ready to be fixed and stained for analysis of myotube formation as described below.

Human SkMDCs were obtained from Cook MyoSite. Cells were cultured according to the supplier recommendations at 37°C and 5% CO₂. Additionally, cells were maintained below 80% confluence in MyoTonic Growth Medium (Cook Myosite) during expansion. Cook's SkMDCs were seeded on substrates at 40,000 cells/cm² and were switched to MyoTonic Differentiation Medium (MDM - Cook Myosite) after cells reached confluence on patterned

lines. MDM was exchanged every 48 hours for 6 days. After differentiation, samples were fixed and stained for analysis of myotube formation.

3.2.3 Immunofluorescence Staining and Imaging

Samples were fixed, stained for myotubes, and imaged to quantify myotube formation as previously described¹². Reagents were obtained from Life Technologies unless otherwise indicated. After 6 days in DM, myotubes were rinsed in PBS (0.625 mM Mg^{2+} and 0.109 mM Ca^{2+}) and fixed with 0°C methanol (Fisher Scientific) for 2 minutes. Samples were then rinsed with PBS 3 times for 5 minutes and incubated with 5% v/v goat serum in PBS for 1 hour. Samples were rinsed in PBS 3 times for 5 minutes prior to incubating for 1 hour with 1:200 and 1:100 dilutions of DAPI and monoclonal mouse MHC antibody in PBS, respectively. Samples were rinsed three times with PBS and incubated for 1 hour with a 1:100 dilution of Alexa Fluor 555 conjugated with goat anti-mouse antibody. Samples were again rinsed 3 times in PBS prior to being mounted onto slides using Prolong Gold Anti-fade. Samples were imaged using a Zeiss LSM 700 laser scanning confocal microscope to obtain z-stacks and tile scans of samples. Tile scans were typically 1.28 mm x 1.28 mm. Some tile scans for myotube length were between 2.56 mm x 0.64 mm and 4.48 mm x 0.64 mm in order to ensure that a measurable number of myotubes did not extend out of the field of view for length and myotube fusion index (MFI) measurements.

3.2.4 Image Analysis

Post-processing of images was performed as previously described^{12,33}. MHC staining was used to identify myotubes and DAPI to identify nuclei. Percent area myotubes, MFI – or nuclei/myotube, and myotube length were used as metrics for myotube maturity. We also

measured myotube alignment relative to the μ CP ECM lines. ImageJ was used to quantify all of these metrics using images with immunofluorescent MHC staining. To quantify percent area myotubes, the MHC channel was isolated, thresholded, converted to an 8-bit binary, and holes where nuclei had been were filled using the ‘fill holes’ feature within the binary menu. The percent of MHC positive pixels were then quantified using the ‘analyze particles’ feature. Myotube lengths and orientation were measured manually using the line tool, and MFI was quantified manually using the cell counter plug-in. Myotubes that extended outside of the field of view were not quantified for length, MFI, or orientation.

3.2.5 Statistical Analysis

All statistics were performed using SigmaPlot (Systat Software Inc.). Statistical analyses were performed as one-way ANOVA or ANOVA on ranks as deemed appropriate based on normality and equal variance tests. Data that failed normality or equal variance tests are reported as median (med) and interquartile range (IQR); data that passed normality and equal variance tests are presented as mean \pm SD. The following post hoc tests were used: Student-Newman-Keuls Method (Figure 3.3D), Dunn’s method (Figures 3.3E, 3.3F, 3.6C, 3.6D, 3.8E, 9F, and 9G), and Holm-Sidak Method (Figures 3.6A, 3.7, 3.12, and 3.10A). Differences were considered statistically significant at $p < 0.05$.

3.3 Results

3.3.1 C2C12 differentiation into myotubes is dependent on ECM composition and patterning

To investigate how specific ECM proteins influenced the differentiation of myoblasts into myotubes we compared C2C12 myotube formation on FN, LAM, Col IV, and Col I. First, we screened myotube formation on coverslips micropatterned with 100x20 lines or uniformly

coated with the ECM proteins as isotropic controls (Figure 3.1). The 100x20 lines were selected based on our previous studies that showed FN lines with these dimensions guided formation of aligned myotubes from C2C12 cells¹². Qualitative results showed that all surfaces supported

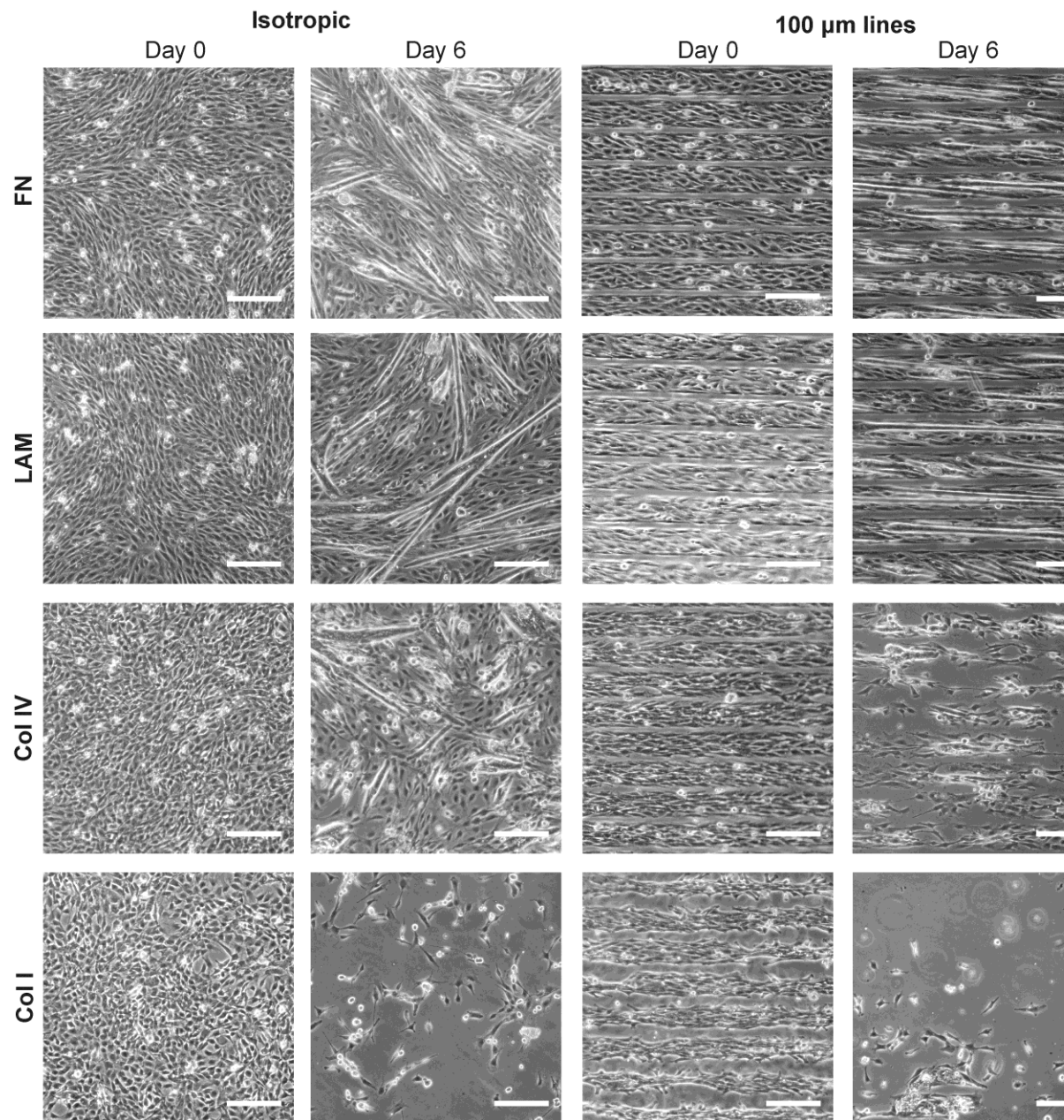


Figure 3.1. Phase contrast images of C2C12 cells differentiated on FN, LAM, Col IV, and Col I. Samples were differentiated on isotropically coated coverslips and 100x20 micropatterns. After 6 days of differentiation, cells begin to delaminate from μ CP lines of Col IV and Col I and isotropically coated Col I. However, myotubes were able to form on both μ CP or isotropically coated LAM and FN. Scale bars 200 μ m.

myoblast adhesion and spreading at day 0 in GM, however by day 6 in DM, cells were no longer attached to the coverslip (delaminated) on isotropic Col I and micropatterned lines of Col I and Col IV. The delamination from the micropatterned lines of Col I and IV began after the switch to DM (see Figure 3.2). This demonstrated adhesion of myoblasts during differentiation depended on both the ECM protein composition and patterning in 2D.

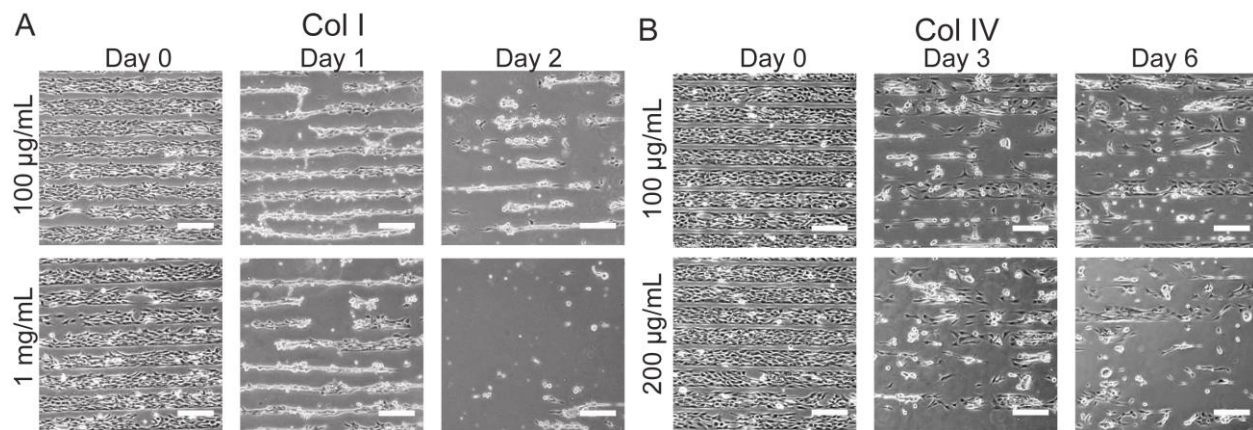


Figure 3.2: C2C12 myoblasts delaminate rapidly on Col I and Col IV. (A) C2C12 myoblasts were switched to DM after reaching confluence on 100x20 micropatterned lines of Col I (Day 0). At both low (100 µg/mL) and high (1 mg/mL) Col I concentrations, myoblasts began peeling off of patterned Col I before fusing to form myotubes (Day 1, Day 2). (B) C2C12 myoblasts were switched to DM after reaching confluence on 100x20 micropatterned lines of Col IV (Day 0). At both low (100 µg/mL) and high (200 µg/mL) Col IV concentrations, myoblasts began peeling off of patterned Col IV before fusing to form myotubes (Day 3, Day 6). Scale bars 200 µm.

To understand this further, we differentiated C2C12s into myotubes, as measured by MHC positive cells, and quantified myotube length, MFI, and myotube area on micropatterned lines of FN, Col IV, and LAM. Note that we included Col IV in the analysis for comparison; even though most of the cells had delaminated once switched to DM, and by day 6 in DM there were very few myotubes present (Figure 3.2B). Results showed that differentiation was highly dependent on ECM protein composition (Figure 3.3 A-C). The C2C12s on the micropatterned LAM lines differentiated into a significantly greater number of myotubes based on MHC positive cells (Figure 3.3D), were significantly longer (Figure 3.3E), and had significantly higher MFI (Figure 3.3F) than cells on FN or Col IV. Importantly, the LAM surface outperformed the

FN surface, which we previously showed was effective for engineering anisotropic 2D skeletal muscle tissue and which other groups have used to pattern cardiac muscle^{34, 35} and vascular smooth muscle^{36, 37}. The median values for myotube area and MFI on LAM were 1.5-times and 2-times those on FN, respectively. This indicates that LAM increased the total number of myoblasts that differentiated into myotubes as well as the number of myoblasts that fused into a single myotube.

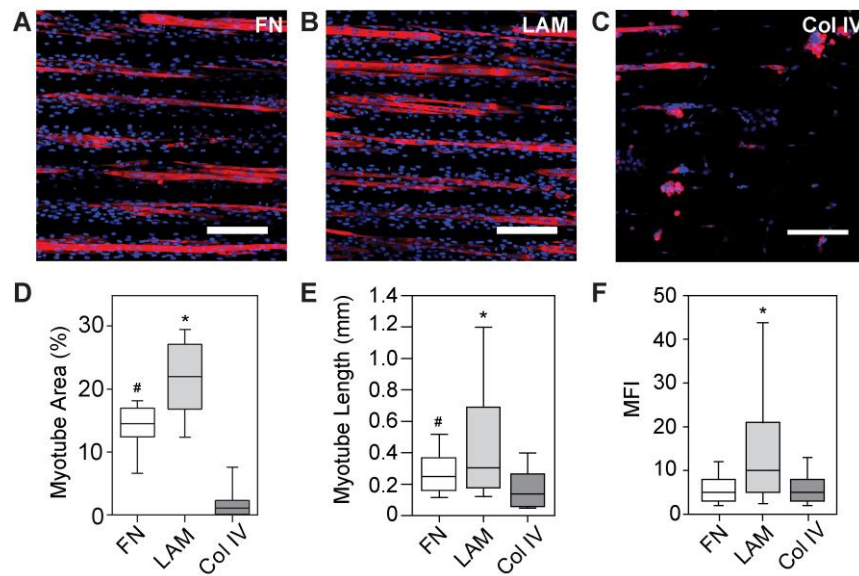


Figure 3.3. C2C12 myoblasts form longer, more nucleated myotubes on LAM lines. C2C12 myotubes differentiated for 6 days on 100x20 lines of (A) FN (B) LAM and (C) Col IV show increased myotube formation on LAM and delamination of myotubes from Col IV after staining for MHC and nuclei. (D) Myotubes formed on LAM lines had significantly higher MFI than those differentiated on FN or Col IV. (E) Myotubes differentiated on LAM were significantly longer than those differentiated on FN or Col IV, and myotubes differentiated on FN were also significantly longer than myotubes that formed on Col IV. (F) Percent area of myotubes formed on LAM lines was also significantly higher than on FN or Col IV, and significantly more percent area myotubes formed on FN than on Col IV. * $p < 0.05$ compared to FN and Col I. # $p < 0.05$ compared to Col IV. Scale bars 200 μm . Blue – DAPI; Red – MHC.

3.3.2 LAM line width and spacing dictates C2C12 myotube differentiation and alignment

Based on the results of the ECM screen (Figure 3.3), we next investigated LAM micropatterned line width and spacing to determine how geometric cues influenced myotube differentiation and uniaxial alignment. We evaluated 16 conditions consisting of 20, 50, 100, and 200 μm line widths and 10, 15, 20, and 30 μm line spacing in addition to an isotropic control (Figure 3.5, Figure 3.4A). These conditions were chosen based on previous results using micropatterned FN lines in our own studies and in the literature^{12, 38}. As expected, the isotropic control sample had C2C12 myotubes oriented in all directions, as confirmed by the MHC stain and histogram of myotube alignment angle (Figure 3.4A-B). At the 10 μm line spacing, the myotubes were able to bridge between the micropatterned lines and as a result aligned at a 20° to 30° angle to the lines (Figure 3.5). At the wider 15, 20, and 30 μm line spacing the myotubes generally followed the micropatterned lines, though there were clear differences in myotube differentiation, orientation, length and MFI.

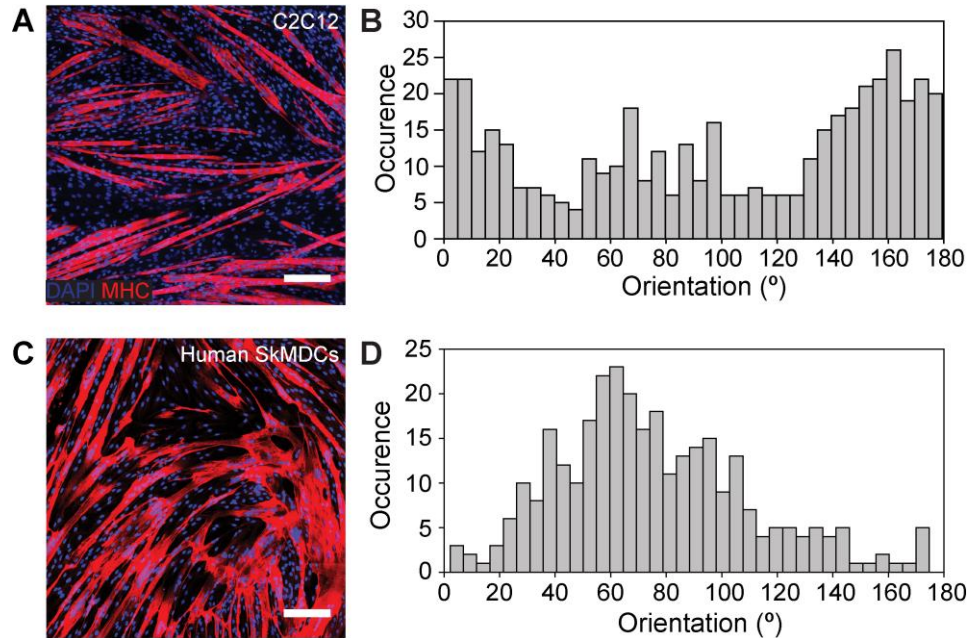


Figure 3.4: Myotubes formed on isotropic coatings of LAM. (A) C2C12 and (B) Cook's human SkMDC myotube formation on isotropic LAM coated coverslips. Histograms of myotubes on isotropic LAM for (C) C2C12 cells and (D) human SkMDCs shows little to no preferential orientation or alignment of myotubes. Blue – DAPI, Red – MHC. Scale Bars 200 μm .

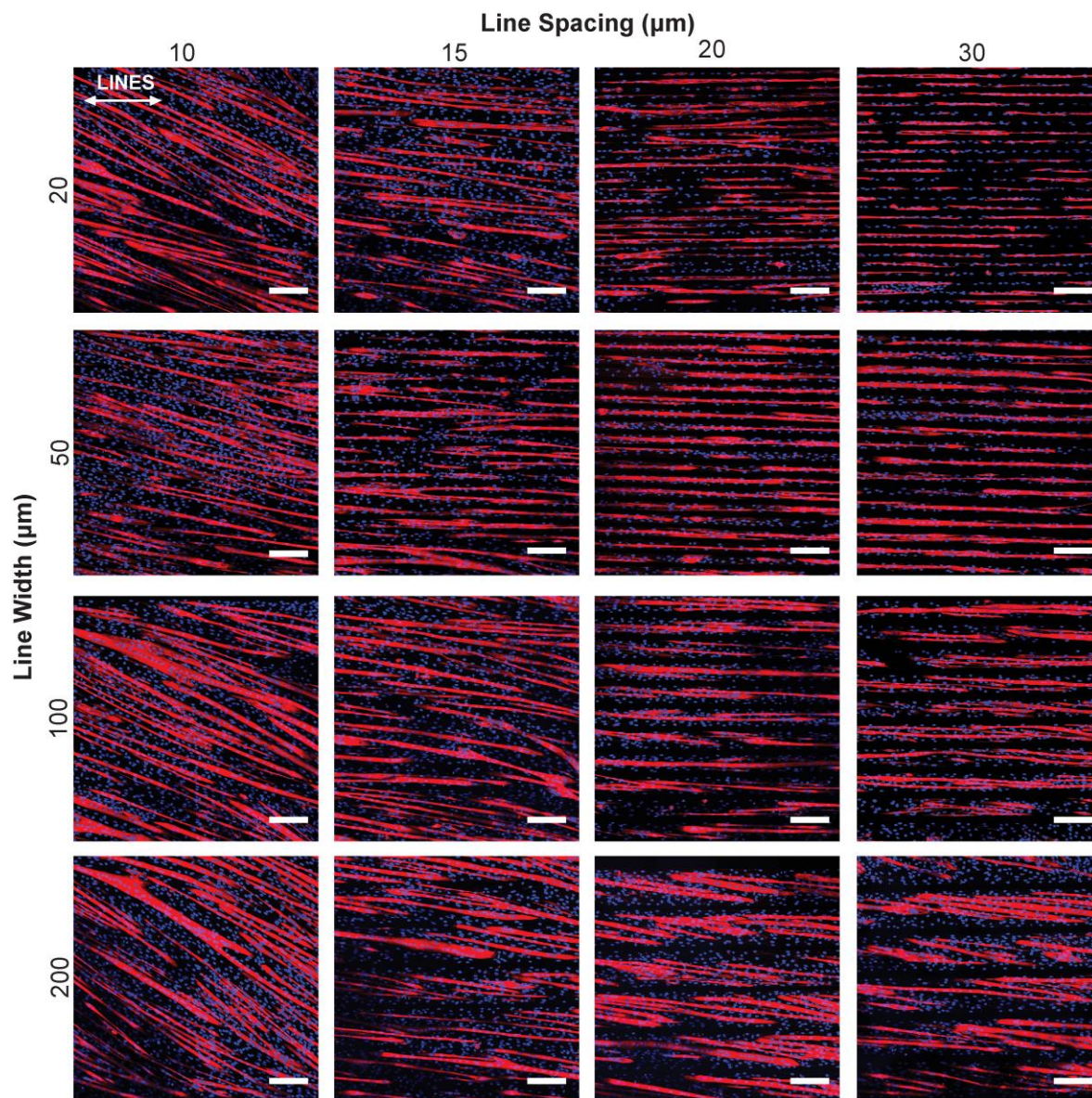


Figure 3.5. Representative images of C2C12 cells differentiated on 16 different line patterns of LAM. Myotubes deviate from aligning with the designated pattern when geometric spacing is too narrow ($<15\ \mu\text{m}$), or when the lines are too wide ($200\ \mu\text{m}$). White arrows represent direction of μCP lines. Scale bars $200\ \mu\text{m}$. Blue – DAPI; Red – MHC.

Next, we quantified the myotube formation on the micropatterned LAM lines in order to determine the patterns that maximized the amount of uniaxially aligned muscle tissue. Similar to our previous results on FN lines¹², the width and spacing of micropatterned LAM lines had a significant impact on myotube differentiation (Figure 3.6A). Myotube area was comparable to

the isotropic controls at the 10 and 15 μm line spacing for all line widths. However, the myotubes on these surfaces bridged between the LAM lines at these narrower spacings. The width of the LAM lines was also found to be an important factor, especially at the 20 and 30 μm line spacing. Differentiation was clearly lowest for the 20 μm line width and increased to a maximum level for the 200 μm line width. However, this seemed to be due to differences in LAM surface area, as normalizing the myotube area by the LAM surface area showed statistically equivalent results for all line widths (Figure 3.7). Myotube orientation generally showed a trend that was opposite to that of myotube area, with uniaxial alignment being better for surface patterns that had lower myotube area. Myotubes grown on lines with spacings of 10 and 15 μm grew aligned relative to each other (Figure 3.6B), but these dimensions enabled bridging across the spacings, resulting in myotubes oriented off axis to the micropatterned lines. The 20 and 30 μm line spacings resulted in uniaxial myotube alignment and prevented myotubes from bridging across LAM lines (Figure 3.6B). However, on the wider LAM lines, particularly 100 and 200 μm wide lines, the myotubes also began to orient off axis to the pattern. Finally, myotube length (Figure 3.6C) and MFI (Figure 3.6D) were similar across most of the micropatterns, with the exception that both metrics were significantly lower on the 20x20 and 20x30 patterns compared to the wider lines. Note that myotube length and MFI were not calculated for the 10 μm spacing because the myotubes did not align well with the pattern and thus were not considered effective for engineering aligned skeletal muscle. Thus, the micropatterns that had the best uniaxial alignment parallel to the lines were also the patterns with the lowest myotube area. Additionally, myotubes differentiated on the 100 and 200 μm wide lines had trends towards longer myotubes length and higher MFI compared to isotropic controls, which suggested that that this more organized guidance of myotube fusion resulted in more

mature myotubes. In total, these results suggested that LAM line geometry influenced C2C12 myotube formation and that patterns that increased differentiation decreased uniaxial alignment.

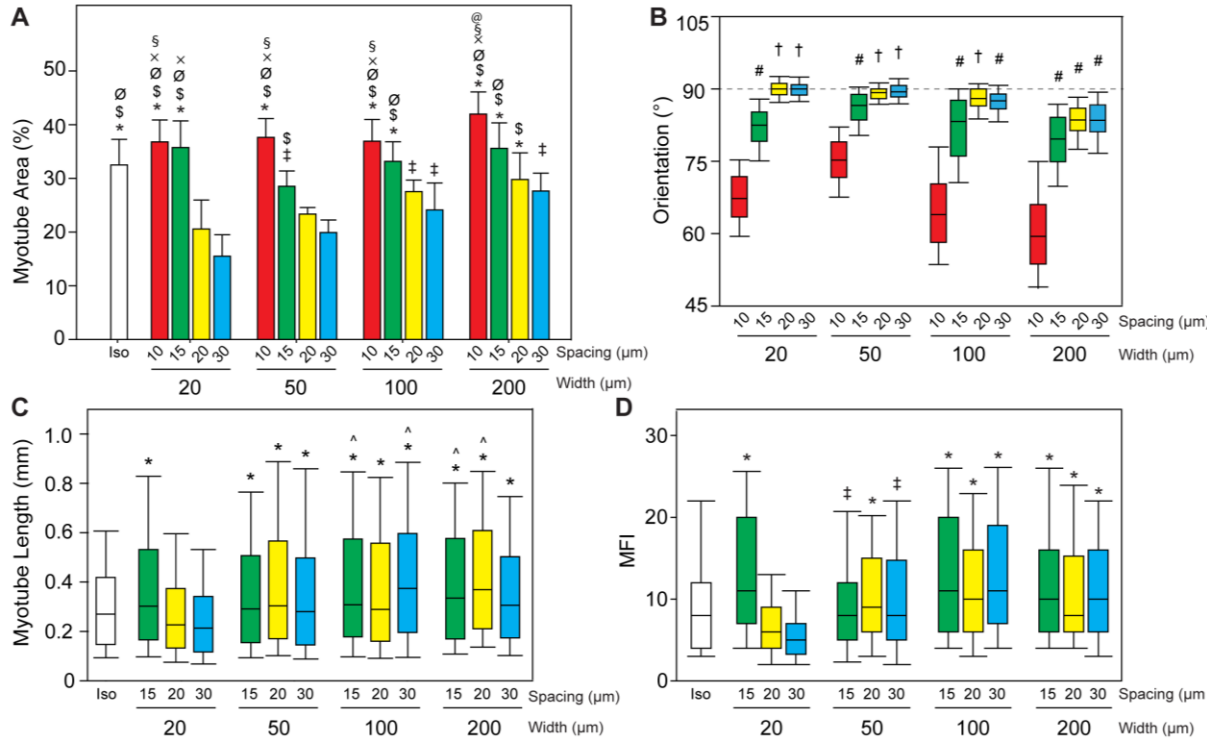


Figure 3.6. Quantification of C2C12 myotube alignment, area, length, and MFI on 16 LAM line geometries. (A) Percent area myotubes is higher on 10 and 15 μm spacing conditions because myotubes have more patterned area of LAM on which to form. (B) The orientation of lines is marked at 90°. Myotubes maintain alignment with the patterned ECM when the line spacing is 20 or 30 μm, and line width is < 200 μm. (C) Longer myotubes formed on from patterned lines >20 μm wide. (D) Myotubes formed on wider lines were the result of fusion of significantly more myoblasts as measured by MFI. Length and MFI were not quantified for line spacings of 10 μm as myotubes were not restricted to form uniaxially along the pattern. † p < 0.05 compared to 10 and 15 μm spacings and all widths; # p < 0.05 compared to 10 μm spacings; * p < 0.05 compared to 20x20 and 20x30; ^ p < 0.05 compared to isotropic; ‡ p < 0.05 than 20x30; \$ p < 0.05 compared to 50x30; Ø p < 0.05 compared to 50x20 and 100x30; § p < 0.05 compared to 50x15 and 200x30; x p < 0.05 compared to 100x20; @ p < 0.05 compared to 100x15 and 200x20.

3.3.3 Human SkMDCs differentiation into myotubes is dependent on ECM composition

To determine if human and mouse myoblasts respond similarly to ECM protein cues, we repeated the ECM protein screen performed for the C2C12 (Figure 3.3) for human SkMDCs on Col I, Col IV, FN, and LAM (Figure 3.8). The human myotubes differentiated poorly and delaminated on Col I and Col IV (Figure 3.8A-B), appeared to differentiate marginally better on

FN (Figure 3.8C) and differentiated robustly on LAM (Figure 3.8D). There was significantly greater myotube formation on LAM, greater than 2-times, compared to on Col I, Col IV, and FN (Figure 3.8E). Myotubes formed on LAM lines were also significantly more mature as measured by myotube length and MFI. Human myotubes formed on LAM were greater than 3-times longer than myotubes formed on Col I, Col IV, and on FN (Figure 3.8F). Similarly, human myotubes formed on LAM had approximately 2-times greater MFI than myotubes formed on Col I and Col IV (Figure 3.8G). In total, these results demonstrated that human SkMDCs, which behave as myoblasts in our system, differentiated better on micropatterned LAM lines as compared to the other ECM proteins evaluated.

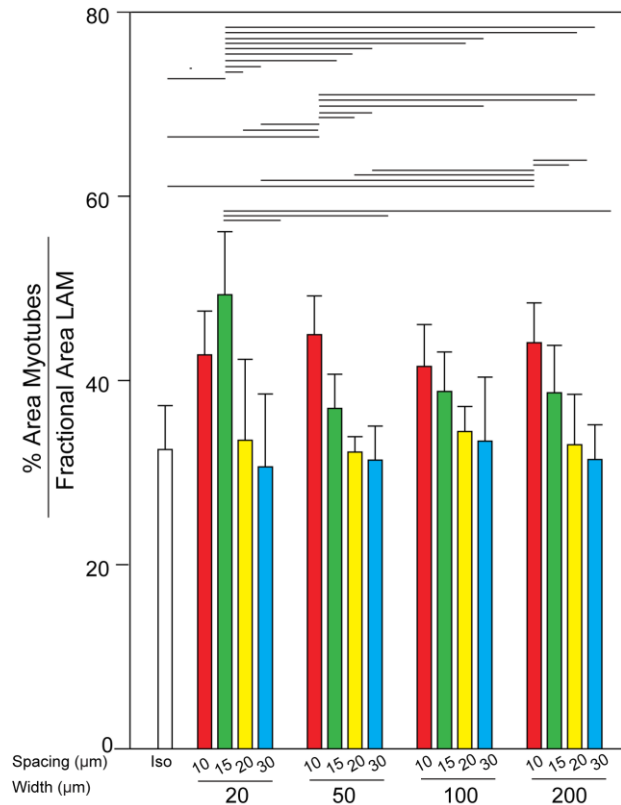


Figure 3.7: C2C12 myotube area normalized for area LAM lines. C2C12 myotube formation measured by percent area myotubes and normalized for percent area of patterned LAM. Significantly more myotubes formed on patterns that allowed C2C12 myoblasts to fuse across line spacings rather than restricting myotube fusion to occur only on μ CP lines. Additionally, guidance cues from μ CP lines appear to increase myotube area/LAM area as several of the conditions have significantly more myotube formation than the isotropic control. $n = 6$. Lines represent $p < 0.05$.

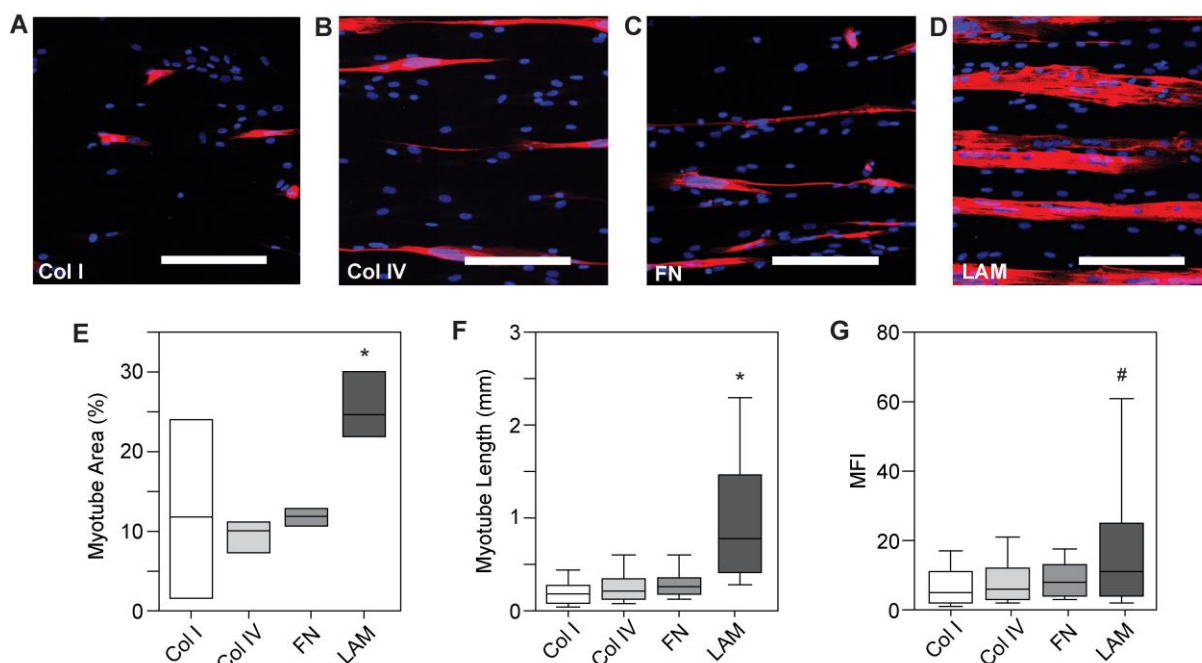


Figure 3.8. Human SkMDCs form longer, more nucleated myotubes on LAM.(A-D) Representative images of MHC and DAPI staining of human myotube formation on 100x20 lines. (E) Quantifying the percent area of myotube formation for human skeletal muscle cells shows significantly higher myotube area on LAM compared to Col I, Col IV, and FN. Myotube formation on Col I is highly variable. (F) Human myotubes formed on LAM lines are significantly longer than myotubes formed on Col I, Col IV, and FN. (G) Human myotubes formed on LAM lines also have significantly higher MFI than those formed on Col I and Col IV lines. * $p < 0.05$ compared to Col I, Col IV, and FN. # $p < 0.05$ compared to Col I and Col IV. Scale bars 200 μm . Blue – DAPI; Red – MHC.

3.3.4 LAM line width and spacing has limited effect on human SkMDC myotube differentiation and alignment

Next, we performed a smaller pattern screen with human SkMDCs to determine if the different micropatterned LAM line geometries affected human myotube formation similarly to the C2C12 cells. We evaluated 9 conditions consisting of 50, 100, and 200 μm wide lines and 10, 15, and 20 μm spacing as well as an isotropic control (Figure 3.9, Figure 3.4C). We did not include 20 μm wide lines as these resulted in poor myotube formation for the C2C12s and did not include 30 μm line spacing because the 20 μm spacing was as effective at aligning myotubes while supporting greater myotube area (Figure 3.6). Interestingly, the human myotubes did not

behave the same as the C2C12 myotubes and instead became similarly aligned on all LAM micropatterns. All the line patterns had significantly less myotube area than the isotropic control but otherwise were comparable with the 50x20 line pattern having

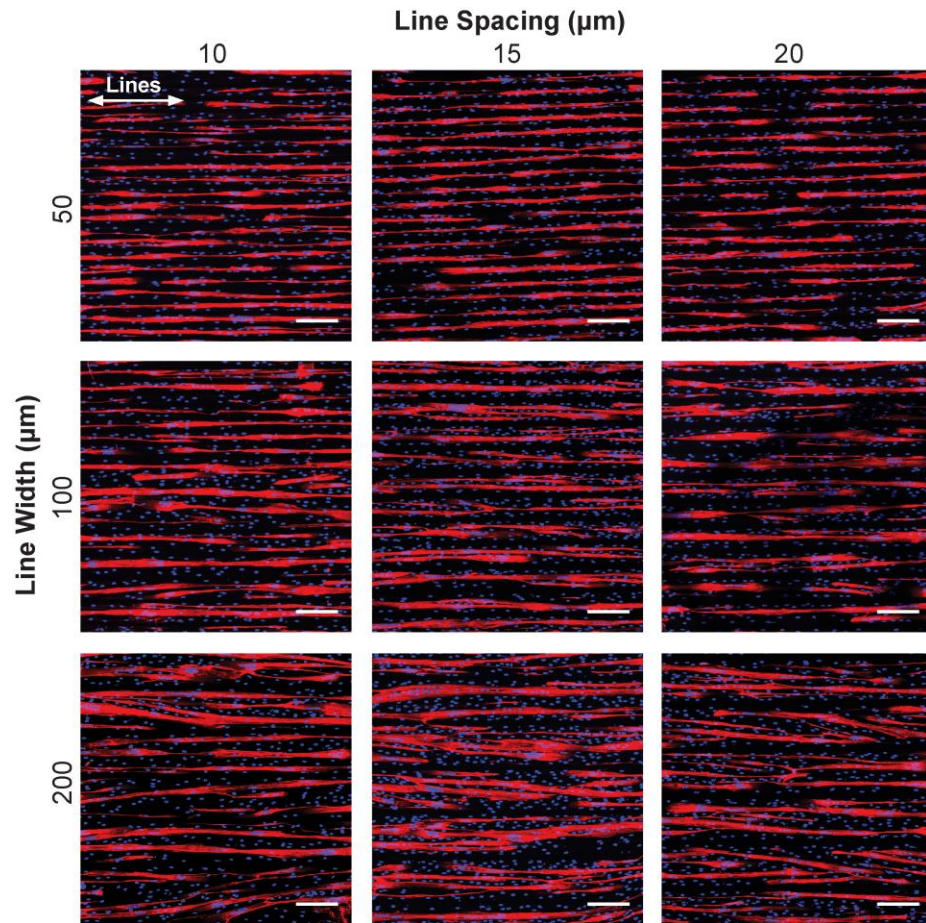


Figure 3.9. Representative images of human myotube formation after 6 days of differentiation on 9 line patterns of LAM. Myotubes do not appear to deviate from line patterns with narrow line spacings ($<20\ \mu\text{m}$) to the extent that C2C12 mouse myoblasts do. Scale bars $200\ \mu\text{m}$. White arrows represent orientation of LAM lines. Blue – DAPI; Red – MHC

approximately half that of myotubes on the 200x10, 200x15, and 200x20 line patterns (Figure 3.10A). Normalizing the myotube area by the LAM surface area indicated that the 50x20 pattern had significantly less myotube formation, but no statistical differences were observed between the other patterns (Figure 3.12). Human myotubes on all LAM patterns were uniaxially aligned to the lines, different than the isotropic control (Figure 3.4D), but with no statistically significant difference between line patterns (Figure 3.10B). Myotube orientation only began to deviate from the line pattern at the $200\ \mu\text{m}$ width, as the distribution angles increased (Figure 3.10B). Similar to the uniaxial alignment of the human myoblasts on all patterns, there were no statistical

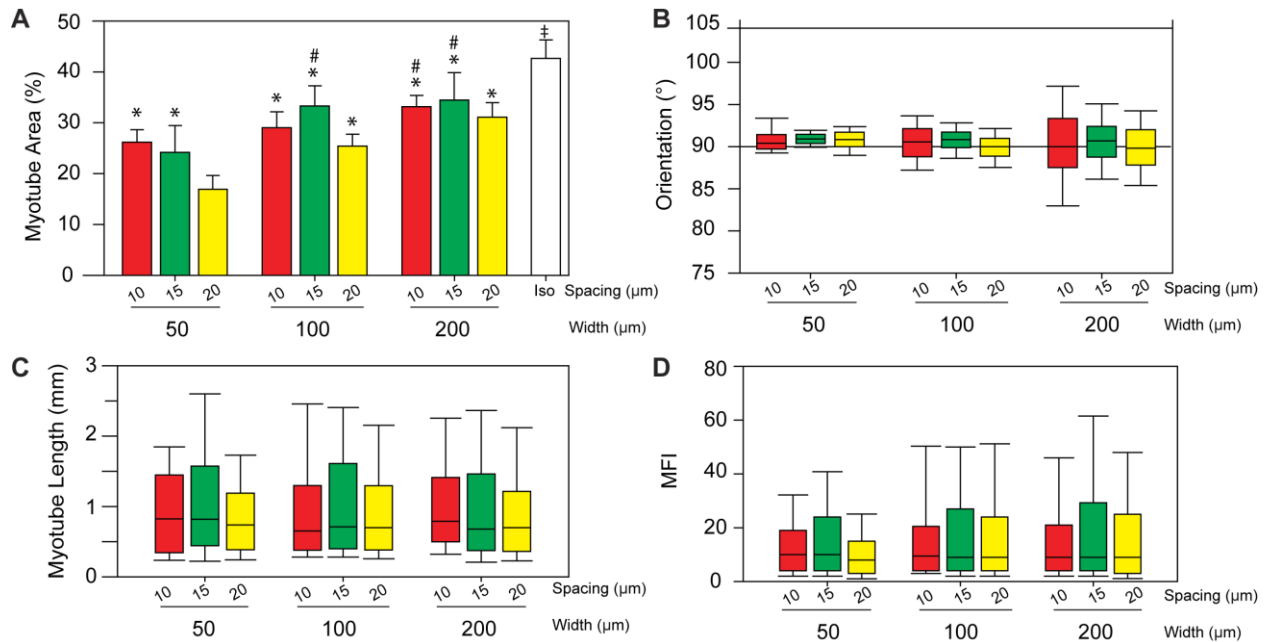


Figure 3.10. Quantification of human SkMDC myotube alignment, area, length, and MFI on 9 LAM line geometries. (A) Percent area myotubes for each LAM line pattern and isotropic control (not normalized for percent area of patterned LAM) shows an increase in myotube formation as the line width increases, as expected. (B) With 90° representing parallel orientation to the μ CP LAM, there was no significant difference in orientation on patterned lines. (C) There is no statistical difference in myotube length or (D) MFI for human myotubes grown on 9 different line width and spacing conditions of LAM. * $p < 0.05$ compared to 50x20; # $p < 0.05$ compared to 50x10, 50x15, and 100x20; ‡ $p < 0.05$ compared to all other conditions.

significant difference in myotube length (Figure 3.10C) and MFI (Figure 3.10D) between the different LAM line widths and spacings. As a further control to account for lot-to-lot variability, we evaluated five additional human SkMDC lines, and while there were differences in differentiation efficiency, all formed well-aligned myotubes on the LAM patterns. This suggests that our results indicated a difference between species, and were representative of human SkMDC cells.

3.3.5 Micropattern geometries that maximize formation of aligned muscle is species specific

Finally, we evaluated the data on myotube area and alignment for both C2C12 and human SkMDC cells to directly compare across species. For the C2C12s, myotube orientation angle was plotted as a function of myotube area, and this confirmed that there was an inverse relationship between these properties (Figure 3.12A). While it was possible to achieve myotube

areas as high as approximately 40%, it was at the expense of alignment. When taking uniaxial alignment in the direction of the line micropatterns into consideration, the maximum myotube area that could be achieved was much lower at approximately 25%. In contrast, for the human SkMDCs, the relationship between myotube orientation angle and myotube area was completely different, showing minimal dependence on the micropattern geometry (Figure 3.12B). For all conditions the human myotubes were uniaxially aligned in the direction of the micropatterned lines. The human myotubes were able to bridge across the LAM lines at the narrower line spacings, but this did not cause the myotubes to change their angle of orientation, as it did for the C2C12 myotubes. Thus, increasing myotube area was dependent primarily on the width of the LAM line, and the maximum that could be achieved was approximately 35%. Together, these results highlight the differential response of human and murine skeletal muscle cells to the LAM micropatterned surface, and that even though the C2C12s could achieve a greater myotube area, the human cells achieved a greater uniaxially aligned myotube area.

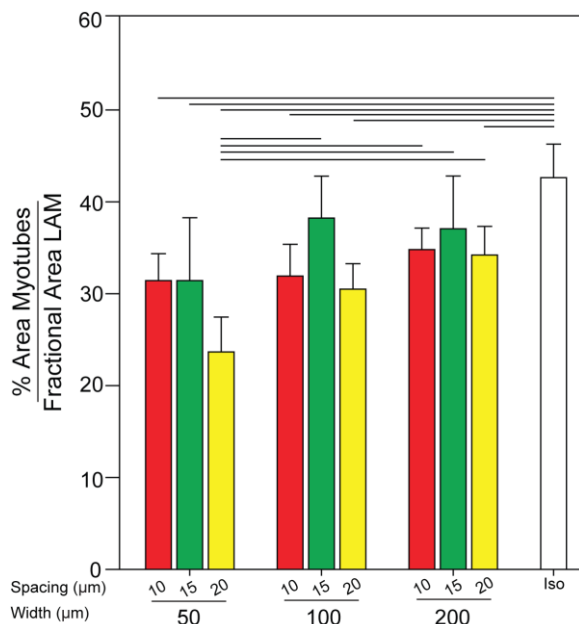


Figure 3.11: Human SkMDC myotube area normalized for area LAM lines. Human SkMDC myotube formation normalized for percent area μ CP LAM for each pattern. Unlike C2C12s, human SkMDCs form higher percent area myotubes/area LAM on isotropically coated LAM. Additionally, myotubes formed on 50x20 patterns had significantly less differentiated myotubes even after normalization for patterned area. Myotubes did not fuse across 10 and 15 μ m line spacings, so there significantly higher myotube formation was not observed on these patterns when normalized for area patterned LAM as observed with C2C12 myotubes. N = 5 for 50x10 and 100x10 patterns. N = 6 for all other conditions. Lines represent $p < 0.05$.

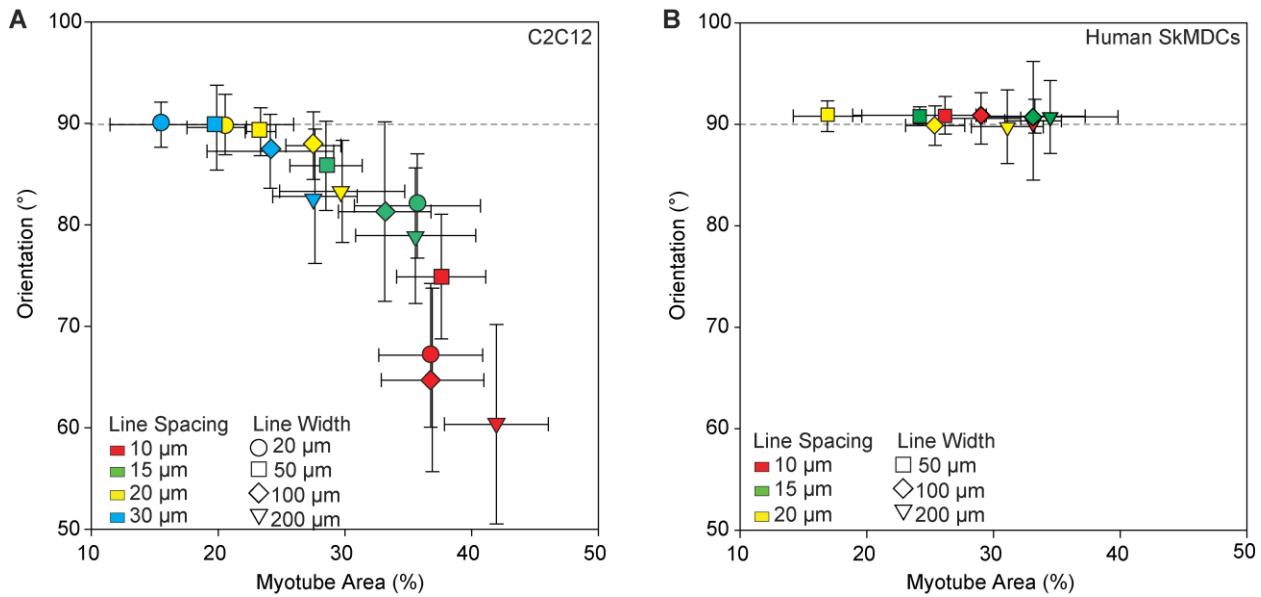


Figure 3.12. Scatterplots of myotube orientation v. percent area myotubes. (A) Scatterplot of percent area myotubes against the orientation of myotubes for each pattern shows a trend of increasing deviation from alignment with the patterned lines as percent area of myotubes increases. There is a tradeoff for increasing the amount of myotube formation and maintaining uniaxial organization of myotubes. (B) Scatterplot with human myotube orientation and percent area shows there is not a decrease in alignment with LAM lines (90°) with an increase in percent area myotubes and decrease in line spacing, as is observed with C2C12 myotubes. Error bars represent standard deviation.

3.4 Discussion

Overall, our results show that myotube formation and uniaxial alignment in 2D engineered skeletal muscle depends on composition and micropatterning of the ECM proteins and the cell source. We observed a tradeoff between myotube orientation and myotube area for C2C12s that was not observed for human SkMDC derived myotubes. This could be attributed to donor variation in the human cells, but 5 different donor lots differentiated on the same patterns all behaved similarly (Figure 3.13). Specifically, we observed that line spacings of 10 or 15 μm enabled C2C12 myotubes to bridge between LAM lines and thus did not align to the pattern (Figure 3.5). However, these same line spacings were able to align human myotubes on the LAM lines parallel to the pattern (Figure 3.8). There are multiple potential reasons for these differences. First, the C2C12s are an immortalized myoblast cell line and behave differently than primary isolated muscle precursor cells. For example, they are more proliferative than human

SkMDCs, reaching confluence at a faster rate (data not shown). This rapid C2C12 proliferation rate may lead to transient overcrowding on the lines that facilitated bridging across the smaller 10 and 15 μm line spacings, and subsequent fusing with cells on adjacent lines. In contrast, the human SkMDCs did not proliferate as rapidly and thus fused with cells on the same LAM line. The large size of the myotubes means that they are unlikely to bridge once they have formed. Thus, the difference in response by the murine and human muscle cells may be due in part to intrinsic differences in growth rate. Second, C2C12s myotubes appeared to have an inherent bias in the direction of alignment relative to the direction of the myotube lines. This was observed on the patterns with 10 and 15 μm spacings as well as on the 100 and 200 μm lines with wider spacings. This was most notable on the 200x20 pattern (Figure 3.5 and Figure 3.6B), where the C2C12 myotubes were entirely confined to the 200 μm wide LAM lines but still aligned 5° to 10° off axis to the pattern. We observed the exact same behavior on FN lines in previous work¹², and other groups have reported similar responses as well for C2C12s on micropatterns^{38, 39}. Thus, there are clearly genetically encoded similarities and differences in cell response to microenvironmental cues between the C2C12 and human muscle cells.

This raises a number of interesting questions regarding the mechanisms involved in

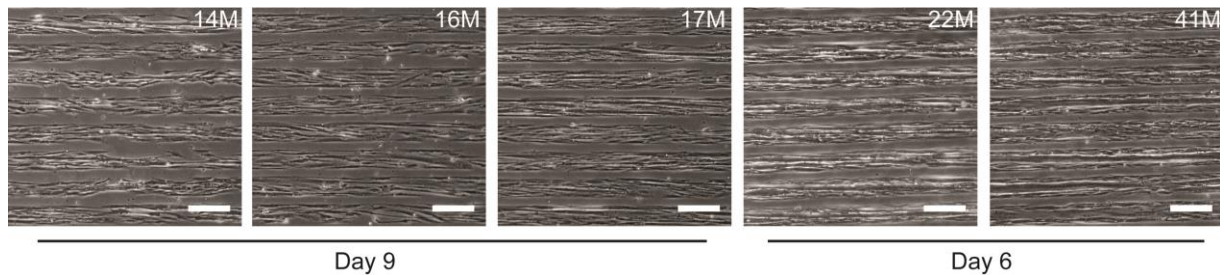


Figure 3.13: Phase images of human SkMDCs on μCP 100x20 lines of LAM. Different donor isolations are represented in each image, with donor age and gender represented in the upper right. Degree of myotube formation varies from sample to sample, but even in phase it is apparent that samples with myotube formation generally have wide, long myotubes that take up most of the patterned line area, just as the samples from the 17F donor that were quantified in the other sections of this chapter. This increased alignment and restriction to patterned lines is a qualitative trend for human SkMDCs isolated by Cook Myosite. Scale bars 200 μm

muscle differentiation across species as well as the interplay between physical and biochemical cues in the microenvironment. For example, both murine C2C12 and human SkMDCs demonstrated significantly increased differentiation on LAM lines compared to FN, Col I and Col IV (Figures 3 and 8). There are multiple potential reasons for this, but one possibility is the different integrins used to attach to these ECM proteins. As noted, we observed poor differentiation of C2C12s and human SkMDCs on both collagens. This could be related to the fact that a 5-fold increase in fibrillary collagens has been observed in very old muscle, as well as increases in $\beta 1$ integrin, suggesting that Col I may inhibit myogenesis *in vivo*⁴⁰. Additionally, when porcine myoblasts were differentiated on Col I, gelatin, FN, Matrigel, and LAM, myogenin, a late myogenic marker, was expressed at the lowest levels on Col I⁴¹. Poor myotube formation has also been observed for murine satellite cells cultured on entactin-laminin-collagen (ECL) substrates, Col IV, poly-d-lysine, and LAM, where higher myotube fusion rates occurred on poly-d-lysine or LAM compared to Col IV or ECL^{42, 43}. Col IV content in skeletal muscle is also higher in patients with Duchenne muscular dystrophy (DMD) and impaired muscle regeneration⁴⁴, which is consistent with increased Col IV gene expression in DMD myotubes⁴⁵. Similarly, in mouse models of DMD, LAM 111 injections, which increased the relative amount of LAM in the ECM, increased muscle strength in treated mice⁴⁶, and LAM 111 injections in mice with muscle damage induced by eccentric exercise resulted in significantly more embryonic-MHC positive fibers⁴⁷. In addition to integrins, it is also known that the dystroglycan (DG) receptor binds to laminin globular domain 4 on the LAM $\alpha 1$ chain⁴⁸. The DG complex activates pathways that increase myoblast growth⁴⁹ and is one of the proteins that is affected by DMD. This results in severe defects in muscle regeneration and eventual loss of structure and function of formerly healthy skeletal muscle^{50, 51}. In terms of ECM composition, our results and

those noted from the literature support the finding that LAM increases murine and human myoblast differentiation into myotubes. However, the reasons for differences in myotube orientation remain unclear and will require further studies to elucidate.

An important aspect of the current study is the delamination of differentiating myotubes on micropatterned lines of Col I and Col IV, which could be influencing the interpretation of our results. Skeletal muscle myotubes are known to form within Col I gels²¹⁻²³, so the inability of myotubes to consistently form on micropatterned lines of Col I and Col IV may be an artifact of the μ CP method itself. It is possible that the poor myotube differentiation is due to lack of cell and/or ECM adhesion to the underlying PDMS, contributing to cell and/or myotube delamination during culture. One question is whether the myoblasts detach from the coverslip, or whether the myoblasts fuse into myotubes and then detach. After initial seeding in GM, myoblasts adhered on both micropatterned and isotropically coated coverlips of Col I and Col IV (Figure 3.1). However, myoblasts began to detach as early as 24 hours after switching to lower serum containing DM, (Figure 3.2A). This would suggest that the loss of cells on the Col I and Col IV occurs prior to fusion into myotubes, perhaps driven by a decrease in fibronectin and vitronectin from FBS removal. It is possible increased cell contractility could result in myoblasts or myotubes detaching from the patterned proteins or peeling the patterned proteins off of coverslips. In fact, even on the FN and LAM micropatterned lines, which support differentiation, myotubes will eventually delaminate after 6-14 days in culture, depending on the specific cell type, ECM protein and micropattern used. Recently it has been shown that covalently crosslinking FN to PDMS using genipin enabled long term smooth muscle cell attachment on micropatterned FN lines⁵². This could potentially be applied to future studies with skeletal muscle on patterned lines of Col IV and Col I but was outside the scope of the presented study.

In general, more in depth studies need to be performed to determine the reason for myoblast or myotube delamination from these proteins at such an early stage of differentiation. Regardless of the cause, this is an inherent limitation of the 2D micropatterned in vitro culture system. However, this 2D approach was used for these studies because it served a starting point that allowed us to probe how ECM composition in conjunction with micropatterned geometry influenced myotube formation.

Future work will explore the role of ECM composition and micropatterning in more advanced 2D and 3D model systems of engineered skeletal muscle. For 2D systems, we are interested in measuring contractile force generation using our previously developed muscular thin film contractility assay. However, the human myotubes start to delaminate after 6 days but must be matured longer than this to become contractile. It may be possible to solve this problem by crosslinking the LAM to the PDMS using genipin or by increasing the surface area for adhesion by using LAM coated micropatterned ridges. However, we are primarily interested in scaling our current findings to engineered 3D skeletal muscle tissues to allow us to differentiate myotubes for at least 2 – 4 weeks^{5, 15, 22, 27}. An open question is whether LAM can have the same effect in 3D muscle differentiation as in 2D, and if so how LAM must be integrated into the Col I and fibrinogen gels typically used. Further, 3D muscle constructs more readily provide functional metrics of skeletal muscle maturity, such as twitch force and calcium handling dynamics. While it is challenging to precisely micropattern LAM cues in 3D, emerging technologies such as decellularization^{53, 54} and engineered LAM nanofibers^{55, 56} suggest that we may be able to engineer 3D scaffolds comparable to our 2D surfaces in the near future.

3.5 Conclusions

In conclusion, we have engineered skeletal muscle from murine C2C12s and human SkMDCs and demonstrated that myotube differentiation and alignment is dependent on ECM protein composition and micropattern geometry. Both C2C12 and human myotube formation were significantly increased on micropatterned LAM, and with poor myotube formation significant delamination on both Col I and Col IV. The C2C12 myotubes required specific geometric cues, line width and spacing, to guide uniaxial myotube alignment compared to human SkMDCs. In general, micropatterns that increased myotube area decreased uniaxial alignment of C2C12 myotubes. In contrast, all LAM line micropatterns guided human SkMDCs to uniaxially align, with no significant differences observed for myotube orientation, length or MFI. This means that myotube formation as guided by ECM composition and geometric cues is species dependent. Looking forward, this means the role of microenvironmental cues is complex, multifactorial and dependent on cell origin. These factors are critical to understand as these tissue engineering technologies are translated to clinical applications, and further demonstrates that utility of the 2D platform to screen multiple parameters as lead up to more targeted studies in 3D.

3.6 Acknowledgements

Financial support from the National Institutes of Health Director's New Innovator Award (DP2HL117750) to Adam Feinberg and the John and Claire Bertucci Fellowship from the Carnegie Institute of Technology to Rebecca Duffy. The lab of Johnny Huard at the University of Pittsburgh graciously provided initial aliquots of Cook Myosite human SkMDC and Cook

MyoSite Inc. provided assistance with human SkMDC lot selection. We thank Lucas Friedman for providing assistance with image analysis.

3.7 References

1. Pette, D. & Vrbova, G. Neural control of phenotypic expression in mammalian muscle fibers. *Muscle Nerve* **8**, 676-89 (1985).
2. Charge, S.B. & Rudnicki, M.A. Cellular and molecular regulation of muscle regeneration. *Physiol Rev* **84**, 209-38 (2004).
3. Sanger, J.W., Wang, J., Fan, Y., White, J. & Sanger, J.M. Assembly and dynamics of myofibrils. *J Biomed Biotechnol* **2010**, 858606.
4. Duffy, R.M. & Feinberg, A.W. Engineered skeletal muscle tissue for soft robotics: fabrication strategies, current applications, and future challenges. *Wiley Interdisciplinary Reviews-Nanomedicine and Nanobiotechnology* **6**, 178-195 (2014).
5. Hinds, S., Bian, W.N., Dennis, R.G. & Bursac, N. The role of extracellular matrix composition in structure and function of bioengineered skeletal muscle. *Biomaterials* **32**, 3575-3583 (2011).
6. Grounds, M.D., Sorokin, L. & White, J. Strength at the extracellular matrix-muscle interface. *Scandinavian Journal of Medicine & Science in Sports* **15**, 381-391 (2005).
7. Mase, V.J., Jr. et al. Clinical application of an acellular biologic scaffold for surgical repair of a large, traumatic quadriceps femoris muscle defect. *Orthopedics* **33**, 511(2010).
8. Engler, A.J., Sen, S., Sweeney, H.L. & Discher, D.E. Matrix elasticity directs stem cell lineage specification. *Cell* **126**, 677-89 (2006).
9. Engler, A.J. et al. Myotubes differentiate optimally on substrates with tissue-like stiffness: pathological implications for soft or stiff microenvironments. *Journal of Cell Biology* **166**, 877-887 (2004).
10. Palchesko, R.N., Zhang, L., Sun, Y. & Feinberg, A.W. Development of Polydimethylsiloxane Substrates with Tunable Elastic Modulus to Study Cell Mechanobiology in Muscle and Nerve. *Plos One* **7** (2012).
11. Altomare, L., Riehle, M., Gadegaard, N., Tanzi, M. & Fare, S. Microcontact printing of fibronectin on a biodegradable polymeric surface for skeletal muscle cell orientation. *International Journal of Artificial Organs* **33**, 535-543 (2010).
12. Sun, Y., Duffy, R., Lee, A. & Feinberg, A.W. Optimizing the structure and contractility of engineered skeletal muscle thin films. *Acta Biomaterialia* **9**, 7885-7894 (2013).
13. Flaibani, M. et al. Muscle differentiation and myotubes alignment is influenced by micropatterned surfaces and exogenous electrical stimulation. *Tissue Eng Part A* **15**, 2447-57 (2009).
14. Eberli, D., Soker, S., Atala, A. & Yoo, J.J. Optimization of human skeletal muscle precursor cell culture and myofiber formation in vitro. *Methods* **47**, 98-103 (2009).
15. Guo, X. et al. In vitro Differentiation of Functional Human Skeletal Myotubes in a Defined System. *Biomater Sci* **2**, 131-138 (2014).
16. Zhao, Y., Zeng, H., Nam, J. & Agarwal, S. Fabrication of skeletal muscle constructs by topographic activation of cell alignment. *Biotechnol Bioeng* **102**, 624-31 (2009).
17. Wang, P.Y., Yu, H.T. & Tsai, W.B. Modulation of alignment and differentiation of skeletal myoblasts by submicron ridges/grooves surface structure. *Biotechnol Bioeng* **106**, 285-94 (2010).
18. Ker, E.D. et al. Bioprinting of growth factors onto aligned sub-micron fibrous scaffolds for simultaneous control of cell differentiation and alignment. *Biomaterials* **32**, 8097-107 (2011).
19. Fujita, H., Shimizu, K. & Nagamori, E. Novel method for measuring active tension generation by C2C12 myotube using UV-crosslinked collagen film. *Biotechnol Bioeng* **106**, 482-9 (2010).
20. Dennis, R.G. & Kosnik, P.E., 2nd. Excitability and isometric contractile properties of mammalian skeletal muscle constructs engineered in vitro. *In Vitro Cell Dev Biol Anim* **36**, 327-35 (2000).
21. Vandenberg, H.H., Karlisch, P. & Farr, L. Maintenance of highly contractile tissue-cultured avian skeletal myotubes in collagen gel. *In Vitro Cell Dev Biol* **24**, 166-74 (1988).
22. Vandenberg, H. et al. Drug-screening platform based on the contractility of tissue-engineered muscle. *Muscle Nerve* **37**, 438-47 (2008).
23. Rhim, C. et al. Morphology and ultrastructure of differentiating three-dimensional mammalian skeletal muscle in a collagen gel. *Muscle Nerve* **36**, 71-80 (2007).

24. Yamamoto, Y. et al. Preparation of artificial skeletal muscle tissues by a magnetic force-based tissue engineering technique. *J Biosci Bioeng* **108**, 538-43 (2009).
25. Powell, C.A., Smiley, B.L., Mills, J. & Vandenburgh, H.H. Mechanical stimulation improves tissue-engineered human skeletal muscle. *Am J Physiol Cell Physiol* **283**, C1557-65 (2002).
26. Cheng, C.S., Davis, B.N., Madden, L., Bursac, N. & Truskey, G.A. Physiology and metabolism of tissue-engineered skeletal muscle. *Exp Biol Med (Maywood)* **239**, 1203-14 (2014).
27. Madden, L., Juhas, M., Kraus, W.E., Truskey, G.A. & Bursac, N. Bioengineered human myobundles mimic clinical responses of skeletal muscle to drugs. *Elife* **4**, e04885 (2015).
28. Boonen, K.J.M. & Post, M.J. The Muscle Stem Cell Niche: Regulation of Satellite Cells During Regeneration. *Tissue Engineering Part B-Reviews* **14**, 419-431 (2008).
29. Wolf, M.T., Daly, K.A., Reing, J.E. & Badylak, S.F. Biologic scaffold composed of skeletal muscle extracellular matrix. *Biomaterials* **33**, 2916-2925 (2012).
30. Gillies, A.R. & Lieber, R.L. Structure and function of the skeletal muscle extracellular matrix. *Muscle Nerve* **44**, 318-31 (2011).
31. Nakamura, Y.N. et al. Three-dimensional reconstruction of intramuscular collagen networks of bovine muscle: A demonstration by an immunohistochemical/confocal laser-scanning microscopic method. *Animal Science Journal* **78**, 445-447 (2007).
32. Grosberg, A., Alford, P.W., McCain, M.L. & Parker, K.K. Ensembles of engineered cardiac tissues for physiological and pharmacological study: heart on a chip. *Lab Chip* **11**, 4165-73 (2011).
33. Schindelin, J. et al. Fiji: an open-source platform for biological-image analysis. *Nat Methods* **9**, 676-82 (2012).
34. Feinberg, A.W. et al. Controlling the contractile strength of engineered cardiac muscle by hierarchical tissue architecture. *Biomaterials* **33**, 5732-5741 (2012).
35. Feinberg, A.W. et al. Muscular Thin Films for Building Actuators and Powering Devices. *Science* **317**, 1366-1370 (2007).
36. Alford, P.W., Nesmith, A.P., Seywerd, J.N., Grosberg, A. & Parker, K.K. Vascular smooth muscle contractility depends on cell shape. *Integrative Biology* **3**, 1063-1070 (2011).
37. Alford, P.W., Feinberg, A.W., Sheehy, S.P. & Parker, K.K. Biohybrid thin films for measuring contractility in engineered cardiovascular muscle. *Biomaterials* **31**, 3613-3621 (2010).
38. Zatti, S. et al. Micropatterning Topology on Soft Substrates Affects Myoblast Proliferation and Differentiation. *Langmuir* **28**, 2718-2726 (2012).
39. Bajaj, P. et al. Patterning the differentiation of C2C12 skeletal myoblasts. *Integr Biol (Camb)* **3**, 897-909 (2011).
40. Ramaswamy, K.S. et al. Lateral transmission of force is impaired in skeletal muscles of dystrophic mice and very old rats. *J Physiol* **589**, 1195-208 (2010).
41. Wilschut, K.J., Haagsman, H.P. & Roelen, B.A. Extracellular matrix components direct porcine muscle stem cell behavior. *Exp Cell Res* **316**, 341-52 (2009).
42. Boonen, K.J., Rosaria-Chak, K.Y., Baaijens, F.P., van der Schaft, D.W. & Post, M.J. Essential environmental cues from the satellite cell niche: optimizing proliferation and differentiation. *Am J Physiol Cell Physiol* **296**, C1338-45 (2009).
43. Schultz, E. Fine structure of satellite cells in growing skeletal muscle. *Am J Anat* **147**, 49-70 (1976).
44. Hayashi, Y.K. et al. Abnormal localization of laminin subunits in muscular dystrophies. *J Neurol Sci* **119**, 53-64 (1993).
45. Zanotti, S. et al. Altered extracellular matrix transcript expression and protein modulation in primary Duchenne muscular dystrophy myotubes. *Matrix Biol* **26**, 615-24 (2007).
46. Goudenege, S. et al. Laminin-111: A Potential Therapeutic Agent for Duchenne Muscular Dystrophy. *Molecular Therapy* **18**, 2155-2163 (2010).
47. Zou, K. et al. Laminin-111 Improves Skeletal Muscle Repair Following Eccentric Exercise-Induced Damage. *Medicine and Science in Sports and Exercise* **46**, 926-926 (2014).
48. Durbeek, M. et al. Dystroglycan binding to laminin alpha1LG4 module influences epithelial morphogenesis of salivary gland and lung in vitro. *Differentiation* **69**, 121-34 (2001).
49. Oak, S.A., Zhou, Y.W. & Jarrett, H.W. Skeletal muscle signaling pathway through the dystrophin glycoprotein complex and Rac1. *J Biol Chem* **278**, 39287-95 (2003).
50. Rando, T.A. The dystrophin-glycoprotein complex, cellular signaling, and the regulation of cell survival in the muscular dystrophies. *Muscle & Nerve* **24**, 1575-1594 (2001).

51. Sciandra, F. et al. Dystroglycan and muscular dystrophies related to the dystrophin-glycoprotein complex. *Ann Ist Super Sanita* **39**, 173-81 (2003).
52. Hald, E.S., Steucke, K.E., Reeves, J.A., Win, Z. & Alford, P.W. Microfluidic Genipin Deposition Technique for Extended Culture of Micropatterned Vascular Muscular Thin Films. *J Vis Exp*, e52971 (2015).
53. Jallerat, Q., Szymanski, J.M. & Feinberg, A.W. in *Bio-inspired Materials for Biomedical Engineering* 195-226 (John Wiley & Sons, Inc., 2014).
54. Ott, H.C. et al. Perfusion-decellularized matrix: using nature's platform to engineer a bioartificial heart. *Nat Med* **14**, 213-221 (2008).
55. Szymanski, J.M., Jallerat, Q. & Feinberg, A.W. ECM Protein Nanofibers and Nanostructures Engineered Using Surface-initiated Assembly. *Journal of Visualized Experiments*, e51176 (2014).
56. Feinberg, A.W. & Parker, K.K. Surface-Initiated Assembly of Protein Nanofabrics. *Nano Letters* **10**, 2184-2191 (2010).

Chapter 4

Trace Amounts of Perlecan in Isolated Laminin Influences 2D Human Myotube Formation

4.1 Introduction

Laminin (LAM), one of the major proteins found in the basal lamina of skeletal muscle, has 15 confirmed isoforms consisting of different α , β , and γ chains¹. In the previous chapter, we focused on the influence of the LAM 111 isoform on myotube formation because it is commercially available as it is sourced from the basement membrane rich Engelbreth-Holm-Swarm (EHS) sarcoma. Additionally, LAM 111 is critical to embryonic skeletal muscle formation and is one of the first isoforms to appear in developing embryos^{2, 3}. For these reasons, we were interested in investigating the mechanism that drove higher skeletal muscle myotube formation on LAM lines, as better understanding of this has applications in engineering functional skeletal muscle models *in vitro*.

More specifically, we observed an interesting phenomenon when we changed our commercial LAM source. We changed from Invitrogen (Inv) LAM to Beckton Dickinson (BD) sourced LAM, and we observed a drastic decrease in myotube formation by both C2C12 and human primary skeletal muscle derived cells (SkMDCs). Despite the fact that both LAMs were sourced from seemingly identical sites (EHS mouse sarcoma) and were listed as LAM 111 according to manufacturer product information, we observed significantly less myotube

formation on BD LAM, independent of lot or batch number from either company. Because proteins are digested out of a larger conglomeration of extracellular matrix (ECM), we hypothesized that trace amounts of another key protein in the basement membrane or small molecules key to skeletal myoblast binding, such as glycans, were present in the Inv LAM but were being stripped from BD LAM during the digestion and purification process.

Determining the key difference between the LAM supplied by the two different companies is necessary to engineer functional skeletal muscle, because many tissue engineering techniques rely on commercially sourced biological ECM proteins. Small discrepancies among isolated protein samples limits the quality control of the field of tissue engineering as a whole since designing functional tissues relies on precise understanding of how ECM protein binding sites influence cell signaling cascades that dictate differentiation processes via integrins and other protein binding complexes. For instance, myoblasts adhere to LAM 111 using several different $\beta 1$ associated integrins⁴, syndecans 1-4^{1, 5}, and perhaps most importantly, α - dystroglycan (α -DG)^{6, 7}. As an example, α -DG is an important part of the dystrophin glycoprotein complex, and mutations in the genes responsible for α -DG formation result in genetic muscular dystrophies^{8, 9}. In this chapter, we will describe our initial findings showing that the stark differences in myotube formation is dependent on the source of LAM as well as demonstrate the steps taken to determine that small traces of perlecan, a heparan sulfate proteoglycan in the basement membrane of skeletal muscle, is likely to account for these drastic differences in 2D skeletal muscle formation.

4.2 Materials and Methods

4.2.1 Microcontact Printing

The LAM protein micropatterned substrates were fabricated based on previously published techniques and as described in Chapter 2^{10, 11}. Briefly, Sylgard 184 polydimethylsiloxane (PDMS; Dow Corning Corp.) base and curing agent were mixed at a 10:1 mass ratio, respectively. PDMS was spincoated onto 25 mm diameter glass coverslips at 4,000 rpm to create an approximately 15 μm thick PDMS layer. PDMS coated coverslips were cured at 65°C for at least 4 hours before use. PDMS stamps for microcontact printing (μCP) were fabricated as previously described with the exception that MF-26A (Dow Electronic Materials) was used as the developer for the SPR 220.3 positive photoresist (MicroChem Corp.)¹⁰. PDMS stamps with 20 μm line spacings and 100 μm line widths were created.

All LAM proteins used for μCP were diluted with distilled water to final concentrations of 200 $\mu\text{g/mL}$. Specifically, we compared Inv LAM, BD mouse LAM (BD LAM >90%), BD ultrapure mouse LAM (BD LAM >95%), and BD Laminin-entactin complex (BD LAM+ENT). The procedure for μCP was followed as previously described¹⁰. Briefly, PDMS stamps were sonicated feature side up for 30 minutes in 50% ethanol solution. Stamps were dried with a nitrogen air gun, the feature side was coated with protein solution and incubated for 1 hour at room temperature. Stamps were rinsed twice in distilled water and dried with the nitrogen gun. PDMS coated coverslips were UV ozone treated for 15 minutes and stamps were inverted and placed in conformal contact with the coverslip for 5 minutes to transfer LAM lines. Stamps were then removed, and the patterned coverslips were incubated with 1% w/v Pluronic F-127 solution for 5 minutes followed by three rinses of phosphate buffered saline (PBS). For isotropically coated coverslips, UV-ozone treated PDMS coverslips were inverted onto 200 μL of protein

solution for 15 minutes, followed by 3 rinses of PBS. Samples were used immediately or stored in PBS at 4°C for up to 2 weeks.

4.2.2 Cell Culture: C2C12

Reagents were obtained from Life Technologies unless indicated otherwise. The murine C2C12 cell line (CRL-1722, ATCC) was cultured and differentiated as recommended by the supplier at 37°C and 10% CO₂. Cells were cultured and expanded in growth media (GM) (high glucose DMEM (Corning) supplemented with 10% fetal bovine serum, 1% penicillin-streptomycin, and 1% L-glutamine (200 mM)) and split at 1:10 ratios at 80% confluence. Cells were used at <12 passages from the supplier and were seeded at a density of 30,000 cells/cm² on micropatterned substrates. C2C12s proliferated in GM on substrates for 24 - 48 hours in order to reach 100% confluence on micropatterned lines. GM was then exchanged for differentiation media (DM) (high glucose DMEM (Corning) supplemented with 2% horse serum, 1% penicillin-streptomycin, and 1% L-glutamine (200 mM)), and exchanged daily for 6 days. After differentiation, samples were ready to be fixed and stained for analysis of myotube formation as described below.

4.2.3 Cell Culture: Human SkMDC

Human SkMDCs were obtained from Cook MyoSite. Cells were cultured according to the supplier recommendations at 37°C and 5% CO₂. Cells were maintained below 80% confluence in MyoTonic Growth Medium (Cook Myosite) during expansion. Cook's SkMDCs were seeded on substrates at 40,000 cells/cm² and were switched to MyoTonic Differentiation Medium (MDM - Cook Myosite) after cells reached confluence on patterned lines. MDM was exchanged every 48 hours for 6 days. After differentiation, samples were fixed and stained for analysis of myotube formation.

4.2.4 Immunofluorescence Staining and Imaging

Samples were fixed, stained for myotubes, and imaged to quantify myotube formation as previously described¹⁰. Reagents were obtained from Life Technologies unless otherwise indicated. After 6 days in DM, myotubes were rinsed in PBS (0.625 mM Mg²⁺ and 0.109 mM Ca²⁺) and fixed with 0°C methanol (Fisher Scientific) for 2 minutes. Samples were then rinsed with PBS 3 times for 5 minutes and incubated with 5% v/v goat serum in PBS for 1 hour. Samples were rinsed in PBS 3 times for 5 minutes prior to incubating for 1 hour with 1:200 and 1:100 dilutions of DAPI and monoclonal mouse myosin heavy chain (MHC) antibody in PBS, respectively. Samples were rinsed three times with PBS and incubated for 1 hour with a 1:100 dilution of Alexa Fluor 555 conjugated with goat anti-mouse antibody. Samples were again rinsed 3 times in PBS prior to being mounted onto slides using Prolong Gold Anti-fade. Samples were imaged using a Zeiss LSM 700 laser scanning confocal microscope to obtain z-stacks and tile scans of samples. Tile scans were typically 1.28 mm x 1.28 mm.

4.2.5 Image Analysis

Post-processing of images was performed as previously described^{10, 12}. MHC staining was used to identify myotubes and DAPI to identify nuclei. Percent area MHC was measured to assess myotube formation. ImageJ was used to quantify percent area myotubes. The MHC channel was isolated, thresholded, converted to an 8-bit binary, and the 'fill holes' feature within the binary menu was used to fill nuclear holes. The percent of MHC positive pixels were then quantified using the 'analyze particles' feature.

4.2.6 Deglycosylation of LAMs and Polyacrylamide Gel Electrophoresis

BD LAM >90% and Inv LAM were deglycosylated using PNGase (Sigma Aldrich) to remove N-linked oligosaccharides. 1 U/μL of PNGase was added to LAM solutions (1 mg/mL)

at 2% v/v dilution. Samples were then incubated at 37°C for 1 hour. Deglycosylated LAMs were then stored at -20°C or used immediately in PAGE gel. Deglycosylated samples are referred to as BD LAM >90% (degly) and Inv LAM (degly). To compare MW of intact LAM samples (Figure 4.4A), 6 µL of 1 mg/mL of each protein was mixed with 2 µL of lithium dodecyl sulfate (LDS) buffer (Thermo Fisher) prior to loading into 3-8% NuPAGE® Tris-Acetate protein gels (Thermo Fisher). To compare denatured LAM samples, 5 µL of 1 mg/mL of each protein was mixed with 2.5 µL of distilled water and 2.5 µL LDS sample buffer, and samples were heated at 70°C for 10 minutes prior to loading into NuPAGE gels. Gels were submerged in Nu-PAGE® Tris-Acetate SDS Running Buffer (Thermo Fisher), and 40V was applied across the gel overnight (~16 hours) to drive proteins through the gel. The gel was then fixed in a solution of 10% acetic acid and 10% methanol in distilled water. Coomassie blue stain (Sigma Aldrich) was diluted in the fixative solution at 2.5 mg/mL, and the gel was submerged in stain solution for 15 minutes followed by 2x30 minute washes with the fixative solution. Gels were imaged using an LAS-3000 Luminescent Image Analyzer (Fujifilm).

To run PAGE gels for glycan staining of BD LAM >90%, BD LAM >90% (degly), Inv LAM, and Inv LAM (degly), 20 µL of 1 mg/mL of each sample was mixed with 10 µL distilled water and 10 µL LDS loading buffer. Samples were then mixed and denatured by heating at 70°C for 10 minutes. Samples were then loaded into a 3-8 % NuPAGE® Tris-Acetate protein gel, and gels were submerged in running buffer and 40V was applied to the samples for 1 hour. As a positive control, 20 µL of 2mg/mL horseradish peroxidase (Thermo Fisher) was mixed with 10 µL distilled water and 10 µL of LDS sample buffer, and was added to the gel after the larger LAM proteins had been driven into the NuPAGE gel. 40V was then applied across the gel for an additional 30 minutes. The gel was fixed in 50% methanol for 30 minutes followed by 2 10-

minute rinses of 3% acetic acid. To stain for glycans, the following reagents used were provided in a Pierce Glycoprotein Staining Kit following the specified protocol (Thermo Fisher). The gel was submerged in oxidizing solution for 15 minutes and rinsed 3x for 5 minutes each in 3% acetic acid. The gel was then submerged in glycostain for 15 minutes and rinsed 3x for 5 minutes each in 3% acetic acid. Finally, the sample was submerged in reducing agent for 5 minutes followed by 3x 5 minute rinses in 3% acetic acid. The gel was then stored in 3% acetic acid and imaged using a Chemidoc Touch Imaging System (Biorad).

4.2.7 Mass spectroscopy

Matrix assisted laser desorption/ionization time of flight (MALDI-TOF) mass spectroscopy was performed by Logan Plath in the Bier lab at Carnegie Mellon University according to their standard protocols. Liquid chromatography mass spectroscopy (LC-MS) was performed by Breanna Duffy in the Black lab at Tufts University according to their standard protocols.

4.2.8 Statistical Analysis

All statistical analyses were performed using SigmaPlot. One Way ANOVAs were performed on data presented in Figures 4.3 and 4.6. All pairwise multiple comparison procedures

| Protein | BD LAM >90% | BD LAM >95% | Inv LAM | BD LAM+ENT |
|------------------------|-----------------|-------------|---------|-----------------------------|
| Purity | ≥90% | ≥95% | ≥95% | ≥90% |
| Tris-HCl Concentration | 50 mM | | | Stored in Dulbecco's PBS |
| NaCl Concentration | 150 mM | | | |
| pH | 7.4 | | | |
| Molecular Weight | 900 kDa | 900 kDa | 850 kDa | 900 kDa |
| Origin | EHS Mouse Tumor | | | |

Table 4.1 Manufacturer Information on Supplied Laminins. Comparison of purity, storage condition, listed MWs, and source of different LAM brands and types. All 'pure' LAMs are sourced from the EHS mouse tumor, and are stored in the same concentrations of Tris-HCl and NaCl at the same pH. They are listed as having a MW difference of 50 kDa (with Inv LAM being lighter), and Inv LAM is listed as having comparable purity to BD LAM >95%.

were performed using the Holm-Sidak method, and results were considered statistically significant at $p < 0.05$.

4.3 Results

4.3.1 C2C12 and Human SkMDC Myotube Formation on LAM Lines is Brand Dependent

To determine if the sudden changes observed in myotube formation were linked to changing the LAM supplier, myoblasts were seeded on micropatterned lines (100 μm wide with 20 μm spacings) of Inv LAM, and three different LAMs from BD: BD LAM >90%, BD LAM

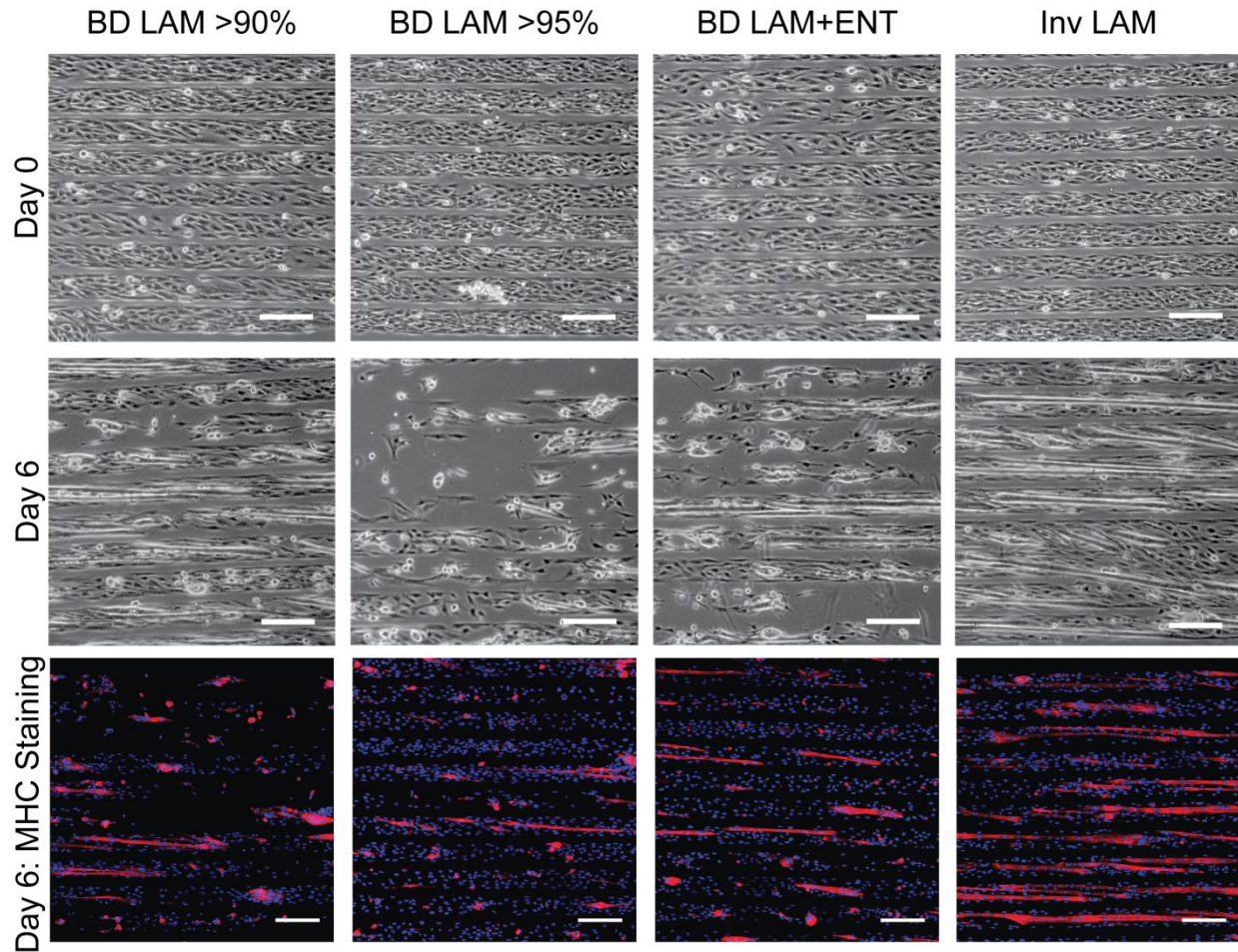


Figure 4.1: C2C12 myoblasts differentiated on BD and Invitrogen brand LAM. Phase Images of C2C12 cells seeded on microcontact printed LAM lines 100 μm wide with 20 μm spaces proliferated to confluence before switching to DM. After 6 days in DM, differentiating myoblasts show significant peeling from patterned lines of BD brand LAM compared to Invitrogen LAM. Samples were fixed and stained for nuclei (blue) and MHC (red), and differences in myotube formation on different brands and purities is apparent. Scale bars 200 μm .

>95%, and BD LAM-ENT. According to manufacturers, all LAM was sourced from the EHS mouse tumor and were supplied with similar concentrations of Tris-HCl and NaCl, with little other observable differences (Table 4.1). C2C12 myoblasts were observed to adhere and proliferate to confluence on the micropatterned LAM regardless of manufacturer source or purity (Figure 4.1). However, after DM was exchanged and cells were kept in differentiation conditions for 6 days, severe myoblast delamination was observed on BD LAM >95%, and less myotube formation was observed on BD LAM 90% and BD LAM-ENT (Figure 4.1).

To determine if this difference in LAMs also affected human myotube formation *in vitro*, we seeded human SkMDCs on the same patterned lines of Inv and BD LAM. When these were differentiated for 6 days, we also observed stark differences in myotube formation on Inv LAM compared to all 3 varieties of BD LAM (Figure 4.2). When we quantified percent area myotube formation as measured by MHC staining, we observed significantly more myotube area measured in C2C12 cells differentiating on Inv LAM ($26.4\% \pm 4.2$) compared to BD LAM >90% ($8.4\% \pm 2.8$), BD LAM > 95% ($4.1\% \pm 2.6$), and BD LAM-ENT ($9.3\% \pm 2.7$) (Figure 4.3A). We also measured that BD LAM >90% and BD LAM-ENT also induced significantly higher myotube formation than BD LAM > 95% (Figure 4.3A). Almost identical trends were observed in human SkMDCs; Inv LAM induced significantly higher myotube formation ($25.7\% \pm 4.5$) compared to BD LAM >90% ($8.9\% \pm 5.2$), BD LAM > 95% ($6.8\% \pm 6.9$), and BD LAM+ENT ($14.5\% \pm 8.3$) (Figure 4.3B). We determined that the BD purification process was likely removing trace amounts of other basement membrane proteins or post-translational modifications of LAM that affect myotube formation, especially since the increase in protein purity resulted in a decrease in myotube formation.

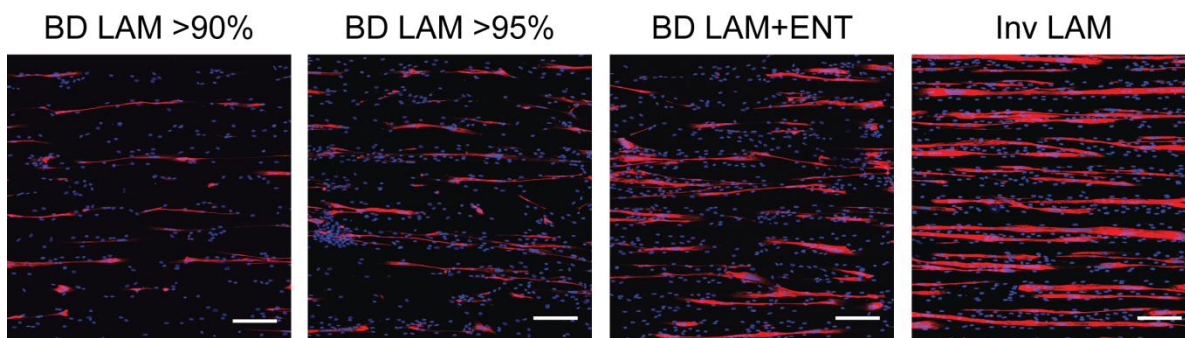


Figure 4.2: Human SkMDCs differentiated on different LAM brands. Human SkMDCs proliferated to confluence on 100 μm lines with 20 μm spacings of BD brand LAM at > 90% purity, > 95% purity, and LAM-ENT complex, as well as Inv LAM. Upon reaching confluence, DM was exchanged, and differentiation was induced for 6 days prior to fixing and staining for nuclei (blue) and MHC (red). Qualitative observation shows higher myotube formation on InvLAM, with more stringy and less robust myotube formation on BD LAMs. Scale bars 200 μm .

4.3.2 Molecular Weight and Glycan Comparison of Laminins

To determine if there were differences in the molecular weight (MWs) of LAMs despite similar MW listings from the manufacturers (Table 4.1), we used SDS-PAGE to compare intact and denatured LAM samples. We also enzymatically removed N-linked glycans to determine if any observable changes in MW were caused by removing glycans as we hypothesized that these post-translation modifications may have been critical to LAM protein conformation and subsequent integrin binding (Figure 4.4). For intact LAM samples, we observed BD LAM >95%, BD LAM+ENT and Inv LAM had similar MWs, and BD LAM >90% appeared to have a slightly higher MW (Figure 4.4A). Deglycosylation of BD LAM appeared to reduce the MW to that of the other LAM proteins, however Inv LAM deglycosylation also resulted in a slight drop in MW as measured by SDS-PAGE (Figure 4.4A). However, due to the large MWs of LAM proteins (800 - 900 kDa) and resulting chain entanglements that can occur in large, non-denatured proteins, we could not accurately measure MW in the gel without a protein standard. Because of this, we also analyzed the samples after denaturing and compared them to a standard protein ladder. We expected to see darker bands near ~200 kDa for β and γ chains and ~400 kDa for α

chains. We also expected to see bands between 100 and 150 kDa for any entactin residues that should be present in LAM+ENT and could be present in Inv LAM and BD LAM >90%. We observed bands in these regions for all proteins, and deglycosylated BD LAM >90% and Inv LAM had relatively smaller MWs than their unmodified counterparts (Figure 4.4B). However, there were not any other obvious differences in the Inv LAM sample that stood out as a potential target MW for identifying the difference in protein composition. In order to finally determine if glycan removal was significant between samples to be the cause of differences in myotube formation, we performed SDS-PAGE on Inv LAM, Inv LAM (degly), BD LAM >90%, and BD LAM >90% (degly) and specifically stained for glycans (Figure 4.4C). We observed darker glycan staining in all samples compared to the positive control, and even the samples treated to remove the N-linked glycans still had sugars intact (Figure 4.4C). This can be explained by the fact that O-linked glycans, were not targeted by our enzymatic removal of some glycans, even though this reaction removed enough N-linked glycans to

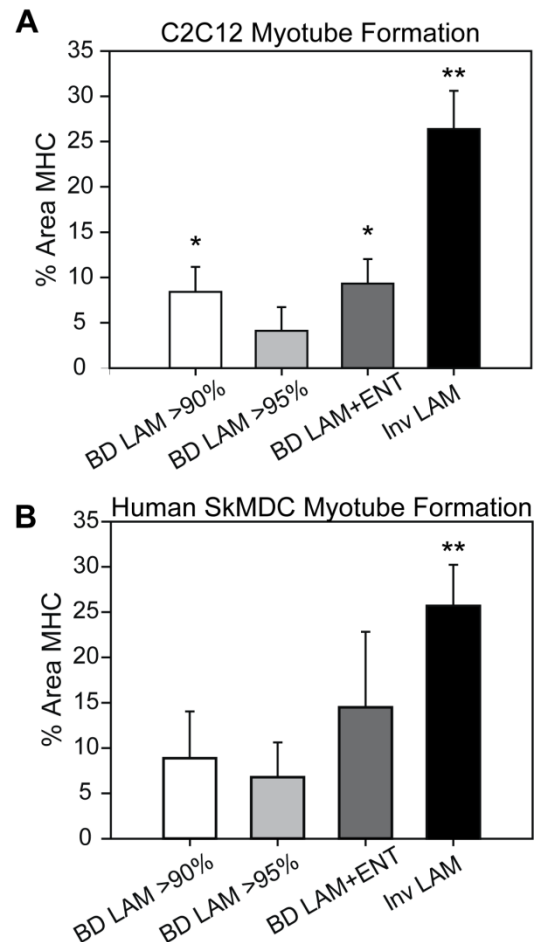


Figure 4.3: Quantification of myotube formation on different brands of LAM. (A) C2C12 myotube formation was measured as percent area MHC staining, and significantly more myotubes formed on Invitrogen brand LAM lines (~26.4%) compared to all BD varieties of LAM (4.1% - 9.3%). Inv LAM and BD LAM >90%: n = 6; BD LAM >95%: n = 8; BD LAM+ENT: n = 9. (B) Human SkMDC myotube formation on Inv LAM lines also showed significantly higher myotube area (25.7%) compared to all BD brand LAMs (6.8% - 14.5%). n = 6 for all samples. ** = p < 0.05 compared to all other conditions. * = p < 0.05 compared to BD LAM >95%.

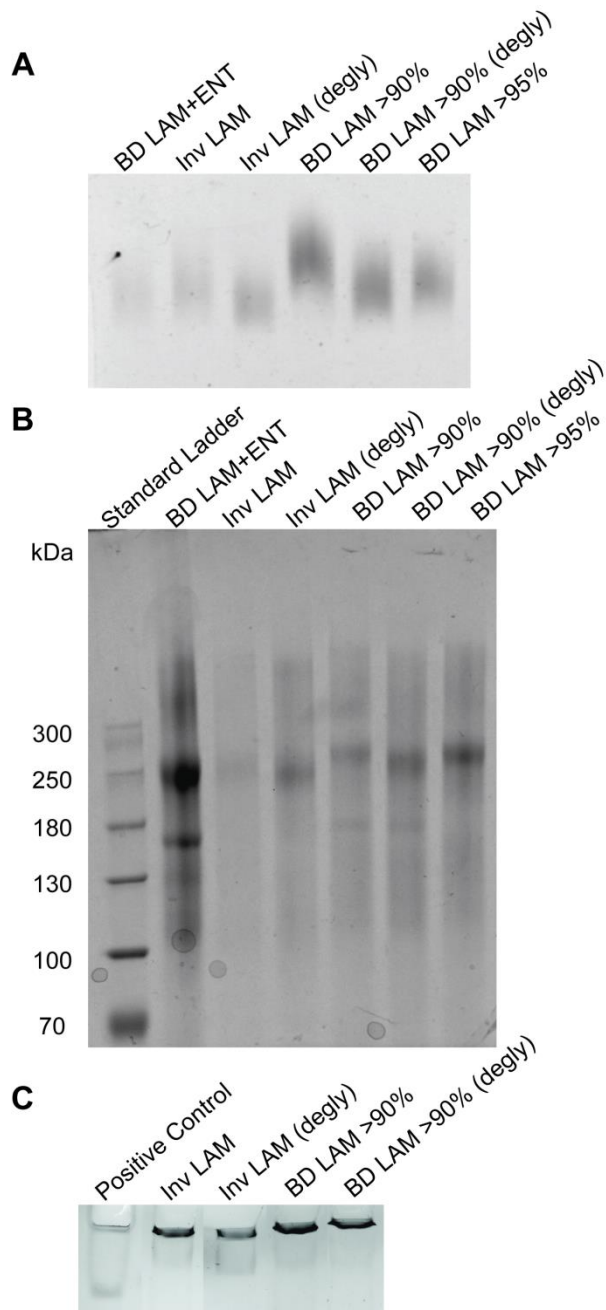


Figure 4.4: SDS-PAGE of various LAM brands. (A) Different LAM brands were run through an SDS-PAGE gel and stained with coomassie blue to determine if there were differences in MW. Samples of Invitrogen LAM and BD LAM >90% were also deglycosylated before loading into the gel to determine if sugars account for a significant weight in the LAM proteins. According to this gel, BD LAM appears to be heavier than Invitrogen LAM, and deglycosylating these proteins brings them closer to a similar MW. (B) Different LAM brands were denatured prior to being run through an SDS-PAGE gel and stained with coomassie blue to determine if there were differences in MW. Additionally, denaturing should limit protein-protein entanglements that may have occurred in (A). Samples of Inv LAM and BD LAM >90% were also deglycosylated before loading into the gel to determine if sugars account for a significant weight in the LAM proteins. Differences in MW are not clear enough in denatured samples to quantify from this gel. (C) Invitrogen and BD LAM >90% were run through an SDS-PAGE gel and stained specifically for glycans. Additional samples of Inv LAM and BD LAM >90% were also deglycosylated before loading into the gel. Despite deglycosylation, all samples of LAM appear to still have sugars attached.

reduce the MW of Inv LAM and BD LAM >90% (Figure 4.3A). We determined that differences in glycans could not be completely ruled out as the cause of differences in myotube formation, but these results did not implicate glycans as the likely cause of differences in myotube formation since they are present in both Inv and BD LAMs.

4.3.3 Mass Spectroscopy Analysis of Laminins

SDS-PAGE experiments were used to qualitatively assess the MWs of LAM samples, but we wanted a more in depth analysis of the composition of Inv LAM and BD LAMs. First, we used MALDI-TOF mass spectroscopy to look at overall MWs of LAMs. We found that all LAM samples appeared to be in the range of MWs reported by manufacturers (800 - 950 kDa) (Figure 4.5). Inv LAM had a slightly higher average MW of 923 kDa compared to BD LAM >90% (850 kDa), BD LAM >95% (858 kDa), and BD LAM+ENT (825 kDa) (Figure 4.5). More interestingly, Inv LAM and LAM+ENT both exhibited peaks with double-hump shapes and additional small spike ~250 kDa (Figure 4.5A, D). The BD LAM >90% and BD LAM >95% had more uniform, narrow peaks without the second peak at 250 kDa (Figure 4.5B,C). These results made it difficult to pinpoint exact MW differences in LAMs due to 'messier' results that are often observed when trying to use MALDI-TOF for analysis of large, biological proteins. However, this supported our hypothesis that trace amounts of other protein(s) or post-translational modifications were being stripped from BD LAMs, which had increasingly narrow peaks with increasing purity of LAM. These proteins or modifications are still left in some capacity on BD LAM+ENT, which induced slightly higher myotube formation than other BD LAMs and had a 'messier' spectra that appeared to mimic the Inv LAM mass spectra shape.

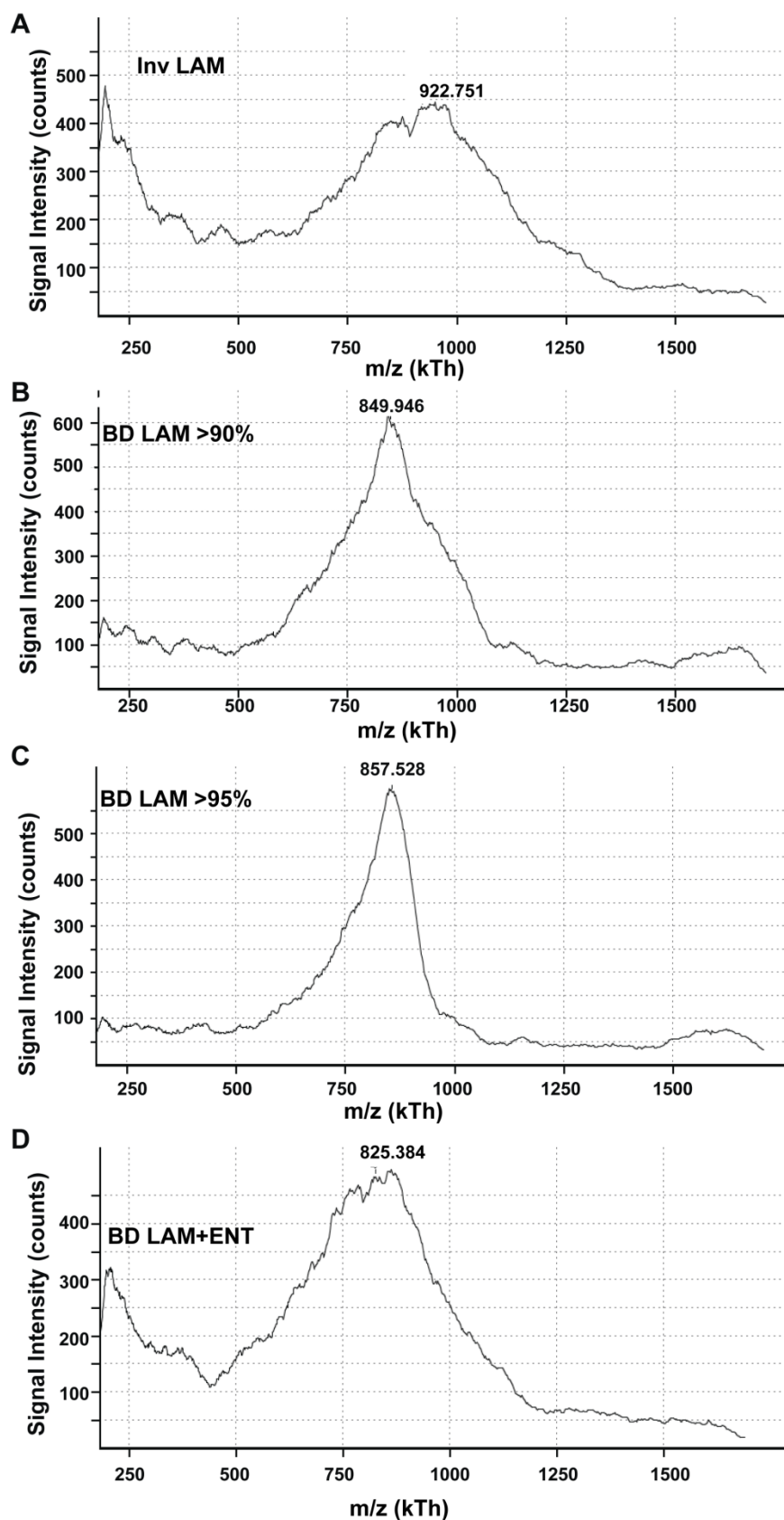


Figure 4.5. MALDI-TOF Mass Spectroscopy Analysis of Different LAM Brands.

Peaks shown are from +1 charge states. (A) MALDI-TOF analysis of Inv LAM showed a double-peak shape with a center of ~923 kDa while (B) BD LAM >90% had a more singular peak centered at ~850 kDa and (C) BD LAM >95% had an even narrower peak centered at ~858 kDa. (D) BD LAM+ENT showed an almost double-peak centered at ~825 kDa. The tested proteins are large enough that the exact MWs measured here may not accurately represent the MWs of each LAM, however, it is clear that the Inv LAM may have additional pieces of the protein or extra post-translational modifications in tact that may be stripped from both BD LAMs during the purification process, resulting in much narrower peaks for both of these proteins.

In order to determine the exact composition of LAMs, we reached out to collaborators at Tufts University to perform LC–MS to identify the specific protein ID compositions within these samples. The following percentages represent the percentage of overall spectral count for each LAM sample that matched with a $\geq 95\%$ confidence to the listed protein ID. As expected, we found that all LAM samples were composed primarily of LAM $\alpha 1$, $\beta 1$, and $\gamma 1$ subunits (Figure 4.6A-D). We also found that higher amounts of entactin-1 were present in Inv LAM ($6.3\% \pm 0.45$) compared to BD LAM $>95\%$ ($1.3\% \pm 0.24$) (Figure 4.6E). However, this does not appear to account for the differences in myotube formation since BD LAM+ENT and BD LAM $>90\%$ were composed of $11.8\% \pm 0.42$ and 13.7 ± 0.15 entactin-1, respectively, significantly higher percentages than both Inv LAM and BD LAM $>95\%$ (Figure 4.6E). Interestingly, basement membrane-specific heparan sulfate proteoglycan core protein, or perlecan, was the third protein present in Inv LAM ($4.5\% \pm 0.42$) after LAM111 and entactin-1 (Figure 4.6A). Trace amounts of perlecan ($1.2\% \pm 0.26$) were present in BD LAM+ENT as well, but absolutely none was registered as being present in BD LAM $>95\%$ or BD LAM $>90\%$ (Figure 4.6B-D). The amount present in Inv LAM was found to be statistically significant compared to all other conditions (Figure 4.6F). While 7.2% of the Inv LAM is composed of trace amounts of other proteins, none of these registered above 1% of total composition (Appendix A), so perlecan appears to be the most likely cause for the differences observed in myotube formation for both C2C12 and human SkMDCs. However, further studies need to be done to confirm that perlecan is responsible for this stark difference in *in vitro* myotube formation.

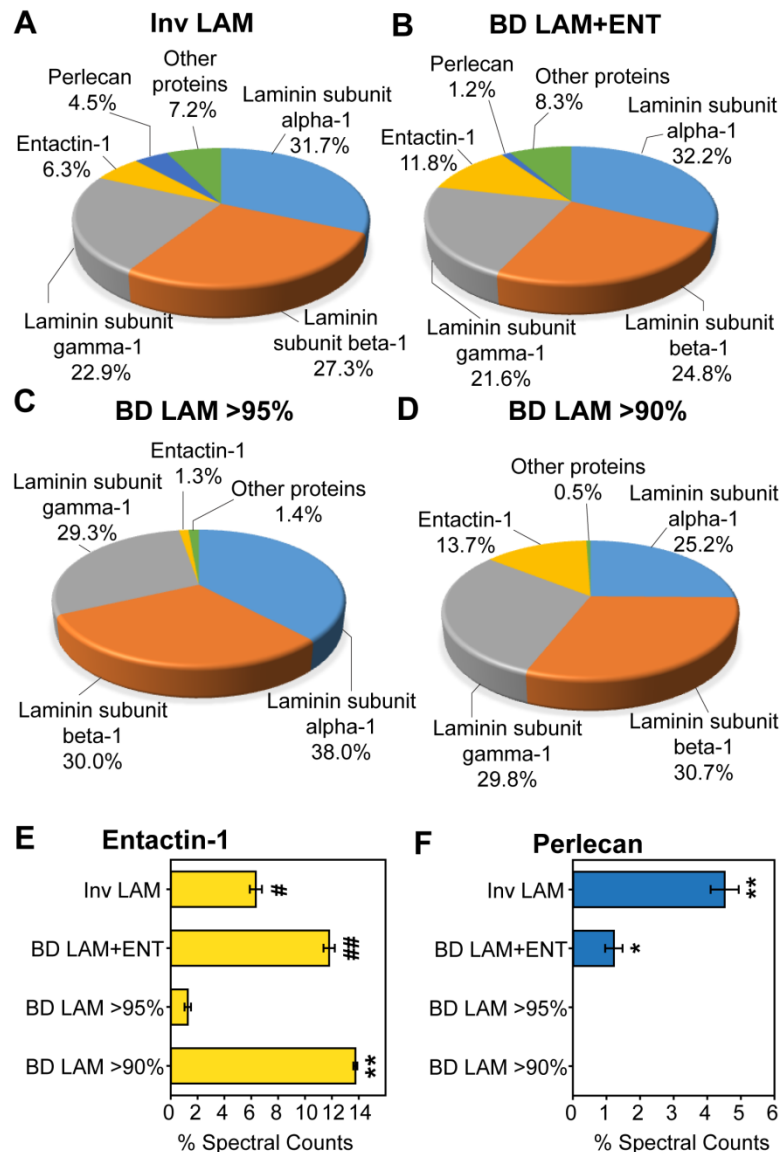


Figure 4.6. Liquid Chromatography Mass Spectrometry Analysis of LAMs.

(A) Inv LAM, that significantly increases myotube formation in 2D, is mainly composed of LAM α , β , and γ subunits, entactin, and 4.5% perlecan. While 7.2% of the composition is accounted for by a mixture of other small protein fragments, perlecan is present in the highest concentration after entactin compared to very small amounts of other protein fragments. (B) BD LAM+ENT has 1.2% perlecan in addition to LAM α , β , and γ subunits with 11.8% entactin and 8.3% trace amounts of other proteins. (C) BD LAM >95% consists almost exclusively of LAM α , β , and γ subunits, and < 2.7% of entactin and other trace proteins, and (D) BD LAM >90% is composed of 85.7% LAM α , β , and γ subunits with 13.7% entactin. (E) Comparison of entactin as % total spectral counts shows a significant difference among groups. Specifically, it was much lower in Inv LAM and BD LAM >95%. It is unlikely that this is the sole cause of increased myotube formation since it is higher in the proteins that do not drive higher myotube formation. (F) Comparison of perlecan as % total composition shows a significant difference among groups. It is likely that this is causing the severe differences in myotube formation on Inv

LAM compared to the other forms. ** = $p < 0.001$ compared to all other groups. * = $p < 0.001$ compared to BD LAM >95% and BD LAM >90%. ## = $p < 0.001$ compared to BD LAM >95% and Inv LAM. # = $p < 0.001$ compared to BD LAM >95%. $n = 3$.

4.4 Discussion and Conclusions

Further experiments are needed to confirm that perlecan is responsible for this drastic increase in C2C12 and human myotube formation on Inv LAM compared to all forms of BD LAM. However, these results indicate that perlecan is critical to *in vitro* myotube formation.

Perlecan, a heparin sulfate proteoglycan with an ~400 kDa core protein structure¹³, is an

important structural component of basement membranes¹⁴, and complete disruption of the gene that encodes for this protein is lethal to embryo formation^{15, 16}. Perlecan has also been found to be crucial to normal development of skeletal muscle during embryogenesis¹⁷. Additionally, our findings that 2D murine and human myotube formation are dependent on a combinatorial effect from LAM 111 and perlecan aligns with findings that LAMs 111 and 511 are first LAMs expressed in mammalian embryos, and perlecan and LAM are key proteins in the basement membrane of any tissue during embryogenesis and adult tissue maintenance³. Further, the interaction with entactin-1 should not be immediately discounted because perlecan binding to both LAM and entactin-1 impacts the structural integrity of the basement membrane¹⁴. In addition to possible synergistic interactions between these matrix proteins, growth factor binding/release from perlecan may also be responsible for this increase in *in vitro* myotube formation as at least 26 different growth factors are known to be released by perlecan turnover¹⁴.

The current understanding of perlecan's role as a critical part of the basement membrane and regulator of tissue formation and function, in conjunction with the results from the LC-MS findings, suggest that this is the cause of significantly increased amounts of myotube formation on Inv LAM. However, additional experiments will need to be performed to confirm these findings. As a first step, perlecan can be added to BD LAMs to determine if patterning C2C12 and human myotubes on BD LAM + perlecan rescues myotube formation to levels comparable to those seen on Inv LAM. To determine if the increase in myotube formation is a synergistic affect of LAM+perlecan or due to perlecan alone, myotube formation of cells cultured on patterned perlecan will be quantified to establish if perlecan alone induces similar myotube formation to that of cells cultured on Inv LAM. Additionally, we can use immunofluorescence and quantitative PCR to determine how differentiating myoblasts are adhering to the different LAMs.

Specifically, we can focus on α -dystroglycan, which attaches to both LAM 111 and perlecan and is critical to skeletal muscle formation^{6, 7, 14} and $\alpha 2\beta 1$ and $\alpha 5\beta 1$ integrins that are also known to bind perlecan, with $\alpha 5\beta 1$ binding only perlecan but not LAM 111¹⁴.

If we can confirm that perlecan is causing this severe difference in myotube formation, it will be interesting to delve further into the mechanism that drives myogenesis from this specific ECM interaction. Importantly, the observation that 2D *in vitro* skeletal muscle formation can be severely impacted by using LAM from a different manufacturer makes it apparent that tissue engineering as a field has many strides to make in terms of quality control when using biologically derived proteins to engineer functional tissues. Regardless of whether these differences in myotube formation are caused by perlecan alone, a synergistic interaction with LAM, interactions with growth factors present in media or secreted by cells, or by trace amounts of another protein, it is clear that using biologically sourced materials to engineer tissues in a controlled fashion has inherent caveats because of the methods used to obtain these ECM proteins. As a field, it is necessary to consider how to engineer more chemically defined matrices that use specific peptide sequences, such as the RGD binding site from fibronectin or the LG and LE globular binding domains of LAMs, rather than using entire proteins isolated from biological systems. However, while isolated binding peptides have been effective at inducing cell spreading and attachment, the other portions of proteins not included in the binding site may have critical impact on other cell and tissue function, such as capturing growth factors. For this reason, methods to use decellurized matrix should not be completely done away with, as many of the findings that have come from studies using intact biological proteins have been critical to better understanding of morphogenesis and how to design tissues from the ground up. It is just as important to keep in mind that 'contaminants' that interfere with results, as in our findings in this

chapter, are always a risk when using biologically derived components, whether derived commercially or in-house. Development of systems that allow precise control of the factors to which differentiating cells are exposed should be performed in parallel to effectively determine the exact factors that control morphogenesis and tissue differentiation.

4.5 References

1. Durbecq, M. Laminins. *Cell Tissue Res* **339**, 259-68 (2010).
2. Thorsteinsdottir, S., Deries, M., Cachaco, A.S. & Bajanca, F. The extracellular matrix dimension of skeletal muscle development. *Dev Biol* **354**, 191-207 (2011).
3. Yurchenco, P.D. Basement membranes: cell scaffoldings and signaling platforms. *Cold Spring Harb Perspect Biol* **3** (2011).
4. Belkin, A.M., Stepp, Mary Ann. Integrins as receptors for laminins. *Microscopy Research and Technique*, 280-301 (2000).
5. Xiaojie Xian, S.G., and John R. Couchman. Syndecans as receptors and organizers of the extracellular matrix. *Cell Tissue Res*, 31-46 (2009).
6. Suzuki, N., Yokoyama, F. & Nomizu, M. Functional sites in the laminin alpha chains. *Connect Tissue Res* **46**, 142-52 (2005).
7. Brancaccio, A. Alpha-dystroglycan, the usual suspect? *Neuromuscul Disord* **15**, 825-8 (2005).
8. Zanolini, S. et al. Altered extracellular matrix transcript expression and protein modulation in primary Duchenne muscular dystrophy myotubes. *Matrix Biol* **26**, 615-24 (2007).
9. Oak, S.A., Zhou, Y.W. & Jarrett, H.W. Skeletal muscle signaling pathway through the dystrophin glycoprotein complex and Rac1. *J Biol Chem* **278**, 39287-95 (2003).
10. Sun, Y., Duffy, R., Lee, A. & Feinberg, A.W. Optimizing the structure and contractility of engineered skeletal muscle thin films. *Acta Biomaterialia* **9**, 7885-7894 (2013).
11. Grosberg, A., Alford, P.W., McCain, M.L. & Parker, K.K. Ensembles of engineered cardiac tissues for physiological and pharmacological study: Heart on a chip. *Lab on a Chip* **11**, 4165-4173 (2011).
12. Schindelin, J. et al. Fiji: an open-source platform for biological-image analysis. *Nat Methods* **9**, 676-82 (2012).
13. Noonan, D.M. et al. The complete sequence of perlecan, a basement membrane heparan sulfate proteoglycan, reveals extensive similarity with laminin A chain, low density lipoprotein-receptor, and the neural cell adhesion molecule. *J Biol Chem* **266**, 22939-47 (1991).
14. Farach-Carson, M.C., Warren, C.R., Harrington, D.A. & Carson, D.D. Border patrol: insights into the unique role of perlecan/heparan sulfate proteoglycan 2 at cell and tissue borders. *Matrix Biol* **34**, 64-79 (2014).
15. Arikawa-Hirasawa, E., Rossi, S.G., Rotundo, R.L. & Yamada, Y. Absence of acetylcholinesterase at the neuromuscular junctions of perlecan-null mice. *Nat Neurosci* **5**, 119-23 (2002).
16. Costell, M. et al. Hyperplastic conotruncal endocardial cushions and transposition of great arteries in perlecan-null mice. *Circ Res* **91**, 158-64 (1999).
17. Zoeller, J.J., McQuillan, A., Whitelock, J., Ho, S.Y. & Iozzo, R.V. A central function for perlecan in skeletal muscle and cardiovascular development. *J Cell Biol* **181**, 381-94 (2008).

Chapter 5

Engineering Skeletal Muscular Thin Films: Troubleshooting and Future Directions

5.1 Introduction

Previously, we adapted established techniques that integrated cardiomyocytes¹⁻³ or smooth muscle cells^{4, 5} onto polydimethylsiloxane (PDMS) thin films (TFs) patterned with fibronectin (FN) lines. We wanted to use this platform as a tool to better understand skeletal muscle formation as dictated by extracellular matrix (ECM) cues, in terms of composition and geometric patterning, and how these ECM cues influence skeletal muscle function as measured by force generation. Engineering MTFs with skeletal muscle presents specific challenges, however, because skeletal muscle must be differentiated from myoblasts into large, multinucleated, fused myotubes directly on the TF substrates. This is in contrast to contractile cardiomyocytes, which can be directly isolated directly from neonatal rat hearts or differentiated until they are beating before seeding in the MTF assay¹. We successfully integrated C2C12 mouse myoblasts into this MTF platform on FN lines, differentiated them into multinucleated and aligned myotubes, electrically paced the MTFs, and measured bending force exerted by the skeletal muscle myotubes⁶. In Chapter 3, the aim was to build on this work using human primary skeletal muscle in order to engineer more clinically relevant MTFs. More specifically, we varied the composition and geometry of the patterned lines of ECM proteins to maximize myotube

differentiation and alignment on patterned PDMS. In this way, we aimed to engineer human skeletal MTFs PDMS using ECM line patterns that maximized human myotube formation. We demonstrated that laminin (LAM) 111 lines 50 and 100 μm wide maximized myotube formation and alignment for both C2C12 and human myotubes differentiating in 2D. However, we still needed to determine if these human derived myotubes were functionally contractile and if they would visibly bend PDMS in the MTF assay.

These muscular thin films (MTFs), or PDMS integrated with a contractile cell layer, are capable of being released from glass coverslips after myotube differentiation in culture using a sacrificial layer of poly(n-isopropylacrylamide) (PIPAAm) that dissolves below 32°C upon exposure to water. Releasing the MTF by dissolving the PIPAAm allowed for a non-invasive way to measure the contractility of the patterned muscle layers by measuring the change in radius of curvature of the bending MTF and calculating the bending stress exerted by the cells. The goal from Chapter 3 of maximizing the alignment and formation of myotubes by C2C12 or human skeletal muscle derived cells (SkMDCs) was to increase the contractile force exerted by differentiated myotubes using specific ECM cues that were found to foster skeletal muscle formation in the previously established skeletal MTF assay⁶.

Ultimately, we found that this method of differentiating skeletal muscle in 2D on patterned PDMS was not an optimal platform for a robust contractility assay for skeletal muscle. More specifically, many have shown that skeletal muscle myoblasts need at least 2 - 4 weeks of differentiation to fuse and form contractile myotubes, especially when using human primary cells⁷⁻⁹. This worked well in 3D platforms where myoblasts are restricted by being cast within 3D collagen I (Col I) or fibrin gel systems¹⁰⁻¹³, but it became problematic when integrating differentiating skeletal muscle on biologically inactive PDMS patterned only with a nanoscale

layer of ECM bound by hydrophobic interactions. During myoblast differentiation, as myotubes fuse, they begin to spontaneously contract against their surrounding environment as part of the maturation process¹⁴. In this 2D MTF assay, this was problematic since stronger myotubes will begin to delaminate from the patterned PDMS surface as early as 1 week into differentiation. While we were able to initially demonstrate that the MTF assay is possible with skeletal muscle, we determined that a 3D platform would enable longer differentiation and maturation of myotubes to yield a more robust, consistent platform in terms of force generated by the engineered muscle. Because PDMS was the thin film substrate, the 2D MTF assay was too limiting to skeletal muscle maturation and resulted in inconsistent myotube formation for both C2C12 and human primary cells. In this chapter, I will discuss the observations made and troubleshooting techniques employed to engineer a consistent skeletal MTF assay before we ultimately determined that better methods are available to study and engineer contractile skeletal muscle *in vitro*.

5.2 Materials and Methods

5.2.1 Stamp Fabrication – SPR 220.3

PDMS stamps for μ CP were fabricated as previously described in Chapter 3. Specifically, SPR220.3 positive photoresist (MicroChem Corp.) was coated onto 45 x 50 mm number 2 cover glasses (Fisher Scientific) and exposed to UV light through a transparency photomask. MF-26A (Dow Electronic Materials) was used as the developer⁶. Sylgard 184 PDMS (Dow Corning) was then mixed at a 1:10 base to curing agent ratio and poured onto patterned wafers to create PDMS stamps with 10, 15, 20, and 30 μ m line spacings and 20, 50, 100, and 200 μ m line widths for a total of 16 micropattern conditions. Stamps were cured at 65°C for at least 4 hours before being

peeled from master wafers and cut out. Line patterns are referred to as width x spacing (e.g. a pattern with 50 μm lines and 10 μm spacings is 50x10).

5.2.2 Stamp Fabrication – SU-8 2015

Wafers with 20 - 40 μm deep features used for creating stamps for use on MTFs with an isolated PIPAAm rectangle or for genipin modified patterning were fabricated in a clean room using SU-8 2015 (Microchem). Silicon wafers were coated with SU-8 2015, soft baked for 5 minutes at 95°C, exposed to UV light through a chrome photomask with the desired pattern according to recommendations based on manufacturer recommendations¹⁵. Wafers were then post baked for 4 minutes at 95°C, typically until features became visible. To develop features, wafers were submerged in SU-8 developer and gently agitated for 6 to 7 minutes. After developing, wafers were rinsed with isopropyl alcohol and dried with a nitrogen gun. To make stamps from these wafers, Sylgard 184 (PDMS; Dow Corning Corp.) was mixed at a 10:1 ratio of base to curing agent as described previously, poured onto SU-8 patterned wafers, and cured for at least 4 hours at 65°C before peeling stamps from wafers.

5.2.3 Thin Film Fabrication and Thickness Measurement

TFs were fabricated as previously described⁶ with minor modifications in later experiments to isolate the area of PIPAAm. Briefly, PIPAAm (polysciences) was dissolved at 10% w/v in butanol. 200 μL of PIPAAm solution was spincoated onto 25 mm diameter glass coverslips at 6,000 RPM, and butanol was allowed to evaporate from coated coverslips prior to PDMS coating. For coverslips with defined areas of PIPAAm, masking tape (Scotch™) was placed on 25 mm coverslips, and a CO₂ laser cutter (Full Spectrum) was used to cut out a 3.23 mm x 8.38 mm rectangle in the tape. The cut rectangle was then peeled from the coverslip, and 200 μL of PIPAAm solution was spincoated at 6,000 RPM on the tape masked coverslips.

Butanol was allowed to evaporate from the PIPAAm solution, and a lab marker was used to mark the PIPAAm border. Tape was then removed prior to coating with PDMS. Sylgard 184 base and curing agent were mixed at a 10:1 mass ratio, respectively. PDMS was spincoated onto PIPAAm coated coverslips at 4,000 RPM to create an approximately 10-15 μm thick PDMS layer. In some cases, PDMS was allowed to cure at room temperature for 3 – 4 hours prior to spincoating to achieve the necessary viscosity to yield the desired PDMS layer thickness. TFs were cured at 65°C for at least 4 hours before use. For PDMS only coverslips, PDMS was spincoated directly onto 25 mm diameter glass coverslips at 4,000 RPM and cured for at least 4 hours at 65°C.

Every third coverslip was taken from each TF batch to obtain thickness measurements. Thickness measurements were taken using the bright field setting on a Zeiss LSM 700 Scanning Confocal Microscope. Markings were made on either side of the PDMS film, and the z-distance was recorded when the markings underneath and on top of the PDMS were in focus. Three fields of view were measured per coverslip and were averaged to obtain the PDMS thickness for TF samples.

5.2.4 Microcontact Printing on Thin Films

All ECM proteins used for μCP were diluted with distilled water to final concentrations of 50 $\mu\text{g/mL}$ for human FN (Sigma-Aldrich) and 200 $\mu\text{g/mL}$ for mouse LAM (Life Technologies). The procedure for μCP was followed as described in Chapters 3 and 4. Briefly, PDMS stamps were sonicated feature side up for 30 minutes in 50% ethanol solution. In a sterile biosafety cabinet, stamps were dried with a nitrogen air gun, and the feature side was coated with protein solution and incubated for 1 hour at room temperature. Stamps were rinsed twice in

distilled water and dried with the nitrogen gun. PDMS coated coverslips were UV-ozone treated for 15 minutes and stamps were inverted and placed in conformal contact with the coverslip for 5 minutes to transfer the ECM protein lines. Stamps were then removed, and the patterned coverslips were incubated with 1% w/v Pluronic F-127 (Sigma) solution for 5 minutes followed by three rinses of phosphate buffered saline (PBS). For isotropically coated coverslips, UV-ozone treated PDMS coverslips were inverted onto 200 μ L of protein solution for 15 minutes, followed by 3 rinses of PBS. Samples were used immediately or stored in PBS at 4°C for up to 2 weeks.

5.2.5 Cell Culture - C2C12

Reagents were obtained from Life Technologies unless indicated otherwise. C2C12 cells were cultured and differentiated as described in Chapters 3 and 4. Specifically, murine C2C12 cell line (CRL-1722, ATCC) was cultured and differentiated as recommended by the supplier at 37°C and 10% CO₂. Cells were cultured and expanded in growth media (GM) (high glucose DMEM (Corning) supplemented with 10% fetal bovine serum, 1% penicillin-streptomycin, and 1% L-glutamine (200 mM)) and split at 1:10 ratios at 80% confluence. Cells were used at <12 passages and were seeded at a density of 30,000 cells/cm² on micropatterned substrates. C2C12s proliferated in GM on substrates for 24 - 48 hours in order to reach 100% confluence on micropatterned lines. GM was then exchanged for differentiation media (DM) (high glucose DMEM (Corning) supplemented with 2% horse serum, 1% penicillin-streptomycin, and 1% L-glutamine (200 mM)), and exchanged daily for 6 days. On studies using genipin modified FN lines, C2C12 cells were maintained in DM up to 12 days. After differentiation, samples were ready to be tested in the MTF assay or fixed and stained for analysis of myotube formation as described below.

5.2.6 Cell Culture - Human SkMDCs

Human SkMDCs were obtained from Cook MyoSite. Cells were cultured according to the supplier recommendations at 37°C and 5% CO₂. Additionally, cells were maintained below 80% confluence in MyoTonic Growth Medium (Cook Myosite) supplemented with 1% Penicillin-Streptomycin (Life Technologies) during expansion. Cook's SkMDCs were seeded on substrates at 40,000 cells/cm² and were switched to MyoTonic Differentiation Medium (MDM - Cook Myosite) supplemented with 1% Penicillin-Streptomycin after cells reached confluence on patterned lines. For cells isolated from 17F donor (Figure 5.8), MDM was exchanged every 24 hours for 6 days. For cells isolated from 22M donor (Figure 5.7C-D), MDM was exchanged 48 hours for 6 days as this increased the time for myotube differentiation without delamination occurring after 4 days of differentiation. After differentiation, samples were fixed and stained for analysis of myotube formation or stimulation of MTFs.

5.2.7 MTF Stimulation

When MTFs had been differentiated for 6 days, samples were transferred to 35 mm petri dishes (Corning) and a scalpel was used to manually cut out thin films, which had photolithographically defined cell-free spaces 200 µm borders, using a Nikon SMZ1500 stereomicroscope. After MTFs were cut out, 37°C normal Tyrode's solution (1.192 g HEPES, 0.203 g MgCl₂, 0.403 g KCl, 7.889 g NaCl, 0.04 g NaH₂PO₄, 0.901 g C₆H₁₂O₆, and 0.265 g CaCl₂ per liter of distilled water, pH 7.4). was added to coverslips and allowed to cool below 32°C to dissolve exposed PIPAAm. Samples were then maintained between 34°C and 37°C using a custom made heated stage controlled by custom LabView software. A GRASS stimulator set to 40 V, 1 Hz, 10 ms square pulse wave was used to electrically stimulate MTFs by

connecting to parallel platinum electrodes spaced 2 cm apart placed in a custom petri dish lid. Videos were captured using a Hamamatsu Orca Flash 2.9 camera controlled by ImageJ.

5.2.8 Patterning Fibronectin Lines with Genipin Crosslinker

FN was crosslinked to PDMS coated coverslips following previously described methods^{16, 17}. Specifically, we used PDMS stamps 40 μm deep channels to create channels to pattern FN by flowing protein solution and crosslinker through the stamp channels as opposed to traditional microcontact printing methods (Figure 5.10A). Stamps were sonicated in 50% ethanol for 30 minutes and dried with a nitrogen gun before being placed in conformal contact with UV-ozone treated PDMS coated coverslips. Stamps with trenches 30, 50, or 200 μm wide were used. Genipin (Sigma-Aldrich), dissolved at 1 mg/mL in water, was pipetted onto one side of the channels created by conformal contact of the stamp with the coverslip, and a vacuum was applied near the opposing side to pull genipin through the channels. Genipin was incubated with coverslips for 1 hour prior to rinsing 3 times with PBS. 50 $\mu\text{g/mL}$ of 30% Alexa-Fluor 546 labelled FN and 70% unlabeled FN was then pulled through the channels in the same manner and allowed to incubate for an additional hour. Excess FN was also washed out with PBS, and coverslips were either stored in PBS for up to 2 weeks before use or used immediately for cell seeding experiments.

5.2.9 Fixing, Immunostaining, and Imaging

Samples were fixed, stained for myotubes, and imaged to quantify myotube formation as described in Chapters 2 and 3. Reagents were obtained from Life Technologies unless otherwise indicated. Samples were rinsed in PBS (0.625 mM Mg^{2+} and 0.109 mM Ca^{2+}) and fixed with 0°C methanol (Fisher Scientific) for 2 minutes. Samples were then rinsed with PBS 3 times for 5

minutes and incubated with 5% v/v goat serum in PBS for 1 hour. Samples were rinsed in PBS 3 times for 5 minutes prior to incubating for 1 hour with 1:200 and 1:100 dilutions of DAPI and monoclonal mouse MHC antibody in PBS, respectively. Samples were rinsed three times with PBS and incubated for 1 hour with a 1:100 dilution of Alexa Fluor 488 or 555 conjugated with goat anti-mouse antibody. Samples were again rinsed 3 times in PBS prior to being mounted onto slides using Prolong Gold Anti-fade. Samples were imaged using a Zeiss LSM 700 laser scanning confocal microscope to obtain z-stacks and tile scans of samples. Tile scans were typically 1.28 mm x 1.28 mm.

5.2.10 Image Analysis

Post-processing of images was performed as described in Chapters 2 and 3. MHC staining was used to identify myotubes and DAPI to identify nuclei. Percent area MHC was quantified to examine myotube formation. ImageJ was used to quantify percent area myotubes in the following way: the MHC channel was isolated, thresholded, converted to an 8-bit binary, and holes where nuclei had been were filled using the ‘fill holes’ feature within the binary menu. The percent of MHC positive pixels were then quantified using the ‘analyze particles’ feature. For studies examining the effect of genipin modified FN lines on C2C12 myotube maintenance, the fluorescent FN channel was also isolated, thresholded, converted to an 8-bit binary, and the percent area FN was measured using the ‘analyze particles’ feature. The percent area MHC was then normalized by dividing by percent area FN since several different patterns were used in these studies.

5.2.11 Statistical Analysis

All statistical analyses were performed using SigmaPlot™ with significant differences

reported at $p < 0.05$. A Two-Way ANOVA with Shapiro-Wilk normality test and Holm-Sidak pairwise comparisons was performed for data in Figure 5.5C. A One-Way ANOVA with Shapiro-Wilk normality test and Holm-Sidak pairwise comparisons was performed for data in Figure 5.8B. An ANOVA on Ranks with Dunn's method pairwise comparisons was performed for data in Figure 5.10C.

5.3 Results

5.3.1 Engineering Skeletal

MTFs with LAM Lines

The results from Chapter 3 were applied to the MTF assay to determine if increased myotube formation on these LAM lines resulted in MTFs capable of generating higher twitch forces than MTFs patterned on FN lines⁶. Initially, C2C12 MTFs were successfully generated using the same techniques we had

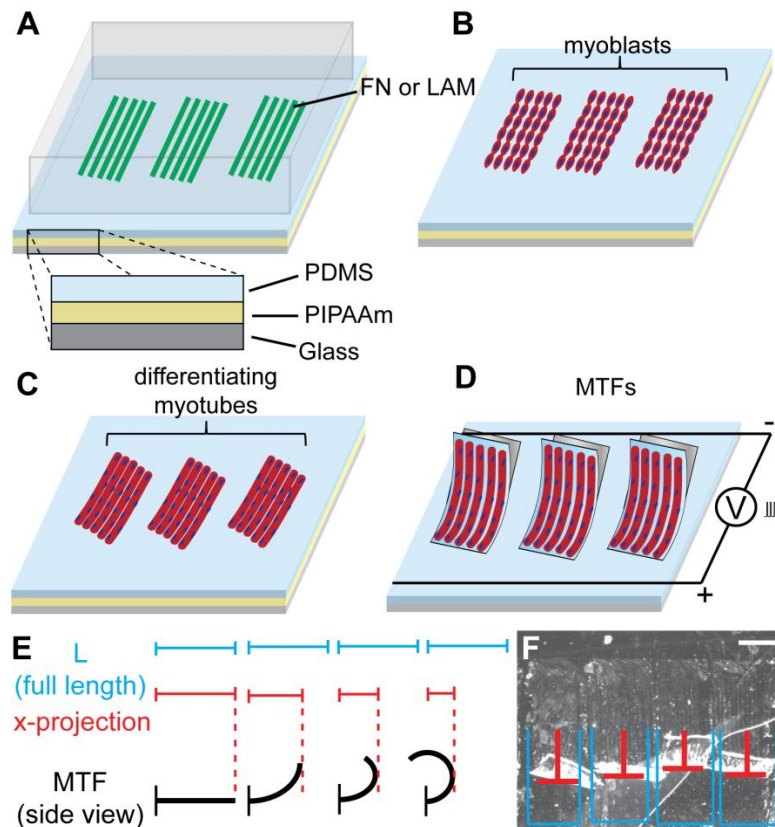


Figure 5.1: Fabrication of MTFs. (A) Traditional microcontact printing techniques are used to pattern LAM lines onto coverslips. Glass coverslips have been coated with a sacrificial layer of PIPAAm followed by a layer of PDMS. (B) Skeletal muscle myoblasts are seeded onto patterned coverslips. (C) Myoblasts are differentiated for 6 - 7 days by switching to low serum media until myotubes form on patterned LAM lines. (D) When myotubes have formed, a scalpel is used to cut around the patterned MTFs. Exposure to 20°C Tyrode's solution dissolves PIPAAm, and MTFs are stimulated using parallel platinum electrodes connected to a Grass Stimulator to perform the contractility assay. (E) Schematic representation of how the radius of curvature that tracks the change in bending is measured from a top down image of contracting MTFs. The x-projection and the full length of the MTF are geometrically related to predict the radius of curvature (adapted from Grosberg et al³). Specifically, when $x/L \leq \pi/2$; $x=r$, and when $x/L > \pi/2$; $x=r \cdot \sin(L/r)$. (F) Top down image of C2C12 MTF with red representing the tracked x-projection and blue representing the full MTF length. Scale bar 1 mm.

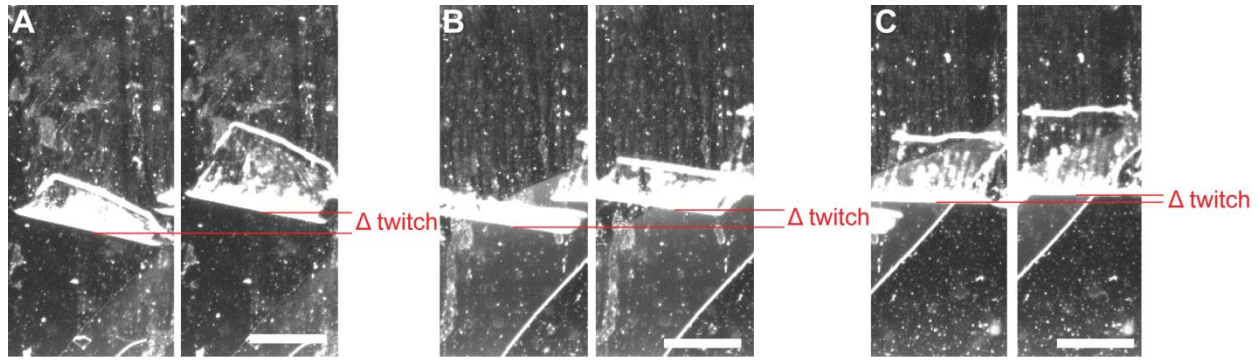


Figure 5.2: Examples of best-case scenario C2C12 MTFs. (A) MTFs from C2C12s differentiated on 100x10 LAM lines, (B) 100x15 LAM lines, and (C) 100x20 LAM lines show measurable bending of PDMS induced by twitch of stimulated myotubes. Scale bars 1 mm.

used to publish the proof of concept⁶ (Figure 5.1A). We recorded stimulation of the LAM MTFs using a top down rather than side on view of the bending since the radius of curvature can be calculated by relating the x-projection and full length of the MTF (Figure 5.1B-C)³. We successfully differentiated contractile C2C12 MTFs on LAM lines and observed muscle twitch in the change in x-projection of the MTFs induced by 1Hz electrical stimulation (Figure 5.2). However, the results Figure 5.2 are a ‘best case scenario’, and we found a significant amount of variability with different lots of the C2C12 cell line or with human SkMDCs, so we wanted to limit this variability by standardizing the MTF assay.

5.3.2 Standardizing Length of Released MTF

We determined that a next step to limiting variability in the MTF assay was to standardize the length of the released portion of the MTF that would be released from the glass coverslip during the contractility assay. During previous experiments, the length of the released MTF was completely dependent on the amount the researcher cut with a scalpel, and this resulted in variability in TF length even for samples on the same coverglass. Other groups had modified the assay to standardize the MTF release length by controlling the area of PIPAAm underneath

the PDMS layer. In order to try to make this assay more robust and determine if variability in MTF contractility results were the result of this inconsistency, we developed a method to control PIPAAm patterned area by using masking tape and a laser cutter to make a mask for PIPAAm (Figure 5.3). In this way, we were able to define the PIPAAm area underneath the patterned PDMS to develop a more to standardized skeletal MTF assay.

After standardizing PIPAAm area, we noticed that differentiating C2C12 cells were peeling from patterned TFs only in regions with underlying PIPAAm (Figures 5.4A-C). In theory, because the PIPAAm layer is nanometers thick and resides under 10 – 15 μm of PDMS, the differentiating myotubes should not have sensed the transition from PDMS to PDMS+PIPAAm since cells are less likely to feel changes in

stiffness at a 10 μm thickness^{18, 19}. We determined some of these initial results of cells peeling in PIPAAm regions were on 8 – 10 μm thick PDMS, so we cured PDMS at room temperature for

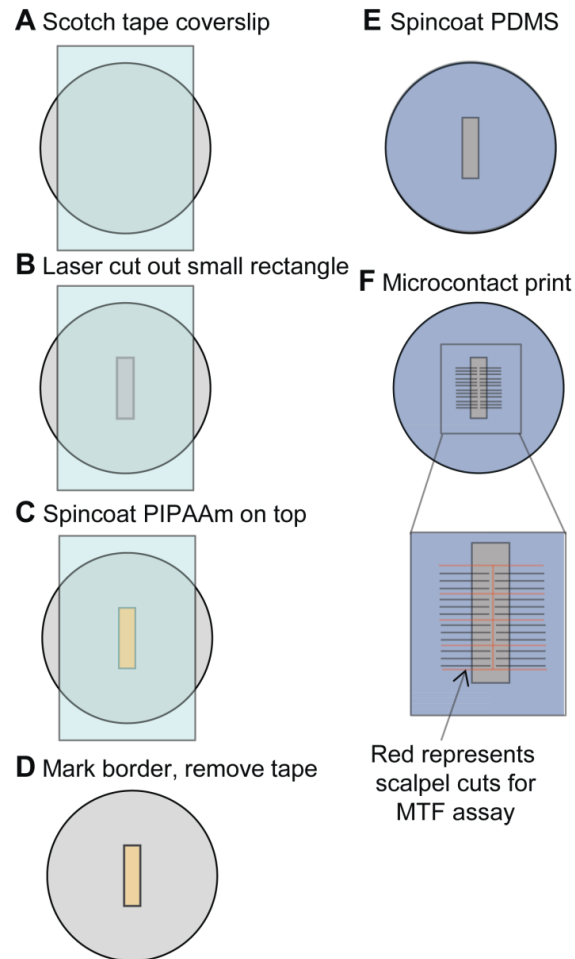


Figure 5.3: Modification of MTF fabrication to standardize MTF release length. (A) Prior to spincoating PIPAAm, glass coverslips are covered with Scotch™ tape. (B) A laser cutter is used to cut out a 3.23 mm x 8.38 mm rectangle in the tape. (C) PIPAAm is spincoated onto the taped coverslip, and the tape acts as a mask to prevent PIPAAm covering the entire coverslip. (D) The PIPAAm rectangle is marked with a lab marker, and the tape is removed. (E) PDMS is spincoated onto the coverslip. (F) After PDMS cures, LAM lines are patterned by traditional microcontact printing. The stamps are centered on isolated PIPAAm rectangle using marked lines as visual guides to orient patterns perpendicular to the long side of the PIPAAm rectangle.

several hours prior to spincoating in order to increase the PDMS layer thickness to the desired 13 – 15 μm range (Figure 5.4D-F). We hypothesized that this thicker PDMS would prevent the cells from sensing any differences below the PDMS layer, but we still observed delamination of the myotubes from the PIPAAm regions of the MTFs (Figure 5.4D-E).

These experiments had been done by μCP lines on the modified substrates, so we hypothesized that the 'evenness' of μCP transfer might be affected by the PIPAAm region under the PDMS. To determine if premature delamination was caused because cells sensed the decoupling of PDMS from glass in the PIPAAm regions or if this was an artifact of uneven transfer of LAM during μCP , we compared myotube formation on isotropically coated PDMS only, PDMS on isolated PIPAAm, and PDMS on full PIPAAm coverage (Figure 5.5A). We compared myotube formation on both LAM and FN to determine if this was a LAM-specific phenomenon since we had previously engineered MTFs with FN (Figure 5.5B). Interestingly, when we quantified myotube formation on these 6 conditions, we observed significantly higher percent area myotube formation on LAM on full PIPAAm under PDMS (12.0%) compared to LAM on PDMS (5.9%) and LAM on isolated PIPAAm under PDMS (4.8%) (Figure 5.6). Additionally, myotubes formed on FN with the isolated PIPAAm region (8.7%) had significantly higher myotube formation than LAM coated substrates within the same condition (4.8%) (Figure 5.6). However, LAM coated PDMS on a full layer of PIPAAm had significantly higher myotube formation (12.0%) than FN coated substrates with the same conditions (5.9%) (Figure 5.6). These results suggested that there could have been an issue with LAM on the isolated PIPAAm region MTFs, but the fact that there was no observable difference in myotube formation on FN on all 3 substrates implied that this difference may have been an artifact of stamping that resulted in poorer LAM transfer in PIPAAm only regions.

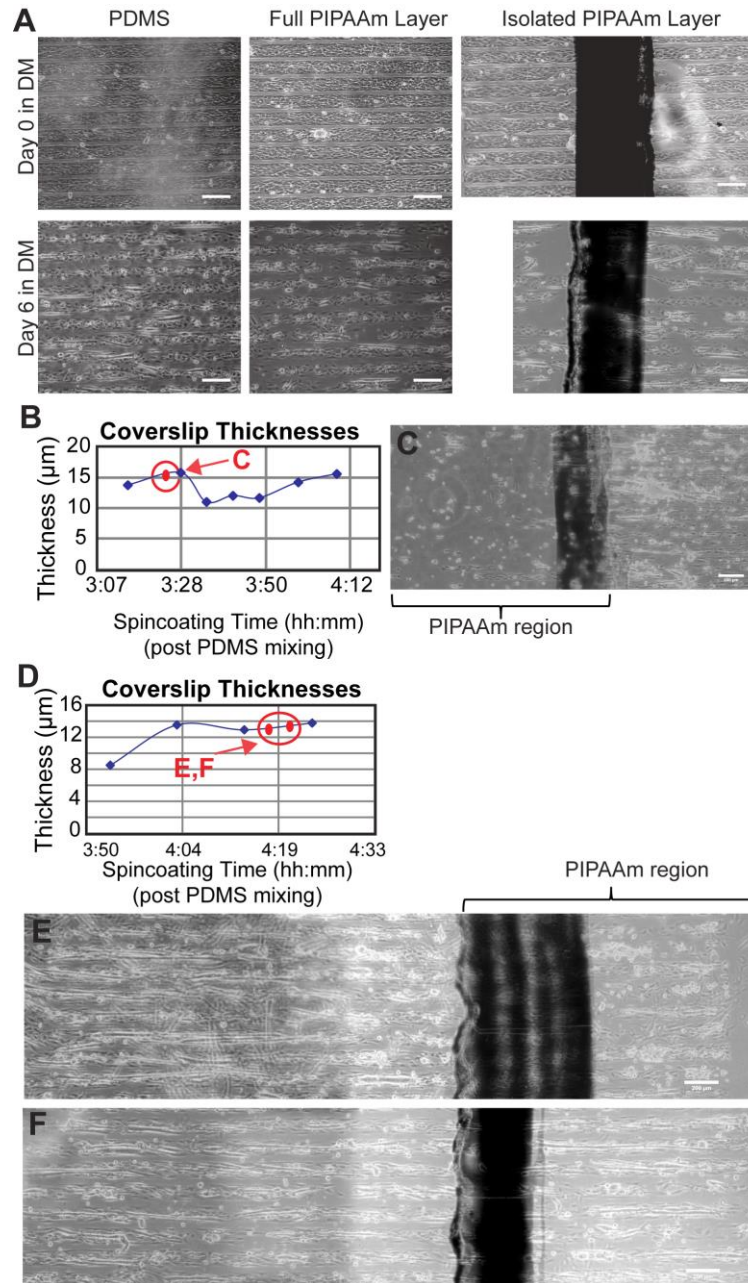


Figure 5.4: C2C12 myotubes delaminate from LAM lines on PDMS with isolated PIPAAm. (A) Day 0 to Day 6 of differentiation of C2C12 myoblasts on 100x20 lines of LAM on PDMS, PDMS on a full layer of PIPAAm, and PDMS on an isolated region of PIPAAm at show myoblast confluence on LAM at Day 0, but substrates with PIPAAm result in myoblast peeling and poorer myotube formation. (B) The PDMS in the coverslip in (C) is ~15 μm thick, and C2C12 cells differentiated on MTFs with the isolated PIPAAm region on 50x15 LAM lines showed significant myotube peeling in the PIPAAm region. (D) Coverslips from the samples in (E) and (F) have ~13 μm thick PDMS layers. (E) C2C12s differentiated on 100x20 and (F) 100x30 LAM lines also showed myotube peeling in the PIPAAm only region. Scale bars 200 μm .

5.3.3 Equalizing ECM Transfer on Modified TFs

In order to ensure more uniform transfer of LAM to TFs during μ CP, we used PDMS stamps with higher aspect ratio features. The standard stamps used for Chapter 3 studies and for patterning MTFs previous only had 2 - 5 μ m raised features for patterning. In order to ensure more uniform transfer of LAM onto TFs with isolated rectangles of PIPAAm under PDMS, we used stamps with higher aspect ratio, or 20 μ m raised features. Using these stamps allowed for more pressure to be applied to stamps during transfer of LAM to TFs without transferring LAM in between desired line patterns. Ultimately, using higher aspect ratio stamps allowed for differentiation of myotubes without delamination before day 6 of differentiation, as established in the initial methods using FN line patterns that resulted in contractile MTFs. Thus, we

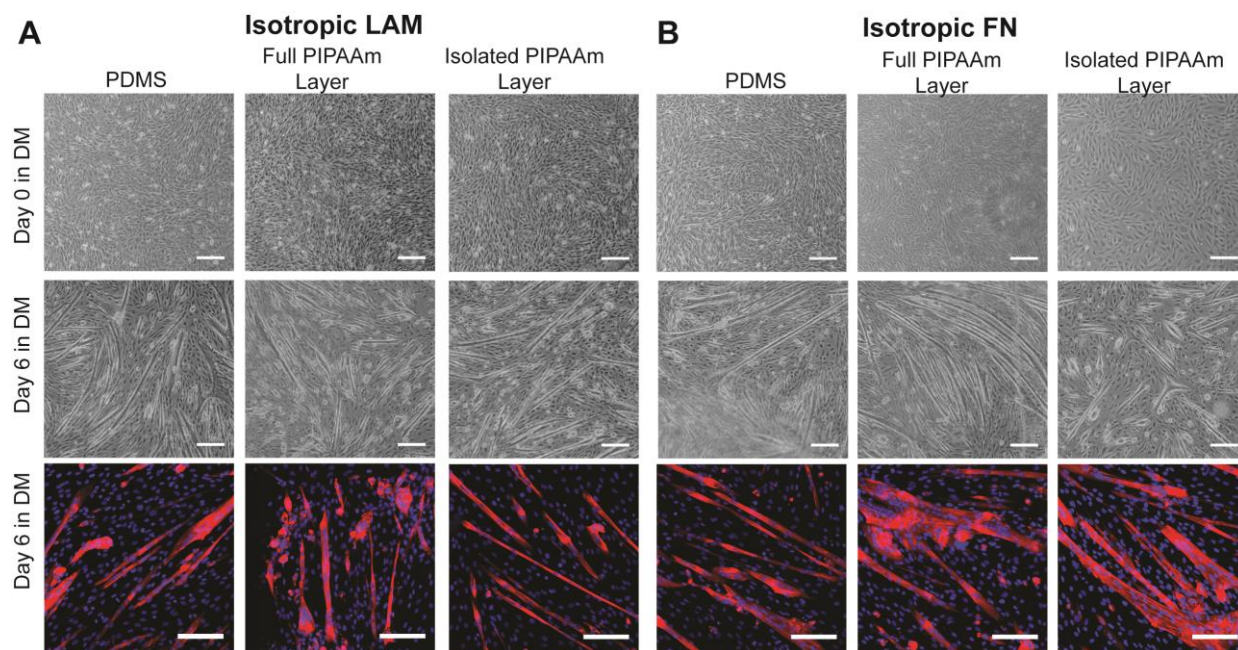


Figure 5.5: Myotube formation on PDMS and thin films with isotropically coated FN or LAM. (A) C2C12 myoblasts seeded on LAM coated PDMS, PDMS on PIPAAm, or PDMS on an isolated rectangle of PIPAAm from Day 0 to Day 6 of differentiation. MHC staining shows possible differences in myotube formation on different substrates. (B) C2C12 myoblasts seeded on FN coated PDMS, PDMS on PIPAAm, or PDMS on an isolated rectangle of PIPAAm from Day 0 to Day 6 of differentiation. MHC staining shows similar myotube formation on all substrates. Red – MHC; blue – nuclei. Scale bars 200 μ m.

successfully modified the method to standardize PIPAAm area and subsequently limit the MTF release length (Figure 5.7A-B). We were also able to differentiate human SkMDCs in this context and induce visible bending in the modified MTF assay (Figure 5.7C-D).

5.3.4 Genipin Crosslinking of Fibronectin to PDMS to Maintain 2D Myotube Culture

Even with a standardized MTF release length, maintaining skeletal muscle myotubes longer than 1 week before they delaminated from the TFs proved to remain problematic. We found that C2C12 myoblasts were typically limited to 6 days of differentiation before myotubes delaminated from μ CP FN lines on PDMS⁶.

Additionally, in pilot studies with human SkMDCs, when differentiation media was exchanged daily, as was done with differentiating C2C12s, myotube delamination occurred more rapidly than observed with the C2C12 cell line (Figure 5.8). Specifically, myotube formation at days 3 and 4 of differentiation was measured at 24.9% and 31.2%, respectively. After 4 days, myotubes delaminated from patterned lines, and myotube area was measured at 21.2% and 10.4% at days 5 and 6, respectively (Figure 5.9). It was determined that the delamination process could be slowed by exchanging media less frequently (every 48 hours instead of every 24), and this resulted in contractile MTFs using human SkMDCs (Figure 5.7C-D). However, these human MTFs appeared significantly less contractile than their mouse cell line counterparts (Figures 5.2 and

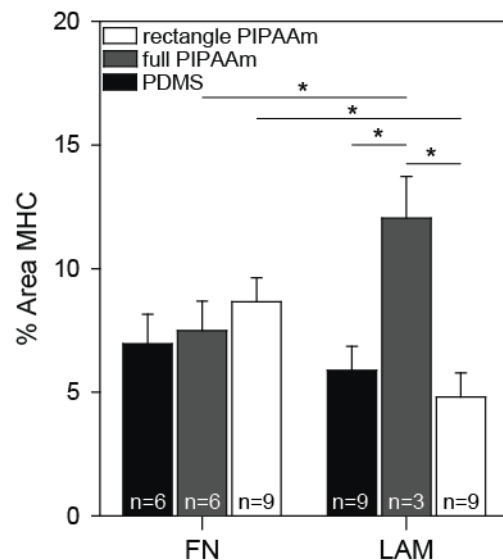


Figure 5.6. Quantification of Myotube Area on FN and LAM PDMS Substrates.

Quantified myotube formation showed a statistically significant interaction, as measured by a 2-way ANOVA between protein (FN or LAM) and substrate fabrication method ($P = 0.007$). # represents significantly higher than other protein condition within same PIPAAm condition. * represents significantly higher than other PIPAAm conditions within same protein condition. ($p < 0.05$).

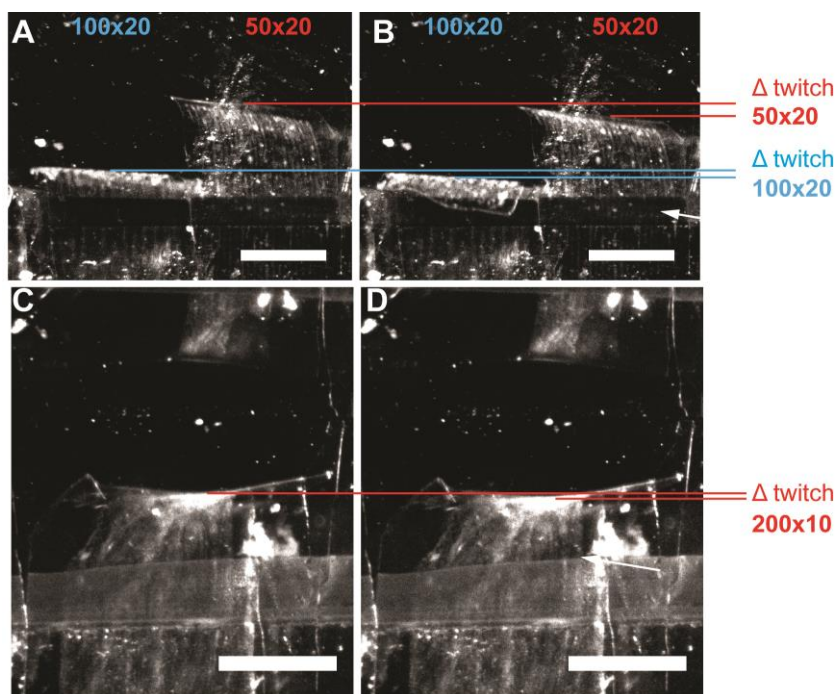


Figure 5.7: MTF assay is not robust enough for further development. (A) C2C12 myotubes on 100x20 and 50x20 LAM lines in their relaxed and (B) fully contracted state after 6 days of differentiation. These MTFs are not contracting to the same degree as MTFs shown in Figure 5.1, and are more consistent with typical results achieved for the MTF assay. (C) Human SkMDCs on 200x10 LAM lines in their relaxed and (D) fully contracted state. This example of a human MTF is the most amount of twitch observed, and is still barely measureable. These examples of contracting MTFs when using patterned ECM on PDMS are not robust enough to allow for maturation of myotubes to consistently induce bending of the thin PDMS film. Scale bars 1 mm. White arrow indicates marker designating boundary between isolated PIPAAm region and PDMS only region.

5.7). Even poorly contracting C2C12 MTFs still contracted with more twitch force than human SkMDC MTFs (Figure 5.7).

Many of the examples of contractile skeletal muscle in the literature allow myoblasts, whether mouse, rat, or human, to differentiate for a minimum of 2 weeks, with the best examples of contractile muscle

differentiated for closer to 1 month in 3D constructs⁷⁻⁹. The MTF assay did not restrict myotubes from delaminating, so we thought that crosslinking the patterned ECM onto PDMS might prevent myotube delamination as it had been used for smooth muscle cells in a similar assay^{16, 17}. To do this, we used genipin to crosslink FN to PDMS and maintained differentiating C2C12 myoblasts on the patterns for twice the amount of time in which they usually delaminated (Figure 5.10A). We fluorescently labeled FN in order to quantify patterned FN area and to determine if FN was being visibly pulled off of PDMS as myotubes delaminated.

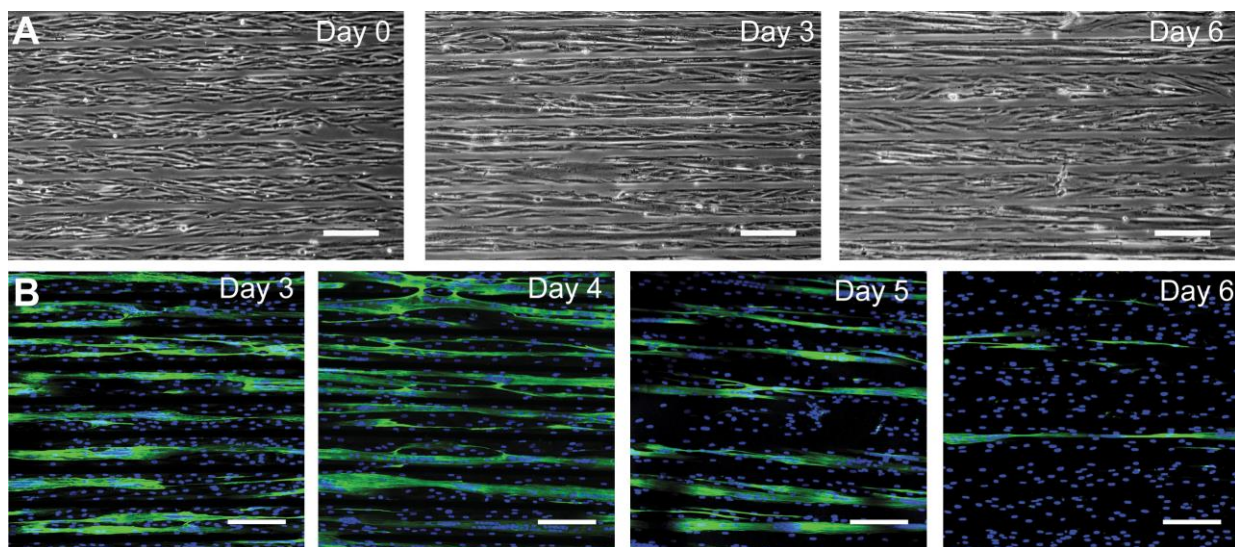


Figure 5.8: Myotube differentiation time is limited by myotube delamination after myotubes reach a certain size. (A) Phase images of human SkMDCs (F17 donor) differentiating on 100x20 LAM lines show that myotubes begin peeling by Day 6 of differentiation. (B) Representative images of MHC staining of human SkMDCs differentiated on 100x20 LAM lines from 3 - 6 days. Green - MHC, Blue - nuclei Scale bars 200 μm.

Myotubes did not appear to peel fluorescently labeled FN from substrates (Figure 5.10B).

However, our results also indicated that genipin crosslinking did not increase myotube culture maintenance after 6 days of differentiation. Significantly higher myotube formation/area FN was measured at day 6 for both FN only (19.8%) and FN+Gen patterned lines (18.7%) compared to myotube % area measured on FN only at day 12 (12.0%)(Figure 5.10C). Additionally, FN only substrates at day 6 had significantly higher percent area myotubes than Day 12 FN+Gen substrates as well (13.3%) (Figure 5.10C).

Ultimately, using genipin to crosslink FN substrates did not appear to increase the length of time skeletal muscle myotubes could be maintained in 2D culture on PDMS.

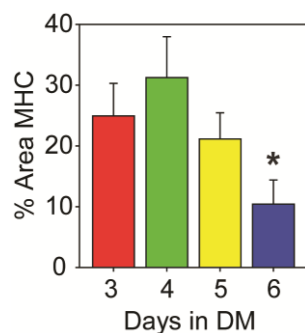


Figure 5.9. Analysis of Percent Area of Human Myotubes Differentiated for 3 to 6 Days. Cook's SkMDCs peeled off of patterned LAM lines by day 6 when DM was exchanged daily. Significantly less myotube area was measured at day 6 ($p < 0.05$). (n=3 for Day 4; n = 4 for Days 3, 5, and 6).

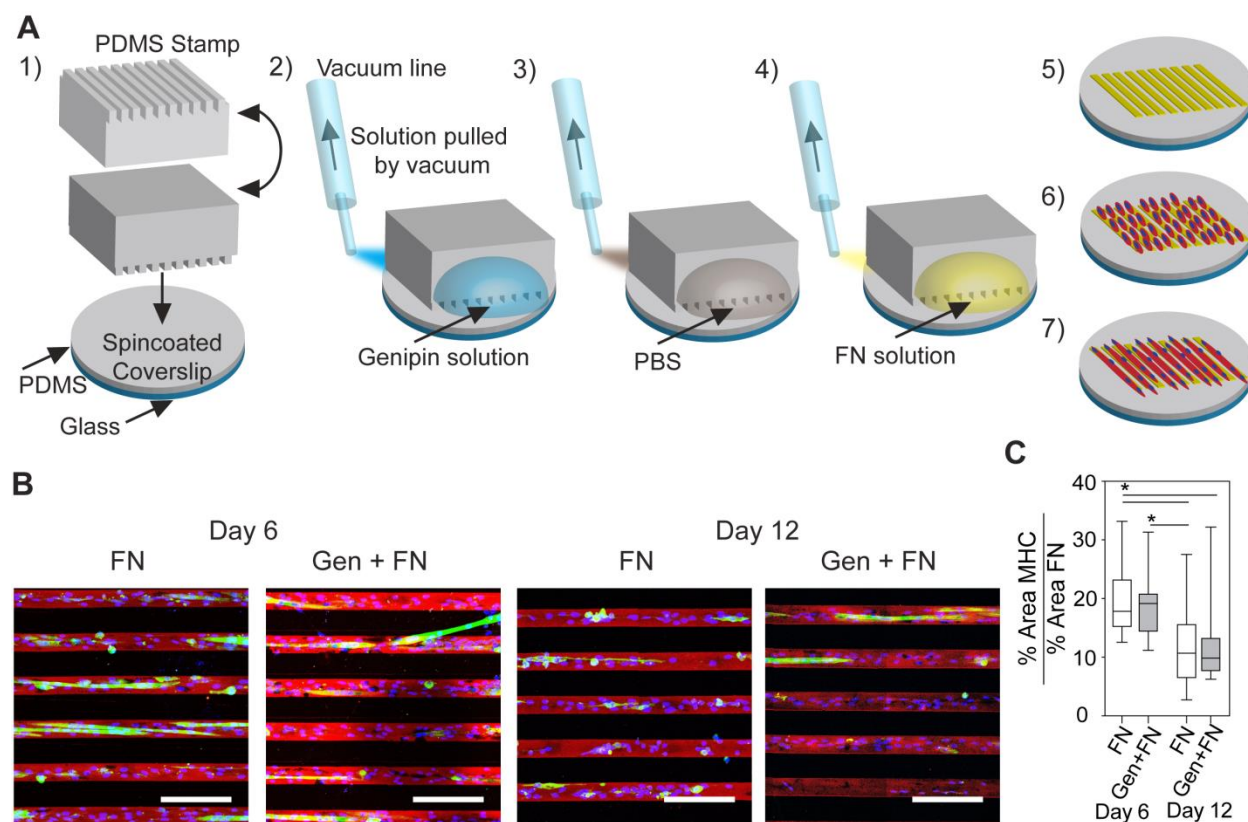


Figure 5.10: Genipin crosslinked FN lines on PDMS to prevent myotube peeling. (A) 1 - A PDMS stamp with 20 μm deep channels is placed in conformal contact with a PDMS coated glass coverslip. 2 - Genipin was pipetted along one side of the PDMS stamp, and a glass pipet pulling a vacuum was placed on the opposing side of the stamp to pull the genipin solution through the channels. Genipin was incubated in the channels for 1 hour. 3) PBS was pulled through the channels in the same manner to wash excess genipin not bound to the PDMS coverslip. 4) FN solution was pulled through the channels after PBS washes and incubated for 1 hour. 5) The stamp was removed to result in patterned FN crosslinked to PDMS using genipin. 6) C2C12 myoblasts were then seeded on the pattern and 7) differentiated into myotubes for 6 - 12 days. (B) Representative images of C2C12 myotubes on FN only or Gen + FN patterned coverslips after 6 to 12 days of differentiation. Red - FN, Green - MHC, Blue - nuclei. Scale bars 200 μm . (C) Myotube formation as measured by MHC staining and normalized for patterned FN area showed genipin crosslinking of FN to PDMS coverslips did not prevent myotube delamination past day 6 of differentiation. (Day 6, FN only: $n = 12$; Day 6, FN + Gen: $n = 10$; Day 12, both conditions: $n = 21$). * represents $p < 0.05$.

5.4 Discussion

Initially, we were able to successfully engineer skeletal MTFs using C2C12 myoblasts differentiated on patterned FN lines²⁰, and we also showed that we could increase the amount of differentiated myotubes by using patterned LAM micropatterned lines²¹. We then modified the MTF assay to standardize PIPAAm area and subsequently MTF release length. Initially,

myotubes peeled from PIPAAm areas, likely due to uneven transfer of LAM. Even after resolving the issues associated with modifying our protocol, we wanted to increase culture time so that we were not limited to 6 days of differentiation. We attempted to use genipin to crosslink FN to PDMS coated coverslips in order to maintain myotube cultures, as this had been successfully achieved with smooth muscle cells^{16, 17}. However, this did not successfully increase the maintenance of differentiating C2C12 myotubes on FN patterned PDMS. It appeared that the myotube delamination is not occurring at the ECM-PDMS interface since fluorescently labeled FN remained on PDMS after myotubes had formed and delaminated. Rather, it is likely that myotubes began to pull against their environment as they matured, as spontaneous contractions are a typical part of *in vitro* myotube differentiation¹⁴. Because nothing confined the myotubes to the PDMS, which has a much stiffer elastic modulus (1.72 MPa)²² than native tissue (~12 kPa)²³, the myotubes worked themselves off of the PDMS surface, even if the FN was crosslinked. We would need to further verify the effectiveness of the genipin crosslinking of FN to the PDMS, but it is clear from the fluorescence images that a layer of fluorescent FN remains even after myotubes have delaminated from the patterns for both FN and Gen+FN conditions. It is possible that myotubes were peeling off FN only a few molecules thick, thus leaving behind much of the patterned FN. If this is what was happening, the fact remains that crosslinking is unlikely to effectively prevent myotube delamination after more than 6 days of differentiation.

To move forward with further development of a 2D skeletal MTF assay, we need to determine the cause(s) of myoblast delamination after prolonged culture time. More specifically, we need to determine if the failure occurs at the ECM-PDMS interface, the integrin-ECM interface, the integrin-cell membrane interface, or if it is occurring in the cytoskeleton of the cell itself. It is likely that using a native ECM hydrogel as the MTF substrate is likely to prevent

delamination after 1 week of differentiation based on the findings presented for maintaining C2C12 myotubes for at least 3 weeks on microgrooved gelatin substrates²⁴. This ability to maintain myotube adhesion to the softer, biologically derived hydrogel suggests that the delamination issues may derive from interactions with the PDMS itself. Patterned ECM adsorbs to the PDMS through hydrophobic interactions, and this may impact the ability of ECM to bind key growth factors or may affect the integrity of the integrin binding sites on the protein because the hydrophobic domains bind to the PDMS and hydrophilic domains are exposed, possibly altering the protein's native conformation. We were hesitant to pattern differentiating myoblasts onto ECM based hydrogel MTFs because of the limited ability to align differentiating C2C12 myoblasts when spacing conditions were too narrow, as demonstrated in Chapter 3²¹. Our lab has established that this can be done successfully with cardiomyocytes, but contractile cardiomyocytes are already differentiated and do not need to fuse in the direction of lines after seeding, as is necessary with differentiating skeletal muscle myotubes, so guiding alignment of already contractile cardiomyocytes on patterned hydrogels is more feasibly controlled²⁵. It may prove beneficial to develop this system with grooved Col I hydrogels coated with LAM. In this way, a synergistic affect from maintaining 2D myotube culture on a hydrogel and providing specific ECM cues that maximized human and C2C12 myotube formation has the potential to result in more mature, contractile skeletal MTFs. Changing the substrate from hydrophobic PDMS to biologically derived, hydrophilic Col I will likely solve the delamination issue if the mechanism of failure is, in fact, directly related to conformational changes in ECM protein due to hydrophobic interactions with PDMS. It is also possible that other factors contributed to myotube delamination after 7 days of differentiation. For example, it is known that proteases, especially the calpain family, play a critical role in skeletal muscle growth and myogenesis²⁶⁻²⁸.

These proteases are important in skeletal muscle formation and myotube fusion as they are important regulators in breaking down and rebuilding the sarcomeric proteins within skeletal muscle myotubes. However, because their function is to break down proteins, it is possible that in the specific context of 2D, *in vitro*, micropatterned PDMS that they may be interrupting the integrin complex within the cell or possibly even altering the attachment sites of patterned ECM protein itself. It is possible to add small amounts of protease inhibitors to culture media to decrease the severity of the resulting myotube delamination if proteases are one of the culprits of 2D myotube delamination. These are several ways we could address the myotube delamination if it the root of the failure is occurring because of PDMS hydrophobic interactions or because of protease activity from the differentiating cells, either of which can affect PDMS-ECM interaction, ECM-integrin binding, or the integrin-membrane-cytoskeleton interactions within the cells.

In order to obtain human myotubes capable of visibly bending the PDMS layer, we would likely need to differentiate myotubes at least 2 - 4 weeks, based on what has been achieved with 3D cultures of human primary myoblasts⁷⁻⁹. The most consistent means to achieve this length of culture time in the literature has typically been to cast cells within a 3D hydrogel for culture. For this reason, we decided to move forward with engineering 3D skeletal muscle constructs. In order to use the similar model of measuring twitch force via bending of a thin elastomer layer, we decided to integrate a U-shaped silicone insert by casting a polymerizing mixture of Col I and muscle cells around the insert ends. The insert was designed to be incorporated into the differentiating muscle microtissue, thus allowing us to potentially exercise these microtissues as well as maintain their differentiation for significantly longer periods of time. These 3D engineered microtissues, with the ability to measure force generation by changes

in insert bending, will allow similar advantages to the initial goals for the MTF assay in allowing measurable responses to pharmacological stimulation and as *in vitro* tools to investigate skeletal and cardiac muscle differentiation and function to better engineer functional tissues in the future. The initial proof-of-concept and demonstration of these functions 3D microtissues is described in Chapter 6.

5.5 Conclusions

In this chapter, we have demonstrated the problems encountered when engineering skeletal MTFs from C2C12 or human derived myoblasts on PDMS. More specifically, we found that we are limited to ~6 days of differentiation of C2C12 or human SkMDC derived myotubes before the myotubes began to delaminate from the LAM lines on PDMS surfaces. Guiding differentiation of myoblasts to aligned, contractile myotubes required more than the 6 days we were limited to, and crosslinking of FN to PDMS surfaces did not retain myotube attachment past 1 week of differentiation. To engineer contractile skeletal muscle from the ground up, we need systems that maintain myotube adherence to allow cells to continue to mature up to 4 weeks in culture. Specifically, we need to move forward with designing 3D platforms that restrict differentiating myoblasts within a 3D ECM hydrogel or possibly even use microtopography of 2D hydrogel surfaces to guide myotube alignment and maintain adherence for longer than 1 week of differentiation.

5.6 References

1. Feinberg, A.W. et al. Muscular thin films for building actuators and powering devices. *Science* **317**, 1366-1370 (2007).
2. Alford, P.W., Feinberg, A.W., Sheehy, S.P. & Parker, K.K. Biohybrid thin films for measuring contractility in engineered cardiovascular muscle. *Biomaterials* **31**, 3613-3621 (2010).
3. Grosberg, A., Alford, P.W., McCain, M.L. & Parker, K.K. Ensembles of engineered cardiac tissues for physiological and pharmacological study: Heart on a chip. *Lab on a Chip* **11**, 4165-4173 (2011).
4. Alford, P.W., Nesmith, A.P., Seywerd, J.N., Grosberg, A. & Parker, K.K. Vascular smooth muscle contractility depends on cell shape. *Integrative Biology* **3**, 1063-1070 (2011).

5. Win, Z. et al. Smooth muscle architecture within cell-dense vascular tissues influences functional contractility. *Integrative Biology* **6**, 1201-1210 (2014).
6. Sun, Y., Duffy, R., Lee, A. & Feinberg, A.W. Optimizing the structure and contractility of engineered skeletal muscle thin films. *Acta Biomaterialia* **9**, 7885-7894 (2013).
7. Madden, L. et al. Novel In Vitro Exercise Model of Engineered Human Skeletal Muscle. *Tissue Engineering Part A* **21**, S46-S46 (2015).
8. Madden, L., Juhas, M., Kraus, W.E., Truskey, G.A. & Bursac, N. Bioengineered Human Myobundles Mimic Clinical Responses of Skeletal Muscle to Drugs. *Elife* **4** (2015).
9. Madden, L.R., Koeberl, D.D. & Bursac, N. Tissue Engineered Human Skeletal Muscle as a Pre-Clinical Model for AAV Treatment of Pompe Disease. *Molecular Therapy* **22**, S157-S157 (2014).
10. Vandenberg, H. et al. Tissue-engineered skeletal muscle organoids for reversible gene therapy. *Human Gene Therapy* **7**, 2195-2200 (1996).
11. Powell, C.A., Smiley, B.L., Mills, J. & Vandenberg, H.H. Mechanical stimulation improves tissue-engineered human skeletal muscle. *American Journal of Physiology-Cell Physiology* **283**, C1557-C1565 (2002).
12. Del Totto, M., Ferland, P., Shansky, J. & Vandenberg, H. Murine skeletal muscle cells tissue engineered for gene therapy. *Faseb Journal* **14**, A445-A445 (2000).
13. Hinds, S., Tyhovych, N., Sistrunk, C. & Terracio, L. Improved Tissue Culture Conditions for Engineered Skeletal Muscle Sheets. *Scientific World Journal* (2013).
14. Tesseraux, I., Gulden, M. & Wassermann, O. Cultured myotubes from skeletal muscle of adult rats. Characterization and action of Anemonia sulcata toxin II. *Naunyn Schmiedeberg's Arch Pharmacol* **336**, 232-9 (1987).
15. Microchem. 5.
16. Hald, E.S., Steucke, K.E., Reeves, J.A., Win, Z. & Alford, P.W. Microfluidic Genipin Deposition Technique for Extended Culture of Micropatterned Vascular Muscular Thin Films. *Jove-Journal of Visualized Experiments* (2015).
17. Hald, E.S., Steucke, K.E., Reeves, J.A., Win, Z. & Alford, P.W. Long-term vascular contractility assay using genipin-modified muscular thin films. *Biofabrication* **6** (2014).
18. Buxboim, A., Rajagopal, K., Brown, A.E.X. & Discher, D.E. How deeply cells feel: methods for thin gels. *Journal of Physics-Condensed Matter* **22** (2010).
19. Rudnicki, M.S. et al. Nonlinear Strain Stiffening Is Not Sufficient to Explain How Far Cells Can Feel on Fibrous Protein Gels. *Biophysical Journal* **105**, 11-20 (2013).
20. Cheng, C.S., Ran, L., Bursac, N., Kraus, W.E. & Truskey, G.A. Cell Density and Joint microRNA-133a and microRNA-696 Inhibition Enhance Differentiation and Contractile Function of Engineered Human Skeletal Muscle Tissues. *Tissue Engineering Part A* **22**, 573-583 (2016).
21. Duffy, R.M., Sun, Y. & Feinberg, A.W. Understanding the Role of ECM Protein Composition and Geometric Micropatterning for Engineering Human Skeletal Muscle. *Ann Biomed Eng* **44**, 2076-89 (2016).
22. Palchesko, R.N., Zhang, L., Sun, Y. & Feinberg, A.W. Development of polydimethylsiloxane substrates with tunable elastic modulus to study cell mechanobiology in muscle and nerve. *PLoS One* **7**, e51499 (2012).
23. Engler, A.J. et al. Myotubes differentiate optimally on substrates with tissue-like stiffness: pathological implications for soft or stiff microenvironments. *J Cell Biol* **166**, 877-87 (2004).
24. Bettadapur, A. et al. Prolonged Culture of Aligned Skeletal Myotubes on Micromolded Gelatin Hydrogels. *Sci Rep* **6**, 28855 (2016).
25. Jallerat, Q. in Biomedical Engineering 105 (Carnegie Mellon University, 2016).
26. Goll, D.E., Thompson, V.F., Taylor, R.G. & Ouali, A. The calpain system and skeletal muscle growth. *Canadian Journal of Animal Science* **78**, 503-512 (1998).
27. Tonami, K. et al. Calpain-6 deficiency promotes skeletal muscle development and regeneration. *PLoS Genet* **9**, e1003668 (2013).
28. Murphy, R.M. Calpains, skeletal muscle function and exercise. *Clin Exp Pharmacol Physiol* **37**, 385-91 (2010).

Chapter 6

Engineering Cardiac Microtissues with Integrated Force Indicators for Force and Beat Frequency Analysis

6.1 Introduction

Engineered *in vitro* models of functional human cardiac muscle have applications as physiologically relevant but more economical platforms for pharmacological testing (compared to human trials), genetically-tailored disease models, and building blocks to engineer functional organ replacements in the future. It is well known that animal models do not always accurately predict the response pharmacological stimuli will have on human patients. Similarly, engineering *in vitro* cardiac muscle from human derived cells instead of animal cardiomyocytes (CMs) brings us one step closer to engineered cardiac muscle that is physiologically more similar to adult human heart muscle. Further, engineered cardiac heart muscle that is representative of human physiology fills a critical void between animal models and human clinical trials. However, human adult CMs are terminally differentiated and cannot be expanded *in vitro*. The only robust source of new human CMs are from pluripotent stem cells, either embryonic stem cells (ESCs) or induced pluripotent stem cells (iPSCs). In fact, much *in vitro* understanding of cardiac function has focused on individual CM behavior. Specifically, focus has been placed on differentiating more functionally mature CMs from ESCs or other human pluripotent stem cells¹. Additional studies have examined individual pluripotent stem cell-CMs or iPSC-CM response to

different pharmacological stimuli in terms of electrical activity, force generation, and gene expression^{2,3}. The challenge with iPSC and ESC-derived CMs is that they are often more functionally immature than *in vivo* adult CMs. Specifically, these CMs are often round rather than spread and classically rod-shaped, exhibit disordered sarcomere organization, and have smaller membrane capacitance than adult CMs⁴⁻⁶. Determining how to differentiate more functionally mature CMs from stem cells is key to engineering functional cardiac tissues, but a necessary next step is developing more complex, physiologically representative, 3D microtissues (μ tissues) by building on these individual CM studies⁴.

We previously demonstrated that *in vitro* functional cardiac muscle constructs can be used as a prototype to engineer functional skeletal muscle models *in vitro* since contractile force is a useful metric for function in both tissue types^{7,8}. This proved to be problematic in 2D skeletal muscle models due to the limitation of ~1 week of culture time before differentiating myotubes delaminated from micropatterned PDMS surfaces. We were able to observe myotube twitching in these muscular thin film (MTF) assays for both C2C12 and primary human skeletal muscle derived cells, but we determined that a more robust contractility assay allowing at least 2 to 4 weeks of differentiation and maturation is necessary for skeletal myoblasts⁹. For this reason, we designed a platform to allow for 3D culture of contractile skeletal muscle or CMs for applications as *in vitro* muscle models, pharmacological test beds for personalized medicine, and applications as building blocks for biological or soft robotics.

Initial efforts to develop 3D CM μ tissues involved suspending CMs in a native ECM gel and casting the cell+gel mixture around a structure. More specifically, CMs isolated from chicken embryos or neonatal Sprague-Dawley rats have been mixed with fibrin or collagen I (Col I) and the suspension is cast into a well with Velcro™ or polydimethylsiloxane (PDMS)

posts¹⁰⁻¹². After matrix polymerization, the PDMS or VelcroTM posts act as anchoring points to induce uniaxial stresses that typically encourage cell alignment along the long axis of the constructs (see Chapter 2, Figure 2.7). Advancements in stem cell technology have since allowed for the development of more clinically relevant 3D engineered constructs by placing HESC-CMs or iPSC-CMs in these μ tissues^{13, 14}. Functional readout, in terms of force generated by cardiac μ tissues, is typically obtained by measuring PDMS beam deflection^{12, 15, 16} or using an optical force transducer¹⁷. Additionally, because CMs generally lack the ability to significantly reorganize or synthesize their surrounding matrix, fibroblasts (FBs) have been added to these 3D μ tissues to assist CMs in remodeling and subsequent compaction of the ECM hydrogel as well as to further mature CMs^{18, 19}. Addition of FBs helped reduce μ tissue size to address issues of diffusion limits in these non-vascularized μ tissues, and their presence has also been shown to increase CM spreading within tissues¹⁹, as well as improve beat synchronicity, beats per minute, conduction velocity, and the expression of muscle contractile proteins^{20, 21}.

To build on previous work in this dissertation we engineered our own contractile 3D CM μ tissue and demonstrated its potential as a cardiac model tissue as well as a template to engineer 3D skeletal muscle models in the future. We designed this 3D system to enable measurement of twitch forces of the contractile μ tissues without invasive probes or force transducers. Specifically, we integrated a thin, U-shaped, PDMS insert into 3D μ tissues and used the change in bending or tissue length as a means to measure twitch force (Figure 6.1A). Specifically, μ tissue contraction induced bending of the PDMS U-shaped insert, and the force required to induce changes in bending can be measured a simple beam or cantilever bending model of the PDMS insert (Figure 6.1B-C). HESC-CMs were used to engineer these initial μ tissues with integrated force indicators (MIFIs). These cardiac MIFIs responded as expected to excitatory

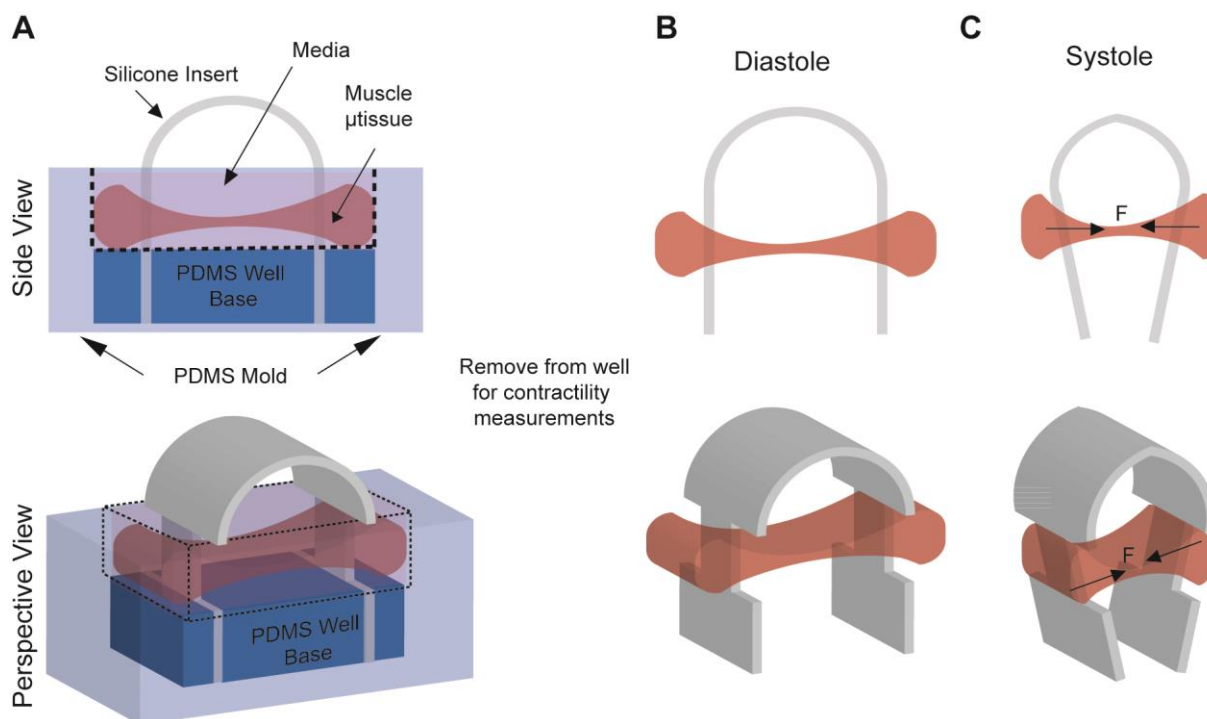


Figure 6.1 Design Concept for Microtissue with Integrated Force Indicator. (A) Views of the PDMS insert, PDMS well base, and muscle tissue as they would appear during culture. The thin, PDMS insert had a narrow necking region for tissue attachment, and the wide base of the insert is hidden in slits in the PDMS well base to constrain the tissue to attach to the necking region of the insert. (B) The wide base of the insert allowed the tissue to be removed from the well with the insert intact to perform the contractility assay and (C) upon contraction of the tissue, the force (F) induced bending of the PDMS insert.

pharmacological stimuli and have the potential to serve as *in vitro* models of human CM function upon further characterization. Further, the MIFI model can serve as a template that we can later apply to iPSC-CMs for patient specific disease modeling or skeletal muscle myoblasts since the well and insert design should readily translate to other contractile cell types. This system has an advantage over traditional PDMS post-bending based tissues because the insert design allowed for easy removal of the MIFIs from culture wells without damaging or altering tissue architecture to investigate the effect of increased exercise load on these cardiac or skeletal muscle model tissues. Specifically, the inserts created a stress field that influenced the cells to align along the long axis of the well, but full force of the 'unfolded' insert is partially hidden because the PDMS well base does most of the work of holding the inserts in place during culture. Thus, when MIFIs

are removed from the PDMS wells, the applied load to the MIFI increased, forcing the cells to work against the insert to maintain μ tissue architecture. For this reason, the platform was designed to serve not only as a tool to better understand cardiac and skeletal muscle normal and disease states but to also allow investigation of combinatorial effects of various small molecule or drug therapies with muscle exercise.

6.2 Materials and Methods

6.2.1 Design and preparation of PDMS wells and inserts

Solidworks was used to design molds for casting PDMS for μ tissue culture. Initial prototypes were printed with acrylonitrile butadiene styrene (ABS) plastic using a Replicator 2X 3D printer (MakerBot), and final molds were printed with Verowhiteplus RGD835 using an Objet Connex350 (Stratasys). To create wells from plastic molds, Sylgard 184 PDMS (Dow Corning) was mixed at 10:1 weight ratio of base to curing agent using a Thinky conditioning mixer (Phoenix Equipment Inc.) set to a 2 minute 2000 RPM mixing cycle and a 2 minute 2000 RPM defoaming cycle. Universal mold release spray (Smooth-On) was sprayed onto plastic molds, and PDMS was poured until the molds were filled. PDMS wells were degassed for 30 minutes and cured in a 65⁰C oven for 2 hours before being removed from the plastic molds.

Well inserts were designed using Adobe Illustrator and a ProtoLaser U3 (LPKF) laser cutter was used to cut dogbone-like inserts from non-reinforced, 0.005" thick medical PDMS sheeting (Bioplexus). Inserts were mounted onto glass microscopy slides and imaged with a VHX-5000 digital microscope to measure thickness. The average of three measurements for each insert was used for later analysis in the contractility assay.

6.2.2 Elastic modulus verification of PDMS inserts

PDMS sheeting was laser cut into dogbone strips for tensile testing using a ProtoLaser U3. 10 samples were mounted on an Instron 5943 and strained at a rate of 1 mm/minute until >10% strain was reached or until samples slipped from the grips. Two of the 10 samples slipped before the strips reached 10% strain, and these were excluded from elastic modulus measurements. Sample cross sections were calculated from average optical measurements of the individual strips prior to testing. Strip thicknesses were obtained by averaging 3 random thickness measurements per strip using a VHX-5000 digital microscope. Stress was calculated in Excel by dividing measured force by measured cross-sectional area. Stress was then plotted against strain, and the linear curve fit was obtained for the first 10% of strain. The slopes of the curves were averaged to obtain a final measurement of 3.10 MPa for the elastic modulus of PDMS inserts. The elastic modulus was used for modeling the force required to bend inserts to specific conformations for the contractility assay.

6.2.3 Cell Culture - HUES9-CMs

HUES9 cells were a gift from the Van der Meer lab at University Medical Center Groningen and protocols for differentiation were obtained from their in-house differentiation protocol based on previous publications by other groups^{22, 23}. Reagents were obtained from Thermofisher unless otherwise indicated. Cells were kept in continuous culture in 6-well tissue culture treated plates pre-coated with 12 $\mu\text{g}/\text{cm}^2$ of Geltrex™ and kept at 37°C and 5% CO₂. All media was supplemented with 1:1000 Mycozap-CL (Lonza). To pre-coat well plates, Geltrex™ was diluted in 4°C DMEM/F12 to a final concentration of 114 $\mu\text{g}/\text{mL}$ before pipetting 1 mL/well. Plates were then incubated with Geltrex™ at room temperature for at least 1 hour prior

to cell seeding or were stored at 4°C for up to 1 week. To passage, cells were rinsed with 1x PBS (GE Healthcare) and incubated with TrypLE Express for 5 minutes. Cells were then detached by pipetting, transferred to DMEM/F12 stopping media and centrifuged at 200 G for 5 minutes. Media was then aspirated from the cell pellet, and cells were re-suspended and seeded at 13.1×10^3 cells/cm² in Essential 8 media (E8) supplemented with 5 µM Y27632 (System Bioscience). After 24 hours, Y27632 supplemented E8 was exchanged for E8 media daily until cells reached 80% confluence, at which point cells were passaged or differentiated.

To induce differentiation, on day 0, cells were rinsed with 1x PBS and 3 mL/well of RPMI 1640 basal media supplemented with 1:50 B27 without insulin (RPMI/B27) and 6 µM CHIR99021 (LC Laboratories). On day 2, cells were washed with 1x PBS before adding 3 mL/well of RPMI/B27 with 2 µM Wnt-C59 (Selleck Chemicals). On days 4 and 6, media was exchanged for 3 mL/well of RPMI/B27. On days 8 and 10, media was exchanged for 3 mL/well of CDM3: RPMI 1640 basal media supplemented with 500 µg/mL of *O. Sativa* derived recombinant human albumin (RHA) (Sigma-Aldrich) and 213 µg/mL of L-ascorbic acid 2-phosphate (AAP) (Sigma-Aldrich). At day 12, if CMs were visibly beating, cells were passaged for purification.

For purification differentiated cells were passaged by washing with 1x PBS and incubating in TrypLE Express for 15 minutes at 37°C. Cells were released from plates by pipetting into DMEM/F12 stopping media (2 mL/well) and were then centrifuged at 200 G for 7 minutes. Cells were seeded on Matrigel™ (Corning) coated 6 well plates. Plates were coated with Matrigel™ following the same protocol used to coat plates with Geltrex™. Cells were resuspended in CDM3L (RPMI 1640 without D-glucose supplemented with 500 µg/mL RHA, 213 µg/mL AAP, 7.1 mM sodium DL-lactate (Sigma-Aldrich) and 5 µM Y27632) media. 3

mL/well of CDM3L (without Y27632) was then exchanged 24 hours after seeding and at day 4. At day 7, cells were passaged by rinsing with 1x PBS, incubating for 15 minutes in TrypLE Express at 37°C, centrifuged at 200 G for 7 minutes, and were then used for experiments.

6.2.4 Cell Culture - Human Cardiac Fibroblasts

Human Cardiac Ventricular FBs (NHCF-V) were obtained from Lonza, used at <15 doublings, and were cultured at 37°C and 5% CO₂. Cells were cultured in FB Growth Medium-3 (FGM3) made from the FGM-3 BulletKit™ (Lonza) consisting of FBM supplemented with 0.1% rhFGF-B, 0.1% insulin, 10% fetal bovine serum, and 0.1% 1000x gentamicin/amphotericin-B. Upon thawing, cells were resuspended in FGM3 and seeded at ~6.5x10³ cells/cm². After reaching 80% confluence, cells were rinsed with 1X PBS and incubated with 0.25% Trypsin-EDTA (Thermofisher) for 3 – 5 minutes at 37°C. After cells began to detach, 2 mL Trypsin Neutralizing Solution (Lonza) was added at per mL of Trypsin-EDTA, and the cell suspension was centrifuged at 220 G for 5 minutes. The media supernatant was aspirated, and cells were either resuspended in FGM3 and passaged at a density of 3.5x10³ cells/cm² or used for casting MIFIs.

6.2.5 Cell Culture - C2C12s

C2C12s were obtained from Abcam and cultured according to manufacturer specifications. Specifically, cells used in experiments were kept below passage 12 and below 80% confluence while in continuous culture. C2C12 cells were kept in growth media (GM) consisting of high-glucose DMEM (Corning) supplemented with 1% 100x Penicillin-streptomycin (Thermofisher), 1% 100x L-glutamine (Thermofisher), and 10% fetal bovine serum (J R Scientific). When cells reached 80% confluence, they were passaged by washing with 1x PBS and incubated with 0.05% Trypsin-EDTA for 3 – 5 minutes. Cells were then resuspended in GM at a 2:1 ratio of GM to Trypsin-EDTA and centrifuged at 2000 RPM

for 5 minutes. The supernatant was aspirated from the cell pellet, and cells were reseeded at $\sim 6.5 \times 10^3$ cells/cm² in a new flask or cast in MIFI construct.

6.2.6 Casting Microtissues with Integrated Force Indicators

Prior to tissue culture, PDMS wells were cleaned by sonicating in 50% ethanol for 30 minutes. PDMS inserts and vacuum grease (Dow Corning) were UV-treated for 15 minutes prior to use. PDMS wells were dried using a nitrogen air gun and then incubated with 1% w/v Pluronic F-127 (Sigma) for 3 - 5 minutes to prevent cell attachment to PDMS. Pluronic F-127 was aspirated and wells were rinsed 3 times with 1x PBS. Inserts were then placed in the wells by securing both ends in the slits in the base of the PDMS wells. Insert bases were visible through the PDMS well, and were adjusted with forceps until the entire base rested flush within the slit. After insert placement, a 1000 μ L micropipette tip was used to manually coat the bottom of the PDMS well with vacuum grease, and wells were then firmly placed in the well of a 6-well culture plate. Wells with inserts were then used immediately or sterilely stored for later use. Micropipettes were used for aspiration instead of a full force vacuum in order to prevent inserts from being disturbed from their resting position.

Rat tail Col I (Corning) was gelled following the neutralization reaction using 1N NaOH (Sigma) as recommended by the manufacturer. MIFIs were cast with final concentrations of 2 mg/mL Col I, 20% v/v Matrigel™, 10% 10x PBS (Hyclone), 2.3% 1 N NaOH, and 18.75×10^6 cells/mL for CMs and 15×10^6 cells/mL for C2C12s. When NHCV-Fs were included with HUES9-CMs, they were mixed at ratios of 10 or 20 % of total cell concentration. After manual mixing, the cell/gel mixture was pipetted gently into wells (80 μ L/well) to avoid creation of bubbles. To prevent MIFIs from coming out of the wells due to vigorous beating at later dates in culture, No. 2 55x45 mm cover glasses (Fisher Scientific) were cut into rectangles <3 mm in

width and at least 10 mm in length using a diamond tip pen, inserted on top of PDMS wells but under inserts and secured with vacuum grease. MIFIs were then placed in a 37°C incubator for 45 minutes to allow gelation of the Col I prior to addition of culture media. CMs were cultured in RPMI 1640 with 1% knock-out serum replacement (Thermofisher) and 1:1000 Mycozap. C2C12s were cultured in GM for 1 week before switching to DM. CM and C2C12 media was exchanged every 48 hours. MIFIs were kept in culture up to 14 days before removal from wells for the contractility assay.

6.2.7 Image Analysis of Tissue Compaction Tracking

MIFIs were imaged on a Nikon SMZ1000 stereo microscope with oblique illumination using a Nikon D5100 DSLR camera during culture for top down images of tissue area. ImageJ was used for image processing. Images were converted to grey-scale, thresholded, and then converted to an 8-bit binary in order to distinguish the tissue area (black) from the rest of the well (white). The tissue area was measured as 'positive' pixels. Occasionally, the outline of the tissue had to be hand drawn due to light-scattering interference from the inserts. The percent area of the tissues was tracked in this way for the duration of culture.

6.2.8 Contractility Assay

MIFIs were removed from wells using forceps and were transferred to a 35 mm petri dish filled with 37°C Tyrode's solution (1.192 g HEPES, 0.203 g MgCl₂, 0.403 g KCl, 7.889 g NaCl, 0.04 g NaH₂PO₄, 0.901 g C₆H₁₂O₆, and 0.265 g CaCl₂ per liter of distilled water, pH 7.4). MIFIs were anchored by placing the wide base of the insert into a slit in a PDMS block glued to the bottom of the stimulation dish. The Tyrode's bath was maintained between 30° and 37°C using a heated stage regulated by an in house LabVIEW program. Videos of samples were taken using a

Nikon D5100 DSLR camera mounted on a Nikon SMZ1500 stereomicroscope. Samples were paced from 2 to 10 Hz using parallel platinum electrodes placed 2 cm apart and immersed in Tyrode's. Samples were stimulated using a Grass Stimulator set to 40V using a 10 ms square pulse wave.

6.2.9 Pharmacology assay

Drugs were obtained from Sigma-Aldrich. Carbachol and isoprenaline were mixed to stock concentrations of 5mM in 1x Tyrode's solution. 5mM epinephrine stock solution was made by dissolving epinephrine at 500mM in HCl before diluting with Tyrode's to a final concentration of 5 mM. Caffeine was dissolved directly in Tyrode's to make a stock solution of 20 mM. All stock solutions were diluted further with Tyrode's to reach concentrations of 50 nM, 500 nM, 5 μ M, and 50 μ M for carbachol, isoprenaline, and epinephrine. Caffeine was used at 500 μ M or 5 mM concentrations. These concentrations were used because this range had been previously demonstrated to elicit changes in force exertion and beats per minute (BPM) from cardiac μ tissues in a dose-dependent manner. During the contractility assay, MIFIs were washed 3x with Tyrode's between drugging conditions, and videos of constructs in Tyrode's only were taken between different drug conditions to determine if the MIFI had recovered to its initial, pre-drugged state.

6.2.10 Fixing and Immunofluorescence Staining

Reagents were obtained from Thermofisher unless otherwise indicated. Samples were fixed in 4% formaldehyde (electron microscopy sciences) in PBS with 1:200 Triton-X 100 (Fisher Scientific) for 1 hour followed by 3 30 minute washes in PBS. Samples were blocked in 5% goat serum in PBS overnight at 20°C followed by 3 30 minute washes in PBS. Mouse anti-

sarcomeric- α -actinin (Sigma-Aldrich) was diluted to 1:100 in PBS, and samples were incubated overnight at 20°C in 500 μ L of antibody solution in 24 well culture plates to ensure coverage of the 3D tissues. Samples were then washed 3 times for 30 minutes each in PBS before incubating with 1:200 DAPI, 3:200 phalloidin tagged with Alexa-Fluor 488, and 1:100 goat anti-mouse antibody tagged with Alexa-Fluor 555 in PBS at 20°C overnight. After the final incubation step, samples were rinsed 3 times for 30 minutes each in PBS before imaging or storing in PBS.

6.2.11 Force measurements from bending inserts

Alkiviadis Tsamis performed the finite element modeling of bending PDMS inserts in Abaqus software (Dassault Systemes) to create lookup tables for inserts ranging in thickness from 125 to 154 μ m (Appendix B). Specifically, The elastic strip was modeled as 3D deformable extruded solid, with extruded thickness varying between 125 and 154 μ m. The elastic strip was considered as linearly elastic, isotropic and incompressible material, with Young's modulus equal to 3.09 MPa according to elastic modulus measurements. The section of the elastic strip was considered as solid homogeneous. The force-driven bending simulation was designed to mimic the experimental procedure. One static general analysis step was used where the elastic strip was deformed by application of equal contractile force in three parallel axial connectors placed in the regions where the tissue was attached during the experiment, so that the total force would equal the sum of the contractile force of the three connectors (Figure 6.8). The total force ranged between 60 and 155 μ N for the experimentally measured tissue length which corresponded to the deformed length of the connectors. Additional boundary conditions were imposed based on geometrical symmetry. The general analysis step did not have automatic stabilization applied, and the step increments were assigned automatically. Finally, the finite element mesh was composed of 20-node quadratic, hybrid, reduced integration brick elements

(C3D20RH), which are suitable for general analysis work. From this model, the change in tissue length could then be used to calculate the force necessary to bend the inserts to these conformations. Custom MATLAB code was used to manually track length changes of contracting MIFIs (Appendix C), and resulting length data was also run through custom MATLAB code to calculate the corresponding force based on tissue length and insert thickness (Appendix D).

To approximate tissue cross-sectional area to normalize measured twitch forces, microtissue width and thickness were measured manually in ImageJ. Specifically, width and thickness measurements were taken per construct, one within 1 mm of either insert attachment site and 1 from the middle of the tissue. Tissues were assumed to have an ellipsoid cross-section, and these width and thickness measurements were used as the long and short diameters of the calculated ellipsoid cross-section. Additionally, muscle cross-sectional area was approximated to normalize force per muscle area by assuming full cell coverage within the outer 100 μm diameter of constructs. Muscle area was then calculated as 90% or 80% of full area for 10% and 20% FB tissues, respectively. In this way, muscle cross-section was likely over estimated, but this allowed for the normalized force to be an underestimation for a worst case scenario. Specific force was calculated by dividing twitch force by the approximate cross-sectional area and for approximate muscle cross-sectional area for each individual tissue.

6.2.12 Statistical Analysis

All statistical analyses were carried out in SigmaPlot (Systat). ANOVA on ranks was performed on data presented in Figures 6.4K, 6.9C-D, and 6.11E using the Dunn's method post-hoc test, and ANOVA on ranks with post-hoc Tukey test was performed on Figure 6.11F. Two-

Way ANOVAs with Holm-Sidak post-hoc comparisons were performed for figures 6.11A-C. A Mann-Whitney Rank Sum test was performed on Figure 6.11D. A One-Way ANOVA was performed on data in Figure 6.9E with no post-hoc test as no significant differences were found. Differences were considered significant at $p \leq 0.05$. Sample sizes for twitch force graphs in 6.9C-D represent 5 technical replicates/sample, i.e. if $n = 30$, then 5 beats/sample for 6 separate samples are represented.

6.3 Results

6.3.1 Design of 3D Platform for Microtissues with Integrated Force Indicators

The goal of this project was to engineer a platform for contractile, 3D muscle μ tissues that could be easily removed from culture wells and analyzed in a side on contractility assay. To do this, we used a U-shaped, thin PDMS insert acting as an indicator to track force exerted by beating μ tissues (Figure 6.1). Inspired by the PDMS post models that have worked for both cardiac and skeletal muscle μ tissues, we wanted to use two anchor points within a PDMS well in order to guide alignment of cells in a Col I+Matrigel™ gel. The insert is designed to have bases hidden in slits in the PDMS culture well and a narrower attachment around which the μ tissue can polymerize, compact, and mature (Figure 6.1A). This wide insert base allowed for eventual removal of the μ tissue from the well, at which point, contraction of the beating cells induced a change in tissue length and bends the insert (Figure 6.1B-C). In this way, MIFIs were easily assessed for overall μ tissue beat frequency and muscle force generation. Typical 3D construct designs in the past had PDMS posts that dictated μ tissue geometry designed as a part of the well itself, and removal of the μ tissue would result in a contractile tissue with no load to work against relative to itself. In order to allow removal of the μ tissue while still maintaining adherence to post-like structures, we initially designed PDMS molds to have a slit in the base of the well

between 2 small posts (Figure 6.2A-B). U-shaped, thin, PDMS dogbone-like insert was designed to be placed perpendicular to either end of the μ tissue during the Col I polymerization process, but hidden between the PDMS posts (Figure 6.2A-D). Initial designs were tested using C2C12 μ tissues, and we observed μ tissue attachment, but there were large holes resulted from the double post design (Figure 6.2C). To reduce resulting holes in the μ tissues but maintain the classical post design, we removed the inner posts and made the wells smaller (Figure 6.2E-F, H). The

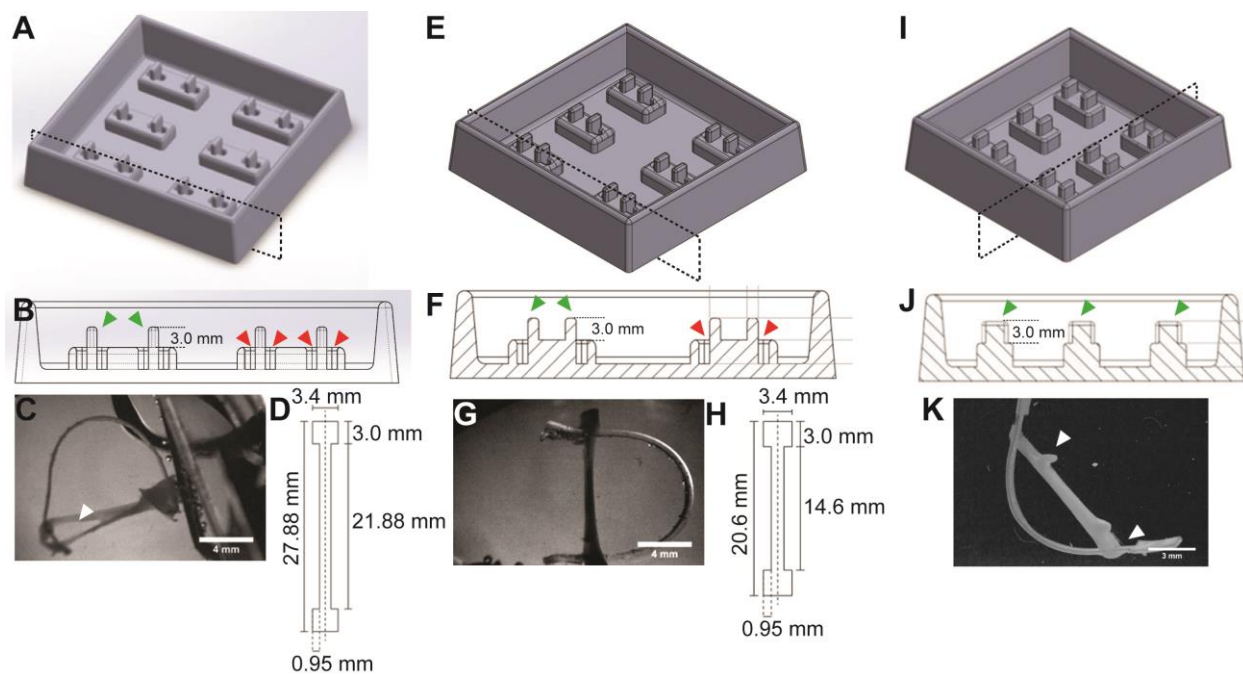


Figure 6.2. Iterative Plastic Mold and PDMS Insert Design Process. (A) Perspective view of CAD model of plastic mold Design 1, intended to hide the insert between 2 PDMS posts on either side. This is the negative of what PDMS wells would look like. A cutaway view of the dotted black rectangle shows (B) Side view of Design 1 where green arrows point out what will become PDMS base slits and red arrows point out what will become PDMS posts. (C) A C2C12 MIFI created using Design 1 resulted in the possibility of large holes in the μ tissue around the insert because it was 'hidden' between 2 PDMS posts (white arrow). (D) PDMS insert dimensions for mold Design 1. (E) Perspective view of CAD model of plastic mold Design 2, intended to hide the insert against 1 PDMS post on either side to decrease hole size in μ tissues. This is the negative of what PDMS wells would look like. A cutaway view of the dotted black rectangle shows (F) Side view of Design 2 where green arrows point out what will become PDMS base slits and red arrows point out what will become PDMS posts. (G) A C2C12 MIFI created using Design 2 has better tissue integrity around the attachment sites, leading us to question if posts could be completely removed. (H) PDMS insert dimensions for mold Design 2 - the insert length was shortened to match the shorter well dimensions after removal of inner posts. (I) Perspective view of CAD model of plastic mold Design 3, intended to completely replace posts with the insert. This is the negative of what PDMS wells would look like. A cutaway view of the dotted black rectangle shows (J) Side view of Design 3 where green arrows point out what will become PDMS base slits. (K) A C2C12 MIFI created using Design 3. We observed small overhangs of μ tissue formed from seeping into the base slits before the Col I had polymerized and the μ tissue was beginning to slip up the insert (white arrows). Scale bars: C, G - 4 mm. K - 3 mm.

resulting MIFIs appeared to have improved tissue integrity at the attachment sites (Figure 6.2G). After successfully removing the inner posts for Design 2, we wanted to determine if posts were necessary or if the PDMS insert alone was enough of an anchor point on either side of the well for μ tissues to attach and compact without any posts. We developed Design 3 to determine if we could cast μ tissues around the insert alone (Figure 6.2I-J). C2C12 MIFIs attached and compacted with no apparent issues in Design 3, however, we did observe that the well slits for insert placement were wide enough to allow the cell+gel mixture to seep into the slits, which were ~ 1 mm wide, before polymerization had occurred, resulting in small tissue overhangs (Figure 6.2K). We also observed that the μ tissues were able to move up the inserts since there was nothing restricting them to the initial attachment sites after removal from wells (Figure 6.2K). Ultimately, we used PDMS wells with 5 x 10 mm wells and insert slots 500 μ m wide (to prevent μ tissue overhangs) and 3 mm deep (Figure 6.3A-B, D-E). The thin, PDMS insert was designed to have a base to sit flush within the well slit, a 1.5 mm necking region for the cast μ tissue attachment, and a small 3.4x1 mm flap above the attachment region to prevent μ tissue slippage (Figure 6.3C). These inserts were laser-cut from pre-made 127 μ m thick PDMS sheeting, and the final PDMS well with inserts placed in allowed for the base of the inserts to sit flush against the well slit portion (Figure 6.3 F-H).

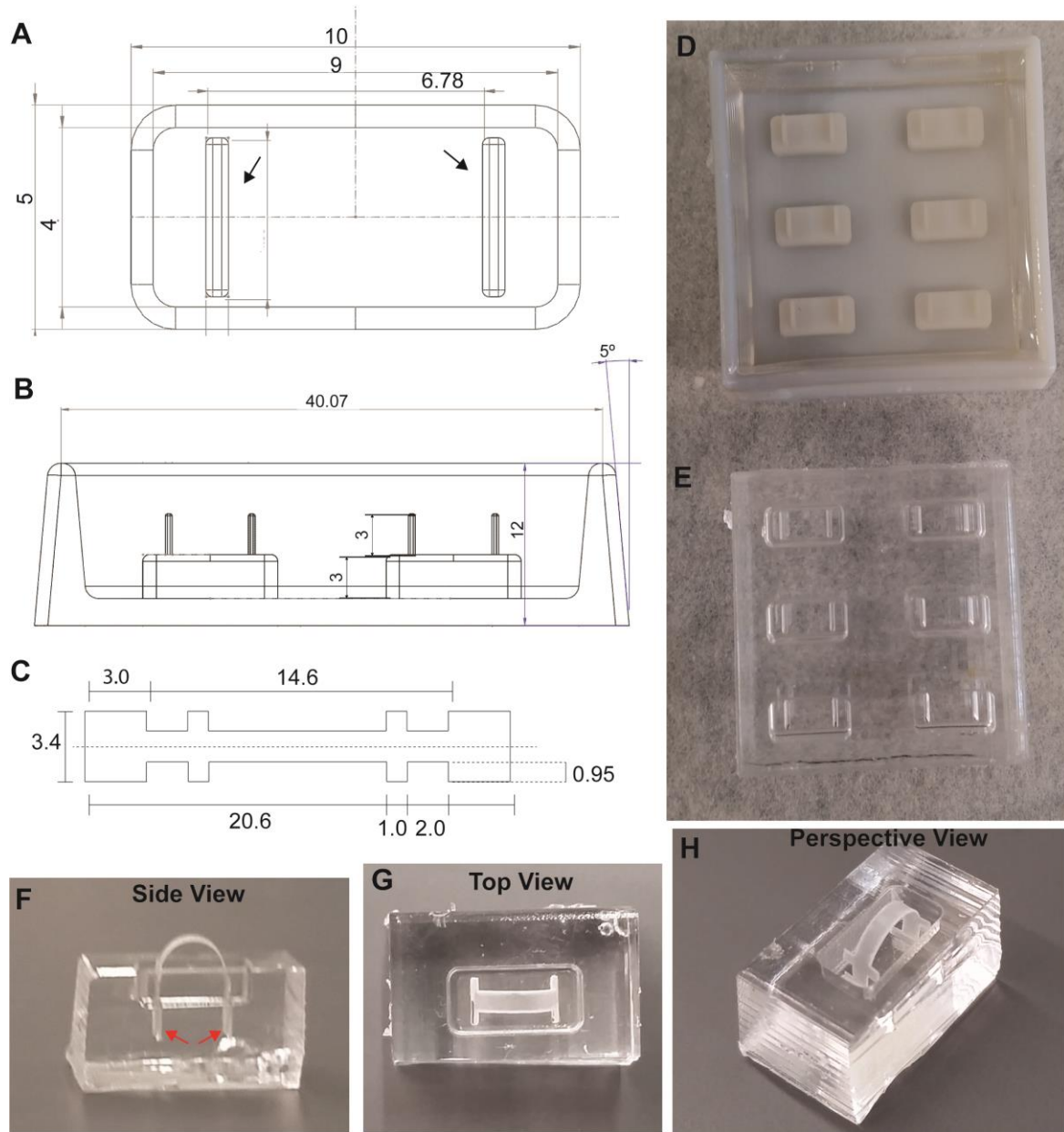


Figure 6.3 Finalized Mold and Insert Design. (A) Top down view of the dimensions of the raised portion of the plastic mold used for casting wells for MIFIs. Smaller rectangles (arrows) served as the insert slots in the PDMS well. (B) The final design had a base with 3 mm deep slots to 'hide' insert base in the PDMS well during culture. (C) Insert design included 3 mm x 3.4 mm regions to be hidden in the PDMS well base, a 1 mm wide necking region for tissue attachment, and a small 3.4 mm wide overhang to prevent the tissue from sliding up the insert. (D) Top down images of the plastic master mold and (E) resulting PDMS wells. (F-G) Side, top, and perspective views of the insert placed in the final well design. The insert can be seen resting flush against the in the PDMS base slits (red arrows). All dimensions are in mm.

6.3.2 Fibroblast Co-culture with HUES9-CM MIFIs

In an initial study to determine if Col I gels with HUES9 derived CMs induced bending of PDMS inserts, μ tissues with CMs only were cast in the prototyped well design and allowed to culture for 10 days after casting (Figure 6.4D). While contraction of MIFIs induced bending of inserts, the CM-only tissues did not significantly remodel the surrounding Col I gel (Figure 6.4H). This was problematic as these μ tissues are diffusion limited to having viable cells within

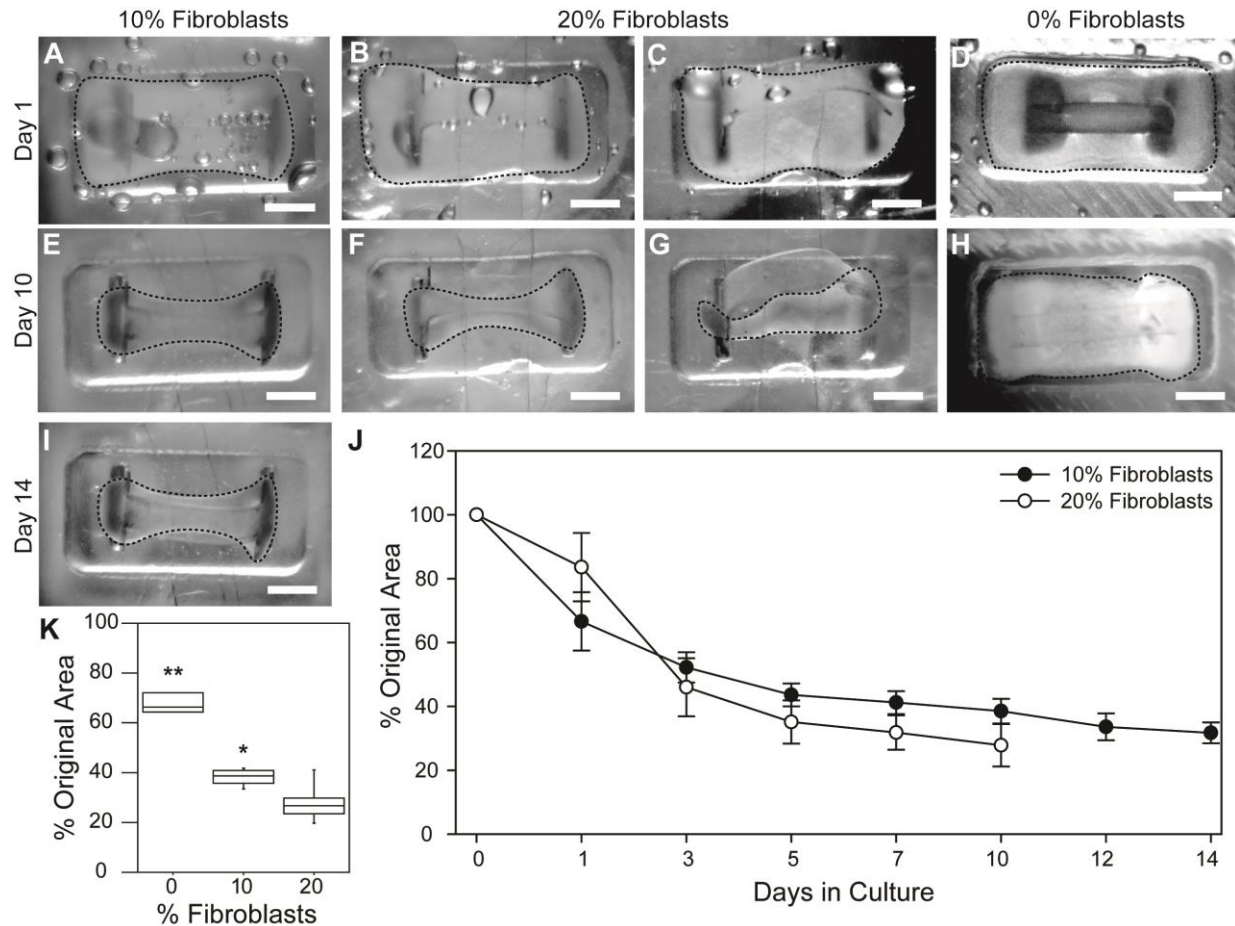


Figure 6.4 Cardiac Fibroblast Coculture is Necessary to Compact 3D Cardiac Microtissues. Day 1 images of constructs cast with HUES9-CMs and (A) 10% FBs, (B-C) 20% FBs and (D) 0% FBs. Day 10 images of (E) 10% FBs, (F-G) 20% FBs and (H) 0% FBs only show visibly more compact tissues in μ tissues seeded with FBs compared to HUES9-CMs only. However, ~30% of μ tissues with 20% FBs exhibit irregular remodeling and break away from the inserts as seen in (G). (I) 10% FB μ tissues continue to uniformly compact at day 14 in culture. (J) Plots of tissue compaction over time, as represented by % original area, show that both 10% and 20% FB tissues have slowed compaction rates after the first 3 days in culture. μ tissues with 20% FBs have less uniform compaction compared to 10% FB tissues, as shown by larger standard deviation bars associated with these tissues. (K) Day 10 of compaction area, as represented by percent of original area, is significantly affected by the addition of FBs. ** = $p < 0.05$ compared to 10 and 20% FBs; * = $p < 0.05$ compared to 20% FBs. 0% FBs: $n = 5$; 10% FBs: $n = 27$; 20% FBs: $n = 22$. Dotted black lines outline the μ tissues. Scale bars 2 mm.

the outer 100 μm of gel, and the initial tissue dimensions ($\sim 1 \times 10 \times 5 \text{ mm}$) were an order of magnitude outside of the diffusion limits of non-vascularized tissues.

In order to engineer more cell-dense MIFIs that compacted over time, we added cardiac ventricular FBs to assist the CMs in remodeling the surrounding Col I+Matrigel™ mixture, a method that had been previously shown to work in 3D engineered cardiac muscle. FB populations used in the literature were derived from varying sources and may behave differently than the commercially available FBs we used, so we added 10% or 20% FBs to MIFIs as ranges of 3% - 30% FBs had been reported as effective¹⁹⁻²¹. We found that the addition of FBs resulted in visual compaction of the MIFIs, and representative images of those with 10% FBs at Days 1, 10, and 14 showed relatively uniform compaction as far as 2 weeks in (Figure 6.4A, E, I). For 20% FB MIFIs, some tissues displayed uniform compaction by Day 10 in culture (Figure 6.4B, F), but as many as 50% of constructs tore due to less uniform compaction by the higher FB population (Figure 6.4C, G). We tracked the compaction area of these tissues from Day 0, when all wells were 100% filled (by area), to Day 10 or 14, depending on FB composition. We found that both FB concentrations resulted in compaction to $\sim 50\%$ of initial area by Day 3 after casting (10% FB - 52.2%, 20% FB - 46.0%) (Figure 6.4J). By Day 10, 20% FB MIFIs had compacted to $\sim 10\%$ less area ($27.8\% \pm 6.62$) than 10% FB MIFIs ($38.5\% \pm 3.88$), but as previously mentioned, these tissues were less uniformly compacted. 10% FB MIFIs, were easily maintained in culture for at least 14 days, when they reached $31.7\% \pm 3.26\%$ of their original area (Figure 6.4I-J). Thus, while 20% FB MIFIs were significantly more compacted by Day 10 than the 10% and 0% FB MIFIs, the compaction was less predictable and often resulted in up to 50% sample loss due to breakage (Figure 6.4K). The 10% FB MIFIs were able to compact significantly more

than 0% FB MIFIs (Figure 6.4K) and were able to be maintained for longer culture times due to more uniform compaction by the smaller FB population.

6.3.3. Immunofluorescence Staining of Microtissues with Integrated Force Indicators

MIFIs with 10% and 20% FBs were fixed and stained for sarcomeric α -actinin, F-actin, and nuclei to qualitatively observe if more spread, striated CMs were observed as length of culture time increased (Figures 6.5 and 6.6). Generally, 10% FB MIFIs appeared to have more spread cells at all time points compared to 20% FB MIFIs, as observed by F-actin staining across

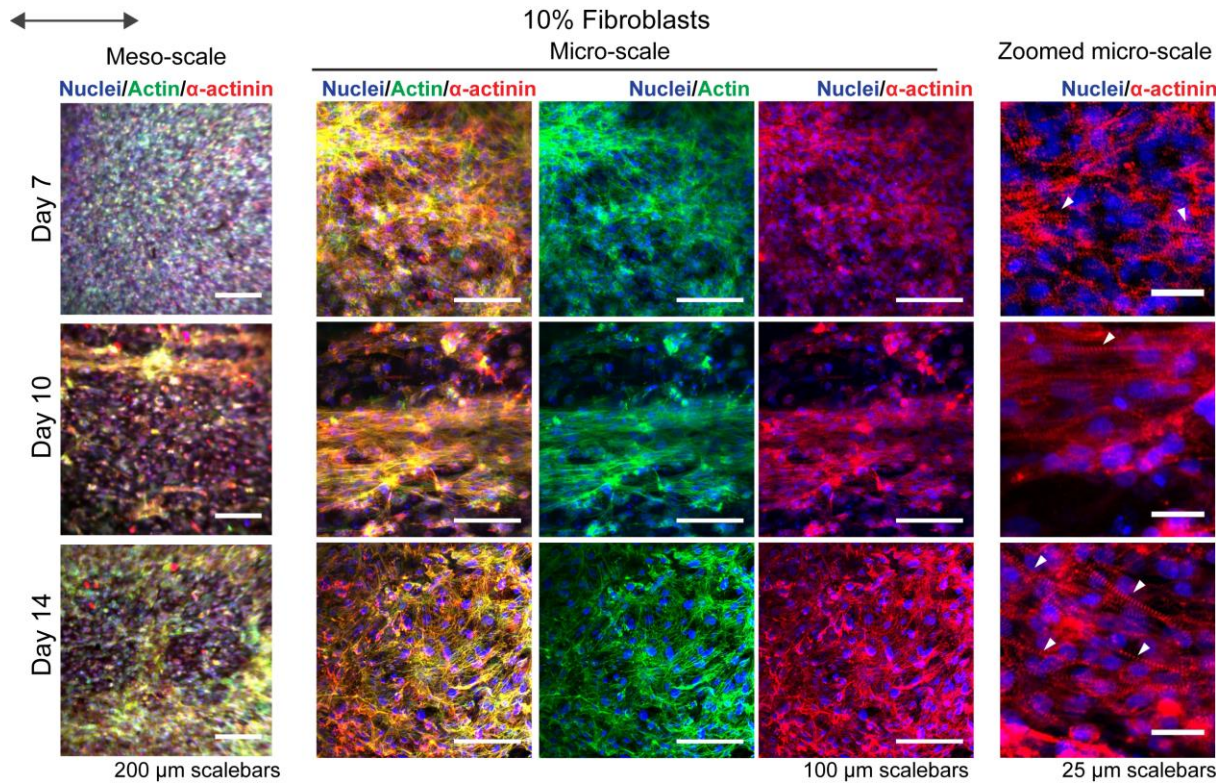


Figure 6.5 Representative Immunofluorescence Staining of Cardiac Microtissues with 10% Fibroblasts. Meso-scale images of CM μ tissues with 10% FBs stained for nuclei, actin, and sarcomeric α -actinin appear to show increased cell spreading as tissues were kept in culture over longer periods of time. Representative microscale images of features of the same tissues show that cells appear well spread for all time points, but the differences observed in meso-scale and microscale images at Day 10 compared to Day 7 and Day 14 may result from remodeling within μ tissues since visible beating was observed in wells beginning around Day 7. Sarcomeric α -actinin staining overlaps with most actin staining, showing that FBs are not overpopulating the μ tissues and CMs were the major cell type at all time points. Finally, zooming in on the microscale images shows striations are present in all of the μ tissues, and they appear to become more organized and uniform over time (white arrows). Black arrows represent long axis of μ tissues.

samples. Additionally, 10% FB MIFIs did not appear to be out-populated by the FB sub-population of cells, as most tissues had cells with well-spread regions of α -actinin throughout, and striations were observed in these CMs as early as 7 days in culture. Tissues appeared to have sarcomeres that were more aligned in the direction of the long-axis of the MIFI as culture time was extended to 14 days (Figure 6.5). 20% FB MIFIs appeared to have less CM coverage until Day 10 of culture, but in these samples, sarcomeres did not appear to organize along the long-axis of the MIFIs as much as was observed in 10% FB MIFIs (Figure 6.6).

The second-harmonic generation of Col I was used to observe the Col I structure in 10%

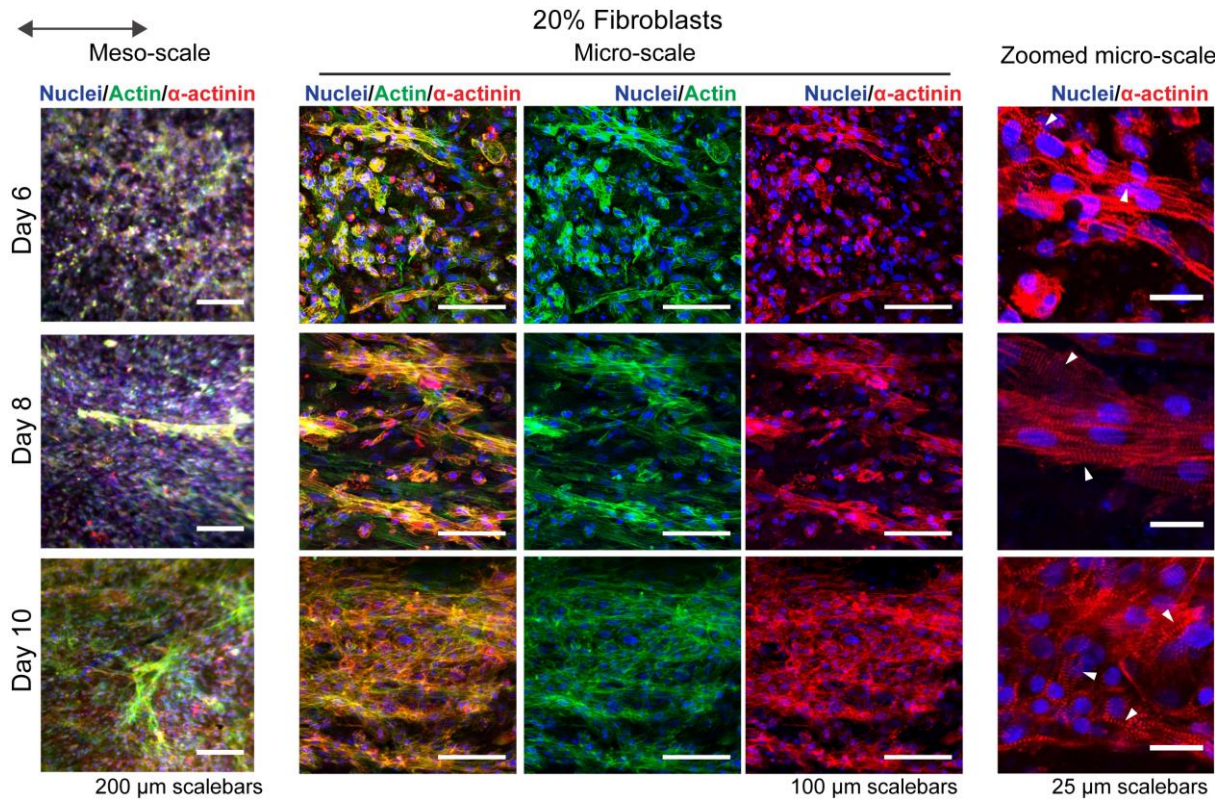


Figure 6.6. Representative Immunofluorescence Staining of Cardiac Microtissues with 20% Fibroblasts. Meso-scale images of CM MIFIs with 20% FBs stained for nuclei, actin, and sarcomeric α -actinin appear to show increased cell spreading as tissues are kept in culture over longer periods of time. Representative microscale images of features of the same tissues show that cells were not as well spread at days 6 and 8 for 20% FB tissues compared to 10% FB tissues at Day 7. Sarcomeric α -actinin staining did not appear as dense at Day 6 and Day 8 tissues compared to Day 7, 10% FB μ tissues. However, zooming in on the microscale images showed striations were present in all of these μ tissues as well (white arrows). Black arrows represent long axis of μ tissues.

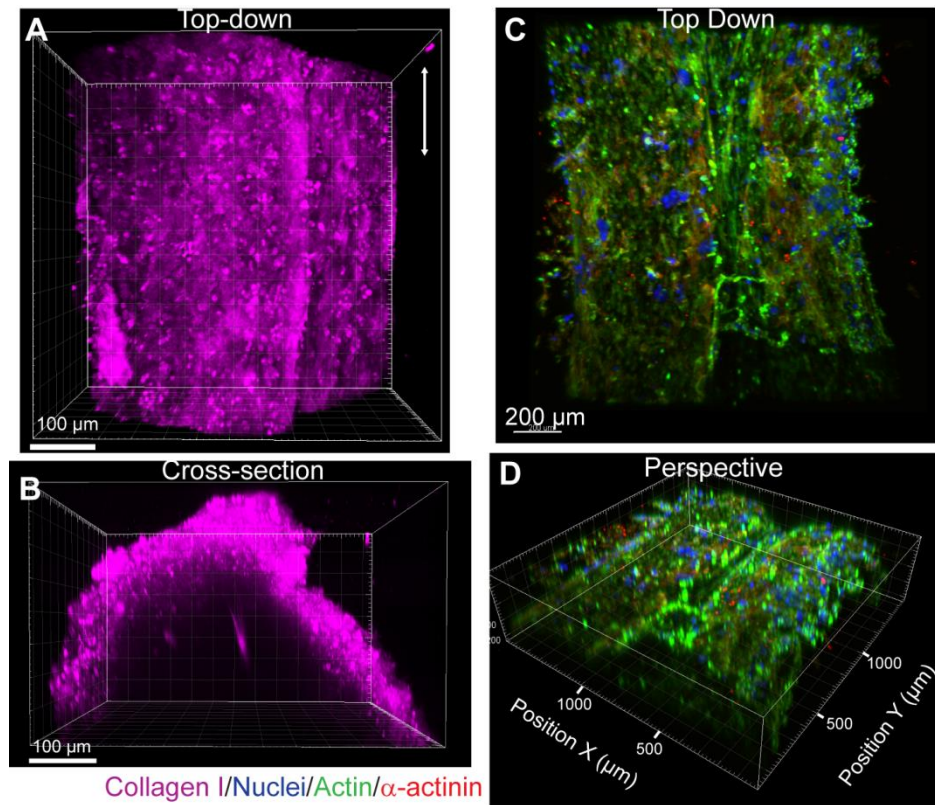


Figure 6.7 3D Collagen I Structure and Cell Organization. (A) Top down image of second-harmonic signal of Col I in fixed tissue with 10% FBs after 10 days in culture shows some alignment in the direction of the long axis of the tissue (represented by white arrows). (B) Cross-sectional view of Col I shows it is more densely packed in the outer 100 μm , likely due to cellular remodeling in this region. The cross section only shows half of the tissue; the Col I and cells caused significant light scattering, and clearing methods will need to be used in the future to analyze full tissue cross-section and structure. (C) Representative top down and (D) perspective images of a day 10, 20% FB tissue stained for nuclei, actin, and α -actinin. A more densely packed middle region appears to be aligning parallel to the long axis of the tissue, resulting in a less elliptical tissue cross-section, a phenomenon observed in several of the 20% FB tissues.

FB MIFIs (Figure 6.7 A-B). The cells and Col I were densely packed in the outer 100 μm of MIFIs, so imaging the Col I structure past 400 μm will not be possible until clearing protocols are implemented to reduce light scattering and allow imaging through the full tissue thickness (Figure 6.7B). Unsurprisingly, cells were generally restricted to the outer 100 μm of the MIFIs

due to diffusion limits in these unvascularized tissues (Figure 6.7 C-D). Interestingly, in several of the 20% FB MIFIs, at Day 10 of culture, the cells remodeled the middle region of the MIFI to be more compact and aligned with the long axis of the MIFI (Figure 6.7 C-D). It is possible that this less-uniform remodeling was also responsible for the breakage of 30-50% of MIFIs/trial that was observed in 20% FB samples.

Overall, striated CMs were found in the MIFIs after Day 6 for both 10% and 20% FB tissues. 10% FB MIFIs appeared to have better spread CMs at later time points and had more evenly distributed CMs at Days 7 and 10 compared to 20% FB MIFIs. Unsurprisingly, tissues had a 'dead zone' 100 μm deep into the tissues, likely because cells migrated to the outer region of the gel and began remodeling from the outside-in. However, more analysis needs to be done on cell-orientation, more precise cell-composition at different time points, and improved clearing or imaging methods must be implemented to further characterize these aspects of the engineered MIFIs.

6.3.4 Microtissues with Integrated Force Indicators Exert Measurable Force and Respond to Drugs in Contractility Assay

Finite element modeling of bending of the thin, PDMS inserts was

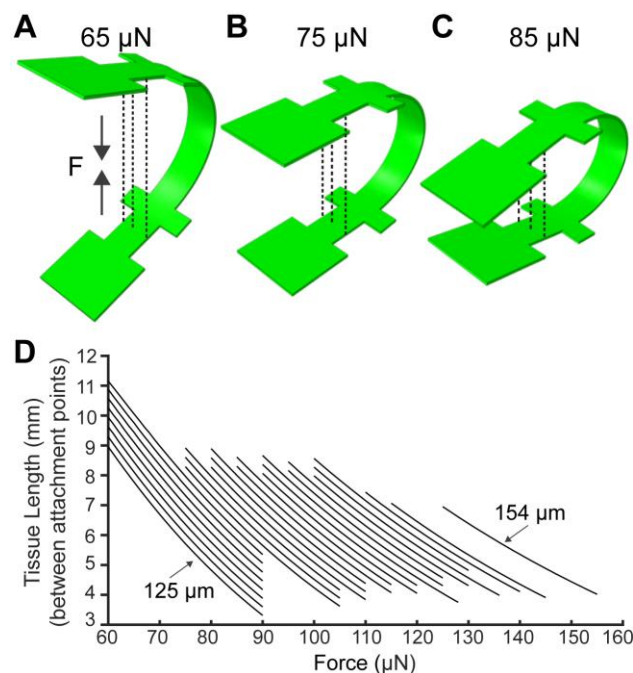


Figure 6.8. Finite Element Modeling of PDMS Insert Bending. Images of finite element modeling of a bending PDMS insert 125 μm thick with the tissue modeled as connectors (dotted black lines) attached to either side of the insert. Images represent insert bending under tissue loads of (A) 65 μN , (B) 75 μN , and (C) 85 μN . (D) Plots of the curves used to generate lookup tables from tissue length. Specifically, tissue length is plotted against and force required to bend the insert to said conformation, and each line represents a separate lookup table for insert thicknesses in 1 μm increments (125 - 150 μm and 154 μm).

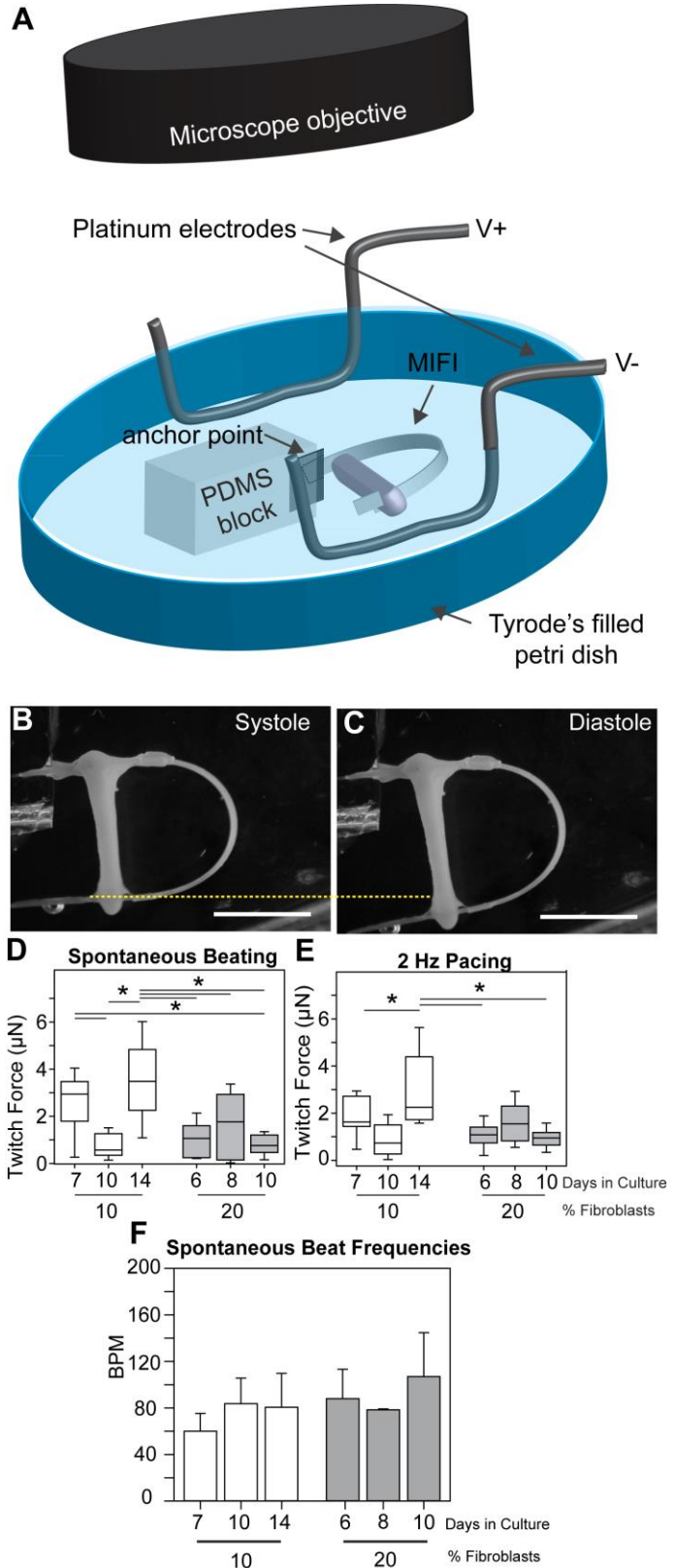
used to generate lookup tables that relate μ tissue length and force required to induce bending of the insert to that conformation (Appendix B). Specifically, the inserts were modeled as having connectors (or the tissue) attached at either side of the necking region of the insert (Figure 6.8A). As the compressive force required to bend the insert increases, the connector (or μ tissue) length decreases (Figure 6.8B-C). In this way, plots of the relationship between μ tissue length and force exerted on PDMS inserts were generated for insert thicknesses ranging from 125 - 154 μ m (Figure 6.8D).

MIFIs were removed from wells for the contractility assay at Day 7, 10, or 14 (10% FBs) or at Day 6, 8, or 10 (20% FBs). By tracking the change in tissue length of beating MIFIs, we calculated force generated by these μ tissues using force lookup tables. MIFIs were removed from wells, one side of the insert was placed in a slit in a PDMS block to anchor the MIFI for side-on viewing, and the construct was submerged in Tyrode's and placed between two parallel platinum electrodes for later stimulation (Figure 6.9A). MIFIs spontaneously beat, resulting in visible deformation of the PDMS insert when imaged in the side-on contractility assay (Figure 6.9B-C). We found that Day 14, 10% FB MIFIs exerted significantly higher twitch force ($3.62 \pm 1.7 \mu$ N) compared to 20% FB tissues at Days 6, 8 and 10 ($1.03 \pm 0.70 \mu$ N, $1.65 \pm 1.4 \mu$ N, and $0.82 \pm 0.45 \mu$ N respectively) (Figure 6.9D). These tissues also beat with higher twitch force than Day 10 MIFIs with the same FB percentage ($0.773 \pm 0.55 \mu$ N) (Figure 6.9D). Interestingly, Day 7 MIFIs with 10% FBs also exerted higher twitch forces ($2.44 \pm 1.3 \mu$ N) than Day 10 MIFIs with 10% or 20% FBs. It is possible that this decrease in contractility at Day 10 was a result of remodeling in these tissues around Day 10, something that was reflected in the fluorescence staining as well (Figures 6.5 and 6.6). Because MIFIs began visibly beating in the wells by Day 7, it is possible that this induced the CMs and FBs to remodel the surrounding matrix at a

mesoscopic level. However, more analysis of tissue composition and organization at each time point will need to be performed in addition to contractility analysis to better understand the morphological changes that occurred as these cardiac MIFIs matured over time. Tissues also responded to electric field stimulation and were capable of being electrically paced. When twitch forces of MIFIs paced at 2Hz were measured, we found that Day 14, 10% FB MIFIs exerted higher twitch force ($3.07 \pm 1.54 \mu\text{N}$) compared to Day 6, 8, and 10 MIFIs with 20% FBs ($1.08 \pm 0.52 \mu\text{N}$, $1.61 \pm 0.89 \mu\text{N}$, and $0.93 \pm 0.426 \mu\text{N}$) (Figure 6.9E). It appeared that, overall, 20% FB MIFIs did not exert as much force as 10% FB MIFIs. In part, this is due to earlier testing dates of the 20% tissues because these tissues were not able to be stably maintained in culture as long as the tissues with 10% FBs. Thus, these MIFIs had less time to mature and reorganize matrix, and it is also possible that the FBs in these tissues overpopulated the MIFIs and prevented CMs from synchronizing throughout the tissue. Constructs at all time points were assessed for spontaneous beat frequencies which ranged from $60 \text{ BPM} \pm 15$ (10% FB, Day 7) to $107 \text{ BPM} \pm 38$ (20% FB, Day 10) (Figure 6.9F). However, no significant differences were found between groups since MIFIs at these time points native beat frequencies are still variable, something that had been observed in individual wells of differentiating CMs as well.

Figure 6.9. Measuring Force Generation and Drug Response of Cardiac MIFIs. (A)

Schematic of the side-on contractility assay for MIFIs. The microscope objective views the top of the set up. The MIFI is placed on its side, with one insert anchored in a slit in a PDMS block glued to the bottom of the petri dish. The MIFI is submerged in Tyrode's and placed between two parallel platinum electrodes for electrical pacing. Side on images of cardiac MIFIs in the contractility assay in (B) systole and (C) diastole, with the yellow dotted line showing the change in tissue length. Scale bars 4 mm. (D) Twitch forces (systole-diastole) for spontaneously beating μ tissues showed that 10% FB μ tissues at Day 14 had significantly higher twitch forces than Day 10 samples with 10% FB and 20% FB samples at all time points. Day 7, 10% FB tissues also had significantly higher spontaneous twitch force than Day 10 samples with 10% or 20% FBs. (E) Twitch forces for electrically paced (2 Hz) samples showed similar trends, with Day 14, 10% FBs exerting significantly higher twitch force than Day 10, 10 and 20% FBs and Day 6, 20% FB samples. Twitch force appears to decrease slightly upon electrical stimulation, but variation in resulting forces decreases. * = $p < 0.05$. (F) Spontaneous beat frequencies (in BPM) of cardiac μ tissues with 10% or 20% FBs analyzed at Day 7, 10, 14 or Day 6, 8, and 10 in culture, respectively. No statistically significant differences were found among samples with $n \geq 3$, with mean values ranging from 60 to 107 BPM (Day 7, 10% FBs and Day 10, 20% FBs, respectively). (D) 10% FBs: Day 7, $n = 15$; Day 10, $n = 35$; Day 14, $n = 25$. 20% FBs: Day 6: $n = 10$, Day 8, $n = 10$; Day 10, $n = 30$ (E) 10% FBs: Day 7, $n = 10$; Day 10, $n = 35$; Day 14, $n = 25$. 20% FBs: Day 6: $n = 10$, Day 8, $n = 10$; Day 10, $n = 30$ (F) 10% FBs: Day 7, $n = 3$; Day 10, $n = 8$; Day 14, $n = 8$. 20% FBs: Day 6: $n = 3$, Day 8, $n = 2$; Day 10, $n = 14$.



Example force vs. time plots of a Day 14, 10% FB MIFIs demonstrate a regular beat frequency and the ability to electrically pace the samples at 2 Hz (Figure 6.10A). Titrating in isoprenaline, an excitatory drug, had the intended stimulatory effect on the native beat frequency of MIFIs at 500 nM and 5 μ M (Figure 6.10B-C), but it did not interrupt the ability to electrically pace the constructs at these concentrations. The addition of isoprenaline did not noticeably affect the twitch force of this specific MIFI at these concentrations, which exerted twitch forces \sim 4.6 μ N when beating spontaneously in Tyrode's and \sim 4.0 μ N when beating spontaneously in 5 M isoprenaline. Washing out the isoprenaline dosage with Tyrode's recovers the MIFI to its initial beat frequency (Figure 6.10D). Subsequent treatment with 5mM caffeine also increased the spontaneous beat frequency with minimal impact on the twitch force, and dosing with the muscarinic agonist, carbachol, reduced the spontaneous beat frequency while having surprisingly little impact on twitch force (Figure 6.10E-F).

While most MIFIs beat more synchronously as culture time increased, occasionally “disease-like” arrhythmic beating was observed in these Day 14 constructs (Figure 6.10G). While this “disease-like” construct was still able to be electrically paced (Figure 6.10G), its’ native and paced beating plots of force reflect the abnormal beating, especially when compared to more synchronous constructs (Figure 6.10A). To determine if the MIFI could recover to a more normal beating phenotype, increasing carbachol doses were administered (500 nM, 5 μ M, and 50 μ M) and resulted in improvement in the spontaneous beat frequency of the constructs, but the twitch force profiles were still \sim 30% the strength of the twitch force of synchronous constructs (Figure 6.10H). We then electrically paced the arrhythmic construct at doses of 5 μ M and 50 μ M of carbachol. Unlike electrical stimulation of the construct with no drug treatment

(Figure 6.10G), the combinatorial effect of carbachol treatment with electric pacing at 2 Hz resulted in significantly higher twitch forces and a normal phenotype beating waveform was observed (Figure 6.10I). More interestingly, a significant interaction between the stimulation and drug treatment was found during 2-way ANOVA analysis of twitch force under these conditions (Figure 6.11A). 2-Hz pacing significantly increased twitch force, with or without drug treatment, and pacing coupled with 5 or 50 μ M carbachol resulted in 2.5x and 2.8x stronger twitch contractions (Figure 6.11A).

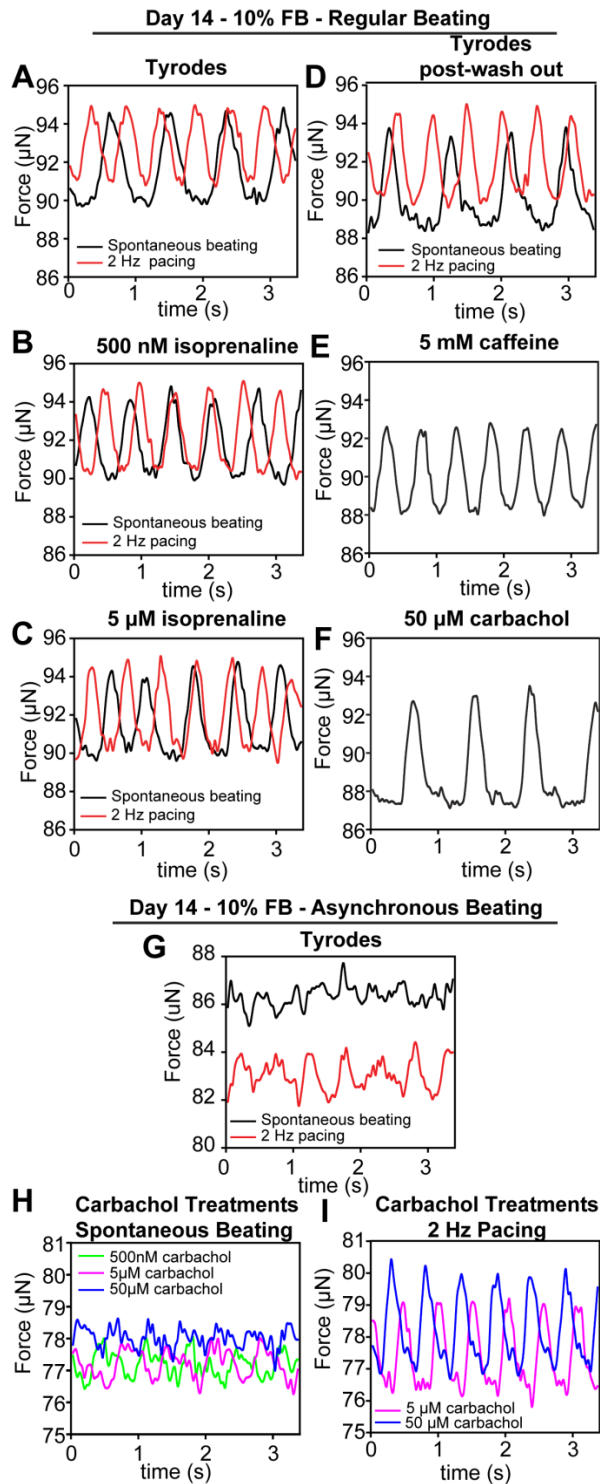


Figure 6.10. Force Plots of Day 14, 10% Fibroblast Constructs. (A) Spontaneous beating of a MIFI sample with consistent beat pattern and plot of 2-Hz paced force generation showed ability to pace the MIFI. (B) The addition of isoprenaline (500nM final concentration) increased the beat frequency, but had little affect on the spontaneous or paced force generation. (C) Increasing isoprenaline concentration to 5 μM resulted in slightly less regular beat frequency, as shown by the force plot. (D) Washing the construct with Tyrode's after isoprenaline treatment appeared to recover the tissue's native beat frequency. (E) Addition of 5mM caffeine increased the spontaneous beat frequency of the construct, while (F) addition of 50 μM of carbachol appeared to reduce beat frequency and return the MIFI closer to baseline twitch force. Overall twitch force of this construct did not appear affected by drug treatments at these concentrations. (G-I) Force/time plots of an irregularly beating Day 10, 10% FB construct. Pacing appeared to slightly improve the beat frequency of the construct. (H) Addition of the cholinergic agent carbachol in increasing doses (500 nM, 5 μM , 50 μM) appeared to improve the spontaneous beat frequency of this construct, but the spontaneous beats still appeared somewhat asynchronous. (I) Pacing of the construct at 5 and 50 μM carbachol, however, had a visible effect on the synchronous beating of this construct.

Additional analysis of specific specimens of Day 14, 10% FB MIFIs showed decreasing twitch force as stimulatory drug dose was increased. Specifically, one MIFI exerted $3.54 \mu\text{N} \pm 0.12$ spontaneous twitch force and $3.34 \mu\text{N} \pm 0.935$ twitch force under 2 Hz pacing with no drug treatment (Figure 6.11B). Dosing with 500 nM isoprenaline resulted in a drop to ~80% of initial twitch force to $2.85 \mu\text{N} \pm 0.84$ and $2.81 \mu\text{N} \pm 0.71$ for spontaneous and 2 Hz paced beating, respectively (Figure 6.11B). Increasing drug dosage to 5 mM resulted in an even further decrease ($1.78 \mu\text{N} \pm 0.21$) to ~50% of initial twitch strength, and electric pacing at 2 Hz was unable to recover full twitch strength ($2.15 \mu\text{N} \pm 0.33$) (Figure 6.11B). Epinephrine treatment of a separate MIFI construct also resulted in a dose-dependent decrease in twitch force (Figure 6.11C). Specifically, during spontaneous beating, no drug treatment and 500 nM drug treatment resulted in $5.93 \mu\text{N} \pm 0.44$ and $5.49 \mu\text{N} \pm 0.25$ twitch force respectively. These values dropped to 66% and 61% of the initial twitch force at 5 μM and 50 μM epinephrine doses (Figure 6.11C). Interestingly, two-way ANOVA analysis found that, the effect of electrical stimulation was significantly higher only as dosage of epinephrine increased (Figure 6.11C). The twitch forces at 5 μM and 50 μM were significantly recovered by electrical pacing back to 85% and 80% of initial twitch force, respectively. While it is not initially intuitive that some stimulatory drugs resulted in decreasing twitch force as dosage increased, it is possible that this was a result of increased beat frequency of the constructs, resulting in an increase diastolic force between beats. This hypothesis is also supported by the evidence that pacing constructs at 2 Hz significantly improved the twitch force of dosed constructs (Figure 6.11 A,C).

We compared the magnitude change in BPM, and normalized each MIFI to its native beat frequency due to the wide range of beat frequencies we observed in all constructs. When we dosed MIFIs with increasing concentrations of isoprenaline, we found that constructs beat at

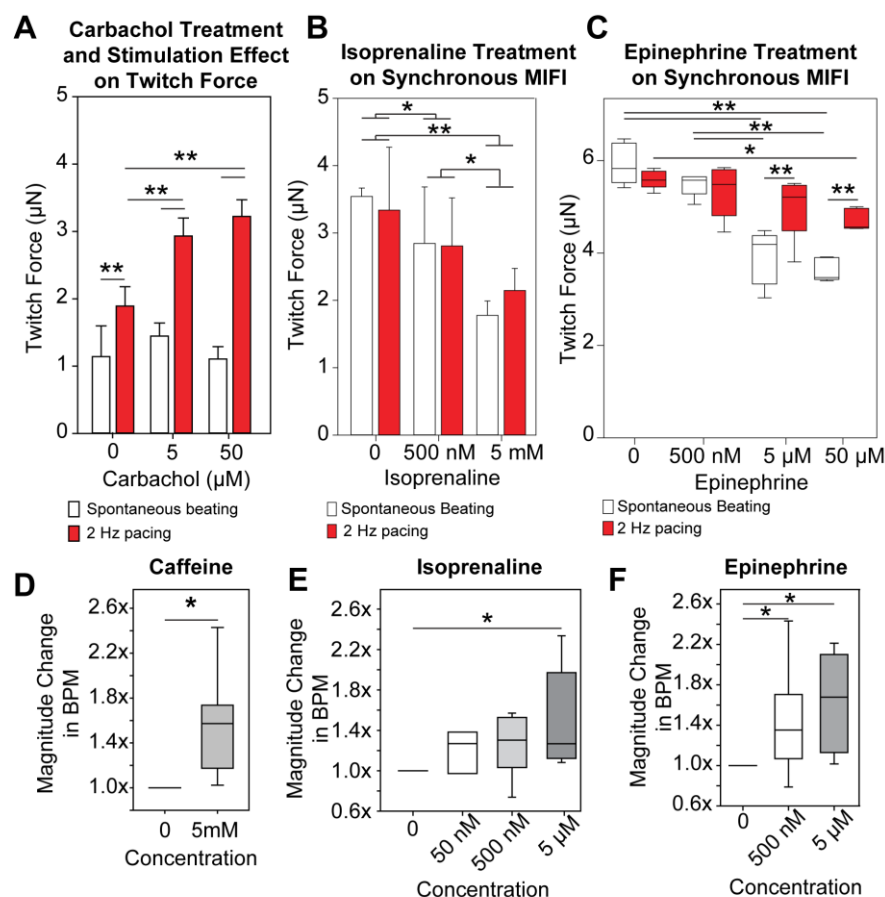


Figure 6.11 Cardiac Microtissues Twitch Force and Beat Frequency Response to Stimulatory Drugs.

(A) Two-way ANOVA analysis of drug-treatment of the arrhythmic tissue from (Figure 5.8G-I) showed an interaction between carbachol dose and 2-Hz electric pacing. Twitch force resulting from pacing the construct was significantly higher than native beat frequency within the same drug treatment group, and carbachol dose paired with 2-Hz pacing resulted in significantly higher twitch force compared to no-drug with electrical pacing. (B) Two-way ANOVA analysis showed that drug treatment significantly affected twitch force, but there was not an interaction between stimulation and drug treatment. Overall, isoprenaline treatment of a MIFI resulted in gradual decrease of overall twitch force. (C) Two-way ANOVA analysis determined that the effect of stimulation on twitch force was dependent upon the level of epinephrine treatment. Overall, epinephrine treatment resulted in significant decrease in twitch force, with 5 μM and 50 μM dosings resulting in a drop to 61% - 66% of initial, spontaneous twitch force. (D-F) Plots of the change in beat frequencies as a response to drug stimulation, normalized to each μtissue's initial beat frequency. (D) Isoprenaline dosing resulted in a gradual increase in BPM compared to initial beat frequency at 50 nM (1.21x initial), 500 nM (1.26x initial), and a statistically significant increase at 5 μM (1.48x initial). (E) Epinephrine dosing resulted in a significant increase in BPM compared to initial beat frequency at 500 nM (1.42x initial) and at 5 μM (1.65x initial). (F) Caffeine dosing at 5 mM also significantly increased beat frequency to 1.59x initial beat frequency. (A-C) Results are from 3 separate constructs. (A) Spontaneous beating: no carbachol, n = 7; 5 μM carbachol, n = 4; 50 μM carbachol, n = 6. 2 Hz pacing: no carbachol, n = 6; 5 μM carbachol, n = 5; 50 μM carbachol, n = 6. (B-C) n = 5 (D) no drug: n = 9, 50 nM: n = 3; 500 nM: 9; 5 μM: n = 7 (E) n = 8 (F) n = 7. Reported values are means; box plots show median values with quartile ranges for data was not normally distributed. * = p < 0.05.

** = p < 0.001

1.21x \pm 0.2, 1.27x \pm 0.10, and 1.48x \pm 0.47 initial beat frequency for 50 nM, 500 nM, and 50 μ M treatments, respectively (Figure 6.11E). Epinephrine dosing similarly affected MIFI beating frequencies by raising it to 1.42x \pm 0.51 and 1.65x \pm 0.47 initial BPM (Figure 6.10F). Finally, caffeine dosing at 5mM significantly increased BPM to 1.59x \pm 0.451 initial BPM (Figure 6.10D). Thus, we successfully engineered a cardiac μ tissue by co-culturing HUES9-CMs and FBs and integrating a U-shaped PDMS insert, and we demonstrated that MIFIs induced visible bending of the insert and responded as expected to pharmacological stimuli.

Additionally, further characterization of MIFIs is necessary to calculate the force measurements per cross-sectional area of the full tissue section as well as the muscle-only cross-section, a step that is necessary to determine if the actual muscle cells in specific tissues are stronger at specific time points. However, we measured average tissue width and thickness to approximate an ellipsoidal cross-section to perform initial normalization calculations (Figure 6.12). We calculated the ellipsoidal cross-section by measuring 3 points per construct, and we observed that the distribution of calculated cross-sections had higher variability in the 20% FB constructs, which is reflective of the less-uniform compaction observed in those tissues (Figure 6.12). When we normalized each MIFI to its average ellipsoidal cross-section, we found that D14, 10% FB MIFIs exerted higher specific force (med = 1.1 Pa) compared to 20% FB MIFIs at D6 (med = 0.45 Pa), D8 (med = 0.56 Pa) and D10 (med = 0.29 Pa) and compared to D10, 10% FB MIFIs (med = 0.30 Pa) (Figure 6.13A). We also calculated that D7 10% FB MIFIs exerted higher specific twitch force (med = 0.85 Pa) compared to D10 MIFIs for both 10% and 20% FB constructs (Figure 6.13A). To further approximate the actual force per muscle cross-section, we assumed that the outer 100 μ m of MIFIs contained cells, based on initial imaging and the diffusion limits of non-vascularized tissues. We also assumed that this outer, cell-containing

region was composed of 90% CMs for 10% FB constructs and 80% CMs for 20% FB constructs to calculate the normalized force per muscle cross-section. These assumptions were made with the intent of over-estimating the actual muscle cross-sectional area to prevent over-estimating the specific force of the CMs. We found that, using these approximations, D14 10% FB MIFIs exerted significantly higher specific force per CM area (med =

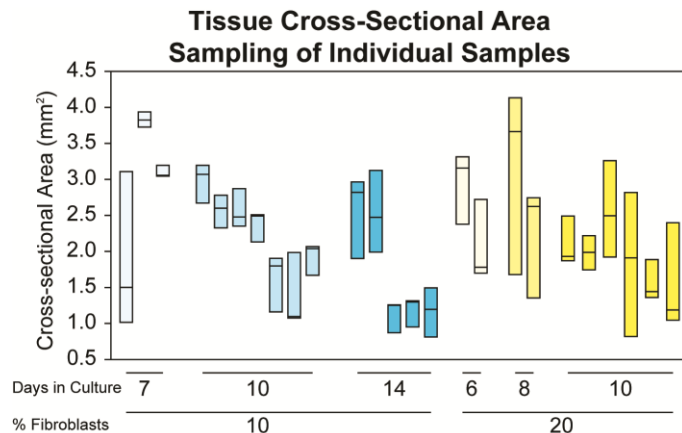


Figure 6.12. Approximate Microtissue Cross-sectional Area Per Sample. The thickness and width of MIFIs were measured at 3 separate points per tissue - the middle and at either end near insert attachment sites - to approximate cross-section by calculating tissue cross-section to be ellipsoid in shape. Overall, MIFIs compacted to smaller cross-sectional areas with increased time in culture. 20% FB MIFIs exhibited higher variability in cross-sectional area compared to 10% FB tissues. Overall cross-sectional area ranged from approximately 1- 4 mm². Bars represent individual MIFIs; n = 3 per sample.

12.0 Pa) compared to D6 and D10 20% FB MIFIs (meds = 4.8 Pa and 3.7 Pa, respectively) and compared to D10 10% FB MIFIs (med = 1.9 Pa) (Figure 6.13B). We also found that D7 10% FB MIFIs exerted higher forces per approximated muscle cross-section (med = 9.4 Pa) than D10 10% FB constructs (Figure 6.13B). This dip in force at D10 for 10% FB constructs may have occurred because of tissue remodeling and cell reorganization that occurred after CMs began to visibly deform the inserts in the wells after Day 7. More importantly, these approximations to normalize force for tissue cross-section and CM cross-section still exhibit that constructs are stronger by D14 of culture, and 10% FB constructs have more uniform remodeling compared to 20% FB constructs.

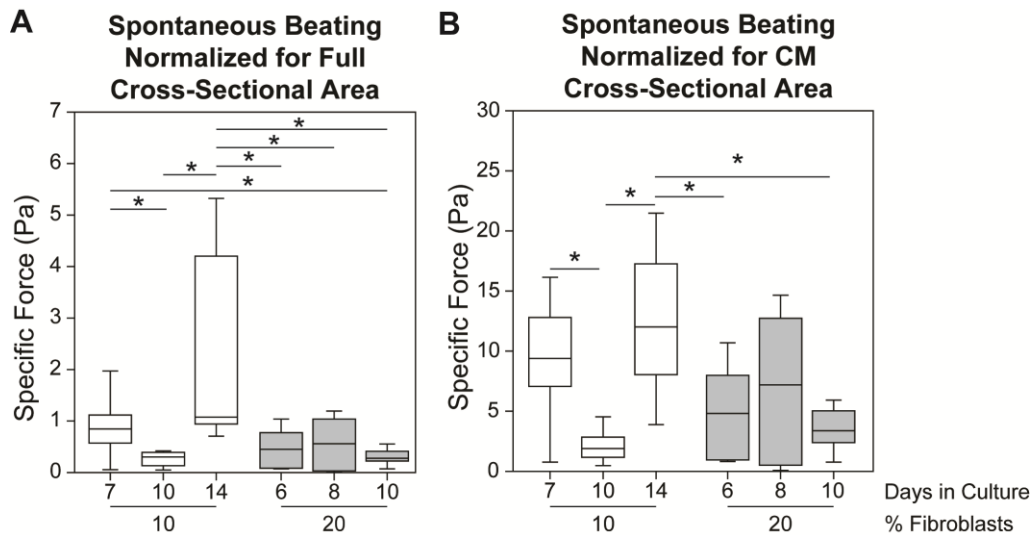


Figure 6.13. Twitch Force Normalized for Approximate Microtissue and CM Area. (A) Twitch force was normalized for full MIFI cross-sectional area, as approximated by assuming an ellipsoidal cross-section and measuring width and thickness of individual samples. Day 14, 10% FB MIFIs exerted higher specific twitch force (1.1 Pa) compared to all 20% FB MIFIs (D6 = 0.45 Pa, D8 = 0.56 Pa, and D10 = 0.28 Pa) and compared to D10, 10% MIFIs (0.30 Pa). D7, 10% FB MIFIs also exerted higher specific twitch force (0.85 Pa) compared to D10 MIFIs with both 10% and 20% FBs. **(B)** Twitch force was also normalized for approximate muscle cross-sectional area by assuming contractile cells only resided within the outer 100 μ m of MIFIs, and assuming that CM populations remained at 90% and 80% of total cell population. These results showed that D14, 10% MIFIs exerted higher specific twitch force (12 Pa) compared to D6 and D10, 20% MIFIs (4.8 Pa and 3.4 Pa, respectively) and compared to D10, 10% FB MIFIs (1.9 Pa). D7, 10% MIFIs also had higher specific twitch force (9.4 Pa) compared to D10, 10% FB MIFIs. Values are reported as medians. 10% FBs: Day 7, n = 15; Day 10, n = 35; Day 14, n = 25. 20% FBs: Day 6: n = 10, Day 8, n = 10; Day 10, n = 30

6.4 Discussion and Conclusions

In this chapter, we designed a 3D platform to study the compaction, contractility, and beating behavior of cardiac μ tissues composed of Col I, Matrigel, HUES9-CMs and cardiac FBs. PDMS wells and inserts enabled casting of 3D muscle tissues around attachment sites at either end of the flexible, PDMS insert, maturation of constructs for at least 2 weeks in culture, and easy removal of MIFIs from the wells to test the contractility and beat frequency as well as probe their response to specific pharmacological stimulation. This platform design will allow for

future studies to examine how *in vitro* exercise, as in removal of MIFIs from culture wells to load μ tissues with the full unfolding force of the deformed insert, affects the strength and contractility of both cardiac and skeletal muscle platforms. This platform can serve as a template for engineered skeletal muscle studies as well, and we hope to incorporate patient-specific induced pluripotent stem cells (iPSCs) into this format to develop patient specific treatments and disease models. We have sent the PDMS wells and inserts to our collaborators in the Van Der Meer lab at the University Medical Center Groningen, and they have reported successful incorporation of patient-derived iPSCs into our designed MIFI format. Future work will include force and beat frequency analysis of these patient-specific MIFIs and development of disease-model MIFIs from patients treated at that facility that have specific genetic mutations that manifest as heart disease.

In initial prototypes of these engineered constructs, we used pure HUES9-CM populations, but found that constructs with CMs only were unable to significantly remodel and compact the surrounding Col I/Matrigel matrix to result in cell-dense, synchronous cardiac μ tissues (Figure 6.4H,K). In addition to being problematic for CM synchronicity from cell-cell gap junctions, we wanted μ tissues to compact further to reduce the cell-free 'dead zone' that often occurs in engineered tissue constructs due to the lack of a blood vessel network and subsequent restriction of viable cells to the first 100 μ m of constructs due to diffusion limits for exchange of nutrients and waste. Based on previous studies, we wanted to incorporate a small sub-population of FBs in order to condense the matrix and increase CM spreading^{19, 21}. Because each FB population is likely to behave differently, and matrix compaction is dependent on Col I and Matrigel concentrations, which often differ lab to lab, we tested 10% and 20% FB constructs since 3% to 33% percent had been shown to be effective in other studies¹⁹⁻²¹. We found that the

particular population of cardiac ventricular FBs in 2.5 mg/mL Col I compacted MIFIs less uniformly when the initial population was 20% FBs, but 10% FB sub-populations were maintained in culture and studied for at least 2 weeks. Up to 50% of 20% FB MIFIs were unable to be maintained by Day 10 of culture due to tearing away from insert attachment sites caused by uneven matrix remodeling by FBs (Figure 6.4G). Because these μ tissues began visibly beating in the wells and effectively exercising against the inserts at this time point, increased culture time was shown to be effective in engineering stronger μ tissues (Figure 6.9C-D). Ongoing studies not included in this chapter have shown that we can keep these 10% FB MIFIs in culture at least 4 weeks after the initial seeding date, so future studies will examine twitch force and drug response of constructs at these 2, 3, and 4 week time points.

To further characterize the cell-subpopulations of these tissues and assess the full cross-sectional area of constructs, further imaging and image analysis must be done. While we can observe that constructs have not compacted enough to completely eliminate a cell-free 'dead zone', we also are limited to observing the first 500 μ m of MIFIs due to severe light scattering of these more cell-dense constructs (Figure 6.7). Future work will include clearing tissues for better visualization during fluorescence microscopy as well as tissue histological sectioning to visualize muscle and gel cross sections. However, we were able to observe that CMs exhibited striations in all 10% and 20% FB constructs (Figures 6.5 and 6.6). Interestingly, it appeared that remodeling of the tissues may be occurring between Day 7, when μ tissues begin to visibly beat in the wells, and Day 14, a fact that was mirrored in the observed decrease in twitch force exerted by MIFIs at Day 10 compared to Day 7 and Day 14 constructs with 10% FBs (Figures 6.5, 6.6, and 6.9). Further analysis needs to be done to quantify sarcomere organization as MIFIs mature as well as

to quantify how much of these μ tissues are CMs and what percentage remain fibroblasts or other non-contractile cells.

Despite a limited analysis of exact cell composition, spreading, organization, and remodeling within these MIFIs, we demonstrated that we have engineered cardiac μ tissues that are easily removed from culture wells and that induce deformations in the PDMS inserts to allow optical measurement of twitch forces of these μ tissues in a side-on contractility assay. We have showed that twitch force of these MIFIs typically fell in the 1- 7 μ N range, and full systolic force in the range of 80 - 100 μ N (typically dependent on insert thickness). Further analysis of the full muscle layers within these μ tissues is necessary to normalize force to twitch stress to determine how this system compares to other engineered cardiac muscle models, but we have been able to approximate the specific force of the most mature MIFIs was in the range of 10s of Pa. Other 3D engineered cardiac μ tissues have been reported to exert full systolic force anywhere from 10's or 100's of μ N^{13, 15, 16} to 1's or 10's of mN^{17, 19}, and though it is difficult to compare constructs since these reported forces are not normalized for cell cross-sectional area, our engineered MIFIs are on par with many of other these other *in vitro* cardiac μ tissues in terms of force generation. Additionally, our calculation of force normalized for approximate cross-sectional area of muscle in the range of 10s of Pa. However, native muscle typically generates forces in the range of 1s to 100s of kPa. It is unlikely that CM twitch forces can be at such a low specific force and still induce visible bending of the PDMS inserts, but there are several factors that may explain this discrepancy 1000x off of the expected measured forces. It is possible that 1) the lookup tables derived from the finite element model may have small errors that need to be addressed, or 2) the Col I hydrogel is restricting full contraction of the CMs and the resulting measurements are not reflective of full cell force due to hindrance by the ECM hydrogel. Further analysis into the

assumptions made in developing the finite element model need to be investigated to determine if this is the root of the problem, if the Col I matrix is limiting full contractions, or if these engineered tissues are a few orders of magnitude weaker than native muscle. These initial studies showed that longer culture time resulted in stronger muscle, future work will examine if culture time of 4 weeks results in specific force closer to the kPa range. We also hypothesize that removal of these MIFIs from culture wells to allow isotonic contraction rather than more isometric-like contractions MIFIs are restricted to in culture wells will result in significantly stronger engineered muscle. Future experiments will determine if this hypothesis proves true. Finally, MIFIs had spontaneous beat frequencies slightly higher (60 - 110 BPM) than other engineered cardiac tissues, which typically range from ~30 BPM^{13, 16} in CM only constructs ~to 60 BPM^{20,21} in constructs co-cultured with FBs. The higher range of beat frequencies was typically observed in 20% FB tissues (Figure 6.9E), and thus may have been a result of less synchronization in these MIFIs with higher FB populations, but further studies on conduction velocity of these tissues will be necessary to determine if this is the cause of higher beat frequencies.

We also demonstrated that MIFIs responded as expected to the stimulatory drugs epinephrine, isoprenaline, and caffeine (Figures 6.10 and 6.11). Specifically, we saw significant increases in BPM for the tissues when increasing doses of these drugs were administered^{4, 21}. We did observe some discrepancies compared to what was expected based in literature, as increased epinephrine and isoprenaline dosing decreased the twitch force of some MIFI constructs. While this was recoverable in the case of epinephrine (Figure 6.11C), isoprenaline dosing resulted in significant twitch force decrease that was not recovered by controlling the MIFI beat rate by 2 Hz electric pacing (Figure 6.11B). However, we were demonstrating these tissues show a dose

dependent response, and many observable increases in twitch force caused by isoprenaline were previously recorded in the 10 - 100 nM range,⁴, concentrations lower than we administered to constructs in this study. Thus, this result may be more attributable to increasing drug dosage to toxic levels, something that these cardiac μ tissue models are designed to detect. We also demonstrated that a case of an asynchronous MIFI could be 'rescued' to a normal beat phenotype by combining carbachol dosing with 2 Hz electric pacing (Figure 6.10G-I, 6.11A). Carbachol has typically been reported to decrease beat frequencies of dosed tissue constructs⁴, so it appears that treating an arrhythmic MIFI while simultaneously pacing, slowed the over-excited tissue and enabled full-tissue depolarization upon stimulation, which initially had insignificant effect on tissue twitch force (Figure 6.11A). While it is problematic that a small percentage of MIFIs exhibited more disease-like states, the nature of the contractility enables easy identification of these 'problem' samples. Additionally, it is promising that in these arrhythmic MIFIs we are able to induce a significant response with drug treatment and pacing, indicating that this design will be useful for modeling both healthy and disease states with patient specific cells in the future.

Future analysis of cardiac MIFIs is required to characterize these cardiac models, in terms of Col I/ECM organization, sarcomere alignment and organization, approximate cell composition, and full μ tissue and muscle layer thicknesses. Future studies will utilize clearing protocols and tissue-sectioning for both fluorescence immunostaining and histological analysis of 10% FB MIFIs at 2, 3, and 4 week time points. Additionally, further confirmation of tissue responsiveness to inhibitory pharmacological agents in addition to the stimulatory agents shown here must be determined. Analysis of conduction velocity of these tissues will also be a useful metric for determining how similarly cardiac MIFIs behave compared to *in vivo* cardiac muscle. Finally, there are several important considerations that were not taken into account for the finite

elemental modeling that may affect the accuracy of calculated twitch force from tissue length. These models were generated assuming that the construct was isolated at specific tissue conformations but was not developed to account for the dynamic movement that the MIFs undergo in the side-on contractility assay. Specifically, the construct is moving through a saline solution, and this solution adds resistance against the construct movement. While this may be negligible, it is important to consider that the insert base is significantly wider than the middle region and attachment region and likely encounters a large amount of resistance during large contractions as it behaves similarly to a paddle. Future work can address these issues by modification of the model to adjust the assumptions initially made that the insert was not working against additional forces. Alternatively, the insert design can be modified to remove the wider base during the contractility assay to reduce the resistance encountered by the paddle-like portion as it moves through the solution. In this scenario, the finite element model will need to be adjusted to account for the change in insert geometry for the contractility assay.

Even with the necessity of these future studies to further verify our findings, we have successfully engineered a contractile muscular tissue by co-culturing HUES9-CMs and FBs in a 3D Col I/Matrigel suspension. These constructs compact significantly from the initial volume and are easily maintained and matured in culture for ≥ 2 weeks. The side on contractility assay, combined with ImageJ and MATLAB analysis derived from Abaqus models of bending PDMS inserts, resulted in easily obtainable force/time curves of these pharmacologically responsive beating cardiac μ tissues. These engineered MIFs have future applications for deriving patient-specific drug therapies and modeling specific genetic mutations that cause cardiac disease, and this 3D platform can also serve as a template for engineering functional skeletal muscle tissues for future applications as controllable soft robotics actuators.

6.5 References

1. Ribeiro, M.C. et al. Functional maturation of human pluripotent stem cell derived cardiomyocytes in vitro - Correlation between contraction force and electrophysiology. *Biomaterials* **51**, 138-150 (2015).
2. Kijlstra, J.D. et al. Integrated Analysis of Contractile Kinetics, Force Generation, and Electrical Activity in Single Human Stem Cell-Derived Cardiomyocytes. *Stem Cell Reports* **5**, 1226-1238 (2015).
3. Burridge, P.W. et al. Human induced pluripotent stem cell-derived cardiomyocytes recapitulate the predilection of breast cancer patients to doxorubicin-induced cardiotoxicity. *Nature Medicine* **22**, 547-556 (2016).
4. Eder, A., Vollert, I., Hansen, A. & Eschenhagen, T. Human engineered heart tissue as a model system for drug testing. *Advanced Drug Delivery Reviews* **96**, 214-224 (2016).
5. Mewes, T. & Ravens, U. L-type calcium currents of human myocytes from ventricle of non-failing and failing hearts and from atrium. *J Mol Cell Cardiol* **26**, 1307-20 (1994).
6. Sheng, X. et al. Human pluripotent stem cell-derived cardiomyocytes: response to TTX and lidocain reveals strong cell to cell variability. *PLoS One* **7**, e45963 (2012).
7. Feinberg, A.W. et al. Muscular thin films for building actuators and powering devices. *Science* **317**, 1366-70 (2007).
8. Sun, Y., Duffy, R., Lee, A. & Feinberg, A.W. Optimizing the structure and contractility of engineered skeletal muscle thin films. *Acta Biomaterialia* **9**, 7885-7894 (2013).
9. Madden, L., Juhas, M., Kraus, W.E., Truskey, G.A. & Bursac, N. Bioengineered human myobundles mimic clinical responses of skeletal muscle to drugs. *Elife* **4**, e04885 (2015).
10. Eschenhagen, T. et al. Three-dimensional reconstitution of embryonic cardiomyocytes in a collagen matrix: a new heart muscle model system. *FASEB J* **11**, 683-94 (1997).
11. Chan, V. et al. Fabrication and characterization of optogenetic, multi-strip cardiac muscles. *Lab Chip* **15**, 2258-68 (2015).
12. Galie, P.A., Byfield, F.J., Chen, C.S., Kresh, J.Y. & Janmey, P.A. Mechanically stimulated contraction of engineered cardiac constructs using a microcantilever. *IEEE Trans Biomed Eng* **62**, 438-42 (2015).
13. Chen, G.P. et al. Phospholamban as a Crucial Determinant of the Inotropic Response of Human Pluripotent Stem Cell-Derived Ventricular Cardiomyocytes and Engineered 3-Dimensional Tissue Constructs. *Circulation-Arrhythmia and Electrophysiology* **8**, 193-U276 (2015).
14. Xiao, Y. et al. Microfabricated perfusable cardiac biowire: a platform that mimics native cardiac bundle. *Lab Chip* **14**, 869-82 (2014).
15. Hansen, A. et al. Development of a Drug Screening Platform Based on Engineered Heart Tissue. *Circulation Research* **107**, 35-U70 (2010).
16. Schaaf, S. et al. Human Engineered Heart Tissue as a Versatile Tool in Basic Research and Preclinical Toxicology. *Plos One* **6** (2011).
17. Zhang, D.H. et al. Tissue-engineered cardiac patch for advanced functional maturation of human ESC-derived cardiomyocytes. *Biomaterials* **34**, 5813-5820 (2013).
18. van Spreeuwel, A.C.C. et al. The influence of matrix (an)isotropy on cardiomyocyte contraction in engineered cardiac microtissues. *Integrative Biology* **6**, 422-429 (2014).
19. Liao, B., Christoforou, N., Leong, K.W. & Bursac, N. Pluripotent stem cell-derived cardiac tissue patch with advanced structure and function. *Biomaterials* **32**, 9180-9187 (2011).
20. Saini, H., Navaei, A., Van Putten, A. & Nikkhah, M. 3D Cardiac Microtissues Encapsulated with the Co-Culture of Cardiomyocytes and Cardiac Fibroblasts. *Advanced Healthcare Materials* **4**, 1961-1971 (2015).
21. Thavandiran, N. et al. Design and formulation of functional pluripotent stem cell-derived cardiac microtissues. *Proceedings of the National Academy of Sciences of the United States of America* **110**, E4698-E4707 (2013).
22. Burridge, P.W. et al. Chemically defined generation of human cardiomyocytes. *Nat Methods* **11**, 855-60 (2014).
23. Lian, X. et al. Directed cardiomyocyte differentiation from human pluripotent stem cells by modulating Wnt/beta-catenin signaling under fully defined conditions. *Nat Protoc* **8**, 162-75 (2013).

Chapter 7

Summary and Future Directions

7.1 Summary

In this dissertation, we have introduced the breadth of literature documenting methods of engineering contractile 2D and 3D skeletal and cardiac muscle engineered tissues *in vitro*. We aimed to build on findings in the literature by further investigating the role the extracellular matrix (ECM) plays guiding the formation and alignment of differentiating skeletal muscle myoblasts. Specifically, we demonstrated that microcontact printed lines of laminin (LAM) increased myotube formation for the popular C2C12 mouse skeletal myoblast cell line as well as for human primary skeletal muscle derived cells (SkMDCs) in comparison to fibronectin and collagen types I and IV. We additionally investigated the effect of microgeometry, in terms of line width and spacing, on C2C12 and human SkMDC myotube alignment, and we found that there was a clear species-specific difference in the line geometries that uniaxially aligned human myotubes compared to C2C12 mouse myotubes. In particular, we found that human myotubes aligned on line spacings that were 'too narrow' to effectively dictate C2C12 myotube alignment, and we also observed less variability in human myotube alignment on 'wider' line widths that also resulted failed to align differentiating C2C12 myotubes. These findings have broader implications overall in that (1) it makes apparent the fact that animal cell line models do not always predict how human primary cells will behave and (2) when engineering functional human skeletal muscle at this scale, we can effectively increase the area of patterned LAM, and

consequently the volume of differentiating human skeletal muscle, while still maintaining myotube alignment in the direction of patterned lines. Had we used the line patterns that resulted in maximal C2C12 alignment and myotube formation to dictate studies using human engineered muscle, we would have less patterned area (narrower lines with wider spacings) and consequently less myotube formation.

We also investigated fundamental differences in composition in LAM from different commercial sources, as these different LAM brands had opposing effects on both C2C12 and human SkMDC myotube formation. Specifically, we found that Invitrogen LAM resulted in significantly increased myotube formation, as presented in Chapter 3, but Beckton Dickinson sourced LAM, at 3 different purities, resulted in myoblast delamination from patterned LAM lines upon inducing differentiation. Ultimately, we determined via liquid chromatography mass spectroscopy that perlecan, an important basement membrane proteoglycan, is the likely contaminant in Invitrogen LAM that significantly increased myotube formation. Further experimentation will need to be done to confirm this finding. However, this observation was supported by other findings in the literature that recently determined that perlecan is crucial to skeletal muscle formation in the embryo, and further work will determine if this is a synergistic effect of LAM with perlecan or an effect of perlecan alone. Either way, we have further information on a critical ECM guidance cue that impacts human myotube formation *in vitro*.

For our final contribution in engineering 2D skeletal muscle, we demonstrated the ability to engineer contractile muscular thin films (MTFs) with C2C12 myoblasts on patterned fibronectin lines. When we built on our previous work that demonstrated that micropatterned LAM lines should result in MTFs with more myotube coverage, we determined that this 2D assay is not ideal for skeletal muscle because of the limited time range in which differentiating

myotubes remained attached to LAM lines on polydimethylsiloxane (PDMS). Specifically, we found that we were limited to 7 days of differentiation at best, but differentiating human primary skeletal muscle needs 2 - 4 weeks to reach a mature, contractile state *in vitro*. Genipin cross-linking ECM to the PDMS surface was ineffective at maintaining myotubes past 1 week of differentiation despite evidence in the literature that this was a feasible solution to maintain smooth muscle cells on fibronectin patterned PDMS. We determined that, while there are other means of attempting to maintain skeletal muscle myotubes in 2D culture for longer periods of time, we ultimately wanted to develop a more robust, 3D assay to enable maintenance of differentiating myoblasts within a 3D construct for significantly longer periods of time.

Finally, we designed a 3D assay for measuring force generation and beat frequency of contractile muscle tissues. Specifically, we used previous designs in the literature of muscle cell and hydrogel mixtures cast around PDMS posts as anchoring points as inspiration to integrate a muscle microtissue (μ tissue) with a U-shaped PDMS insert that would act as a force indicator. More specifically, after an iterative design process using C2C12 cells suspended in collagen type I + Matrigel™, we designed a thin ($\sim 130\ \mu\text{m}$) dogbone-shaped PDMS insert to be bent to a U-shaped conformation and inserted into PDMS well to act as an anchor point on either end of the rectangular well. In this way, the polymerizing Col I + Matrigel based μ tissue attached to the insert at designated attachment points, and the entire tissue construct with insert intact was easily removed from the culture wells without damaging the μ tissue. These μ tissues with integrated force indicators (MIFIs) were further developed using HUES9 derived cardiomyocytes (CMs) co-cultured with fibroblasts, and we demonstrated that these μ tissues were easily maintained up to 14 days when 10% fibroblasts were present. We also showed that we could measure the twitch force exerted by these μ tissues by measuring change in tissue length and relating this changes to

lookup tables derived from finite element modeling of the force required to bend silicone inserts. These engineered cardiac muscle μ tissues responded as expected to stimulatory drugs and exhibited CMs that became more spread with more aligned sarcomeres as the μ tissues were maintained in culture for longer periods of time.

7.2 Future Directions

Our findings on the micropatterned LAM geometries that maximized human SkMDC myotube formation and alignment have future impact in engineering more complex, contractile human skeletal muscle *in vitro*. More specifically, we determined that the MTF assay is a less feasible route for engineering robust, contractile human skeletal muscle when using PDMS as the patterning substrate, future work can use topographical cues on softer, biological hydrogels to align and maintain differentiating myotubes. To build on that, it may prove useful to coat topographically patterned biologically-derived hydrogels with LAM to maximize myotube formation. Additionally, to determine if perlecan is in fact that critical protein in Invitrogen LAM that has been influencing 2D myotube formation, we need to run additional experiments, such as addition of recombinant perlecan to the perlecan-free LAM to determine if this rescues myotube formation. These findings all have application in understanding the specific role that ECM cues provide in guiding *in vitro* skeletal muscle formation. More thorough studies on the mechanism responsible for this significant increase in myotube formation on Invitrogen LAM will also prove useful. For instance, it is crucial to determine the integrin binding mechanism and subsequent internal signaling cascade that dictate this improved myotube formation. Investigating the integrin responsible for increased myotube formation may also support findings of whether it is in fact perlecan contamination that is critical to 2D myotube formation on LAM.

Future work with the 3D MIFI system will focus on further characterization of these cardiac μ tissues. Additionally, ongoing experiments (not shown in this dissertation) have shown that the 10% fibroblast cardiac MIFIs are capable of being maintained in culture for 4 weeks, double the amount of time presented in Chapter 6. Further contractility and pharmacological stimulation experiments on MIFIs carried out to time points of 2, 3, and 4 weeks will need to be carried out to determine if these longer culture times result in stronger μ tissues with more mature CMs. Additionally, we have engineered the MIFI design with the potential to perform exercise modeling of cardiac or skeletal muscle μ tissues. Specifically, removal of MIFIs from wells at specific time points would force the μ tissues to take on the load of the insert that is normally held in place by the PDMS well base. We could then compare MIFIs that have been removed from wells (or forced to 'exercise') to control MIFIs that remain in wells for the duration of culture.

We also want to further investigate the feasibility of applying the techniques used to engineer cardiac MIFIs to skeletal muscle myoblasts to determine if this platform is applicable for other contractile muscle cells. This will allow us to build on the work presented in this dissertation on engineered 2D mouse and human contractile skeletal muscle as differentiating myoblasts from both sources would be capable of being maintained >1 week, the limiting factor we encountered when engineering 2D MTFs with skeletal muscle. We also hypothesize that this cardiac MIFIs can also be readily developed with human induced pluripotent stem cell (iPSC) derived CMs. Specifically, we used HUES9-CMs because they were the most consistently differentiated stem cell line in use in our laboratory. However, we also have an iPSC line that has been generating CMs on a consistent basis recently. Additionally, we have been working with collaborators at the University Medical Center Groningen in the Netherlands who have reported

successfully incorporating patient derived iPSC-CMs in our MIFI design. This has potential impacts developing patient specific models of engineered cardiac tissues, and the collaborators we are working with are specifically interested in using the MIFIs to determine if genetic mutations from patients will present themselves as disease phenotypes when these iPSC-CMs are used in the context of the MIFI assay. Overall, this method of engineering a contractile tissue with a PDMS insert that acts as both an anchor during culture as well as a force indicator after removal from the well has potential applications in engineering genetic cardiac or skeletal muscle disease models, as an *in vitro* platform for testing pharmacological stimuli, as a tool to investigate how ECM cues influence skeletal muscle or cardiac formation *in vitro*, and as a stepping stone for engineering functional muscle building blocks or soft robotics actuators.

Appendix A - LCMS Spectral Counts

| | BD LAM >90% | | Inv LAM | | BD LAM+ENT | | BD LAM >95% | |
|--|-------------|--------|---------|--------|------------|--------|-------------|--------|
| Protein Names | Average | SD | Average | SD | Average | SD | Average | SD |
| Laminin subunit alpha-1 | 25.2% | 0.0105 | 31.7% | 0.0034 | 32.2% | 0.0201 | 38.0% | 0.0092 |
| Laminin subunit beta-1 | 30.7% | 0.0085 | 27.3% | 0.0068 | 24.8% | 0.0099 | 30.0% | 0.0202 |
| Laminin subunit gamma-1 | 29.8% | 0.0021 | 22.9% | 0.0005 | 21.6% | 0.0079 | 29.3% | 0.0071 |
| Nidogen-1 | 13.7% | 0.0015 | 6.3% | 0.0045 | 11.8% | 0.0042 | 1.3% | 0.0024 |
| Basement membrane-specific heparan sulfate proteoglycan core protein | - | - | 4.5% | 0.0042 | 1.2% | 0.0026 | - | - |
| Laminin subunit beta-2 | - | - | - | - | 0.4% | 0.0003 | 0.6% | 0.0019 |
| Actin, cytoplasmic 1 | - | - | 0.5% | 0.0010 | - | - | - | - |
| Fibrinogen beta chain | - | - | 0.5% | 0.0017 | 0.3% | 0.0007 | - | - |
| SPARC | - | - | - | - | 0.4% | 0.0012 | - | - |
| Tubulin alpha-1B chain | - | - | 0.4% | 0.0013 | - | - | - | - |
| Nidogen-2 | - | - | 0.5% | 0.0010 | 0.2% | 0.0009 | - | - |
| Clathrin heavy chain 1 | - | - | 0.7% | 0.0011 | 0.0% | 0.0000 | - | - |
| Myosin-9 | - | - | - | - | 0.3% | 0.0033 | - | - |
| Tubulin beta-5 chain | - | - | 0.4% | 0.0012 | 0.1% | 0.0003 | - | - |
| Myosin-10 | - | - | - | - | 0.3% | 0.0000 | - | - |
| Fibrinogen alpha chain | - | - | 0.4% | 0.0013 | 0.3% | 0.0007 | 0.0% | 0.0000 |
| Glyceraldehyde-3-phosphate dehydrogenase | - | - | 0.3% | 0.0005 | 0.2% | 0.0000 | - | - |
| Actin, cytoplasmic 2 | 0.2% | 0.0002 | - | - | 0.2% | 0.0006 | 0.2% | 0.0000 |
| Transitional endoplasmic reticulum ATPase | - | - | 0.2% | 0.0006 | 0.2% | 0.0018 | - | - |
| Fibrinogen gamma chain | - | - | 0.3% | 0.0008 | 0.3% | 0.0006 | 0.0% | 0.0001 |
| Histone H2A type 2-A | - | - | 0.2% | 0.0005 | - | - | - | - |
| Vimentin | - | - | 0.1% | 0.0002 | 0.3% | 0.0008 | - | - |
| Collagen alpha-1(IV) chain | 0.1% | 0.0000 | 0.2% | 0.0001 | 0.3% | 0.0008 | 0.2% | 0.0002 |
| Heat shock cognate 71 kDa protein | - | - | 0.1% | 0.0003 | 0.3% | 0.0004 | - | - |
| Lamin-B1 | - | - | 0.1% | 0.0000 | 0.3% | 0.0012 | - | - |
| Protein disulfide-isomerase A6 | - | - | - | - | 0.2% | 0.0000 | - | - |

| | | | | | | | | |
|--|------|--------|------|--------|------|--------|------|--------|
| Histone H2A.J | - | - | 0.2% | 0.0004 | - | - | - | - |
| ATP synthase subunit beta, mitochondrial | - | - | - | - | 0.2% | 0.0008 | - | - |
| Histone H3.2 | 0.2% | 0.0000 | 0.2% | 0.0005 | - | - | - | - |
| 78 kDa glucose-regulated protein | - | - | 0.1% | 0.0006 | 0.4% | 0.0010 | 0.0% | 0.0000 |
| Filamin-B | - | - | 0.3% | 0.0008 | 0.0% | 0.0000 | - | - |
| Clathrin light chain A | - | - | 0.1% | 0.0002 | - | - | - | - |
| Histone H2B type 3-A | - | - | 0.1% | 0.0000 | - | - | - | - |
| Fibulin-1 | - | - | 0.0% | 0.0000 | 0.3% | 0.0016 | - | - |
| Complement factor H | - | - | - | - | 0.1% | 0.0010 | - | - |
| Protein disulfide-isomerase | - | - | 0.1% | 0.0004 | 0.2% | 0.0013 | - | - |
| Elongation factor 1-alpha 1 | - | - | 0.1% | 0.0003 | 0.2% | 0.0000 | - | - |
| Pregnancy zone protein | - | - | 0.1% | 0.0005 | - | - | - | - |
| Serum albumin | - | - | 0.0% | 0.0000 | 0.2% | 0.0002 | - | - |
| Collagen alpha-2(IV) chain | - | - | 0.1% | 0.0002 | 0.2% | 0.0004 | 0.1% | 0.0003 |
| Peptidyl-prolyl cis-trans isomerase FKBP9 | - | - | - | - | 0.1% | 0.0007 | - | - |
| Serpin H1 | - | - | 0.1% | 0.0003 | 0.2% | 0.0004 | 0.0% | 0.0000 |
| Hemoglobin subunit beta-1 OS | - | - | - | - | 0.1% | 0.0000 | - | - |
| Small nuclear ribonucleoprotein Sm D3 | - | - | - | - | 0.1% | 0.0000 | - | - |
| Lamin-B2 | - | - | - | - | 0.1% | 0.0000 | - | - |
| Heterogeneous nuclear ribonucleoprotein A1 | - | - | - | - | 0.1% | 0.0000 | - | - |
| Nucleoprotein TPR | - | - | 0.1% | 0.0001 | 0.2% | 0.0012 | - | - |
| 40S ribosomal protein S3 | - | - | 0.1% | 0.0002 | 0.1% | 0.0004 | - | - |
| Heterogeneous nuclear ribonucleoproteins A2/B1 | - | - | - | - | 0.1% | 0.0001 | - | - |
| Splicing factor, proline- and glutamine-rich | - | - | - | - | 0.2% | 0.0006 | 0.0% | 0.0000 |
| 60S ribosomal protein L10a | 0.1% | 0.0000 | - | - | - | - | - | - |
| Histone H4 | - | - | 0.1% | 0.0009 | - | - | 0.0% | 0.0000 |
| Elongation factor 1-alpha 2 | - | - | - | - | 0.1% | 0.0000 | - | - |
| Ig kappa chain | - | - | - | - | 0.1% | 0.0000 | - | - |
| Laminin subunit alpha-5 | - | - | 0.0% | 0.0000 | 0.2% | 0.0000 | - | - |
| Spectrin alpha chain, non-erythrocytic 1 | - | - | 0.1% | 0.0000 | 0.1% | 0.0000 | - | - |

| | | | | | | | | |
|--|------|--------|------|--------|------|--------|------|--------|
| Prolactin-7C1 | 0.1% | 0.0000 | - | - | - | - | - | - |
| 40S ribosomal protein SA | - | - | 0.1% | 0.0000 | 0.1% | 0.0003 | - | - |
| Kininogen-1 | - | - | - | - | 0.1% | 0.0001 | - | - |
| 60S ribosomal protein L14 | - | - | 0.1% | 0.0001 | - | - | 0.1% | 0.0000 |
| MAP7 domain-containing protein 2 | - | - | - | - | - | - | 0.1% | 0.0000 |
| 60S ribosomal protein L18 | - | - | 0.1% | 0.0001 | 0.0% | 0.0000 | - | - |
| Prelamin-A/C | - | - | 0.0% | 0.0000 | 0.2% | 0.0009 | - | - |
| Peptidyl-prolyl cis-trans isomerase FKBP10 | - | - | - | - | 0.1% | 0.0003 | - | - |
| Actin, alpha skeletal muscle | 0.1% | 0.0000 | - | - | 0.0% | 0.0000 | 0.1% | 0.0007 |
| Heterogeneous nuclear ribonucleoprotein F | - | - | 0.1% | 0.0000 | 0.1% | 0.0005 | - | - |
| Clusterin | - | - | 0.1% | 0.0000 | 0.0% | 0.0001 | - | - |
| Ceruloplasmin | - | - | - | - | 0.1% | 0.0000 | - | - |
| Heterogeneous nuclear ribonucleoprotein K | - | - | - | - | 0.1% | 0.0000 | - | - |
| Vitamin D-binding protein | - | - | - | - | 0.1% | 0.0000 | - | - |
| Vinculin | - | - | - | - | 0.1% | 0.0000 | - | - |
| Fibronectin | - | - | - | - | 0.1% | 0.0000 | - | - |
| Stress-70 protein, mitochondrial | 0.1% | 0.0000 | - | - | 0.0% | 0.0000 | - | - |
| Keratin, type II cytoskeletal 1 | 0.1% | 0.0000 | - | - | - | - | 0.0% | 0.0000 |
| 60 kDa heat shock protein, mitochondrial | 0.1% | 0.0000 | - | - | 0.0% | 0.0002 | - | - |
| Histone H3.3 | 0.1% | 0.0001 | - | - | 0.0% | 0.0002 | - | - |
| Annexin A7 | - | - | - | - | - | - | 0.1% | 0.0000 |
| Tubulin alpha-1C chain | - | - | - | - | 0.1% | 0.0003 | 0.0% | 0.0000 |
| Lactadherin | - | - | 0.1% | 0.0000 | - | - | - | - |
| Eukaryotic translation initiation factor 3 subunit C | - | - | 0.1% | 0.0000 | - | - | - | - |
| Collagen alpha-3(IV) chain | - | - | 0.1% | 0.0000 | - | - | - | - |
| Heat shock protein HSP 90-beta | - | - | 0.0% | 0.0002 | 0.1% | 0.0003 | - | - |
| Collagen alpha-1(XIV) chain | - | - | 0.1% | 0.0000 | - | - | - | - |
| Collagen alpha-1(XII) chain | - | - | 0.1% | 0.0000 | - | - | - | - |
| 40S ribosomal protein S6 | - | - | 0.1% | 0.0000 | - | - | - | - |

| | | | | | | | | |
|---|------|--------|------|--------|------|--------|------|--------|
| ATP-dependent RNA helicase Dhx29 | - | - | 0.0% | 0.0000 | 0.1% | 0.0000 | - | - |
| Histone H1.3 | - | - | 0.1% | 0.0001 | - | - | - | - |
| 40S ribosomal protein S8 | - | - | 0.1% | 0.0000 | - | - | - | - |
| Receptor of activated protein C kinase 1 | - | - | 0.1% | 0.0000 | - | - | - | - |
| Tripartite motif-containing protein 30A | - | - | 0.1% | 0.0000 | - | - | - | - |
| 40S ribosomal protein S2 | - | - | 0.1% | 0.0003 | 0.0% | 0.0002 | - | - |
| 60S ribosomal protein L6 | - | - | 0.0% | 0.0000 | 0.0% | 0.0000 | 0.1% | 0.0000 |
| Cytoplasmic dynein 1 heavy chain 1 | - | - | 0.0% | 0.0004 | 0.1% | 0.0000 | - | - |
| Complement C3 | - | - | 0.0% | 0.0000 | 0.1% | 0.0001 | - | - |
| Alpha-actinin-1 | - | - | 0.0% | 0.0000 | 0.1% | 0.0001 | - | - |
| 60S ribosomal protein L13 | 0.1% | 0.0000 | - | - | 0.0% | 0.0000 | - | - |
| Thioredoxin domain-containing protein 12 | - | - | 0.1% | 0.0004 | 0.0% | 0.0000 | - | - |
| Keratin, type II cytoskeletal 6B | - | - | 0.1% | 0.0001 | 0.0% | 0.0000 | 0.0% | 0.0000 |
| Basigin | - | - | 0.0% | 0.0000 | - | - | - | - |
| Murinoglobulin-1 | - | - | 0.0% | 0.0000 | - | - | - | - |
| Dihydrolipoyllysine-residue acetyltransferase component of pyruvate dehydrogenase complex, mitochondrial OS | - | - | 0.0% | 0.0000 | - | - | - | - |
| Procollagen-lysine,2-oxoglutarate 5-dioxygenase 3 | - | - | 0.0% | 0.0000 | - | - | - | - |
| Filamin-A | - | - | 0.0% | 0.0000 | - | - | - | - |
| Bifunctional glutamate/proline--tRNA ligase | - | - | 0.0% | 0.0000 | - | - | 0.0% | 0.0000 |
| 40S ribosomal protein S28 | - | - | - | - | 0.0% | 0.0000 | - | - |
| EF-hand and coiled-coil domain-containing protein 1 | - | - | - | - | - | - | 0.0% | 0.0000 |
| Granulins | - | - | - | - | 0.0% | 0.0000 | - | - |
| Growth hormone-inducible transmembrane protein | - | - | - | - | 0.0% | 0.0000 | - | - |
| Tyrosine-protein kinase Src | - | - | - | - | 0.0% | 0.0000 | - | - |
| Glutathione peroxidase 3 | - | - | - | - | 0.0% | 0.0000 | - | - |
| Eukaryotic translation initiation factor 3 subunit | - | - | 0.1% | 0.0001 | 0.0% | 0.0000 | - | - |

| | | | | | | | | |
|---|---|---|------|--------|------|--------|------|--------|
| A | | | | | | | | |
| Kinectin | - | - | 0.1% | 0.0000 | 0.0% | 0.0000 | - | - |
| Vitronectin | - | - | 0.1% | 0.0004 | 0.0% | 0.0000 | - | - |
| 40S ribosomal protein S26 | - | - | 0.0% | 0.0000 | 0.0% | 0.0000 | - | - |
| Galectin-1 | - | - | - | - | 0.0% | 0.0001 | - | - |
| ATP synthase subunit alpha, mitochondrial | - | - | - | - | 0.0% | 0.0000 | - | - |
| Probable helicase senataxin | - | - | - | - | - | - | 0.0% | 0.0000 |
| Alpha-actinin-4 | - | - | 0.0% | 0.0003 | 0.0% | 0.0000 | - | - |
| Prolyl 3-hydroxylase 1 | - | - | - | - | 0.0% | 0.0000 | - | - |
| Isoleucine--tRNA ligase, cytoplasmic | - | - | - | - | 0.0% | 0.0000 | - | - |
| Elongation factor 1-gamma | - | - | - | - | 0.0% | 0.0000 | - | - |
| Protein transport protein Sec23A | - | - | - | - | 0.0% | 0.0000 | - | - |
| Signal transducing adapter molecule 1 | - | - | - | - | 0.0% | 0.0000 | - | - |
| Tumor protein D54 | - | - | - | - | 0.0% | 0.0000 | - | - |
| Cartilage-associated protein | - | - | - | - | 0.0% | 0.0000 | - | - |
| Cleavage and polyadenylation specificity factor subunit 6 | - | - | - | - | 0.0% | 0.0000 | - | - |
| Methionine--tRNA ligase, cytoplasmic | - | - | - | - | 0.0% | 0.0000 | - | - |
| ATP-dependent RNA helicase DDX3X | - | - | - | - | 0.0% | 0.0000 | - | - |
| Coatomer subunit delta | - | - | - | - | 0.0% | 0.0000 | - | - |
| Creatine kinase B-type | - | - | - | - | 0.0% | 0.0000 | - | - |
| IgE-binding protein | - | - | - | - | 0.0% | 0.0000 | - | - |
| Ig gamma-1 chain C region, membrane-bound form | - | - | - | - | 0.0% | 0.0000 | - | - |
| Paraspeckle component 1 | - | - | - | - | 0.0% | 0.0000 | - | - |
| T-complex protein 1 subunit alpha | - | - | - | - | 0.0% | 0.0000 | - | - |
| Polyadenylate-binding protein 1 | - | - | - | - | 0.0% | 0.0000 | - | - |
| Procollagen-lysine,2-oxoglutarate 5-dioxygenase 2 | - | - | - | - | 0.0% | 0.0000 | - | - |
| Galactokinase | - | - | - | - | 0.0% | 0.0000 | - | - |

| | | | | | | | | |
|---|---|---|------|--------|------|--------|------|--------|
| Heterogeneous nuclear ribonucleoproteins C1/C2 | - | - | - | - | 0.0% | 0.0000 | - | - |
| Vacuolar protein sorting-associated protein 35 | - | - | - | - | 0.0% | 0.0000 | - | - |
| Eukaryotic translation initiation factor 3 subunit K | - | - | - | - | 0.0% | 0.0000 | - | - |
| Protein FAM210A | - | - | - | - | 0.0% | 0.0000 | - | - |
| Non-POU domain-containing octamer-binding protein | - | - | - | - | 0.0% | 0.0000 | - | - |
| Peroxiredoxin-1 | - | - | - | - | 0.0% | 0.0000 | - | - |
| Myosin light polypeptide 6 | - | - | - | - | 0.0% | 0.0000 | - | - |
| Bifunctional purine biosynthesis protein PURH | - | - | - | - | 0.0% | 0.0000 | - | - |
| Calreticulin | - | - | - | - | 0.0% | 0.0000 | - | - |
| Histidine-rich glycoprotein | - | - | - | - | 0.0% | 0.0000 | - | - |
| Small nuclear ribonucleoprotein-associated protein N | - | - | - | - | 0.0% | 0.0000 | - | - |
| Chymotrypsinogen B | - | - | - | - | 0.0% | 0.0000 | - | - |
| KH domain-containing, RNA-binding, signal transduction-associated protein 1 | - | - | - | - | 0.0% | 0.0000 | - | - |
| Nesprin-1 | - | - | - | - | 0.0% | 0.0000 | - | - |
| Pyruvate kinase PKM | - | - | 0.0% | 0.0000 | 0.1% | 0.0000 | - | - |
| Apolipoprotein A-I | - | - | 0.1% | 0.0000 | 0.0% | 0.0000 | - | - |
| Histone H2B type 1-P | - | - | 0.0% | 0.0003 | - | - | - | - |
| 60S ribosomal protein L4 | - | - | 0.0% | 0.0003 | - | - | - | - |
| 40S ribosomal protein S11 | - | - | 0.0% | 0.0003 | - | - | - | - |
| Cyclin-dependent kinase 18 | - | - | - | - | 0.0% | 0.0002 | - | - |
| Cytosolic 5-nucleotidase 1A | - | - | 0.0% | 0.0000 | - | - | 0.0% | 0.0000 |
| Galectin-3 | - | - | 0.0% | 0.0002 | 0.0% | 0.0000 | 0.0% | 0.0000 |
| Ribosome-binding protein 1 | - | - | 0.0% | 0.0000 | 0.0% | 0.0000 | - | - |
| Spectrin beta chain, non-erythrocytic 1 | - | - | 0.0% | 0.0000 | 0.0% | 0.0000 | - | - |
| Elongation factor 2 | - | - | 0.0% | 0.0000 | 0.0% | 0.0000 | - | - |
| Low-density lipoprotein receptor-related protein | - | - | - | - | 0.0% | 0.0002 | - | - |

| | | | | | | | | |
|--|------|--------|------|--------|------|--------|------|--------|
| 2 | | | | | | | | |
| Elongation factor 1-delta | - | - | 0.0% | 0.0000 | 0.0% | 0.0001 | 0.0% | 0.0000 |
| Pro-epidermal growth factor | 0.0% | 0.0000 | - | - | - | - | - | - |
| Eukaryotic translation initiation factor 3 subunit I | - | - | 0.0% | 0.0000 | - | - | - | - |
| Calumenin | - | - | 0.0% | 0.0000 | - | - | - | - |
| 40S ribosomal protein S16 | - | - | 0.0% | 0.0000 | 0.0% | 0.0000 | - | - |
| 60S ribosomal protein L34 | - | - | 0.0% | 0.0000 | - | - | - | - |
| Collagen alpha-1(XVI) chain | - | - | 0.0% | 0.0000 | - | - | - | - |
| Myotubularin-related protein 10 | - | - | 0.0% | 0.0000 | 0.0% | 0.0000 | - | - |
| Transcription intermediary factor 1-beta | - | - | 0.0% | 0.0000 | - | - | - | - |
| Disks large-associated protein 2 | - | - | 0.0% | 0.0000 | - | - | - | - |
| 60S ribosomal protein L10 | - | - | 0.0% | 0.0000 | - | - | - | - |
| Apolipoprotein E | - | - | 0.0% | 0.0000 | - | - | - | - |
| Long-chain-fatty-acid--CoA ligase 6 | - | - | 0.0% | 0.0000 | - | - | 0.0% | 0.0000 |
| Coagulation factor XIII A chain | - | - | 0.0% | 0.0000 | - | - | - | - |
| Ras and EF-hand domain-containing protein homolog | - | - | 0.0% | 0.0000 | - | - | - | - |
| 116 kDa U5 small nuclear ribonucleoprotein component | - | - | 0.0% | 0.0000 | - | - | - | - |
| Coatomer subunit alpha | - | - | 0.0% | 0.0000 | - | - | - | - |
| Hemoglobin subunit alpha | - | - | 0.0% | 0.0000 | - | - | - | - |
| Ubiquitin-conjugating enzyme E2 K | - | - | 0.0% | 0.0000 | - | - | - | - |
| Galactocerebrosidase | - | - | 0.0% | 0.0000 | - | - | - | - |
| Testis-specific Y-encoded-like protein 5 | - | - | 0.0% | 0.0000 | - | - | - | - |
| Ig gamma-2A chain C region | - | - | - | - | 0.0% | 0.0000 | - | - |
| UPF0193 protein | - | - | - | - | 0.0% | 0.0000 | - | - |
| Putative thiamine transporter SLC35F3 | - | - | - | - | 0.0% | 0.0000 | - | - |
| Protein FAM65B | - | - | - | - | 0.0% | 0.0000 | - | - |

| | | | | | | | | |
|--|-------------|----------------------|-------------|----------------------|-------------|---------------------|-------------|--------------------|
| Helicase ARIP4 | - | - | - | - | 0.0% | 0.0000 | - | - |
| ATP-dependent RNA helicase A | - | - | - | - | 0.0% | 0.0000 | - | - |
| Bromodomain and WD repeat-containing protein 3 | - | - | - | - | 0.0% | 0.0000 | - | - |
| Heterogeneous nuclear ribonucleoprotein A3 | - | - | - | - | 0.0% | 0.0000 | - | - |
| DnaJ homolog subfamily C member 10 | - | - | - | - | 0.0% | 0.0000 | - | - |
| AP-2 complex subunit beta | - | - | - | - | 0.0% | 0.0000 | - | - |
| Developmental pluripotency-associated protein 4 | - | - | - | - | 0.0% | 0.0000 | - | - |
| Heat shock protein HSP 90-alpha | - | - | - | - | 0.0% | 0.0000 | - | - |
| Structural maintenance of chromosomes protein 4 | - | - | - | - | 0.0% | 0.0000 | - | - |
| ELAV-like protein 1 | - | - | - | - | 0.0% | 0.0000 | - | - |
| Protein PTHB1 | - | - | - | - | 0.0% | 0.0000 | - | - |
| Matrin-3 | - | - | - | - | 0.0% | 0.0000 | - | - |
| UV excision repair protein RAD23 homolog B | - | - | - | - | 0.0% | 0.0000 | - | - |
| Vacuolar protein sorting-associated protein 13C | - | - | - | - | 0.0% | 0.0000 | - | - |
| Maestro heat-like repeat-containing protein family member 2A | - | - | - | - | 0.0% | 0.0000 | - | - |
| 40S ribosomal protein S17 | - | - | - | - | 0.0% | 0.0000 | - | - |
| CAP-Gly domain-containing linker protein 2 | - | - | - | - | 0.0% | 0.0000 | - | - |
| CAP-Gly domain-containing linker protein 2 | - | - | - | - | 0.0% | 0.0000 0 | - | - |
| | | | | | | | | |
| Sum | 1.008 | | 1.013 | | 1.035 | | 1.007 | |
| Other protiens | 0.5% | 0.00071 4 | 7.2% | 0.00207 5 | 8.3% | 0.0326 3 | 1.4% | 0.002 9 |

Appendix B - MIFI Length to Force Lookup Tables

| 126 μm | | 127 μm | | 128 μm | | 129 μm | | 130 μm | | 131 μm | |
|----------------------------------|-----------------------|----------------------------------|-----------------------|----------------------------------|-----------------------|----------------------------------|-----------------------|----------------------------------|-----------------------|----------------------------------|-----------------------|
| Total force [μN] | Tissue length [mm] | Total force [μN] | Tissue length [mm] | Total force [μN] | Tissue length [mm] | Total force [μN] | Tissue length [mm] | Total force [μN] | Tissue length [mm] | Total force [μN] | Tissue length [mm] |
| | | | | | | | | | | | |
| 60 | 9.290 | 60 | 9.616 | 60 | 9.941 | 60 | 10.259 | 60 | 10.570 | 60 | 10.880 |
| 61 | 9.048 | 61 | 9.394 | 61 | 9.713 | 61 | 10.021 | 61 | 10.343 | 61 | 10.641 |
| 62 | 8.809 | 62 | 9.139 | 62 | 9.469 | 62 | 9.803 | 62 | 10.106 | 62 | 10.417 |
| 63 | 8.573 | 63 | 8.907 | 63 | 9.236 | 63 | 9.559 | 63 | 9.883 | 63 | 10.191 |
| 64 | 8.341 | 64 | 8.675 | 64 | 9.006 | 64 | 9.330 | 64 | 9.650 | 64 | 9.967 |
| 65 | 8.113 | 65 | 8.446 | 65 | 8.777 | 65 | 9.107 | 65 | 9.441 | 65 | 9.759 |
| 66 | 7.889 | 66 | 8.221 | 66 | 8.554 | 66 | 8.881 | 66 | 9.206 | 66 | 9.525 |
| 67 | 7.668 | 67 | 7.998 | 67 | 8.331 | 67 | 8.660 | 67 | 8.983 | 67 | 9.305 |
| 68 | 7.450 | 68 | 7.783 | 68 | 8.113 | 68 | 8.441 | 68 | 8.767 | 68 | 9.092 |
| 69 | 7.236 | 69 | 7.568 | 69 | 7.897 | 69 | 8.225 | 69 | 8.554 | 69 | 8.874 |
| 70 | 7.026 | 70 | 7.356 | 70 | 7.687 | 70 | 8.014 | 70 | 8.341 | 70 | 8.661 |
| 71 | 6.822 | 71 | 7.149 | 71 | 7.478 | 71 | 7.806 | 71 | 8.131 | 71 | 8.455 |
| 72 | 6.619 | 72 | 6.944 | 72 | 7.273 | 72 | 7.600 | 72 | 7.925 | 72 | 8.246 |
| 73 | 6.421 | 73 | 6.748 | 73 | 7.071 | 73 | 7.397 | 73 | 7.722 | 73 | 8.058 |
| 74 | 6.228 | 74 | 6.549 | 74 | 6.873 | 74 | 7.198 | 74 | 7.522 | 74 | 7.844 |
| 75 | 6.034 | 75 | 6.359 | 75 | 6.682 | 75 | 7.003 | 75 | 7.325 | 75 | 7.648 |
| 76 | 5.849 | 76 | 6.169 | 76 | 6.491 | 76 | 6.813 | 76 | 7.132 | 76 | 7.453 |
| 77 | 5.666 | 77 | 5.984 | 77 | 6.303 | 77 | 6.624 | 77 | 6.940 | 77 | 7.261 |
| 78 | 5.485 | 78 | 5.804 | 78 | 6.118 | 78 | 6.439 | 78 | 6.757 | 78 | 7.071 |
| 79 | 5.320 | 79 | 5.626 | 79 | 5.939 | 79 | 6.258 | 79 | 6.574 | 79 | 6.889 |
| 80 | 5.140 | 80 | 5.450 | 80 | 5.764 | 80 | 6.076 | 80 | 6.393 | 80 | 6.705 |
| 81 | 4.972 | 81 | 5.282 | 81 | 5.591 | 81 | 5.904 | 81 | 6.215 | 81 | 6.530 |
| 82 | 4.804 | 82 | 5.113 | 82 | 5.421 | 82 | 5.729 | 82 | 6.040 | 82 | 6.354 |
| 83 | 4.643 | 83 | 4.949 | 83 | 5.256 | 83 | 5.562 | 83 | 5.872 | 83 | 6.180 |
| 84 | 4.485 | 84 | 4.786 | 84 | 5.092 | 84 | 5.396 | 84 | 5.702 | 84 | 6.012 |
| 85 | 4.329 | 85 | 4.631 | 85 | 4.932 | 85 | 5.232 | 85 | 5.540 | 85 | 5.846 |
| 86 | 4.177 | 86 | 4.475 | 86 | 4.774 | 86 | 5.076 | 86 | 5.377 | 86 | 5.681 |
| 87 | 4.028 | 87 | 4.323 | 87 | 4.620 | 87 | 4.920 | 87 | 5.218 | 87 | 5.521 |
| 88 | 3.881 | 88 | 4.175 | 88 | 4.470 | 88 | 4.766 | 88 | 5.065 | 88 | 5.361 |
| 89 | 3.737 | 89 | 4.029 | 89 | 4.321 | 89 | 4.616 | 89 | 4.913 | 89 | 5.210 |
| 90 | 3.599 | 90 | 3.886 | 90 | 4.176 | 90 | 4.469 | 90 | 4.763 | 90 | 5.059 |

| 132 μm | | 133 μm | | 134 μm | | 135 μm | | 136 μm | | 137 μm | |
|----------------------------------|-----------------------|----------------------------------|-----------------------|----------------------------------|-----------------------|----------------------------------|-----------------------|----------------------------------|-----------------------|----------------------------------|-----------------------|
| Total force [μN] | Tissue length [mm] | Total force [μN] | Tissue length [mm] | Total force [μN] | Tissue length [mm] | Total force [μN] | Tissue length [mm] | Total force [μN] | Tissue length [mm] | Total force [μN] | Tissue length [mm] |
| | | | | | | | | | | | |
| 60 | 11.153 | 75 | 8.288 | 75 | 8.604 | 75 | 8.916 | 80 | 8.278 | 80 | 8.586 |
| 61 | 10.938 | 76 | 8.091 | 76 | 8.408 | 76 | 8.723 | 81 | 8.094 | 81 | 8.403 |
| 62 | 10.718 | 77 | 7.898 | 77 | 8.216 | 77 | 8.531 | 82 | 7.914 | 82 | 8.224 |
| 63 | 10.498 | 78 | 7.709 | 78 | 8.025 | 78 | 8.339 | 83 | 7.735 | 83 | 8.044 |
| 64 | 10.275 | 79 | 7.522 | 79 | 7.838 | 79 | 8.151 | 84 | 7.558 | 84 | 7.868 |
| 65 | 10.058 | 80 | 7.337 | 80 | 7.652 | 80 | 7.965 | 85 | 7.383 | 85 | 7.692 |
| 66 | 9.846 | 81 | 7.156 | 81 | 7.470 | 81 | 7.783 | 86 | 7.214 | 86 | 7.521 |
| 67 | 9.622 | 82 | 6.977 | 82 | 7.289 | 82 | 7.603 | 87 | 7.045 | 87 | 7.353 |
| 68 | 9.422 | 83 | 6.804 | 83 | 7.113 | 83 | 7.426 | 88 | 6.881 | 88 | 7.184 |
| 69 | 9.195 | 84 | 6.633 | 84 | 6.939 | 84 | 7.247 | 89 | 6.717 | 89 | 7.019 |
| 70 | 8.983 | 85 | 6.462 | 85 | 6.771 | 85 | 7.076 | 90 | 6.558 | 90 | 6.860 |
| 71 | 8.776 | 86 | 6.294 | 86 | 6.601 | 86 | 6.907 | 91 | 6.399 | 91 | 6.700 |
| 72 | 8.571 | 87 | 6.126 | 87 | 6.436 | 87 | 6.741 | 92 | 6.244 | 92 | 6.544 |
| 73 | 8.367 | 88 | 5.969 | 88 | 6.270 | 88 | 6.576 | 93 | 6.090 | 93 | 6.389 |
| 74 | 8.166 | 89 | 5.811 | 89 | 6.111 | 89 | 6.415 | 94 | 5.940 | 94 | 6.238 |
| 75 | 7.968 | 90 | 5.655 | 90 | 5.953 | 90 | 6.256 | 95 | 5.792 | 95 | 6.085 |
| 76 | 7.771 | 91 | 5.502 | 91 | 5.800 | 91 | 6.097 | 96 | 5.646 | 96 | 5.940 |
| 77 | 7.581 | 92 | 5.351 | 92 | 5.647 | 92 | 5.945 | 97 | 5.504 | 97 | 5.794 |
| 78 | 7.393 | 93 | 5.202 | 93 | 5.498 | 93 | 5.794 | 98 | 5.361 | 98 | 5.652 |
| 79 | 7.205 | 94 | 5.060 | 94 | 5.349 | 94 | 5.645 | 99 | 5.223 | 99 | 5.512 |
| 80 | 7.022 | 95 | 4.917 | 95 | 5.205 | 95 | 5.499 | 100 | 5.090 | 100 | 5.372 |
| 81 | 6.844 | 96 | 4.777 | 96 | 5.065 | 96 | 5.353 | 101 | 4.953 | 101 | 5.237 |
| 82 | 6.667 | 97 | 4.638 | 97 | 4.924 | 97 | 5.213 | 102 | 4.823 | 102 | 5.104 |
| 83 | 6.494 | 98 | 4.502 | 98 | 4.789 | 98 | 5.077 | 103 | 4.692 | 103 | 4.975 |
| 84 | 6.321 | 99 | 4.371 | 99 | 4.653 | 99 | 4.940 | 104 | 4.565 | 104 | 4.845 |
| 85 | 6.153 | 100 | 4.240 | 100 | 4.520 | 100 | 4.804 | 105 | 4.439 | 105 | 4.719 |
| 86 | 5.988 | 101 | 4.112 | 101 | 4.391 | 101 | 4.673 | 106 | 4.316 | 106 | 4.592 |
| 87 | 5.826 | 102 | 3.986 | 102 | 4.262 | 102 | 4.543 | 107 | 4.195 | 107 | 4.468 |
| 88 | 5.667 | 103 | 3.861 | 103 | 4.138 | 103 | 4.413 | 108 | 4.075 | 108 | 4.346 |
| 89 | 5.508 | 104 | 3.741 | 104 | 4.013 | 104 | 4.288 | 109 | 3.957 | 109 | 4.227 |
| 90 | 5.350 | 105 | 3.621 | 105 | 3.891 | 105 | 4.162 | 110 | 3.842 | 110 | 4.110 |

| 138 μm | | 139 μm | | 140 μm | | 141 μm | | 142 μm | | 143 μm | |
|----------------------------------|-----------------------|----------------------------------|-----------------------|----------------------------------|-----------------------|----------------------------------|-----------------------|----------------------------------|-----------------------|----------------------------------|-----------------------|
| Total force [μN] | Tissue length [mm] | Total force [μN] | Tissue length [mm] | Total force [μN] | Tissue length [mm] | Total force [μN] | Tissue length [mm] | Total force [μN] | Tissue length [mm] | Total force [μN] | Tissue length [mm] |
| | | | | | | | | | | | |
| 80 | 8.894 | 85 | 8.305 | 85 | 8.611 | 90 | 8.065 | 90 | 8.362 | 90 | 8.665 |
| 81 | 8.712 | 86 | 8.126 | 86 | 8.437 | 91 | 7.905 | 91 | 8.202 | 91 | 8.501 |
| 82 | 8.529 | 87 | 7.962 | 87 | 8.267 | 92 | 7.742 | 92 | 8.039 | 92 | 8.338 |
| 83 | 8.352 | 88 | 7.794 | 88 | 8.096 | 93 | 7.581 | 93 | 7.880 | 93 | 8.176 |
| 84 | 8.175 | 89 | 7.627 | 89 | 7.932 | 94 | 7.425 | 94 | 7.723 | 94 | 8.019 |
| 85 | 8.000 | 90 | 7.462 | 90 | 7.765 | 95 | 7.275 | 95 | 7.566 | 95 | 7.864 |
| 86 | 7.825 | 91 | 7.302 | 91 | 7.603 | 96 | 7.120 | 96 | 7.413 | 96 | 7.709 |
| 87 | 7.657 | 92 | 7.141 | 92 | 7.441 | 97 | 6.969 | 97 | 7.261 | 97 | 7.555 |
| 88 | 7.486 | 93 | 6.984 | 93 | 7.286 | 98 | 6.819 | 98 | 7.114 | 98 | 7.405 |
| 89 | 7.324 | 94 | 6.833 | 94 | 7.130 | 99 | 6.672 | 99 | 6.966 | 99 | 7.257 |
| 90 | 7.160 | 95 | 6.679 | 95 | 6.976 | 100 | 6.530 | 100 | 6.819 | 100 | 7.113 |
| 91 | 6.999 | 96 | 6.528 | 96 | 6.823 | 101 | 6.385 | 101 | 6.676 | 101 | 6.965 |
| 92 | 6.845 | 97 | 6.380 | 97 | 6.675 | 102 | 6.246 | 102 | 6.534 | 102 | 6.825 |
| 93 | 6.688 | 98 | 6.234 | 98 | 6.527 | 103 | 6.108 | 103 | 6.396 | 103 | 6.686 |
| 94 | 6.535 | 99 | 6.089 | 99 | 6.380 | 104 | 5.972 | 104 | 6.258 | 104 | 6.544 |
| 95 | 6.382 | 100 | 5.950 | 100 | 6.238 | 105 | 5.840 | 105 | 6.121 | 105 | 6.407 |
| 96 | 6.235 | 101 | 5.811 | 101 | 6.099 | 106 | 5.707 | 106 | 5.990 | 106 | 6.273 |
| 97 | 6.087 | 102 | 5.673 | 102 | 5.959 | 107 | 5.578 | 107 | 5.857 | 107 | 6.139 |
| 98 | 5.943 | 103 | 5.539 | 103 | 5.823 | 108 | 5.449 | 108 | 5.728 | 108 | 6.009 |
| 99 | 5.800 | 104 | 5.404 | 104 | 5.689 | 109 | 5.323 | 109 | 5.601 | 109 | 5.879 |
| 100 | 5.661 | 105 | 5.277 | 105 | 5.555 | 110 | 5.198 | 110 | 5.474 | 110 | 5.755 |
| 101 | 5.524 | 106 | 5.147 | 106 | 5.427 | 111 | 5.077 | 111 | 5.352 | 111 | 5.628 |
| 102 | 5.386 | 107 | 5.022 | 107 | 5.296 | 112 | 4.956 | 112 | 5.230 | 112 | 5.505 |
| 103 | 5.255 | 108 | 4.897 | 108 | 5.170 | 113 | 4.837 | 113 | 5.110 | 113 | 5.383 |
| 104 | 5.124 | 109 | 4.773 | 109 | 5.047 | 114 | 4.721 | 114 | 4.993 | 114 | 5.263 |
| 105 | 4.996 | 110 | 4.652 | 110 | 4.924 | 115 | 4.607 | 115 | 4.872 | 115 | 5.145 |
| 106 | 4.867 | 111 | 4.532 | 111 | 4.805 | 116 | 4.492 | 116 | 4.760 | 116 | 5.026 |
| 107 | 4.743 | 112 | 4.415 | 112 | 4.684 | 117 | 4.381 | 117 | 4.645 | 117 | 4.913 |
| 108 | 4.620 | 113 | 4.300 | 113 | 4.569 | 118 | 4.271 | 118 | 4.535 | 118 | 4.800 |
| 109 | 4.500 | 114 | 4.186 | 114 | 4.453 | 119 | 4.162 | 119 | 4.424 | 119 | 4.687 |
| 110 | 4.380 | 115 | 4.075 | 115 | 4.340 | 120 | 4.053 | 120 | 4.316 | 120 | 4.579 |
| | | | | | | | | | | 121 | 4.470 |
| | | | | | | | | | | 122 | 4.363 |
| | | | | | | | | | | 123 | 4.256 |
| | | | | | | | | | | 124 | 4.154 |
| | | | | | | | | | | 125 | 4.050 |
| | | | | | | | | | | 126 | 3.948 |
| | | | | | | | | | | 127 | 3.849 |
| | | | | | | | | | | 128 | 3.752 |

| 144 μm | | 145 μm | | 146 μm | | 147 μm | | 148 μm | | 149 μm | |
|----------------------------------|-----------------------|----------------------------------|-----------------------|----------------------------------|-----------------------|----------------------------------|-----------------------|----------------------------------|-----------------------|----------------------------------|-----------------------|
| Total force [μN] | Tissue length [mm] | Total force [μN] | Tissue length [mm] | Total force [μN] | Tissue length [mm] | Total force [μN] | Tissue length [mm] | Total force [μN] | Tissue length [mm] | Total force [μN] | Tissue length [mm] |
| | | | | | | 100 | 8.275 | | | | |
| 95 | 8.164 | 95 | 8.453 | 100 | 7.983 | 101 | 8.126 | 100 | 8.565 | 110 | 7.437 |
| 96 | 8.002 | 96 | 8.300 | 101 | 7.839 | 102 | 7.980 | 101 | 8.416 | 111 | 7.302 |
| 97 | 7.852 | 97 | 8.143 | 102 | 7.692 | 103 | 7.838 | 102 | 8.270 | 112 | 7.174 |
| 98 | 7.699 | 98 | 7.991 | 103 | 7.550 | 104 | 7.694 | 103 | 8.122 | 113 | 7.041 |
| 99 | 7.550 | 99 | 7.843 | 104 | 7.407 | 105 | 7.555 | 104 | 7.982 | 114 | 6.919 |
| 100 | 7.402 | 100 | 7.694 | 105 | 7.266 | 106 | 7.414 | 105 | 7.840 | 115 | 6.789 |
| 101 | 7.256 | 101 | 7.547 | 106 | 7.127 | 107 | 7.276 | 106 | 7.700 | 116 | 6.666 |
| 102 | 7.112 | 102 | 7.403 | 107 | 6.993 | 108 | 7.138 | 107 | 7.561 | 117 | 6.545 |
| 103 | 6.973 | 103 | 7.259 | 108 | 6.858 | 109 | 7.008 | 108 | 7.425 | 118 | 6.423 |
| 104 | 6.830 | 104 | 7.116 | 109 | 6.725 | 110 | 6.875 | 109 | 7.289 | 119 | 6.300 |
| 105 | 6.692 | 105 | 6.979 | 110 | 6.594 | 111 | 6.744 | 110 | 7.154 | 120 | 6.185 |
| 106 | 6.559 | 106 | 6.844 | 111 | 6.463 | 112 | 6.617 | 111 | 7.022 | 121 | 6.068 |
| 107 | 6.423 | 107 | 6.706 | 112 | 6.334 | 113 | 6.487 | 112 | 6.896 | 122 | 5.950 |
| 108 | 6.291 | 108 | 6.572 | 113 | 6.211 | 114 | 6.361 | 113 | 6.767 | 123 | 5.835 |
| 109 | 6.159 | 109 | 6.443 | 114 | 6.088 | 115 | 6.238 | 114 | 6.637 | 124 | 5.725 |
| 110 | 6.032 | 110 | 6.311 | 115 | 5.963 | 116 | 6.114 | 115 | 6.515 | 125 | 5.613 |
| 111 | 5.904 | 111 | 6.183 | 116 | 5.841 | 117 | 5.995 | 116 | 6.390 | 126 | 5.503 |
| 112 | 5.781 | 112 | 6.058 | 117 | 5.723 | 118 | 5.875 | 117 | 6.268 | 127 | 5.395 |
| 113 | 5.657 | 113 | 5.933 | 118 | 5.605 | 119 | 5.758 | 118 | 6.148 | 128 | 5.289 |
| 114 | 5.535 | 114 | 5.810 | 119 | 5.489 | 120 | 5.643 | 119 | 6.031 | 129 | 5.185 |
| 115 | 5.416 | 115 | 5.687 | 120 | 5.375 | 121 | 5.528 | 120 | 5.912 | 130 | 5.080 |
| 116 | 5.296 | 116 | 5.568 | 121 | 5.260 | 122 | 5.415 | 121 | 5.796 | 131 | 4.975 |
| 117 | 5.181 | 117 | 5.451 | 122 | 5.150 | 123 | 5.305 | 122 | 5.684 | 132 | 4.876 |
| 118 | 5.067 | 118 | 5.335 | 123 | 5.040 | 124 | 5.197 | 123 | 5.570 | 133 | 4.775 |
| 119 | 4.952 | 119 | 5.220 | 124 | 4.931 | 125 | 5.086 | 124 | 5.459 | 134 | 4.677 |
| 120 | 4.840 | 120 | 5.107 | 125 | 4.823 | 126 | 4.981 | 125 | 5.349 | 135 | 4.580 |
| 121 | 4.733 | 121 | 4.997 | 126 | 4.720 | 127 | 4.874 | 126 | 5.239 | 136 | 4.483 |
| 122 | 4.624 | 122 | 4.886 | 127 | 4.616 | 128 | 4.769 | 127 | 5.134 | 137 | 4.388 |
| 123 | 4.516 | 123 | 4.778 | 128 | 4.513 | 129 | 4.668 | 128 | 5.029 | 138 | 4.294 |
| 124 | 4.411 | 124 | 4.670 | 129 | 4.410 | 130 | 4.567 | 129 | 4.925 | 139 | 4.201 |
| 125 | 4.307 | 125 | 4.566 | 130 | 4.310 | 131 | 4.465 | 130 | 4.821 | 140 | 4.108 |
| | | | | | | 132 | 4.368 | | | | |
| | | | | | | 133 | 4.268 | | | | |
| | | | | | | 134 | 4.174 | | | | |
| | | | | | | 135 | 4.080 | | | | |
| | | | | | | 136 | 3.986 | | | | |

| 150 μm | | 154 μm | |
|----------------------------------|-----------------------|----------------------------------|-----------------------|
| Total force [μN] | Tissue length [mm] | Total force [μN] | Tissue length [mm] |
| | | | |
| 115 | 7.067 | 125 | 6.951 |
| 116 | 6.944 | 126 | 6.838 |
| 117 | 6.820 | 127 | 6.724 |
| 118 | 6.697 | 128 | 6.609 |
| 119 | 6.577 | 129 | 6.499 |
| 120 | 6.456 | 130 | 6.388 |
| 121 | 6.336 | 131 | 6.278 |
| 122 | 6.220 | 132 | 6.171 |
| 123 | 6.105 | 133 | 6.067 |
| 124 | 5.990 | 134 | 5.961 |
| 125 | 5.879 | 135 | 5.858 |
| 126 | 5.767 | 136 | 5.752 |
| 127 | 5.660 | 137 | 5.652 |
| 128 | 5.551 | 138 | 5.552 |
| 129 | 5.443 | 139 | 5.452 |
| 130 | 5.339 | 140 | 5.357 |
| 131 | 5.233 | 141 | 5.259 |
| 132 | 5.132 | 142 | 5.162 |
| 133 | 5.030 | 143 | 5.069 |
| 134 | 4.929 | 144 | 4.976 |
| 135 | 4.832 | 145 | 4.884 |
| 136 | 4.733 | 146 | 4.793 |
| 137 | 4.638 | 147 | 4.701 |
| 138 | 4.543 | 148 | 4.614 |
| 139 | 4.448 | 149 | 4.526 |
| 140 | 4.355 | 150 | 4.439 |
| 141 | 4.263 | 151 | 4.353 |
| 142 | 4.173 | 152 | 4.269 |
| 143 | 4.083 | 153 | 4.184 |
| 144 | 3.996 | 154 | 4.101 |
| 145 | 3.910 | 155 | 4.019 |

Appendix C - MATLAB Code - MIFI Length Measurement

```
% Basic script to load a stack of tiff images of MIFI constructs (side view
of bending)
% in diastole and systole and determine tissue length change. The user
% click points of attachment of the tissue to the insert to measure change
% in length of the tissue
% Rebecca Duffy, Regenerative Biomaterials Group, Carnegie Mellon University
(07/09/2016)

clear all
% ask user to select file
[file,path]=uigetfile({'*.tif'; '*.bmp'; '*.jpg'; '*..*'}, 'Select Image
File...', 'D:/Parker Lab/');
filename = [path file];

% get file info
info = imfinfo([filename]);
frames = length(info);
X = info(1).Height;
Y = info(1).Width;

prompt = {'Enter image calibration factor (mm/pixel):'};
dlg_title = 'Input constants to calculate stress';
num_lines = 1;
def = {'0.00849'};
answer = inputdlg(prompt,dlg_title,num_lines,def);
calibration = str2double(answer);

cal_factor = calibration(1);

% load in image stack
for frame=1:frames
    [stack(:, :, frame)] = imread([filename], 'tif', frame);
end

% Instructions for selecting points
disp('Left mouse button picks points.')
disp('Right mouse button picks last point.')

% Set frame to 1
frame = 1;

% View each frame and select point for fitting the circle
while frame <= frames
    % display image
    image(stack(:, :, frame));
    colormap(gray(256));
    text(15,15,sprintf('Frame:
%g', frame), 'BackgroundColor', 'white', 'FontWeight', 'bold');

    % Code to select point
    hold on
    % Initially, the list of points is empty.
    %     xy = [];
```

```

n = 0;
% Loop, picking up the points.
btn = 1;
while btn == 1
    [xi,yi,btn] = ginput(1);
    h1 = plot(xi,yi,'ro');
    n = n+1;
    frame_stack(frame).x(n)=xi;
    frame_stack(frame).y(n)=yi;
    %xy(:,n+frame) = [xi,yi];

end
%measuring x and y relative distances and length where length converts
%pixels to mm
frame_stack(frame).diff(1) = abs(frame_stack(frame).x(2)-
frame_stack(frame).x(1));
frame_stack(frame).diff(2) = abs(frame_stack(frame).y(2)-
frame_stack(frame).y(1));
frame_stack(frame).length = sqrt(frame_stack(frame).diff(1)^2 +
frame_stack(frame).diff(2)^2)*cal_factor;

    hold off

    % Any key to repeat point selection on current frame, else click left
mouse button to continue to next frame
w = waitforbuttonpress;
if w == 0
    disp('Processing next slice...' )
    % xlsfile(frame,:) = [xc yc Re 0 0];
    frame = frame+1;
else
    disp('Re-analyze slice...')
end

end

%make array to save into excel from frame_stack.length
for cnt=1:length(frame_stack)
    length_array(:,cnt) = frame_stack(cnt).length;
end
length_array_c=length_array';
% save data
save(strrep(file, '.tif', 'mat'));
xlswrite(strrep(file, '.tif', '_length.xlsx'),length_array_c);

```

Appendix D - MATLAB Code - MIFI Force from Lookup Tables

```
clear all

%select excel file
[file,path]=uigetfile({'*.xlsx'; '*.xls'; '*.csv'; '*..*'}, 'Select Excel
File...');
filename = [path file];

%select Matlab workspace; variable is called 'length_array_c'
% [file,path]=uigetfile({'*.mat'; '*..*'}, 'Select Matlab Workspace File...');
% filename = [path file];

%load lookup tables
load lookup_tables.mat;

%get file data
%length data should be in first column of sheet1
length_array_c = xlsread(filename, 'Sheet1', 'A:A');

%prompt which lookup table to access based on insert thickness
%e.g. if insert is 135 um thick, 'm135' will be the excel file name
prompt = {'Enter lookup table based on insert thickness (t###):'};
dlg_title = 'Select lookup table';
num_lines = 1;
def = {'t149'};
answer = inputdlg(prompt,dlg_title,num_lines,def);
%calls specific force lookup table based on insert thickness
force_table = getfield(lookup_tables,char(answer));

%create matrix for points to calculate 'weighted' force averages from
%lookup table
%force1,force2 are the force 'coordinates' of lesser and greater forces for
the
%measured tissue length in the lookup table. length1 and length2 are the
matching
%length values for those forces. calculate slope and y intercept to solve
%'y=ax+b' to find force for the specified length value
for a = 1:length(length_array_c)
    for b=1:length(force_table)
        if length_array_c(a,1)>force_table(b,1)
            force1 = force_table(b,2);
            force2 = force_table(b-1,2);
            length1 = force_table(b,1);
            length2 = force_table(b-1,1);
            slope = (force2-force1)/(length2-length1);
            y_int = force1 - slope*length1;
            length_array_c(a,2) = slope*length_array_c(a,1) + y_int;
            break;
        end
    end
end
% save data
xlswrite(strrep(file, '.xlsx', '_length_force.xlsx'),length_array_c);
```

Appendix E - Publications, Presentations, and Posters

Publications:

- **Duffy R**, Sun Y, and Feinberg AW. “Understanding the role of ECM protein composition and geometric micropatterning in engineering human skeletal muscle.” *Annals of Biomedical Engineering*. 16 March 2016, pp 1 - 14
- **Duffy R** and Feinberg AW. “Engineered skeletal muscle tissue for soft robotics: fabrication strategies, current applications and future challenges.” *WIREs Nanomedicine and Nanobiotechnology*. 2013.
- Sun Y, **Duffy R**, Lee A and Feinberg AW. “Optimizing the Structure and Contractility of Skeletal Muscle Thin Films.” *Acta Biomaterialia*, 9(8), 2013, pp 7885-7894.

Presentations:

- “Driving 2D and 3D Muscle Formation Using Extracellular Matrix Cues and Additive Manufacturing”. **R Duffy** and AW Feinberg. McGowan Institute for Regenerative Medicine Retreat, Rapid Fire Trainee Presentation. Nemaclin Woodlands, March 2016.
- “Engineering Laminin Micropatterned Surfaces to Maximize the Alignment and Contractility of Skeletal Muscle Tissue”. **Duffy R** and Feinberg AW. Biomedical Engineering Society Annual Meeting, Seattle, WA, September 2013.

Posters:

- "Using micropatterned laminin lines to increase human myotube density and alignment". **R Duffy**. Y Sun. AW Feinberg. World Biomaterials Congress. Montreal, QC. May 2016
- “Using Micropatterned Extracellular Matrix Cues to Guide Murine and Human Myotube Formation”. **R Duffy**, Y Sun, AW Feinberg. McGowan Institute for Regenerative Medicine Retreat, Nemaclin Woodlands, March 2016.
- “Tracking Cell-Generated Compaction Strains in 3D Tissue Using Fibronectin Based Nanomechanical Biosensors”. S Liu, A Tsamis, **R Duffy**, T Hinton, AW Feinberg. Biomedical Engineering Society Annual Meeting, Tampa, FL, October 2015.
- “Maintaining In Vitro Myotube Cultures by Genipin Modification of Micropatterned Fibronectin Lines” S Chang, **R Duffy**, AW Feinberg. Biomedical Engineering Society Annual Meeting, Tampa, FL, October 2015.
- “Skeletal Muscle Thin Films: A Tool for Understanding the Effect of 2D Extracellular Matrix Cues on Myotube Density, Alignment, and Contractility”. **R Duffy**, Y Sun, A Feinberg. TERMIS World Congress, Boston, MA, September 2015.
- “Development of Spatially Patterned Extracellular Matrix Cues to Direct the Differentiation and Alignment of Human Skeletal Muscle Tissue” **R Duffy**, L Friedman, AW Feinberg. Biomedical Engineering Society Annual Meeting, San Antonio, TX, October 2014.

- “Engineering ECM Composition and Geometric Patterning to Maximize Skeletal Muscle Myogenesis and Contractility” **R Duffy**, Y Sun, A Feinberg Gordon Research Conference: Signal Transduction by Engineered Extracellular Matrices, Bentley University, July 2014.
- “Extracellular Matrix Composition Influences Differentiation and Contractility of Human Skeletal Muscle Constructs In Vitro” **R Duffy**, L Friedman, AW Feinberg. McGowan Institute for Regenerative Medicine Retreat, Nemaquin Woodlands, March 2014.
- “Engineering Skeletal Muscle via Micropatterning Techniques for Optimization of Structure and Contractility” **R Duffy**, Y Sun, A Feinberg. McGowan Institute for Regenerative Medicine Retreat, Nemaquin Woodlands, March 2013.

